



HAL
open science

Decomposition of the scattered field into singularities for object classification using artificial intelligence algorithms

Yasmina Yehia Aly Hassan Zaky

► **To cite this version:**

Yasmina Yehia Aly Hassan Zaky. Decomposition of the scattered field into singularities for object classification using artificial intelligence algorithms. Machine Learning [cs.LG]. Université Côte d'Azur, 2022. English. NNT: 2022COAZ4007 . tel-03664747

HAL Id: tel-03664747

<https://theses.hal.science/tel-03664747>

Submitted on 11 May 2022

HAL is a multi-disciplinary open access archive for the deposit and dissemination of scientific research documents, whether they are published or not. The documents may come from teaching and research institutions in France or abroad, or from public or private research centers.

L'archive ouverte pluridisciplinaire **HAL**, est destinée au dépôt et à la diffusion de documents scientifiques de niveau recherche, publiés ou non, émanant des établissements d'enseignement et de recherche français ou étrangers, des laboratoires publics ou privés.

THÈSE DE DOCTORAT

Pré-traitement par décomposition en singularités du champ diffracté pour la classification d'objets par des algorithmes d'intelligence artificielle

Yasmina Zaky

Laboratoire d'Electronique, Antennes et Télécommunications (LEAT)

**Présentée en vue de l'obtention
du grade de docteur en électronique**
d'Université Côte d'Azur

Dirigée par : Jean-Yves Dauvignac

Co-encadrée par : Nicolas Fortino

Soutenue le : 25 Mars 2022

Devant le jury, composé de :

Amélie Litman, Maître de conférences,
Université Aix-Marseille

Benoît Miramond, Professeur des
universités, Université Côte d'Azur

Cyril Decroze, Professeur des universités,
Université de Limoges

Herve Aubert, Professeur des universités,
Institut National Polytechnique de Toulouse

Jean-Yves Dauvignac, Professeur des
universités, Université Côte d'Azur

Nicolas Fortino, Maître de conférences,
Université Côte d'Azur

Pré-traitement par décomposition en singularités du champ diffracté pour la classification d'objets par des algorithmes d'intelligence artificielle

Jury :

Président

Cyril Decroze, Professeur des universités, Université de Limoges

Rapporteurs

Amelie Litman, Maître de conférences, Université Aix-Marseille

Hervé Aubert, Professeur des universités, Institut National Polytechnique de Toulouse

Examineurs

Benoit Miramond, Professeur des universités, Université Côte d'Azur

Jean-Yves Dauvignac, Professeur des universités, Université Côte d'Azur

Nicolas Fortino, Maître de conférences, Université Côte d'Azur

Résumé

La détection et l'identification d'objets à partir de leurs champs diffractés ultra-large bande est l'une des applications du radar. En effet, des travaux de ce type ont été initiés par C.E. Baum qui a proposé d'appliquer des méthodes d'expansions en singularités (SEM) au champ diffracté d'un objet éclairé par une onde incidente large bande. L'extraction et l'étude des pôles de résonance de ces signaux mesurés permet de distinguer les différents objets par l'identification des pôles naturels qui leur sont propres. Dans cette thèse, la SEM est explorée afin d'établir un modèle compact qui représente, avec précision, le champ diffracté ultra-large bande d'un objet indépendamment de l'angle d'observation et de son orientation. Dans cette optique, plusieurs techniques SEM ont été comparées : TLS Matrix Pencil pour des signaux dans le domaine temporel, TLS Cauchy et Vector Fitting pour des signaux dans le domaine fréquentiel.

Suite à la discrimination fréquentielle des objets issue des pôles obtenus par la SEM, des techniques de classification supervisées de type Machine Learning et Deep Learning sont appliquées pour classer les différents objets en fonction de leurs paramètres caractéristiques. Ainsi, différents algorithmes de classification ont été étudiés : Support Vector Machine (SVM), Decision Tree (DT), réseaux de neurones multicouches (MLP) et réseaux de neurones convolutifs (CNN). Cette étude montre que l'association d'une technique SEM la plus robuste au bruit avec des classifieurs à base de réseaux de neurones permet de classer la forme ou la matière d'un objet à partir d'une seule mesure et avec un faible cout de calcul. De plus, on propose une procédure qui permet de déterminer la direction de l'antenne de réception et l'orientation d'un objet à partir des résidus qui sont associés à chaque pôle de résonance. Cette procédure de classification avec des données issues de la SEM est très prometteuse en particulier lorsqu'il s'agit de généraliser à des données non incluses dans l'ensemble d'apprentissage.

Mots clés— Champs diffractés ULB, Décomposition en singularités, Vector Fitting, Classification d'objets, Machine Learning, Deep Learning

Abstract

One of the applications of radar is the detection and identification of objects from their ultra-wideband scattered field response. Indeed, work of this type was initiated by C.E. Baum who proposed to apply the singularity expansion methods (SEM) to the scattered field of an object illuminated by a broadband incident wave. The extraction and study of the resonant poles of these measured signals allows to distinguish different objects by identifying their natural poles. In this thesis, the SEM is explored in order to establish a compact model that accurately represents the ultra-wideband scattered field of an object independently of the observation angle and its orientation. In this perspective, several SEM techniques were compared: TLS Matrix Pencil for time domain signals, TLS Cauchy, and Vector Fitting for frequency domain signals.

Following the frequency discrimination of objects obtained by the SEM technique, supervised classification algorithms of the Machine Learning and Deep Learning type are applied to classify different objects from their characteristic parameters. Hence, several classification algorithms have been studied: Support Vector Machine (SVM), Decision Tree (DT), Multi-Layer Perceptron (MLP) and Convolutional Neural Network (CNN). This study shows that the combination of a noise-robust SEM technique with neural network-based classifiers allows to classify the shape or the material of an object from a single measurement and with a low computational cost. Moreover, we propose a procedure that allows to determine the direction of the receiving antenna and the orientation of an object from the residues that are associated with each resonant pole. This classification procedure using data from the SEM is very promising especially when generalizing to data not included in the training set.

Keywords— Scattered field, Singularity expansion method, Vector Fitting, Object classification, Machine Learning, Deep Learning

Acknowledgements

I would like to thank Cyril Decroze, professor at the Xlim research institute in Limoges, for his interest in my work and for granting me the honour of chairing the jury of my thesis.

I would like to express my gratitude to Hervé Aubert, professor at the Institut National Polytechnique de Toulouse, and to Amelie Litman, associate professor at Aix-Marseille Université, who have agreed to act as reviewers for this work. I thank them for their careful reading of my manuscript and their constructive remarks.

A very special thank you to Benoit Miramond, professor at the Université Côte d'Azur, for accepting to be a member of the jury of my thesis and for his kind help and remarks.

Many thanks to Claire Migliaccio, professor at the Université Côte d'Azur and head of the doctoral school EDSTIC, for her presence amongst my jury.

I would like to thank my thesis director, Jean-Yves Dauvignac, Professor at the Université Côte d'Azur, for having opened the doors of the research world to me. I thank him for being so attentive, his availability, his precious advice and above all the trust he has placed in me. It has been an immense honour working with him.

I also wish to thank my co-supervisor, Mr Nicolas Fortino, associate professor at the Université Côte d'Azur, for his guidance throughout this thesis, his kindness, and his availability in difficult moments. It was a great pleasure for me to share these moments with him.

To the Factas team of INRIA, Mr. Fabien Seyfert, Mme Martine Olivi, Mr. Laurent Baratchart, Mme Juliette LeBlond and Mr. Sylvain Chevillard, thanks everyone for our collaboration and the interest you placed in my work.

Many thanks to Robert Staraj, the director of LEAT, for having welcomed me during the last years in the laboratory. And of course, I do not forget all the permanent staff and doctoral students of LEAT with whom I have shared all these moments of doubt and pleasure.

To my parents, Yehia and Sherine, I cannot thank them enough for everything they have done and continue to do for me regardless of the distance. It is only thanks to them that I have achieved so much. To my brother Aly, his wife

Nagwan, and to all my family, thanks for always encouraging me and being there for me.

Last but not least, I would like to thank my best friend Heba for her genuine support and encouragement throughout my PhD journey. She has always been there to share moments of joy and sadness. I also thank her for her incredible patience and her unconditional friendship.

A very special thought to Nassim with whom I have shared unforgettable moments during these last few years.

Contents

Abstract	vii
Acknowledgements	ix
1 General introduction	1
1.1 Objectives	3
1.2 Contributions	4
1.3 Thesis outline	5
2 Theoretical background	7
2.1 Introduction	7
2.2 Feature extraction techniques from UWB signals	8
2.3 Singularity Expansion Method	11
2.4 SEM in Time domain	14
2.4.1 Matrix Pencil	14
2.4.2 Late time / Early time separation	18
2.5 SEM in frequency domain	19
2.5.1 TLS Cauchy	19
2.5.2 Vector Fitting	22
2.5.3 Selection of physical poles	24
2.6 Representation using the Q-factor and resonant frequencies	25
2.7 Validation of SEM using a synthetic signal	26
2.7.1 Extraction in a noiseless environment	27
2.7.2 Extraction in a noisy environment	28
2.8 Conclusion	30
3 Characterization of objects from their natural resonances	33
3.1 Introduction	33
3.2 Scattered field simulation setup	34
3.2.1 Analytical solution	35
3.2.2 Numerical full wave simulation	36
3.3 SEM applied to the scattered field of a PEC sphere	38

3.3.1	Phase compensation in frequency domain	39
3.3.2	Early and late time separation	41
3.3.3	Comparison between VF, TLS Cauchy and TLS MP meth- ods regarding poles extraction	44
3.3.3.1	Poles extraction from backscattered field	44
3.3.3.2	Sensitivity of SEM to phase variations in frequency domain	47
3.3.3.3	Extraction of poles from multiple observation angles	47
3.3.3.4	Poles extraction results for different sphere sizes	49
3.3.4	Study of the robustness to noise	49
3.3.5	Discussion and interpretation of the physical poles and their residues	54
3.3.5.1	Physical and mathematical poles	54
3.3.5.2	Comparison between residues and scattered field	55
3.4	SEM applied on the scattered field of a thin wire	60
3.4.1	Comparison between VF, TLS Cauchy and TLS MP meth- ods regarding poles extraction	62
3.4.2	Study of the robustness to noise	64
3.4.3	Discussion and interpretation of the physical poles and their residues	66
3.4.3.1	Physical and mathematical poles	66
3.4.3.2	Comparison between residues and scattered field	66
3.5	Conclusion	74
4	Classification of objects using their EM signatures	77
4.1	Introduction	77
4.2	Supervised Learning Techniques	78
4.2.1	Multi-class SVM	78
4.2.2	Decision Tree	81
4.2.3	Artificial Neural Network	81
4.3	Classification of the sphere's material	83
4.3.1	Dataset construction	84
4.3.1.1	Scattered Field dataset	86
4.3.1.2	SEM dataset	87
4.3.2	Training Phase	88
4.3.2.1	Multi-class SVM	89
4.3.2.2	Decision Tree	89

4.3.2.3	Artificial Neural Networks	89
4.3.3	Test Phase	93
4.3.4	Noisy test data	96
4.3.5	Generalization using different sphere sizes	98
4.3.5.1	Noiseless responses	98
4.3.5.2	Noisy responses	101
4.3.6	Discussion	101
4.4	Normalization of the resonant frequencies	103
4.5	Classification of spherical and non-spherical objects	104
4.5.1	NN training results	107
4.5.2	Classification results	107
4.6	Calculation of object dimensions	112
4.7	Conclusion	112
5	Identification of the object's orientation	115
5.1	Introduction	115
5.2	Geometrical definition of the problem	116
5.2.1	Detection of the angular sector	116
5.2.2	Rotation of the antenna around the scattered wave direction	117
5.3	Identification of angular sector for spherical objects	118
5.3.1	Dataset Construction	118
5.3.1.1	Scattered Field dataset	118
5.3.1.2	Residues dataset	119
5.3.2	Training Phase	120
5.3.2.1	Multi-class SVM	121
5.3.2.2	Decision Tree	121
5.3.2.3	Artificial Neural Networks	121
5.3.3	Test Phase	125
5.3.4	Noisy data	125
5.3.5	Generalization using different sphere sizes	127
5.3.5.1	Noiseless responses	127
5.3.5.2	Noisy responses	128
5.3.6	Optimization of dataset construction	129
5.4	Identification of angular sectors for non spherical objects	131
5.4.1	Thin wire	132
5.4.2	Rectangular solid	134
5.4.3	Discussion	138
5.5	Calculation of object orientation	139

5.6	Case study: cylinder with one hemispherical end	141
5.7	Conclusion	145
6	General Conclusion	147
6.1	Thesis objectives review	147
6.2	Thesis contributions summary	147
6.3	Thesis limitations and perspectives	149
	Bibliography	151
A	Extraction of poles from the E_ϕ component	161
B	Comparisons between residues extracted by TLS MP and VF	167
C	Resonances of non spherical PEC objects	169
D	Scattered field dataset construction	173
E	Angular sector classification	175

List of Figures

2.1	Early and late time responses of an arbitrary object.	12
2.2	Reconstructed impulse and frequency responses using the set of fixed poles and residues.	28
2.3	Poles extraction using VF, TLS Cauchy and TLS MP for multiple model orders	29
2.4	(a) Reconstruction error as a function of SNR; (b) CNRs extracted at 10 dB SNR	29
3.1	Thin wire along z axis illuminated using a plane EM wave with incident wave vector \vec{k}_{inc}	35
3.2	Sphere illuminated using a plane EM wave travelling along $z > 0$	36
3.3	(a) Amplitude and (b) unwrapped phase of the back-scattering response of a PEC sphere of 15 cm diameter using CST and HFSS simulation tools and analytical solutions (Mie)	37
3.4	Amplitude of the scattered field (E_θ) of the PEC sphere and thin wire in the back-scattering direction when illuminated with a normal incident.	38
3.5	Theoretical poles of a PEC sphere of 15cm diameter computed from Mie theory. The damping factors α are presented on the ordinate as a function of resonant frequencies on the abscissa.	39
3.6	(a) Amplitude of the power spectrum in the back-scattering direction; (b) Poles extracted using VF with $M = 40$ (M is the model order).	40
3.7	Theoretical and over-compensated phase of a PEC sphere of 15 cm diameter.	41
3.8	Impulse response of the back-scattered field for a PEC sphere with a diameter of 0.15 m.	42
3.9	CNRs extracted from the back-scattered field for windows with different time width.	43

3.10	Normalized singular values of the PEC sphere extracted from the back-scattered field for windows with different time widths.	44
3.11	Poles extraction using VF and TLS Cauchy for multiple model orders varying from 16 to 26.	45
3.12	Estimated Physical CNRs of a 0.15 m diameter PEC sphere compared with the theoretical ones.	46
3.13	Mean relative error versus channel compensation distance.	48
3.14	CNRs extracted from a 15 cm diameter PEC sphere by using VF on different directions of observation.	48
3.15	Poles distribution for EC spheres of different sizes.	50
3.16	(a) Poles estimated for a 65 dB SNR; (b) Relative error for 65 dB SNR; (c) Poles estimated for 30 dB SNR; (d) Relative error for 30 dB SNR.	51
3.17	Mean relative error of poles for different iterations using VF when applying 30 dB SNR.	52
3.18	(a) Frequency domain reconstruction using estimated poles from Cauchy and VF for 30 dB SNR; (b) Late Time response reconstruction using MP for 30 dB SNR.	52
3.19	Poles extracted using VF for 65 & 30 dB SNR when taking into account all observation angles of the scattered field.	53
3.20	Mean relative error versus the number of input data (observation angles) using VF.	53
3.21	Scattered field reconstruction error versus the model order values for VF and TLS Cauchy.	54
3.22	Comparison between the amplitude of the back-scattered field response and the reconstruction using only physical poles.	55
3.23	Early and late time reconstruction (Rec) using mathematical and physical poles respectively.	56
3.24	Normalized amplitude of scattered field, scattered field from late time response only and residues related to the first resonant frequency ($f_1 = 0.55 \text{ GHz}$).	57
3.25	Normalized amplitude of scattered field, scattered field from late time response only and residues related to the second resonant frequency ($f_2 = 1.15 \text{ GHz}$).	58
3.26	Normalized amplitude of scattered field, scattered field from late time response only and residues related to the third resonant frequency ($f_3 = 1.75 \text{ GHz}$).	59
3.27	Theoretical CNRs of a thin wire of 15 cm length.	60

3.28	(a) Back-scattered impulse response at normal incidence and (b) singular values distribution extracted for windows at multiple time steps.	61
3.29	CNRs extracted using VF, TLS Cauchy and TLS MP for two incident angles	62
3.30	Back-scattered field of a thin wire for both incident directions. . .	63
3.31	Mean relative error for different phase errors of a thin wire.	63
3.32	Plan wave impinging at 45° on the thin wire: (a) Poles estimated for a 65 dB SNR; (b) Relative error for 65dB SNR; (c) Poles estimated for 30 dB SNR; (d) Relative error for 30dB SNR.	64
3.33	Thin wire's (a) frequency domain reconstruction using estimated poles from Cauchy and VF at 30 dB SNR, and (b) late Time reconstruction using MP at 30 dB SNR.	65
3.34	Poles extracted for 65 & 30 dB SNR for all 37 directions of the thin wire.	66
3.35	Early and late time reconstruction (Rec) using mathematical and physical poles respectively.	67
3.36	Normalized amplitude of scattered field, late Time and residues related to the first resonant frequency ($f_1 = 0.9 \text{ GHz}$) of the thin wire for an incidence of 45°	68
3.37	Normalized amplitude of scattered field, late Time and residues related to the third resonant frequency ($f_3 = 2.9 \text{ GHz}$) of the thin wire for an incidence of 45°	69
3.38	Normalized amplitude of scattered field, late Time and residues related to the fifth resonant frequency ($f_5 = 4.9 \text{ GHz}$) of the thin wire for an incidence of 45°	70
3.39	Normalized amplitude of scattered field, late Time and residues related to the first resonant frequency ($f_1 = 0.9 \text{ GHz}$) of the thin wire for normal incidence.	71
3.40	Normalized amplitude of scattered field, late Time and residues related to the third resonant frequency ($f_3 = 2.9 \text{ GHz}$) of the thin wire for normal incidence.	72
3.41	Normalized amplitude of scattered field, late Time and residues related to the fifth resonant frequency ($f_5 = 4.9 \text{ GHz}$) of the thin wire for normal incidence.	73
4.1	Optimal hyperplane separation for a linearly separable bi-class classification	79
4.2	Decision Tree classifier diagram	81

4.3	Amplitude of the frequency response in the back-scattering direction for the 5 classes of spheres. The diameter of the spheres is 10 <i>cm</i>	84
4.4	(a) The first five natural poles and (b) Q-factors as a function of natural frequency of the 5 spheres of 10 cm diameter.	85
4.5	Impulse response of 10 cm diameter sphere (a) PEC and (b) dielectric with permittivity 4	87
4.6	SVM learning parameters when using rbf kernel function with: (a) FD data, (b) TD data and (c) SEM data. * indicates the optimum values chosen.	90
4.7	Decision tree flowchart when DT algorithm is learning with: (a) FD data, (b) TD data and (c) SEM data	91
4.8	Train and validation accuracy vs number of epochs when CNN classifier is learning with: (a) FD data, (b) TD data and (c) SEM data. 400 epochs are used with FD and TD data, while 100 epochs are used with SEM data.	92
4.9	(a) Mean accuracy of the 5 spheres; (b) number of parameters vs. number of neurons in one hidden layer for the 3 datasets.	94
4.10	Test results for the 3 cases of SEM datasets construction using MLP classifier while varying # neurons.	95
4.11	Accuracy (%) of noisy data when testing several classifiers using the different datasets	98
4.12	Accuracy (%) of 19 and 30 cm diameter spheres using all classifiers with all datasets	99
4.13	Accuracy (%) for the 30 cm diameter spheres' noisy responses at various SNRs when using CNN classifier with the different datasets	102
4.14	Accuracy (%) of noisy responses for smaller spheres having 1 resonance in the frequency band at various SNRs when using CNN classifier with the different datasets	102
4.15	Normalized confusion matrix using CNN classifier when testing 20% remaining samples of : (a) non normalized frequencies and (b) normalized frequencies	104
4.16	Normalized confusion matrix using CNN classifier when testing generalization at 10 dB SNR for spheres of 30 cm diameter of : (a) non normalized frequencies and (b) normalized frequencies	105

4.17	Normalized confusion matrix using CNN classifier when testing generalization at 10 dB SNR for spheres having 1 resonance in frequency band of : (a) non normalized frequencies and (b) normalized frequencies	105
4.18	Amplitude response of a thin wire and a cube of size = 10 cm when simulated using CST and interpolated	107
4.19	Train and validation's accuracy for CNN classifiers vs number of epochs when learning with: (a) FD data, (b) TD data and (c) SEM data. 800 epochs are used with FD and TD data, while 200 epochs are used with SEM data	108
4.20	Normalized confusion matrix using CNN classifier when testing 20% remaining samples of: (a) FD data, (b) TD data and (c) SEM data.	111
4.21	Accuracy (%) of noisy responses of objects' dimension included in the training phase at various SNRs when using CNN classifier with the different datasets	111
4.22	Simulation of a PEC cube of unknown size	113
4.23	Amplitude response of the PEC cube	113
5.1	Coordinate system for an antenna radiation pattern (Balanis, 2005).	116
5.2	Rotation of the incident field by an angle α around the travelling direction of the wave.	117
5.3	Sphere's angular sectors.	119
5.4	Residues amplitude associated to the first resonant frequency for PEC spheres of 3 different diameters.	120
5.5	SVM learning parameters when using rbf kernel function with: (a) FD data, (b) TD data and (c) residues data. * illustrates the selected optimum values.	122
5.6	Decision tree flowchart-like tree structure when learning with the three datasets.	123
5.7	Train and validation accuracy for CNN classifiers when learning with the three datasets.	124
5.8	Accuracy (%) of noisy data when identifying the angular sectors of a PEC sphere.	126
5.9	Accuracy (%) of angular sectors classification of larger PEC spheres.	127
5.10	Angular classification accuracy (%) of a 30 cm diameter PEC spheres at various SNRs when using CNN classifier with the three datasets	129

5.11	Angular classification accuracy (%) of noisy responses of a smaller PEC sphere having 1 resonance at various SNRs when using CNN classifier with the three datasets	129
5.12	E_θ Amplitude response of a thin wire orientated along z axis, when illuminated with a normal incident wave having different polarizations.	132
5.13	Accuracy (%) on the 20% remaining samples of thin wire when using CNN.	133
5.14	Accuracy (%) of noisy data of the thin wire at different SNRs when using CNN.	134
5.15	Accuracy (%) of generalization to noiseless data of larger and smaller thin wires when using CNN.	134
5.16	Normalized confusion matrices of noisy data when identifying the angular sectors of the thin wire using residues for two different sizes.	135
5.17	Rectangular solid when partitioned into (a) 8 sectors and then (b) 10 sectors.	136
5.18	Accuracy (%) on the 20% remaining samples of rectangular solid when using CNN.	137
5.19	Accuracy (%) of noisy data of the rectangular solid at different SNRs when using CNN.	137
5.20	Accuracy (%) of generalization to noiseless data of larger and smaller rectangular solids when using CNN.	138
5.21	Normalized confusion matrices of noisy data when identifying the angular sectors of the rectangular solid using residues for two different sizes not included in the datasets.	138
5.22	Rotation of the incident wave (left) and the object (right) by an angle α with respect to the object and the antenna axis respectively.	140
5.23	The simulated PEC cylinder with a hemispherical end oriented along z axis	142
5.24	(a) Amplitude response of E_θ in the back-scattering direction and (b) the first 5 CNRs of the cylinder with a hemispherical end	142
5.25	Train and validation accuracy for CNN classifier when trained using residues of the new object	143
5.26	Normalized confusion matrix of the 20% remaining samples used during the test phase	144
5.27	Amplitude response at different supplementary observation angles of the cylinder with a hemispherical end	144

5.28	Estimated angle α computed for each observation angle and at two SNR values.	145
A.1	Impulse response and amplitude response of E_ϕ of the PEC sphere in the back-scattering direction	162
A.2	Estimated Physical poles of 0.15 m diameter sphere compared with the theoretical ones	162
A.3	Normalized amplitude of scattered field, scattered field from late time response only and residues related to the first resonant frequency ($f_1 = 0.55 \text{ GHz}$)	163
A.4	Normalized amplitude of scattered field, scattered field from late time response only and residues related to the second resonant frequency ($f_2 = 1.15 \text{ GHz}$).	164
A.5	Normalized amplitude of scattered field, scattered field from late time response only and residues related to the third resonant frequency ($f_3 = 1.75 \text{ GHz}$).	165
B.1	Residues' amplitude related to the first resonant frequency ($f_1 = 0.55 \text{ GHz}$) extracted using (a) MP and (b) VF	167
B.2	Residues' amplitude related to the second resonant frequency ($f_2 = 1.15 \text{ GHz}$) extracted using (a) MP and (b) VF	168
B.3	Residues' amplitude related to the third resonant frequency ($f_3 = 1.75 \text{ GHz}$) extracted using (a) MP and (b) VF	168
B.4	Residues' amplitude related to the fourth resonant frequency ($f_4 = 2.35 \text{ GHz}$) extracted using (a) MP and (b) VF	168
C.1	Non spherical PEC objects.	169
C.2	Amplitude response and CNRs of E_ϕ of the metal ring in the back-scattering direction	170
C.3	Amplitude response and CNRs of the thick cylinder in the back-scattering direction	170
C.4	Amplitude response and CNRs of an ovoid in the back-scattering direction	171
C.5	Amplitude response and CNRs of a cube in the back-scattering direction	171
C.6	Amplitude response and CNRs of a rectangular solid in the back-scattering direction	172
C.7	Amplitude response and CNRs of a pyramid in the back-scattering direction	172

List of Tables

2.1	CNRs and residues used to construct the synthetic signal	27
4.1	Diameters (cm) of spheres versus the number of resonances (N) for each sphere class	86
4.2	Selected parameters of SVM classifier according with the datasets	89
4.3	Time consumption (sec.) of the four classifiers trained using the different datasets	94
4.4	Accuracy (%) and standard deviation σ_d of each classifier when using the 3 cases of SEM data	95
4.5	Accuracy (%) of the 20% test sets when using the four classifiers with the four datasets	96
4.6	Sens and Spec (%) for SNR = 10 dB using CNN with the different datasets	97
4.7	Sens and Spec (%) of 30 cm diameter sphere using CNN with the different datasets	99
4.8	Smaller sphere diameters (cm) used for testing the generaliza- tion ability of the classifiers	100
4.9	Accuracy (%) for different number of resonances (N) using all classifiers with the different datasets	100
4.10	Sens and Spec (%) for $N=1$ resonance using CNN with noiseless responses	101
4.11	Dimension properties and the propagating directions of the inci- dent wave of each simulated object	106
4.12	Accuracy results of the generalization of noiseless and noisy re- sponses from larger object sizes (30 cm) and smaller objects hav- ing 1 resonance in the frequency band	109
5.1	Parameters of SVM classifier for angular sector classification . . .	121
5.2	Accuracy (%) of angular sectors classification for the 20% test sets	125
5.3	Accuracy (%) of angular sectors classification for different num- ber of resonances N of the PEC sphere	128

5.4	Comparison of the accuracy obtained using residues from the old dataset having 13 sphere sizes and the new dataset with only one sphere size	130
D.1	Accuracy (%) and σ_d of CNN trained using each dataset of FD data	173
E.1	Accuracy (%) of angular sectors classification of different test data for the 5 spheres using CNN classifier trained using SEM data	175
E.2	Accuracy (%) of angular sectors classification of different test data for the non spherical PEC objects using CNN classifier trained with SEM data	176

List of Abbreviations

AI	Artificial Intelligence
ANN	Artificial Neural Network
AR	Axial Ratio
AWGN	Additive White Gaussian Noise
CNN	Convolutional Neural Network
CNR	Complex Natural Resonance
DL	Deep Learning
DT	Decision Tree
EM	Electro-Magnetic
ESPRIT	Estimation Signal Parameters Rotational Invariance Technique
FD	Frequency Domain
FFT	Fast Fourier Transform
IFFT	Inverse Fast Fourier Transform
LS	Least Square
LTI	Linear Time Invariant
ML	Machine Learning
MLP	Multi-Layer Perceptron
MP	Matrix Pencil
NN	Neural Network
NRF	Normalized Resonant Frequency
PCA	Principal Component Analysis
PEC	Perfect Electric Conductor
Q-factor	Quality factor
RCS	Radar Cross Section
RBF	Radial Basis Function
ReLU	Rectified Linear Unit
SEM	Singularity Expansion Method
SF	Scattered Field
SNR	Signal-to-Noise Ratio

SVD	Singular Value Decomposition
STMP	Short Time Matrix Pencil
SVM	Support Vector Machine
TD	Time Domain
TLS	Total Least Square
UWB	Ultra-Wide Band
VF	Vector Fitting

Author's publication list

Pre-Print

- Yasmina Zaky et al. (June 2021c). *Submitted: Generalization Ability of Deep Learning Algorithms Trained using SEM Data for Objects Classification*. URL: https://www.techrxiv.org/articles/preprint/Generalization_Ability_of_Deep_Learning_Algorithms_Trained_using_SEM_Data_for_Objects_Classification/14706390/1.

International Conferences

- Yasmina Zaky et al. (2021b). “Objects classification based on UWB scattered field and SEM data using machine learning algorithms”. In: *2021 18th European Radar Conference (EuRAD)*.
- Y. Y. Zaky et al. (2020). “Comparison of SEM methods for poles estimation from scattered field by canonical objects”. In: *IEEE Radar Conference (RadarConf20)*, pp. 1–6. DOI: [10.1109/RadarConf2043947.2020.9266410](https://doi.org/10.1109/RadarConf2043947.2020.9266410).

National Conferences

- Yasmina Zaky et al. (2022). “Classification d’objets à partir de leurs signatures électromagnétiques en utilisant les réseaux neuronaux convolutifs”. In: *Journées Nationales Microondes (JNM2022)*.
- Yasmina Zaky et al. (2021a). *Classification d’objets à partir de leurs résonances en utilisant les réseaux neuronaux*. Neuvième Conférence Plénière du GDR ONDES. Poster. URL: <https://hal.archives-ouvertes.fr/hal-03485167>.

Presentations

- Y. Zaky, N. Fortino, and J-Y. Dauvignac (2021). “Classification by Deep Learning and SEM”. in: *Webinaire Groupement De Recherche (GDR) Ondes*.

- Yasmina Zaky (2020). In: *Ma thèse en 180 secondes*. URL: <https://youtu.be/N6Wy7rNYIzs>.

Chapter 1

General introduction

Radar (Radio Detection and Ranging) is universally known for radio detection and was introduced around the year 1935. As the name indicates, a radar system uses radio signals to detect targets. Its first developments took place during the Second World War and since then, it has continued to develop technologically and in terms of applications. For many years, the applications of radar were only in the military domain. However, the radars have found several applications in the civilian field, such as navigation aids, anti-collision, speed control, vision in robotics, surveillance, imaging and finally meteorology.

The primary reason for developing a radar was to detect the presence of passive objects by using their radio echoes to determine their positions. The process involved in a radar is to emit an electromagnetic wave; a part of which is reflected by obstacles and creates a back-scatter wave which is detected with a receiving module. By calculating the round-trip time of the wave, we can deduce the distance to the detected obstacle. Other radars can also perform target recognition or tracking. The most traditional radar technologies are correlation radars, pulse radars and frequency modulated continuous wave radars.

The classification and recognition of targets using a radar has become very popular in the past years (Jouny, Garber, and Ahalt, 1993). The purpose of classification is to divide a set of elements into several categories, called classes. The motivation behind integrating a classification module in a radar is due to: first, the desire to know more about a detected target than just its presence, both in military and in a variety of civilian radars; and second, the potential for the application of target classification techniques to many research areas, including geophysical and meteorological applications. The developments made in this area has led to the emergence of several new techniques capable of meeting this need. Thus, artificial intelligence (AI) and the study of its various techniques has become a popular trend among researchers in different fields. One of the

most developed AI forms that has led to its rapid development is artificial neural network (ANN) that mimics the human brain mechanism. Although neural models have been attracting a lot of interest in recent years, they date back to the 1940s with the advent of the first computer.

As for ensuring the proper operation of the radar, it must be able to provide both appropriate spatial resolution and sufficient penetration depth for the intended application. Most of the traditional radar systems employ narrow-band signals, which means that the resolution is poor as the bandwidth is relatively small. Those signals are mostly used for the detection of objects as they can be easily generated. However, with recent electronic developments, the need for more advanced applications, like target recognition, have increased. In fact, the ability of a radar to recognize objects depends on several parameters : the bandwidth, the central frequency associated with this bandwidth (the wavelength), and spatial diversity, a combination of which can enhance the recognition resolution. Thus, narrow-band signals have insufficient information on target characteristics due to the small bandwidth, leading to reduced efficiency in target classification and recognition, and, in that case, it is beneficial to have spatial diversity of the measurements for a better target recognition. Hence, to circumvent the need for spatial diversity, development of a technology that uses wider bandwidth to gather more data about the target, and benefit from spectral diversity, is needed.

Unlike conventional radar systems that use narrow-band signals, Ultra-Wide Band (UWB) radars transmit short electromagnetic (EM) signals across a bandwidth greater than 25 percent of the center frequency. They appeared in the 1960's where the use of EM waves in time domain was undertaken experimentally when microwave circuit operation in the time regime was mastered (Bennett and Ross, 1978). With UWB pulses, the spatial resolution is high, and they can penetrate dielectric materials. Moreover, by using very short pulses, it is easier to separate the responses of different objects. The uses for radars in the UWB domain range from applications in the military fields, such as the detection of buried landmines, to civilian fields, such as medical imaging, ground penetrating radars, and materials characterization. With technological advancements, it has become possible to use UWB radar for target recognition and classification as the radar's large bandwidth enables more information and a higher probability of target detection by analyzing the signal spectrum.

Classification using Machine Learning (ML) and Deep Learning (DL) algorithms, that are both sub-branches of AI, have been receiving much attention

in recent years. In fact, multiple data types have been exploited for target classification, which can be broken into two categories: raw data and pre-processed data. In the first category, we find Radar Cross Section (RCS) responses that can be directly used to classify different objects or human targets (Bufler, Narayanan, and Dogaru, 2015). In addition, Micro-Doppler measurements are used for the detection of humans and the classification of moving targets or human activities (Yinan Yang et al., 2006; Hadhrami et al., 2018). However, those measurements usually depend upon the angle of observation making the classifiers sensible to a change in the object orientation or in the position of the antenna. Additionally, as the frequency band is very wide, there is a huge amount of data contained in those measurements.

Pre-processing has many interests, one of which is to perform identification and classification in a different space from that of the measurement. Thus, radar imaging techniques can be applied to generate pre-processed data. The Synthetic Aperture Radar (SAR) or inverse SAR (ISAR) images are deployed for classification (Chapelle, Haffner, and Vapnik, 1999; Schwegmann et al., 2017; Ning, Chen, and Zhang, 2003). This requires the acquisition of many measurements to construct an image, which generates large databases and constitutes huge computational time in terms of measurements. Furthermore, while the previous techniques can deliver high accuracy results in target classification, they still require the use of large classifiers as they contain significant amount of data. Therefore, it is beneficial to implement a method that permits to recognize and classify objects from few parameters and from a single measurement. To compact these information, solutions are being explored, in particular the use of natural resonance frequencies of objects.

1.1 Objectives

The objective of this thesis is to apply a pre-processing method allowing the extraction of characteristic parameters of the UWB scattered field for object recognition and classification. This will be done by studying several feature extraction methods and selecting the most suitable one for our application. Then, the selected technique will be used to compress the UWB scattered field from different objects into characteristics parameters that will be combined with various classification algorithms (ML and DL) to classify those objects.

Several feature extraction techniques are available but the extracted parameters are often dependent on the observation angle and the orientation of the object.

The natural resonances are parameters that allow to model the UWB scattered field of a target using the Singularity Expansion Method (SEM) (Baum, 1976). These resonances are intrinsic to the object and are independent of the incident and observation angles, making the SEM a very interesting method in an operational context when the target position is not completely controlled. Those parameters are largely explored for characterization of objects, but rarely for classification.

Indeed, the SEM allows to compress the scattered field data by decomposing it into natural resonant frequencies and residues. Part of the work in this thesis is based on LEAT experience in scattered field measurements and is in the continuation of the thesis of Abdellah Roussafi (Roussafi, 2016), where a compact model representing accurately the antenna radiation characteristics was established, allowing to find the field at various distances with a minimum amount of data. This was achieved by using a double compression technique: the SEM method for frequency/temporal modeling, and the vector spherical wave expansion for spatial modeling. We aim at using only the SEM modeling to characterize and classify different objects.

Therefore, based on the UWB scattered EM field, the objective is to identify and classify objects from their resonances using ML and DL algorithms. In fact, ML techniques, and especially deep learning, have been widely used in image classification (LeCun, Bengio, and Hinton, 2015) and now AI algorithms are showing better performance than human doctors in identifying cancer in X-ray images, not only in speed but also in accuracy. While they have undergone an exciting evolution in recent years, their full potential for radar applications has yet to be explored. That is why, instead of working directly with the raw UWB scattered field, we aim to test several ML and DL algorithms by combining them with pre-processed data from SEM to be able to classify different objects from few parameters and with no angle dependency.

1.2 Contributions

One of the principal limitations of the SEM technique is its sensitivity to noise. Thus, the first contribution in this thesis consists in evaluating different methods which can be used to extract the resonances of an object, in a noisy and noiseless environments, in order to conclude on their robustness. This study will allow to define a protocol for poles extraction and to select the most robust SEM technique.

Indeed, the pole analysis using the SEM is currently used as a compact modeling method to reduce the data required for the characterization of objects. Each extracted pole is associated with its corresponding residue that depends upon observation angle and incident wave. Since the residues are aspect dependent, they are not considered to be characteristic of the object, and to our knowledge they have not been exploited. Thus, the second contribution consists in utilizing these SEM data for classification of several objects by associating them with various classifiers of ML and DL type.

Despite the advantages of SEM, it has hardly been employed for classification, mainly because of its sensitivity to noise, which would lead to decision errors. This thesis will therefore focus on providing solutions, in both the constitution of the datasets, and in the choice of classification algorithms, in order to overcome this drawback and retain only the powerful advantages of the SEM. Particularly, we investigate the use of four algorithms for solving the classification problem, two of which are ML: Support Vector Machine (SVM) and Decision Tree (DT), and the other two are DL: Multi-Layer Perceptron (MLP) and Convolutional Neural Network (CNN). During this phase, we will be able to select the important parameters for classification and highlight their advantages.

Additionally, not only the natural resonances of an object are considered but also the residues associated to each pole. Our last contribution consists in using those residues to determine the orientation of an object and the position of the receiving antenna relative to an object. This will be achieved by, first, studying the residues of several objects and their relationship with the scattered field response. Then, we will proceed by determining the orientation of an object from its residues using the classification algorithms.

1.3 Thesis outline

The remaining part of this thesis manuscript is composed of 5 chapters. First, chapter 2 sets the context of this study. We give a brief description of techniques used to characterize the UWB response of an object. Then, we describe the background of the SEM technique along with its application in radar domain. We also present different algorithms based on SEM technique and used within this work to extract the resonances of objects from their UWB response and validate them on analytical data.

Then, in chapter 3, we present results from the application of those algorithms on the EM field scattered by PEC objects of simple forms. For that, we define

the steps needed to be done in time and frequency domains to accurately extract the complex natural resonances (CNRs) of those objects. Then, we discuss the robustness to noise of those methods. We also study the residues associated to each resonant pole and their spatial distribution.

Following, in chapter 4, we describe a procedure allowing to classify multiple objects using pre-processed data from SEM and to determine their size from their resonant frequency. Different classification algorithms of ML and DL type are presented and used to determine the most robust one. To do so, a study on the structuring of datasets will be carried out using SEM data extracted in chapter 3. In this context, a comparative study on the accuracy and computation time of classification between raw data, in time and frequency domains, and SEM data is conducted. We also evaluate the generalization ability of the algorithms to object sizes and to noisy data not included in the constructed training datasets.

Last but not least, in chapter 5, the residues are explored for the detection and classification of the observation angle and to determine the orientation of each object in relation with the receiving antenna used to collect the scattered field. The classification algorithms will be applied on SEM and raw data to test their generalization capability and their robustness to noisy data.

Finally, we outline the thesis conclusions in chapter 6 and discuss potential future directions.

Chapter 2

Theoretical background

2.1 Introduction

One of the objectives of this thesis is to study feature extraction methods that allow the characterization of an object from its scattered field, and that can be used as a pre-processing step in the classification process. For that, the Ultra-Wide Band (UWB) scattered field of this object can be decomposed into several parameters related to its geometry and material. Indeed, it is possible to derive a unique set of features for each object and create a library of these features. The whole processing system would then be to extract the characteristic parameters from the target response and compare them to the existing library. This comparison will be done by the way of Machine Learning (ML) and Deep Learning (DL) algorithms.

So, in this chapter, we present the context of this work by describing theoretical methods that are used for characterizing the scattered field of an object illuminated by an UWB electromagnetic (EM) wave. First, we give a brief review of techniques commonly used for target identification from their UWB responses. The features extracted using these techniques are known to depend highly on the propagation direction and polarization of the illuminating wave. Second, we present an alternative technique, the Singularity Expansion Method (SEM), that is characterized by its ability to extract specific parameters which are independent of the properties of the incident wave. Then, we describe the methods implemented in this work that can be applied either in time domain or in frequency domain.

Following, we aim to have a first general idea about the performances of each SEM technique using a simple synthetic signal and comparing the extracted poles with analytic ones. To test the robustness of each method, we add noise to the signals and extract the resonances from those noisy signals.

2.2 Feature extraction techniques from UWB signals

The recognition and classification of objects using a radar can be separated into two principal stages: feature extraction and classification. In this section, we focus on the feature extraction stage by introducing some of the most used concepts to recognize an object from its UWB response.

Indeed, illuminating an object by a broadband EM wave results in scattered waves. Multiple ways exist to characterize an object from its UWB scattered wave. Raw radar data, like the Radar Cross Section (RCS) (Taylor, 1995), can be used to quantify the intensity of the scattered wave in a specific direction. In fact, raw data depend on multiple parameters such as: travelling direction and polarization of incident wave, observation angle, frequency, object material, shape, and size. Thus, a change in those parameters generates a change in the measured scattered field (i.e. raw data).

To reduce the dependency on those parameters, it is possible to characterize the scattered field using a variety of feature extraction algorithms. In addition, those algorithms allow reducing and compressing the resulted raw data. Some of these feature extraction techniques are briefly described below.

Polarization techniques

Polarization techniques (Copeland, 1960) allow to model the response of an object through its polarization properties at a fixed observation angle and at a specific frequency. Polarization extraction methods require the radar to have dual polarization (vertical and horizontal) for both transmitter and receiver. Polarization properties can be monitored by rotating a linearly polarized radar antenna around the line of sight, and measuring the complex voltage presented across the receiving antenna. This polarimetric information can be utilized in object detection and classification. In (Kennaugh, 1952), it was shown that the radar target scattering matrix models the scattering process characterizing the target polarization transformation properties. Broadband polarimetric data were treated in Wanielik, 1995 by using several frequency sub-bands to detect and classify the object.

An object's scattering matrix under certain angle and frequency can be expressed as follows:

$$S = \begin{bmatrix} S_{11} & S_{12} \\ S_{21} & S_{22} \end{bmatrix} \quad (2.1)$$

where, the subscripts "1" and "2" denote a set of orthogonal polarization components. Hence, polarization features (scattering matrix determinant, the trace of power matrix, eigen polarization direction angle, and ellipticity angle) fully determine the backscattering characteristics of the target at a given orientation and maximize the target information provided by the viewing angle of the radar in the line-of-sight direction.

Wavelet Transform

The wavelet transform (WT) is largely used to transform non-stationary signals into the "wavelet domain" which is more representative of the signal, in the same way as the Fourier transform (FT) (Rioul and Vetterli, 1991). It employs short windows at high frequencies and long windows at low frequencies, thus, the notion of time-scale representation appears.

The WT is seen as the decomposition of the signal onto a set of basis functions called the "wavelets". It consists of the convolution of the wavelet function with the signal. The Discrete WT has been developed to compress the large amount of information contained in the classical WT (Rothwell et al., 1994). Hence, it produces wavelet coefficients that are the features representing the objects. In this context, multiple types of wavelets exist (Haar, Coiflet, Daubechies, etc.). It is important to choose a wavelet that best matches the shape of the signal under test and the intended application.

High Resolution Range Profile

A high-resolution range profile (HRRP) is a one-dimensional signature of an object obtained by a wideband radar. It is the magnitude of the coherent summations of the time domain complex echoes of the object scatterers in each range cell. This represents the projection of the complex echoes returned from the target's scattering centers onto the radar line of sight (Du et al., 2006; Penghui WANG, 2011). It contains several information about the object such as object size and the RCS distribution in a specific direction.

HRRP has been sought for classification (Penghui WANG, 2011; Liu et al., 2012) and it can provide high target recognition rates. However, it requires high storage space and high computing time.

Scattering centers

The scattering characteristics of an object structure is one of its inherent properties. A target in the high-frequency region can be coarsely modelled by a discrete set of points called scattering centers. They correspond to the spatial distribution of the reflection of the EM wave at a given incident and observation angle. Thus, the capacity for scattering is concentrated in a few small areas of an object, such as edges and tips, called scattering points or scattering centers (Kim and Kim, 1999). ESPRIT (Estimation of Signal Parameters using Rotational In-variance Technique) is a spectral-analysis method that allows to extract scattering centers that characterize an object either from its impulse response (Roy and Kailath, 1989) or from its X-band image (Burrows, 2004). **ESPRIT** : The motivation behind ESPRIT is derived from the geometric theory of diffraction where the scattering field is of the form (Carriere and Moses, 1991):

$$S(\omega) = \sum_{n=1}^N A_n(j\omega)^{\alpha_n} e^{j\omega t_n} \quad (2.2)$$

where N is the model order representing the number of scattering centers, $\{A_n, \alpha_n, t_n\}$ are the model parameters. ESPRIT is originally designed to deal with stationary signals by exploiting the eigen-structure of the data covariance matrix. It requires the received harmonic signals to not be fully correlated to ensure that the covariance matrix is full rank. The approach relies on a naturally occurring shift invariance between discrete time series resulting in a rotation invariance between the signal subspaces.

Resonant frequency characteristics

This method is based on illuminating the object with a sufficiently wideband signal that allow to excite the resonant frequencies of that object. These resonances constitute the set of characteristics used to distinguish one object from another and only depend upon the physical attributes of an object. This means that those features are independent of the incidence angle, observation angle and polarization of incident wave.

The singularity expansion method (SEM) allows to describe the scattering behaviour of an object through those resonances (Baum, 1976). The information contained in them can provide details about the shape, size and composition of the target.

Choice of feature extraction technique

The polarization parameters, wavelet coefficients, HRRP, and scattering centers are features that have been explored for object characterization from its UWB response, and they contain important information about the objects. However, the extracted parameters depend on the polarization, the direction of propagation of the incident wave, and the orientation of the object. This makes them less general and therefore less suitable to our context of object identification and classification from a fast and simple mono- or bistatic acquisition system, with no prior knowledge of the position and orientation of the object.

Indeed, in this thesis, we seek to characterize an object by extracting characteristic parameters or features independently from the incidence angle, observation angle and polarization of incident wave. One method that overcomes this angle dependency limitation is based on the natural resonant frequencies of an object using SEM technique.

The resonance extraction process is very delicate in a noisy environment. We will therefore explore the SEM approach in a more thorough manner in the remainder of the manuscript.

2.3 Singularity Expansion Method

In scattering theory, an object illuminated by an EM plane wave has three scattering regions with respect to the wavelength (λ) of the incident wave: Rayleigh, resonance and optical (Mautz and Harrington, 1978). The object is considered in resonance region when its size is comparable to λ (object size $\sim 0.1-10\lambda$). Creeping waves and internal reflections are very strong in this region and produce resonances in the scattered responses (Heyman and Felsen, 1983).

In the 1970s, Baum introduced the SEM which is based on the analysis of the scattered transient responses of various structures. This method describes the overall behaviour of a target illuminated by an EM wave (Baum, 1976). In this work, Baum noticed that the transient responses of an object behave as a combination of exponentially damped sinusoids. Since the response is real, each damped sinusoid corresponds to a pair of complex conjugated poles in the frequency domain. Identification by SEM is therefore a feature extraction of the singularities of the target's transient response. The benefit of those poles is their independency from the observation angle as they are unique to each object. In contrast, the residues associated to these poles are dependent on the position

of the observation angle. Such singularities are also known as resonance poles or Complex Natural Resonances (CNRs).

In fact, the impulse response from an object illuminated using an EM wave can be decomposed into two parts: the early time response and the late time response. When an incident EM wave illuminates an object, currents are induced on its surface. It then goes into an excited state and current distributions flow along its surface. A part of this wave is reflected directly by the object which constitutes the early time response. This part of wave is called "specular reflection" that mostly depends on the distance between the incident wave and the object, and the object orientation. The late time response begins when the resonance phenomenon is fully established, and the target begins to resonate freely. It depends on the physical characteristic of the object, like its size and material. Fig. 2.1 describes this phenomenon with an object of arbitrary shape. The natural resonances of an object are therefore included in the second portion of the time response, i.e. the late time response.

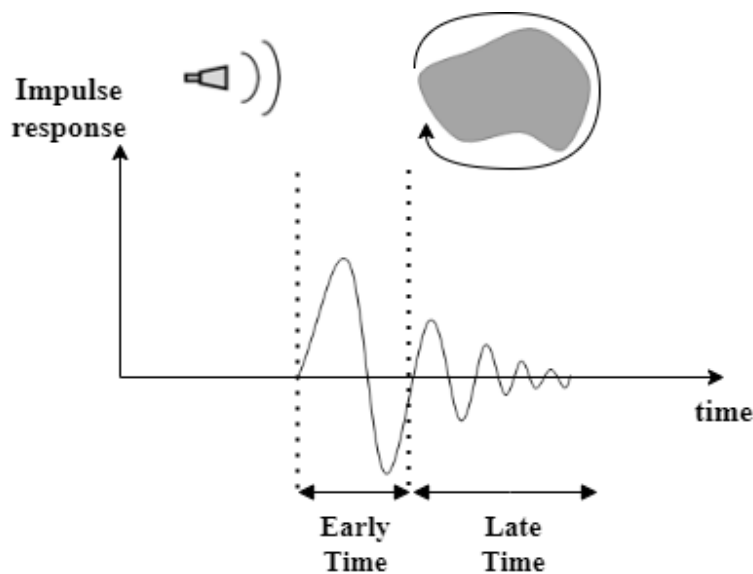


Figure 2.1 – Early and late time responses of an arbitrary object.

The identification of the poles and their associated residues can be performed in the time domain from the late time impulse response or in frequency domain from the complex frequency response. In time domain, the most known methods are Prony's method, State-Space methods, and TLS MP method (Chuang and Moffatt, 1976; Rao, 1990; Hua and Sarkar, 1989). In Grant and Crow, 2011 and Sarrazin et al., 2011, it was shown that TLS MP is more robust to noise than Prony where it can extract more accurate poles from noisy signals. Additionally, in Jang et al., 2005, a quantitative comparison between State-Space

methods and TLS MP have been carried and it was shown that TLS MP allows to accurately determine the resonances, for noisy and noiseless signals, in the least time. Esprit and Root-MUSIC techniques have also been investigated and compared with TLS MP in Khodjet-Kesba, 2014 where it was shown that TLS MP is the least sensitive to noise. Both of those techniques are, in fact, mostly used for computation of the direction of arrival and estimation of the scattering centers parameters.

Finally, in frequency domain, two methods have been chosen to extract the signal's CNRs, which are the Cauchy method and Vector Fitting (VF) (Kumaresan, 1990; Gustavsen and Semlyen, 1999). We will later present the details of each technique implemented in this work.

SEM application in the radar field

Owing to its interesting properties, the SEM has been extensively researched for application to the characterization and identification of radar targets. The SEM has been studied since the 1970s to characterize simple perfect electric conductor (PEC) objects in free space (Moffatt and Mains, 1975; Baum et al., 1991). One particular object studied over the years is the PEC sphere (Chen and Westmoreland, 1981). Indeed, the scattered response of a PEC sphere has been analytically established by Mie in 1908 (Mie, 1908). Another object studied is the thin wire that can be regarded as a short-circuited dipole with a very small ratio of diameter over length (Tesche, 1973). Additional analytical poles solution of other PEC objects has been studied (Chaudhuri, 1980; Kristensson, 1984; Long, 1994).

Following, a more realistic approach, instead of the analytic one, has been realized by computing the natural resonances of the simulated scattered response of those PEC objects (Chauveau, de Beaucoudrey, and Saillard, 2007b; Lee et al., 2012; Bhattacharyya, Siddiqui, and Antar, 2019). Additionally, the SEM has been extended to more complex targets like the characterization of an aircraft modelled by means of several thin wires (Chantasan, Boonpoonga, and Burintramart, 2014) or modelled in a more realistic approach (Sathyamurthy, Varalakshmi, and Balakrishnan, 2019).

If the PEC target is not in free space and is buried in a loss or lossless ground, Baum has developed a representation to compute the resonance of this object in such scenario from its poles in free space (Baum, 1993). Then, Lee et al. also

proposed a methodology to identify the resonances of a PEC object located in the ground (Lee et al., 2013).

Similarly, identification of dielectric targets using SEM has been investigated. In fact, when an object has a dielectric material, two resonance phenomena occur which are: Internal resonances due to the reflections inside the object and External resonances due to creeping waves propagating on the surface of the object. Multiple studies have been conducted to compute the natural resonances of either a dielectric sphere or a PEC sphere coated with a dielectric material (Chi-Chih Chen, 1998; Chauveau, de Beaucoudrey, and Saillard, 2007a; Mei et al., 2014). It is shown that having a dielectric material or a dielectric coating increases the resonating behaviour of an object.

In addition, the identification of an unripe fruit using a non-destructive method is also an interesting challenge. In Leekul, Krairiksh, and Sarkar, 2014 and Leekul and Krairiksh, 2018, the SEM technique has been applied to determine the maturity of a mangosteen fruit. It is shown that it is possible to identify a normal fruit from a translucent one from its resonant frequencies. The same study has been done using a different fruit, the Durian fruit, and it shows the identification of the stage of maturity using its natural frequencies (Tantisoparak et al., 2016).

Now that we have seen the main applications and possibilities offered by SEM for our work, we will describe the methods which will be implemented in this thesis, starting with a temporal method: MP.

2.4 SEM in Time domain

2.4.1 Matrix Pencil

In general, the late time portion of an impulse response can be formulated as a sum of complex exponentials as follows:

$$y(t) = \sum_{m=1}^M R_m e^{s_m t} + b(t) \quad (2.3)$$

with s_m the complex poles, R_m their respected complex residues, M is the model order which represent the number of poles and $b(t)$ is the noise observed in the signal.

After the signal's sampling, $y(t)$ can be subsequently rewritten from the K samples $y(0), \dots, y(K-1)$ in the form of:

$$y(k) = \sum_{m=1}^M R_m e^{s_m k T_s} + b(k) \quad (2.4)$$

where k is the number of samples in a signal and T_s is the sampling period.

In 1990, Matrix Pencil (MP) was proposed by Hua and Sarkar as an alternative to Prony's method for modelling the scattered response of an illuminated object in time domain (Hua and Sarkar, 1990). A singular value decomposition (SVD) is performed on a matrix constituted by the sampled signal $y(t)$. It enables the identification of the physical poles of the signal by direct computation of the eigenvalues of a matrix of a reduced order. This procedure involves the analysis of singular values in order to estimate the order of the data matrix. In fact, M in equation 2.4, which is also the number of singular values computed, is an important parameter which must be determined adequately to separate the noise from the signal.

We start to consider the following matrix:

$$Y_1 - \lambda * Y_2 \quad (2.5)$$

with λ being a scalar parameter. The Hankel matrices Y_1 and Y_2 constructed from the K samples of y_k presented in (Hua and Sarkar, 1989) are as follows:

$$Y_1 = \begin{bmatrix} y(1) & y(2) & \cdots & y(L) \\ y(2) & y(3) & \cdots & y(L+1) \\ \vdots & \vdots & \ddots & \vdots \\ y(K-L) & y(K-L+1) & \cdots & y(K-1) \end{bmatrix}_{(K-L)*L} \quad (2.6)$$

$$Y_2 = \begin{bmatrix} y(0) & y(1) & \cdots & y(L-1) \\ y(1) & y(2) & \cdots & y(L) \\ \vdots & \vdots & \ddots & \vdots \\ y(K-L-1) & y(K-L+2) & \cdots & y(K-2) \end{bmatrix}_{(K-L)*L} \quad (2.7)$$

where L is the pencil parameter and K is the samples number. The L parameter is important to eliminate some effects of the noise in the signal. Both matrices

Y_1 and Y_2 can be decomposed as follows:

$$Y_1 = Z_1 R Z_2 \quad (2.8)$$

$$Y_2 = Z_1 R Z_0 Z_2 \quad (2.9)$$

where Z_1 and Z_2 are two Vandermonde matrices defined as:

$$Z_1 = \begin{bmatrix} 1 & 1 & \cdots & 1 \\ z_1^1 & z_2^1 & \cdots & z_M^1 \\ \vdots & \vdots & \ddots & \vdots \\ z_1^{K-L-1} & z_2^{K-L-1} & \cdots & z_M^{K-L-1} \end{bmatrix}_{(K-L)*M} \quad (2.10)$$

$$Z_2 = \begin{bmatrix} 1 & z_1^1 & \cdots & z_1^{L-1} \\ 1 & z_2^1 & \cdots & z_2^{L-1} \\ \vdots & \vdots & \ddots & \vdots \\ 1 & z_M^1 & \cdots & z_M^{L-1} \end{bmatrix}_{M*L} \quad (2.11)$$

R and Z_0 are both diagonal matrices of length $M * M$.

Using equation 2.8 and 2.9 we can rewrite the expression in 2.5 as:

$$Y_1 - \lambda * Y_2 = Z_1 R (Z_0 - \lambda I) Z_2 \quad (2.12)$$

where I is the identity matrix of length $M * M$. In general, the rank of the matrix $\{Y_1 - \lambda * Y_2\}$ can be shown to be equal to M assuming that $M \leq L \leq K - M$. However, in the case where $\lambda = z_i$, $i \in \{1, M\}$, the rank of this matrix becomes $M - 1$. Therefore, z_i can be found as the generalized eigenvalues of the pair of matrices (Y_1, Y_2) or equivalently from the eigenvalues of the following matrix:

$$Y_1^+ s Y_2 - \lambda I \quad (2.13)$$

where the exponent $+$ designates the Moore-Penrose pseudo-inverse. Hence, the poles can be identified as the eigenvalues of $Y_1^+ Y_2$ matrix.

Modified Matrix pencil

The previous technique does not take into account the noise present in the signal, hence, the TLS MP is proposed (Hua and Sarkar, 1991). A matrix Y is

constructed from the noise contaminated signal $y(t)$ by combining Y_1 and Y_2 :

$$Y = \begin{bmatrix} y(0) & y(1) & \cdots & y(L) \\ y(1) & y(2) & \cdots & y(L+1) \\ \vdots & \vdots & \ddots & \vdots \\ y(K-L-1) & y(K-L) & \cdots & y(K-1) \end{bmatrix}_{(K-L)*(L+1)} \quad (2.14)$$

The choice of the parameter L plays a key role in noise filtering, and it is proposed to choose it as (Hua and Sarkar, 1990)

$$\frac{K}{3} < L < \frac{K}{2} \quad (2.15)$$

Following, a singular value decomposition (SVD) is carried out

$$Y = USV^H \quad (2.16)$$

where U and V are both orthogonal matrices of length $(K-L) * (K-L)$ and $(L+1) * (L+1)$ respectively, S is a diagonal matrix containing the singular values of $(K-L) * (L+1)$ dimension. When the data is noiseless, the matrix Y has exactly M non-zero singular values. Nevertheless, because of the noise, the singular values are perturbed and are non-zero. However, the singular values related to noise remain small and can be identified by fixing a threshold ϵ . Hence, only the highest singular values are retained. This threshold is expressed as follows:

$$\frac{\sigma_M}{\sigma_{max}} \geq \epsilon \quad (2.17)$$

where σ_M is the singular value related to the model order M and σ_{max} is the highest singular value. This allows the selection of only the dominant singular values, thus, the number of the most significant singular values will define the order M of the system.

Next, we consider the S' and the filtered V' matrix containing the M dominant values, S' is, thus, equal to the matrix extracted from S corresponding to the first M columns. V' is as follows:

$$V' = \begin{bmatrix} v_1 & v_2 & \cdots & v_M \end{bmatrix}. \quad (2.18)$$

Once an estimate of the order has been determined, the singular value decomposition of the matrix Y given by equation 2.14 will allow to rewrite Y_1 and Y_2

as

$$Y_1 = US'V_1'^H \quad (2.19)$$

$$Y_2 = US'V_2'^H \quad (2.20)$$

V_1' is obtained by removing the last row of V' and V_2' by removing the first row of V' . Therefore, the poles are computed from the non-null eigenvalues of $\{V_1'^H\}^+ V_2'^H$. The residues R_m can then be computed once the poles have been determined by solving a linear system:

$$\begin{bmatrix} R_1 \\ R_1 \\ \vdots \\ R_M \end{bmatrix} = \begin{bmatrix} 1 & 1 & \cdots & 1 \\ z_1^1 & z_2^1 & \cdots & z_M^1 \\ \vdots & \vdots & \ddots & \vdots \\ z_1^{K-1} & z_2^{K-1} & \cdots & z_M^{K-1} \end{bmatrix}^{-1} \cdot \begin{bmatrix} y(1) \\ y(2) \\ \vdots \\ y(K) \end{bmatrix} \quad (2.21)$$

2.4.2 Late time / Early time separation

In the scientific literature, one of the quantitative definitions of the beginning of the late time of a signal propagating in free space is given by (Kennaugh and Moffatt, 1965) (assuming a mono-static configuration)

$$T_{Late} = \frac{2L_c}{c} + 2T_v + T_p \quad (2.22)$$

where L_c is the characteristic length of the target, c is the light's celerity, T_v is the travel time from the transmitting antenna to the target and T_p is the pulse width. However, the application of this formula requires a priori knowledge about the object's geometry and orientation, and the distance between the antenna and the object which is not always possible. Thus, the late-time response must be identified from the impulse response.

The Short Time Matrix Pencil (STMP) was proposed by Rezaiesarlak and Manteghi to estimate the start of the late time response. It is a modification of the MP where a sliding window is applied on the impulse response (Rezaiesarlak and Manteghi, 2013). In STMP, a window having a pre-determined constant width moves along the entire time response and TLS MP is applied to each window to extract the resonances. Then, the start of the late time is identified when natural poles start to converge to stable values. However, it is difficult to observe the poles convergence point for weak resonating objects as their impulse is very short in time. Another approach was proposed by Boonpoonga et al. that is based on investigating how similar the received scattering response

was to the transmitted signal (Boonpoonga et al., 2017). This was done by performing a cross-correlation between these signals where the output peak presented the late time commencement. Nevertheless, they showed that this procedure can only be applied on the received back-scattering signal, thus it is not suitable when there is a bi-static configuration. Thus, as the early time and late time separation is a key point in CNRs estimation, we will search and try to propose an alternative approach that will allow to identify the start of the late time for any observation angle and for weak resonating objects.

Equation 2.22 and the previous techniques assume that the object under test is a perfect electric conductor (PEC), thus, the wave propagates only on the surface, and we only have external resonances. However, if the object has a dielectric material, we will have internal and external resonances as a part of the wave will propagate inside the object causing internal reflections. Thus, equation 2.22 will no longer be applicable on a dielectric object and applying the proposed methods do not achieve accurate separation. Hence, it may be preferable to extract the resonances from the scattered field of a dielectric object in frequency domain as there are more efficient methods allowing to automatically separate CNRs related to early time response.

2.5 SEM in frequency domain

2.5.1 TLS Cauchy

This method originates from the classical Cauchy method and is based on the approximation of the transfer function $H(f)$ by a ratio of two polynomial functions $A(k)$ and $B(k)$ by considering a Linear Time Invariant (LTI) system (Kumaresan, 1990). An SVD approach has been proposed to make the Cauchy method more robust to noise. The first step consists on computing the coefficients of those two polynomial functions:

$$H(f) = \frac{A(k)}{B(k)} \approx \frac{\sum_{k=0}^P a_k f^k}{\sum_{k=0}^Q b_k f^k} \quad (2.23)$$

with a_k and b_k the coefficients of the polynomials $A(k)$ and $B(k)$ respectively. P and Q orders and both coefficients must be estimated from the transfer function $H(f)$ (Kottapalli et al., 1991).

Equation 2.23 can be rewritten as:

$$\sum_{k=0}^P a_k f^k - \sum_{k=0}^Q b_k f^k H(f) = 0 \quad (2.24)$$

Previous equation is given in a simpler matrix form as follows:

$$[C] \begin{bmatrix} a \\ b \end{bmatrix} = [A \mid B] \begin{bmatrix} a \\ b \end{bmatrix} = 0, \quad (2.25)$$

where the coefficients of the numerator and denominator to be computed are $a = [a_0, a_1, \dots, a_P]$ and $b = [b_0, b_1, \dots, b_Q]$. The matrix C is of order $N \times P + Q + 2$. The two sub-matrices A and B are built as (Adve and Sarkar, 1994):

$$A = \begin{bmatrix} 1 & f_1 & \cdots & f_1^P \\ 1 & f_2 & \cdots & f_2^P \\ \vdots & \vdots & \ddots & \vdots \\ 1 & f_N & \cdots & f_N^P \end{bmatrix} \quad (2.26)$$

$$B = \begin{bmatrix} -H(f_1) & -H(f_1)f_1 & \cdots & -H(f_1)f_1^Q \\ -H(f_2) & -H(f_2)f_2 & \cdots & -H(f_2)f_2^Q \\ \vdots & \vdots & \ddots & \vdots \\ -H(f_N) & -H(f_N)f_N & \cdots & -H(f_N)f_N^Q \end{bmatrix} \quad (2.27)$$

A SVD applied on the C matrix results in:

$$[C] = [U_1] [\Sigma_1] [V_1^H] \quad (2.28)$$

The rank R of the matrix Σ_1 is the number of non null dominant singular values that satisfy this condition:

$$\frac{\sigma_R}{\sigma_{max}} = 10^{-p} \quad (2.29)$$

Once R is defined, P and Q have to satisfy the following relation:

$$R + 1 = P + Q + 2 \quad (2.30)$$

In practice, P and Q are fixed, at the beginning, higher than the number of estimated poles. Then, R is estimated from the number of non-zero singular values of $[C]$. Finally, from equation 2.30 we get new estimates for P and Q .

The sub-matrix A depends only on the frequency and is not affected by noise. However, the sub-matrix B is affected by noise as it includes measured parameters $H(f)$. To take into account this difference between the two sub-matrices, a QR decomposition is applied on the C matrix:

$$\begin{bmatrix} R_{11} & R_{12} \\ 0 & R_{22} \end{bmatrix} \begin{bmatrix} a \\ b \end{bmatrix} = 0 \quad (2.31)$$

This gives us the following systems:

$$R_{22}b = 0 \quad (2.32)$$

$$R_{11}a = -R_{12}b \quad (2.33)$$

A second SVD is applied on R_{22} giving the following relation:

$$\begin{bmatrix} U_2 \end{bmatrix} \begin{bmatrix} \Sigma_2 \end{bmatrix} \begin{bmatrix} V_2^H \end{bmatrix} b = 0 \quad (2.34)$$

Yet, according to the TLS approach, the b vector is proportional to the last column of the matrix $[V_2]$:

$$b = \begin{bmatrix} V_2 \end{bmatrix}_{Q+1} \quad (2.35)$$

In this manner, the poles are determined by calculating the zeros of the denominator in equation 2.23. Once a and b have been determined, $H(f)$ can be rewritten as:

$$H(f) = \frac{\sum_{k=0}^P a_k f^k}{\sum_{k=0}^Q b_k f^k} \approx \sum_{k=1}^Q \left(\frac{R_k}{f - (\frac{\alpha_k}{j2\pi} + f_k)} + \frac{R_k^*}{f - (\frac{\alpha_k}{j2\pi} - f_k)} \right) \quad (2.36)$$

where R_k is the residue, R_k^* is its conjugate, α_k is the damping factor and f_k is the resonant frequency of the k^{th} pole.

The residues R_k can then be computed from Sarrazin et al., 2014

$$R_k = \frac{\sum_{k=0}^P a_k f_n^k}{b_Q \prod_{k=1, k \neq n}^Q (f_n - f_k)} \quad (2.37)$$

2.5.2 Vector Fitting

Gustavsen and Semlyen have proposed VF to be used for fitting a frequency domain response by a rational function approximation (Gustavsen and Semlyen, 1999):

$$H(s) = \sum_{n=1}^N \frac{R_n}{s - a_n} + d + se \quad (2.38)$$

where $s = j\omega$, R_n are the residues and a_n are the poles. d and e are optional real numbers.

The first step is to identify the poles in equation 2.38 by solving a linear approximation of the problem using the least square (LS) method in an iterative manner:

$$\sigma(s)H(s) = p(s) \quad (2.39)$$

where $\sigma(s)$ and $p(s)$ are rational approximations given by:

$$\sigma(s) = \sum_{m=1}^N \frac{\tilde{r}_m}{s - q_m} + 1 \quad (2.40)$$

$$p(s) = \sum_{m=1}^N \frac{r_m}{s - q_m} + d + se \quad (2.41)$$

q_m is a set of initial complex poles fixed at the beginning of the iteration process as shown in section 2.5.2. Then, 2.39 can be solved as an over-determined linear system of the form:

$$A_k x = B_k, \quad (2.42)$$

where x is the vector holding the unknowns. They are expressed as follows:

$$A_k = \begin{bmatrix} \frac{1}{s_1 - a_1} & \cdots & \frac{1}{s_1 - a_N} & 1 & s_1 & -\frac{H(s_1)}{s_1 - a_1} & \cdots & -\frac{H(s_1)}{s_1 - a_N} \\ \vdots & \ddots & \vdots & \vdots & \vdots & \vdots & \ddots & \vdots \\ \frac{1}{s_k - a_1} & \cdots & \frac{1}{s_k - a_N} & 1 & s_k & -\frac{H(s_k)}{s_k - a_1} & \cdots & -\frac{H(s_k)}{s_k - a_N} \end{bmatrix} \quad (2.43)$$

$$x = [c_1 \quad \cdots \quad c_N \quad d \quad e \quad \tilde{c}_1 \quad \cdots \quad \tilde{c}_N]^T, \quad b_k = H(s_k) \quad (2.44)$$

The uncertainty of the solution for $\sigma(s)$ is eliminated by forcing it to be close to unity at very high frequencies. In Gustavsen and Semlyen, 1999, it is shown that the poles of $H(s)$ are equal to the zeros of $\sigma(s)$. They are calculated as the

eigenvalues of the matrix in Gustavsen and Semlyen, 1999:

$$a_m = \text{eig}(A - bc^T) \quad (2.45)$$

where A is a diagonal matrix encompassing the initial poles q_m , b is a unit vector and c^T is a row vector comprising the residues \tilde{r}_m .

This process can be carried out in an iterative pattern in which 2.39 and 2.45 are repeatedly solved by replacing the previous poles q_m with new ones.

In order to satisfy equation 2.39, the number of initial poles q_m needs to be equal to or higher than the number of natural poles a_m of $H(s)$. Additionally, if the data are noisy, there will be a high error in the LS solution which affects the convergence of poles. Hence, a modification of the VF algorithm is proposed in Gustavsen, 2006 by replacing 2.40 with:

$$\sigma(s) = \sum_{m=1}^N \frac{\tilde{r}_m}{s - q_m} + \tilde{d} \quad (2.46)$$

where \tilde{d} is a real number. Hence, we remove the necessity of forcing $\sigma(s)$ to be equal to 1 at high frequencies, as seen in equation 2.40. Equation 2.45 must now be replaced by:

$$a_m = \text{eig}(A - b\tilde{d}^{-1}c^T) \quad (2.47)$$

Once the poles have been determined, the residues can be computed through another LS problem similar to 2.42.

The formulation of VF presented above is presented for scalar mathematical functions (i.e. for a single observation angle). Nevertheless, VF may be applied directly to vector functions as well by supposing that all elements of the vector have identical poles. This is beneficial when doing several measurements of the same object at different observation or incident angles as the CNRs are independent of those parameters. Thus, VF can compute a single vector containing the resonant poles of the object and produces different residues for each measurement.

Choice of starting poles

As mentioned before, VF starts by assuming a set of starting poles that are uniformly distributed over the frequency band of interest. Those initial poles must be complex conjugate and the model order must be overestimated to get

accurate solution. They are of the form:

$$q_n = -\sigma + j\omega, \quad q_{n+1} = -\sigma - j\omega, \quad (2.48)$$

where ω is the pulsation evenly distributed over the frequency range and σ is the damping factor. We start with a weak attenuation, where $\sigma = \omega/100$, thus, we guarantee that the LS problem under consideration has a well-conditioned system matrix. If the data are noise free, the convergence to the final poles distribution from the starting ones happens fast, with only two iterations. However, if there is noise, further iterations are needed until convergence.

In Gustavsen and Semlyen, 1999, it was stated that a poor choice of starting poles might still lead to accurate results by increasing the number of iterations. However, the convergence speed will be reduced. It has also been demonstrated that the accuracy will not decrease if an excessive number of poles are utilized in a noiseless case. In a noisy environment, an excessive number of poles might affect the convergence of poles, especially when there are many resonances in the frequency range.

In this thesis, ω is defined linearly spaced over the frequency range of interest. As we do not have a priori knowledge about the object, the model order needed to compute the CNRs will be investigated and a minimum of two iterations will be applied.

2.5.3 Selection of physical poles

The CNRs extracted using VF or TLS Cauchy allow to characterize an object from its frequency response. Given that in frequency domain there is no separation between early and late time responses, since they are intertwined, physical or natural poles as well as mathematical poles (or spurious poles) appear after applying TLS Cauchy or VF. Physical poles are characteristic of the object, however, mathematical poles have no physical meaning and do not correspond to singularities of the function $H(f)$ to be approximated (Stahl, 1998). They arise as we overestimate the model order to get accurate physical poles. Some of the mathematical poles correspond to the early time response of an object. It is essential to be able to dissociate the physical and mathematical poles to accurately characterize the objects.

Indeed, when computing the poles with a fixed model order N we get physical poles that come in complex conjugate pairs and have a negative damping factor σ_m . As for the mathematical poles, they might have a positive damping factor

and depend upon the model order. To be able to identify them, we can vary the model order and consequently, if the model order is sufficient, only the physical poles will be stable for various N while the mathematical poles will vary. Additionally, Lee et al. propose some criteria to automatically remove those mathematical poles by eliminating the following (Lee et al., 2012):

- poles having very high damping factor $\alpha_m > 8$ since they are quickly damped;
- poles with positive damping factor α_m because they are unstable due to the increasing oscillations;
- poles outside the frequency range;
- poles having weak residues ($|\frac{R_m}{\alpha_m}| < 10^{-p}$) as they have a negligible contribution in the scattered field.

2.6 Representation using the Q-factor and resonant frequencies

It is possible to represent the resonance phenomena of an object using the quality factor (Q-factor) by relating it to an RLC resonant circuit (Chauveau, Beaucoudrey, and Saillard, 2007). The Q-factor is also useful for estimating the intensity of resonance of an antenna (Li and Liang, 2004). Janic Chauveau proposed to represent the CNR using the Q-factor and the natural pulsation rather than the classical representation using the damping factor.

The transfer function $A(\omega)$ of a parallel RLC circuit is written as (Chauveau, de Beaucoudrey, and Saillard, 2006):

$$A(\omega) = Z(\omega) = \frac{V_0}{I} = \frac{R}{1 + jRC\omega + \frac{R}{j\omega L}} \quad (2.49)$$

where Z is the impedance of the circuit. It is possible to replace the parameters of the circuit components by the Q-factor and the pulsation resonance as follows:

$$A(\omega) = \frac{R}{1 + jQ(\frac{\omega}{\omega_0} - \frac{\omega_0}{\omega})} \quad (2.50)$$

where $Q = RC\omega_0 = \frac{R}{L\omega_0}$ and $\omega_0 = \frac{1}{\sqrt{LC}}$ is the natural pulsation. Here, the bandwidth of this circuit is defined as $\Delta\omega = \frac{\omega_0}{Q}$. In order to define the poles of this system, 2.50 can be redefined in terms of the Laplace variable $s = j\omega$. This

resonant circuit approximation is now applied to the scattering transfer function of an object that can be formulated as a sum of transfer functions $A_m(s)$ of basic resonators $\{\omega_{0,m}; Q_m\}$. $\omega_{0,m}$ and Q_m are the natural pulsation of resonance and quality factor of the m_{th} singularity (s_m) respectively:

$$\omega_{0,m} = |s_m|, \quad Q_m = -\frac{\omega_{0,m}}{2\alpha_m} \quad (2.51)$$

Applying this descriptive to an object allows to describe its resonance behaviour through the Q -factor. Strong resonating objects have high Q -factor, whereas weak resonating objects have low Q -factor.

At this point, we have introduced the main SEM methods that will be used in this thesis and the efficient ways to parameterize them. We are now going to work towards validating our choices on synthetic signals, and exploring one of the key points of this thesis, namely the behaviour of these SEM methods in presence of noise.

2.7 Validation of SEM using a synthetic signal

The objective here is to investigate the efficiency of the following methods presented above: TLS MP in time domain, TLS Cauchy and VF in frequency domain. Our aim is to have a first general idea about the performances of these SEM techniques using a simple synthetic signal by comparing the extracted poles with analytic ones.

First, we start by defining a set of complex poles and their corresponding residues that come in complex pair as seen in table 2.1. α_m is the damping factor and f_m is the resonant frequency. Following, we construct the time and frequency responses from the fixed set of parameters using equations 2.3 and 2.36 respectively. In fact, the values of the residues should not be real numbers as it will cause the signal to have a fast discontinuity at $t = 0$ in time domain (cosine form) which causes a problem when applying Fast Fourier Transform (FFT) or Inverse Fast Fourier Transform (IFFT). This way, we use a set of imaginary residues to have a signal that has a null amplitude at $t = 0$ (sine form).

The constructed signals are presented in fig. 2.2. The time interval is set between 0 and 126 ns with a 1 ns step (127 samples). The frequency band is from -0.5 to 0.5 GHz with 0.08 GHz frequency step. The negative frequencies represent the complex conjugate part of the frequency spectrum as the time response

Table 2.1 – CNRs and residues used to construct the synthetic signal

$Pole_m$	α_m	$f_m(\text{GHz})$	R_m
1	-0.05	± 0.08	$\pm j0.4$
2	-0.1	± 0.15	$\pm j0.8$
3	-0.18	± 0.2	$\pm j1.2$

is real. From the amplitude of the frequency response, we can notice a peak at 0.08 GHz which corresponds to the first pole ($pole_1$). Additionally, the impulse response has several oscillations and is damped starting from 60 ns. To evaluate the error between the initial response E_{org} constructed using the fixed CNRs and the reconstructed one E_{rec} using the estimated physical CNRs, we will use the mean relative error expressed as follows:

$$Err(f) = \frac{\sum_{\theta} \sum_{\phi} |E_{org}(f, \theta, \phi) - E_{rec}(f, \theta, \phi)|^2}{\sum_{\theta} \sum_{\phi} |E_{org}(f, \theta, \phi)|^2} \quad (2.52)$$

2.7.1 Extraction in a noiseless environment

All three SEM extraction algorithms are now applied directly to the time and frequency responses of figure 2.2. We first evaluate the behaviour of those methods when the model order M is under or over-estimated. The CNRs for multiple M are shown in fig. 2.3 with damping factors plotted as a function of the resonant frequencies. The resulting poles and residues are identical for $M \geq 6$ and correspond perfectly with the original values. As expected, by overestimating M , there are additional poles that appear on the positive side of the axis, that have very weak damping factors or with out of band frequencies so they are not presented on those figures for visibility. Those poles can be eliminated by the criteria mentioned before.

However, if M is under-estimated, it is not possible to extract accurately the CNRs. Therefore, it is possible to overestimate the number of poles without perturbing the extraction of the CNRs from the response. If the number of poles is unknown, it is preferable to choose a higher order to avoid the risk of underestimating the number of poles.

At this stage, all the methods perform equally well as the synthetic signal is noiseless and there is no early time response that perturbs the CNRs extraction

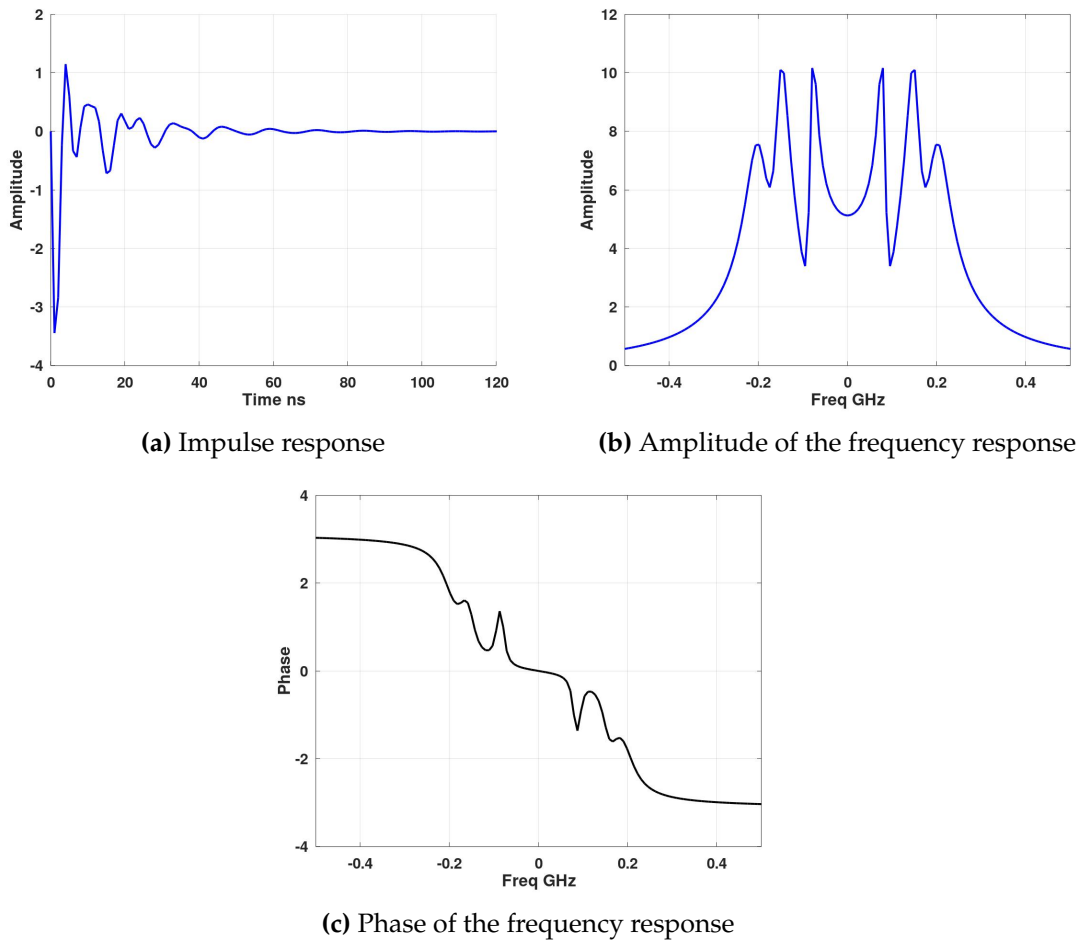


Figure 2.2 – Reconstructed impulse and frequency responses using the set of fixed poles and residues.

in frequency domain because the synthetic signal was constructed using only physical poles.

2.7.2 Extraction in a noisy environment

We now propose to test these algorithms in the presence of noise. For this purpose, additive white Gaussian noise (AWGN) is added to the time and frequency responses before applying the extraction algorithms. Furthermore, the mean error rate is computed over 30 trials to reduce the noise variations which are randomly distributed. In this context, the SEM methods provide in addition to the physical poles, mathematical poles due to the presence of noise. Nevertheless, in a characterization and identification process, only the physical poles need to be retained. In this case, the physical poles are the ones given in table 2.1 and the additional ones are eliminated using the criteria mentioned before. We will then evaluate the reconstruction from those physical poles and their

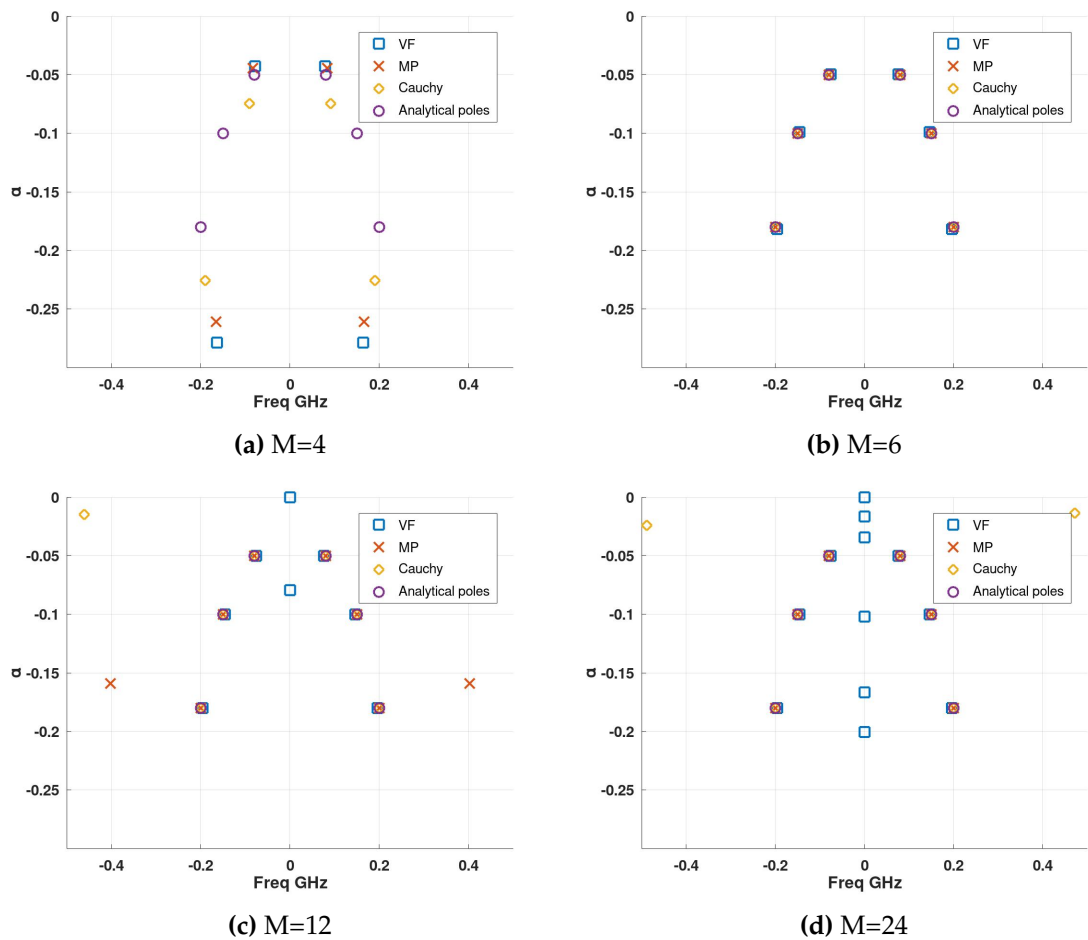


Figure 2.3 – Poles extraction using VF, TLS Cauchy and TLS MP for multiple model orders

associated residues derived from the three algorithms using equation 2.52.

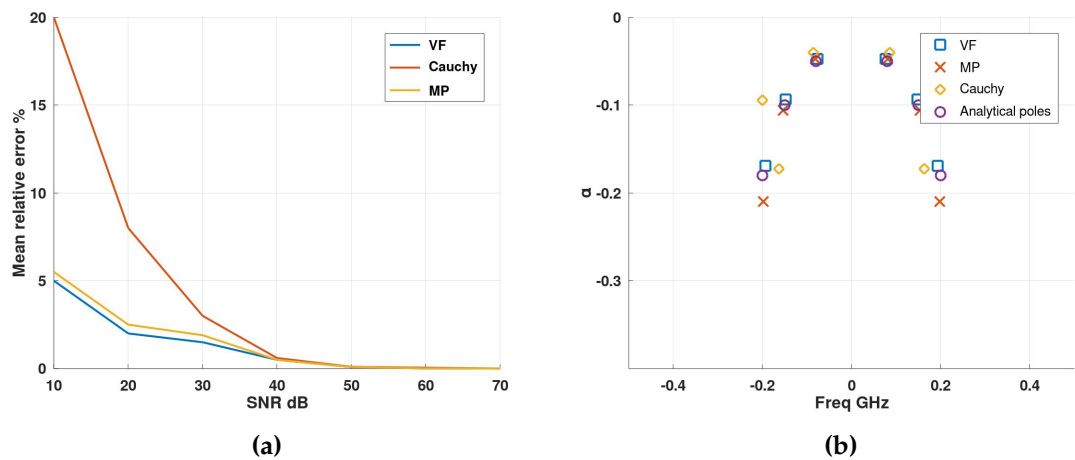


Figure 2.4 – (a) Reconstruction error as a function of SNR; (b) CNRs extracted at 10 dB SNR

Fig. 2.4a shows the mean relative error of the reconstructed signals as a function

of Signal to Noise Ratio (SNR). We can see that at low SNR, Cauchy has the highest reconstruction error. In addition, we observe in fig. 2.4b that, at 10 dB SNR, Cauchy is unable to extract all resonances correctly in contrast to MP and VF that have higher accuracy especially on the first two resonances.

By comparing the results obtained with the different methods presented and illustrated above, TLS MP and VF appears to be the most efficient with, in particular, a better accuracy of the CNRs estimation in the presence of noise when applied to a simple synthetic signal constructed using three pairs of complex CNRs and their residues.

2.8 Conclusion

In this chapter, we have described the basic theoretical notions that are necessary for target recognition in an UWB radar context. When working in a broad band, the amount of data to be stored in order to fully characterize an object is becoming increasingly important. Thus, in addition to selecting an effective characterization technique regardless of the viewing angle, we explored different techniques allowing to compress the UWB scattered field from objects.

First, we gave a summary about the techniques that exist for UWB target recognition. We selected the SEM technique that corresponds to the specific requirements and specifications of this thesis. Indeed, the CNRs are intrinsic to the object and can therefore be used in an identification process. Second, we presented in detail the SEM allowing to extract CNRs and residues that are features proposed to reduce the amount of data of the UWB scattered field. It can be applied either in time domain by the use of TLS MP, or in frequency domain using VF or TLS Cauchy. The mathematical background of those methods was presented as well as the treatments required for their proper application. This theoretical study allowed us to comprehend the principle of SEM and to identify the most suitable SEM methods in both time and frequency domains. Finally, we have presented the validation results of those methods when applied to a synthetic signal.

For that, we have constructed synthetic time and frequency responses using a set of fixed poles and residues on which the SEM methods have been applied. Through this example, we were able to assess the model order M that allows to properly extract the resonance poles. Indeed, it is better to over-estimate M to be able to extract all CNRs correctly as it was seen that by underestimating M , not all poles have been well extracted and computed. Then, we evaluated the

behaviour of those techniques in presence of noise. It was noticed that MP and VF are less sensitive to noise than Cauchy. By adding noise to this synthetic signal, the notion of mathematical poles began to emerge and by means of the criteria for eliminating mathematical poles, they were successfully removed.

After the validation step of SEM techniques, we will begin to apply them on scattered field from simulated objects where we will evaluate their robustness to noise, and the notion of mathematical poles will be present due to the presence of early time component and noise.

Chapter 3

Characterization of objects from their natural resonances

3.1 Introduction

In the previous chapter, three SEM techniques have been introduced, selected, and evaluated using a synthetic signal. Indeed, it is interesting to be able to characterize an object with just a set of few parameters extracted from its scattered field whatever the observation angle. The objective of this chapter is to apply those techniques on the simulated scattered fields of simple PEC objects and to investigate their robustness.

Two objects are considered for this study: a PEC sphere and a thin metal wire. These objects are both simple, well described analytically (for the sphere) and have very different properties: the PEC sphere is a low resonating object, while the thin wire is a strong resonating object. The sphere is simultaneously a challenging object because of its numerous resonances and a well analytically described structure thanks to the Mie theory. A set of analytical poles of both objects is calculated and will then be used as a reference to compare these methods at different noise levels or with channel compensation errors.

First, we explain the steps required to be done in frequency and time domain before the pole's extraction procedure. The extracted CNRs from noiseless scattered fields are, hence, compared with the theoretical ones of each object. Then, the robustness to noise for each technique is studied and presented. In addition, we will study the residues associated to each CNR and particularly their spatial distribution. This study will be conducted on both the PEC sphere and the thin wire.

3.2 Scattered field simulation setup

We start by generating the scattered field from a PEC sphere and a thin wire in free space. An analytic solution for spheres exists using Mie series (Mie, 1908) and we also use numerical full wave simulation tools: HFSS (High Frequency Structure Simulator) and CST Microwave Studio. We validated our simulation protocol by comparing the simulated results with those obtained by Mie series for the sphere. Thus, we can accurately simulate other objects that do not have an analytical solution (i.e. the thin wire in this chapter).

The frequency band is maintained from 10 MHz to 5 GHz with a 10 MHz step (500 samples). This very low frequency will allow to compute resonances of large objects and to cover their fundamental frequency. Indeed, this bandwidth enables the characterization of objects that range in size from a centimeter to several decimeters. However, in an operational context, building an antenna with such a low frequency can be delicate, but it might be possible to have a frequency range starting at 100 MHz instead of 10 MHz which will also permit to extract the resonances and to include the fundamental one for small objects.

In this chapter, the dimension of each object is chosen such that their resonances are present in this frequency range and their size is of the same order as the electromagnetic wavelength. The PEC sphere has a diameter (D) of 0.15m and the wire has a length of 0.15m with a ratio of diameter over length (D/L) = 0.01. They are illuminated using a plane EM wave as shown in fig. 3.1. The incident wave vector \vec{k}_{inc} is defined as follows:

$$\vec{k}_{inc} = \begin{bmatrix} \cos(\phi_{inc})\sin(\theta_{inc}) \\ \sin(\phi_{inc})\sin(\theta_{inc}) \\ \cos(\theta_{inc}) \end{bmatrix} \quad (3.1)$$

The scattered field is recovered in the far field for multiple views (i.e. angles of observation) in a bi-static way; θ varying from 0° to 180° with 5° step and ϕ from -180° to 180° with 10° step. θ and ϕ are defined from the standard 3D cartesian coordinate system. Thus, we obtain 37 angles in both θ and ϕ directions. In the far field, the scattered field can be expressed as follows:

$$\vec{E}(\vec{r}, \theta, \phi) = \frac{e^{-j\vec{k}\vec{r}}}{r} \cdot \vec{E}^0(\theta, \phi) \quad (3.2)$$

The distance r between the probe, where the scattered field is collected, and the

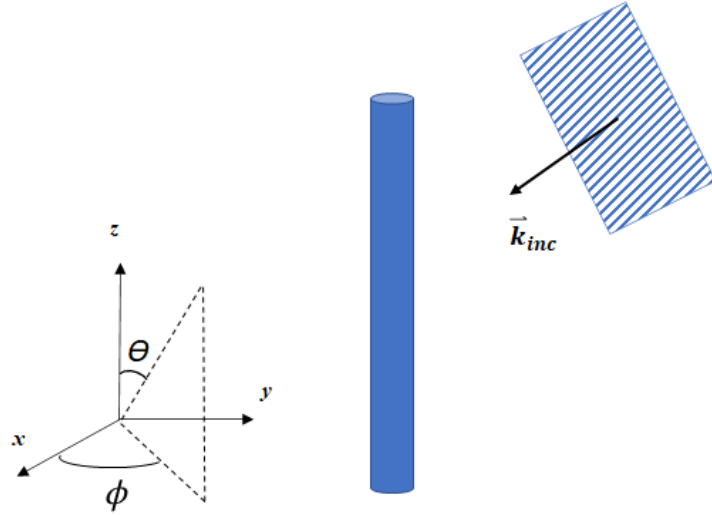


Figure 3.1 – Thin wire along z axis illuminated using a plane EM wave with incident wave vector \vec{k}_{inc}

object's center will be considered to estimate and compensate the propagation channel. With CST and HFSS a probe is placed at a finite distance (1m) from the object to recover the scattered far field within the calculation volume (radiation box). The scattered field is retrieved for both E_θ and E_ϕ components to take into account the field polarization.

Note that the back-scattered field will be defined as the field scattered in the opposite direction of the incident wave (equivalent to mono-static mode).

3.2.1 Analytical solution

First, we compute the scattered field of the PEC sphere analytically using Mie series (Mie, 1908). The plane wave is traveling along z axis and polarized along x axis (θ is 180° and ϕ is 0° in equation 3.1 as in fig. 3.2). Assuming that the incident field has a unit amplitude, the scattered field can be computed in the far-field region for both θ and ϕ components as follows:

$$E_\theta = \frac{e^{-ikr}}{-ikr} \cos\phi \cdot S_2(\cos\theta) \quad (3.3)$$

$$E_\phi = \frac{e^{-ikr}}{ikr} \sin\phi \cdot S_1(\cos\theta) \quad (3.4)$$

where k is the wave number, ϕ is the angle between the incidence plane (defined by the incident electric field and \vec{k}_{inc}) and the plane where the scattered field is recorded, and r is the distance from the sphere's center to the point of observation which is fixed at 1m. This value of 1 m is taken as reference by CST

and HFSS for the determination of the phase of the scattered far-field, so we apply the same value in relations 3.3 and 3.4 to ensure a relevant comparison. S_1 and S_2 are the scattering amplitudes expressed as:

$$S_1(\cos\theta) = \sum_{n=1}^{n_{max}} \frac{2n+1}{n(n+1)} (a_n \pi_n + b_n \tau_n) \quad (3.5)$$

$$S_2(\cos\theta) = \sum_{n=1}^{n_{max}} \frac{2n+1}{n(n+1)} (a_n \tau_n + b_n \pi_n) \quad (3.6)$$

where a_n and b_n are the Mie coefficients. n is the index that is truncated to n_{max} where n_{max} is fixed according to the size parameter $x = ka$ (a is the sphere's radius and k the wave number) as given by Bohren and Huffman, 1983. τ_n and π_n are the functions describing the angular scattering patterns.

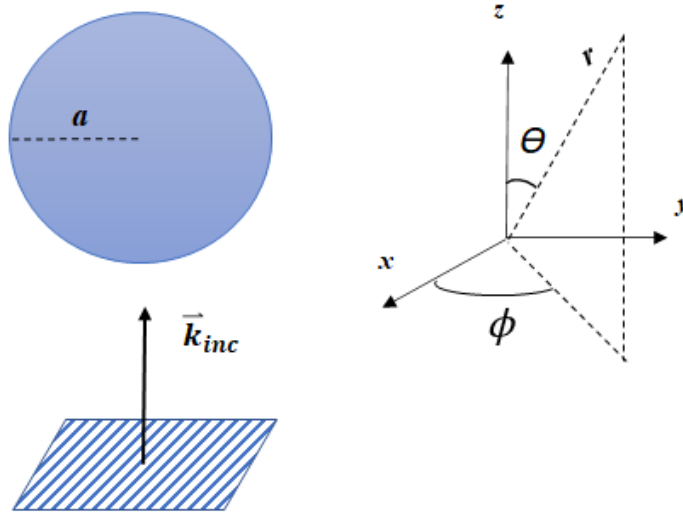


Figure 3.2 – Sphere illuminated using a plane EM wave travelling along $z > 0$

3.2.2 Numerical full wave simulation

Using HFSS, we get scattered field in frequency domain that we compare with the one obtained using CST with the time domain solver when illuminating the objects using a Gaussian pulse. The CST time solver is used because the far-field probes in time domain are more efficient and less time consuming than frequency domain probes.

The PEC sphere is illuminated by a plane EM wave whose propagation and polarization are identical to those of the analytical solution. Fig. 3.3, shows an

excellent agreement between the scattered field obtained using Mie series and both simulation software. We present only the results for a sphere's radius of 15 cm for concision, but we obtain the same results for any radius value. Thus, for the rest, we use Mie series to get the scattered field of a sphere because it is less time consuming.

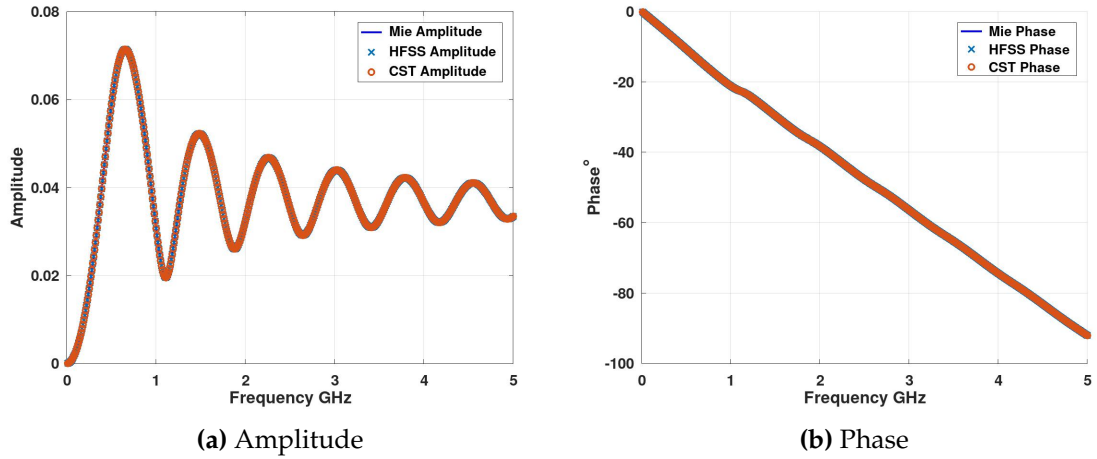


Figure 3.3 – (a) Amplitude and (b) unwrapped phase of the back-scattering response of a PEC sphere of 15 cm diameter using CST and HFSS simulation tools and analytical solutions (Mie)

The metal wire (fig. 3.1) is illuminated using a plane wave where we simulate two cases of \vec{k}_{inc} (two directions of incidence) : first, $\theta = 90^\circ$ and $\phi = 0^\circ$ to provide a normal incidence regarding the axis of the wire, and second, $\theta = 45^\circ$ and $\phi = 0^\circ$. In fact, the polarization of the incident wave is important when dealing with a thin structure as the thin metal wire. If the plane wave is polarized horizontally (i.e. y axis), then the structure will not be excited as the wave does not interact with the object.

From the scattered field of both objects in fig. 3.4, we can see that for the thin wire, which is a strong resonating object, resonance peaks appear clearly in its amplitude response. On the contrary, the PEC sphere is a weak resonating object, so it is more difficult to observe the resonances from its response.

Following, we will apply the three SEM techniques on the field scattered by the PEC sphere and the thin wire and compare the extracted poles with theoretical ones in both noiseless and noisy environments. The scattered fields are simulated as shown before. The SEM methods will be applied on the E_θ component of the scattered field of both objects for results presented in this chapter. They are also applied not only on the positive frequency data, but we also complement it with the negative frequency response (complex conjugate)

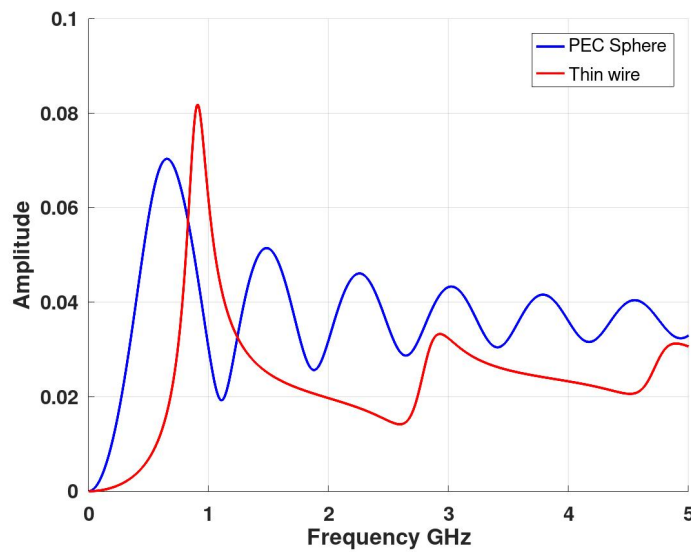


Figure 3.4 – Amplitude of the scattered field (E_θ) of the PEC sphere and thin wire in the back-scattering direction when illuminated with a normal incident.

to get complex CNRs. Thus, we get the same scattered field as the one obtained from FFT of the real impulse response. The SEM techniques can equally be applied on the other component of the scattered field (E_ϕ) as seen in appendix A. During the classification stage that will be presented in chapter 4, we will make use of both field components.

3.3 SEM applied to the scattered field of a PEC sphere

First, we study the SEM techniques on the scattered field in the back-scattered observation angle for E_θ ($\phi = 0^\circ$, $\theta = 180^\circ$) of a PEC sphere of 15 cm diameter.

Mie theory is used to directly compute the theoretical SEM poles that characterize the scattered field by a spherical conducting object that will be used as reference. These resonating frequencies are related to the zeros of spherical Hankel functions H_n^2 and other derivatives. As these admit a rational form, their zeros can be computed almost analytically by using root finding procedures for polynomials (Harrington, 2001, p. 265, p. 464). Truncated endless series of these theoretical poles, that will be used as reference, are presented in fig. 3.5. The computation of the CNRs of a PEC sphere was done in collaboration with INRIA Factas Team.

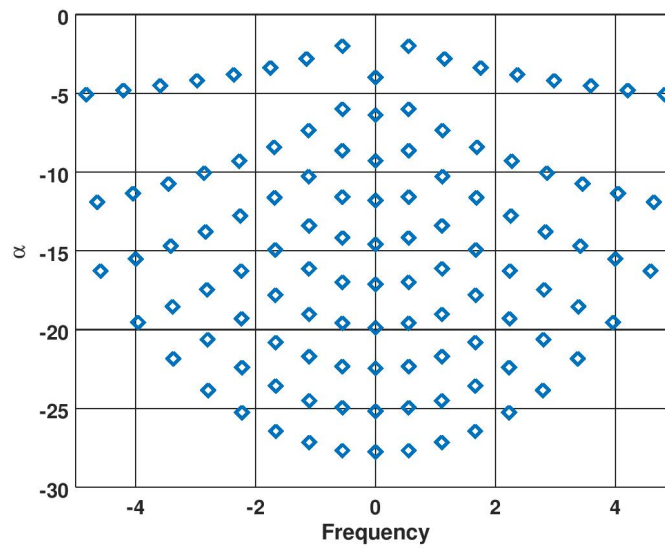


Figure 3.5 – Theoretical poles of a PEC sphere of 15cm diameter computed from Mie theory. The damping factors α are presented on the ordinate as a function of resonant frequencies on the abscissa.

3.3.1 Phase compensation in frequency domain

In the far field, when an incident EM wave is considered as plane, channel compensation has minor impact on the amplitude response. However, the distance between the receiving antenna and the scattering object cannot be accurately determined and the problem of phase origin arises. In addition, in frequency domain, SEM techniques cannot be directly applied on the complex SF response as the phase varies rapidly in the far-field region and they become unable to approximate the solution. This problem does not arise in the time domain because this phase shift corresponds only to a delay. The processing is then done directly on the delayed pulse.

One way to circumvent this issue is to compute the power spectrum of the scattered field $H(f)$ (Yang and Sarkar, 2016) as follows:

$$|H(f)|^2 = H(f) \times H^*(f) \quad (3.7)$$

Hence, we remove the phase dependency. This is similar to not take into account the phase of the scattered field which amounts to considering it to be zero. Fig. 3.6 shows the amplitude and the CNRs extracted from the power spectrum using VF. We can see that they can be accurately extracted from the power spectrum by comparing them to the analytical ones.

However, by removing the phase we lose important information contained in the residues. To overcome this issue, we have to include the phase in our calculations as it brings information as well as the magnitude. That is why, we need to compensate the length of the channel of propagation to apply properly the SEM techniques in frequency domain.

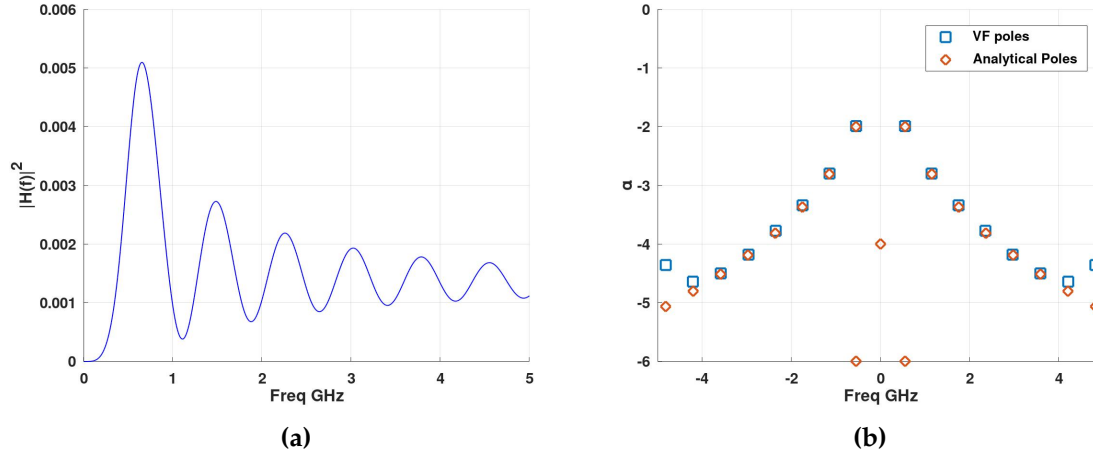


Figure 3.6 – (a) Amplitude of the power spectrum in the back-scattering direction; (b) Poles extracted using VF with $M = 40$ (M is the model order).

In the present case, the distance d between the object and the receiver is already known (1m). Hence, we can compute the compensation distance r accordingly. The phase compensation (ϕ_{ic}) is computed as follows:

$$\phi_i = \frac{2\pi}{\lambda_i} \times r \quad (3.8)$$

$$\phi_{ic} = \phi_{i_{original}} - \phi_i \quad (3.9)$$

where i is the frequency index.

For a PEC sphere of 0.15 m diameter, $r_{theoretical}$ is 0.85 m ($d - 2 \times a$, with a being the radius) for the back-scattering direction. However, as we don't know the distance at which the object is placed in real-life measurements, we need to compensate this phase variation that characterizes the channel but not the object.

There are several possibilities for compensating the far-field channel:

- The use of the time response to calculate and then compensate the time delay using equation 3.8.

- Accurate estimation of an average group delay and compensation of this delay.
- This group delay can be estimated quickly by considering that the phase shift due to the object's response is negligible compared to that induced by the channel.

The latter solution will be chosen for its simplicity since the estimated group delay is therefore computed at the maximum frequency ($r = \phi_{f_{max}} \times \lambda_{f_{max}} / 2\pi = 0.88$ m), making an estimation error of 0.03 m relatively to $r_{theoretical}$ for this PEC sphere. The theoretical compensated phase computed from $r_{theoretical}$ and the over-compensated one can be seen in fig. 3.7. This compensation (equations 3.8 and 3.9) where we determine r will also be applied to all observation angles.

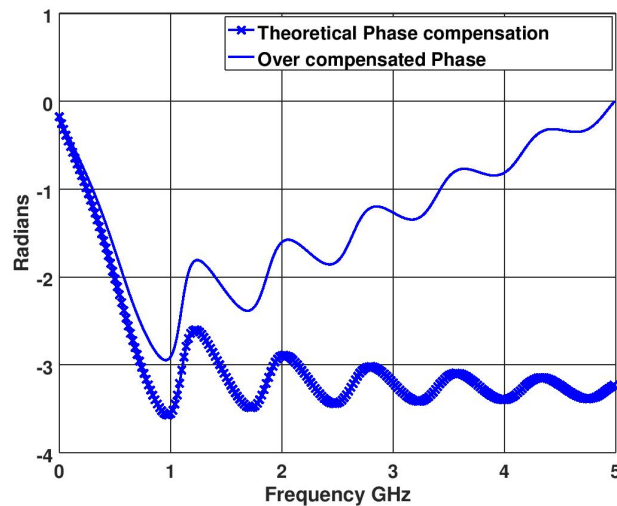


Figure 3.7 – Theoretical and over-compensated phase of a PEC sphere of 15 cm diameter.

The phase compensation of the scattered field is therefore a necessary pre-processing step for the proper estimation of the CNRs using SEM techniques in frequency domain. The sensitivity of each method to phase compensation errors will be evaluated later in this chapter.

3.3.2 Early and late time separation

As discussed in chapter 2, obtaining the characteristic poles of an object from time-domain SEM methods requires the isolation of the "late-time" part of the scattered field containing the natural resonances of the object.

To separate the early time component from the late time, we first compute analytically the start of the late time using equation 2.22 as the object's size and geometry are known. In this case, the late time depends on the distance travelled by the creeping waves that circulate along the circumference of the sphere. This distance depends on the sphere's radius and, hence, the late time should start at: $\{2r + \pi \times r\} / c = 1.28$ ns after the early time; c is the celerity of light. However, in practice we do not have apriori knowledge about the target's shape and size, hence, it is desirable to estimate the start of the late time from the impulse response directly. The calculation of the theoretical late time will therefore only be used here to validate our method of estimating the late time.

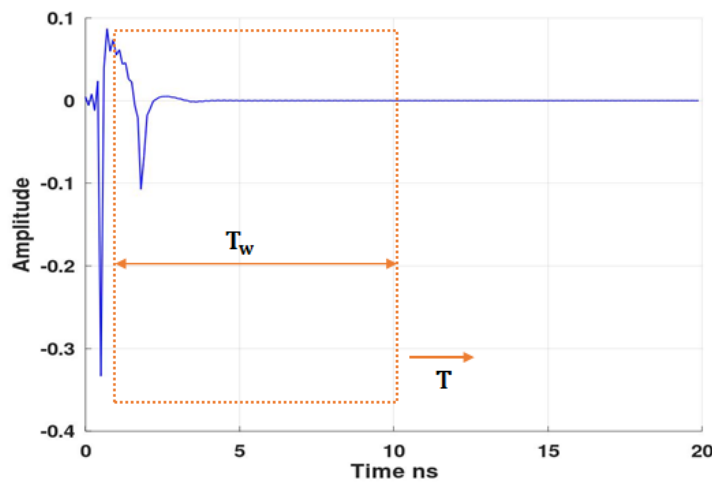


Figure 3.8 – Impulse response of the back-scattered field for a PEC sphere with a diameter of 0.15 m.

For that, we apply a sliding time window of width T_w , as presented in chapter 2, that is shifted by T step and at each step we apply TLS MP as seen in fig.3.8. In (Rezaiesarlak and Manteghi, 2013), it was indicated that the window's width can be fixed according to the frequency of the fundamental pole or the object's size. However, both information are unavailable to us in real measurement conditions, thus, T_w is chosen wide enough to include as much information as possible. In fact, in the case of the PEC sphere, which is a weak resonating object, the start of the late time should be carefully selected as the impulse response has a very short duration (fig. 3.8). If the window is fixed too late beyond the late time, we risk to not be able to extract all the natural poles as their energy will be too low and thus, harder to extract.

Now, we start by evaluating the stability of poles to determine the beginning of late time response in the back-scattering direction as described in (Rezaiesarlak and Manteghi, 2013). We show the poles extracted for each window in fig. 3.9

and we see that it is hard to determine the delay where the poles become stable as the late time has a very short duration.

Hence, to overcome this ambiguity, we propose to focus on the singular values. Fig. 3.10 shows the distribution of the normalized singular values for each window. From 3.10c, we can see that at 0.9 ns the distribution of the first 10 singular values starts to become stable which indicates the start of the late time. The difference between this value and the analytic one (1.28 ns) is due to the very low resonating behaviour of the PEC sphere which has a very typical backscattering field with strong discontinuities and a very short response. In this case, the boundary between late time and early time is tenuous, and it is preferable to ensure that the signature of the PEC sphere in the late time is complete, even if it means not removing the early time part entirely. It is then possible to calculate the CNRs of the PEC sphere efficiently.

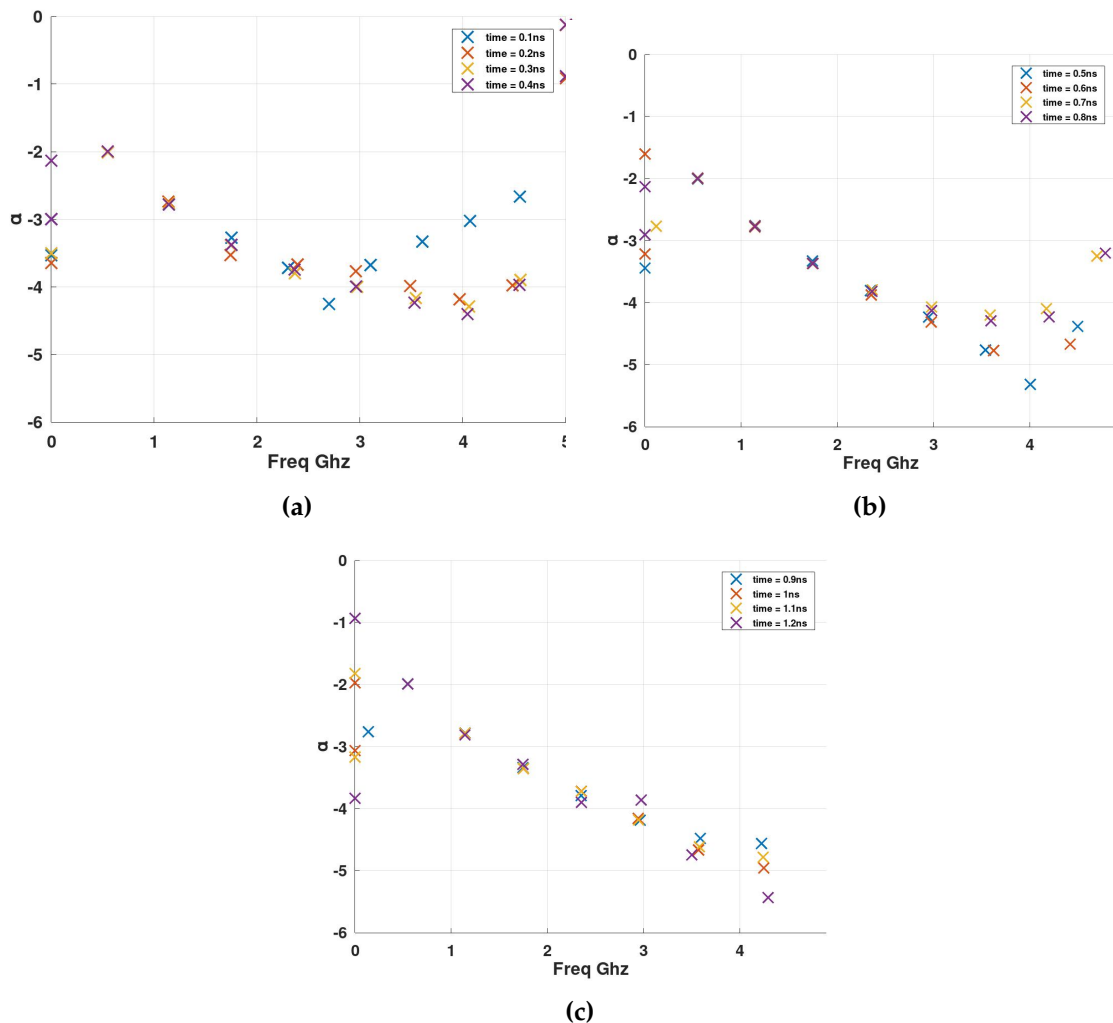


Figure 3.9 – CNRs extracted from the back-scattered field for windows with different time width.

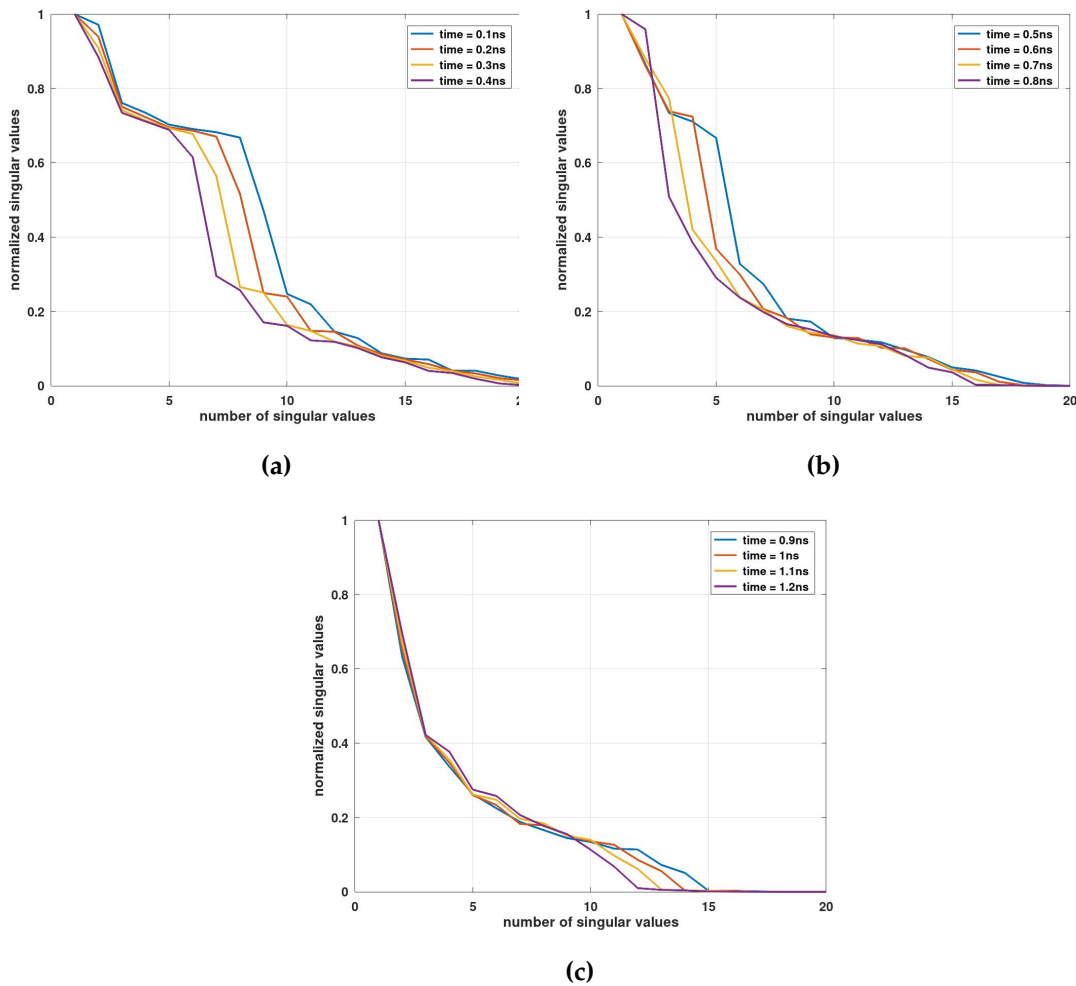


Figure 3.10 – Normalized singular values of the PEC sphere extracted from the back-scattered field for windows with different time widths.

3.3.3 Comparison between VF, TLS Cauchy and TLS MP methods regarding poles extraction

3.3.3.1 Poles extraction from backscattered field

After the phase compensation in frequency domain, we begin by estimating the model order M of VF and TLS Cauchy. Indeed, this is a recurrent problem of the SEM methods. By varying the model order, we notice that starting from $M = 24$ the extracted poles start to converge towards the theoretical poles as seen in fig. 3.11. This confirms that M needs to be overestimated to be able to extract the physical poles accurately. We recall that the frequency response includes not only the late time response but also the early time. Thus, the model order of VF and TLS Cauchy is overestimated to 26. It includes complex pairs

of SEM poles characterizing physical resonances of the PEC sphere and “mathematical” poles due to early time. In fig. 3.11e and 3.11f there are additional

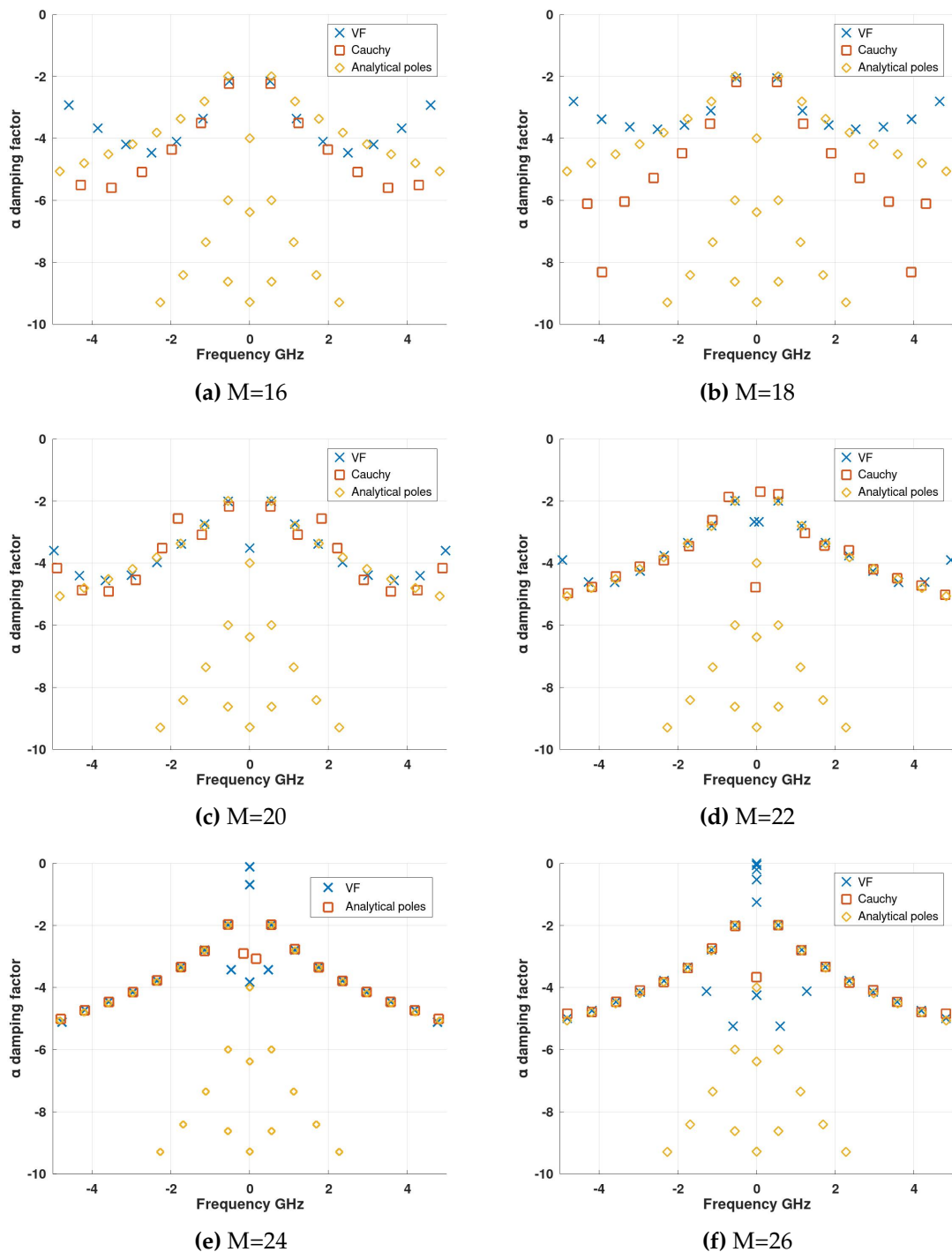


Figure 3.11 – Poles extraction using VF and TLS Cauchy for multiple model orders varying from 16 to 26.

mathematical poles that appear for both VF and Cauchy that are not presented on both figures for visibility. They are as follows: poles outside of the frequency range, poles with damping factor higher than 10 and others that exist on the

positive side of the ordinate axis. We apply the criteria mentioned in chapter 2 to eliminate mathematical poles resulting from the application of SEM methods in frequency domain. Only physical CNRs of the first branch will be retained to characterize the object.

For VF, only two iterations are enough for the convergence of the CNRs in noiseless case. For TLS Cauchy, the order p in equation 2.29 is fixed at 19 (10^{-19}). This value is chosen after multiple trials of several values ranging from 10^{-2} to 10^{-20} . This very low value might be due to the weak resonating behaviour of the PEC sphere. This will be verified for the thin wire in section 3.4, where we expect that p will be lower as it is a strong resonant object.

In time domain, after identifying the late time, as proposed in the previous section, TLS MP is applied on the late time response where the threshold ϵ in equation 2.17 is fixed to 10^{-9} . Thus, the very weak singular values are removed. The model order is fixed to 20.

Fig. 3.12 shows the physical poles estimated by TLS MP, VF and TLS Cauchy. The three methods match well with the 16 theoretical CNRs of the first branch. Interestingly, none of these methods succeed in estimating the natural resonant frequencies from the other branches (with damping factors higher than 6), neither when they are directly applied to the analytic scattered response. This is due to the fact that those CNRs have high damping factors and very weak residues rendering their precise estimation nearly impossible.

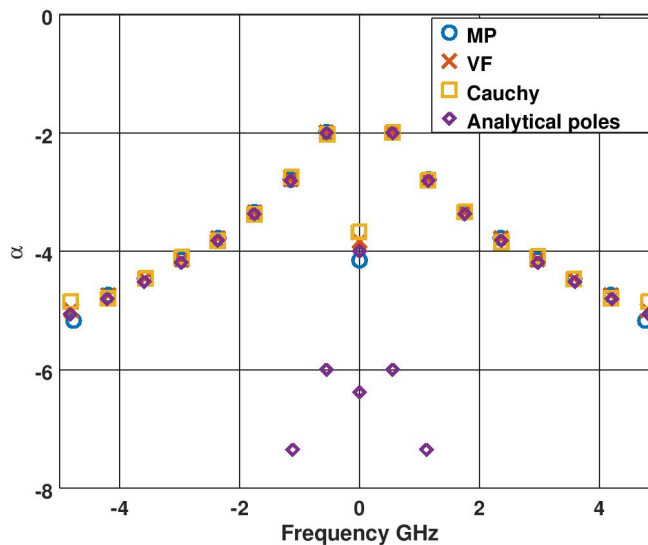


Figure 3.12 – Estimated Physical CNRs of a 0.15 m diameter PEC sphere compared with the theoretical ones.

3.3.3.2 Sensitivity of SEM to phase variations in frequency domain

As seen in section 3.3.1, there is an error between the theoretical compensation's distance and the computed one which leads to an error on the compensated phase. In fact, this error will only affect VF and TLS Cauchy as they are applied on frequency responses, while TLS MP is applied on time responses where a phase error implies only a time shift. Thus, we explore the robustness of both TLS Cauchy and VF regarding phase compensations errors.

This way, we test the sensitivity of both methods to small error variations that vary from $-2\lambda_{f_{max}}$ to $2\lambda_{f_{max}}$ (i.e. $\lambda_{@5GHz} = 0.06$ m) representing a maximum of 12% error on the compensation distance. Then, we compute the relative error of each estimated complex pole (s) compared to the theoretical one as follows:

$$\epsilon = \frac{|s_{sem} - s_{th}|}{|s_{th}|} \quad (3.10)$$

Results presented in fig. 3.13, show the mean relative error computed over the first eight physical CNRs. They indicate that TLS Cauchy is sensitive to phase reference errors, while VF is much less affected (an error less than 1%). Furthermore, by increasing the phase compensation error, we have to increase the model order as the pole extraction becomes more difficult for both methods.

Thus, VF is the most accurate SEM method in frequency domain when confronted to imprecise channel compensation. Whereas, in time domain, TLS MP involves the precise evaluation of the early-time part of the temporal response. This shows that VF is more robust as its results will be less dependent on poor estimations of the channel compensation or early time, which is an advantage in the development of an automatic recognition tool.

3.3.3.3 Extraction of poles from multiple observation angles

As discussed in the previous chapter, CNRs are independent with regard to the direction of observation. This means that for any observation angle, the CNRs are expected to be the same. Thus, we study the effect of varying the observation (bi-static mode) on the extraction of CNRs to check if the method will be robust, regardless of the position of the transmitter and receiver with respect to the sphere.

Indeed, in some directions, the scattered field could be weaker or the signature of the sphere less present. To verify this, we extract the CNRs from different directions of observation in the plane having $\phi = 0^\circ$ and θ varies. In this plane,

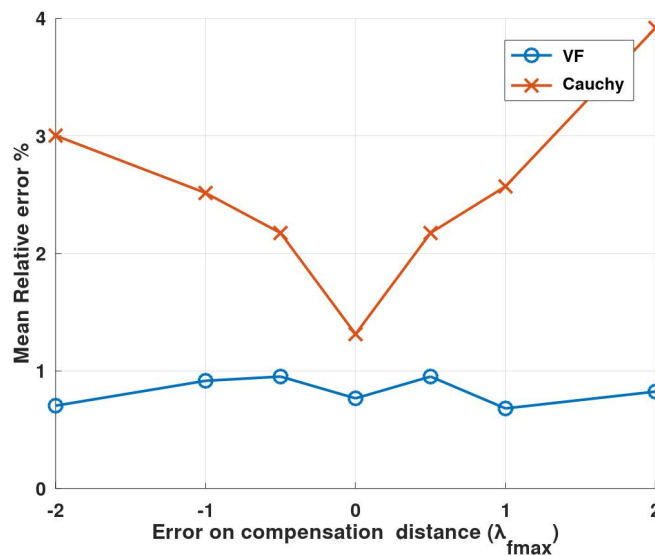


Figure 3.13 – Mean relative error versus channel compensation distance.

the dominant component of the field is the E_θ component and the other one is negligible.

From fig. 3.14 we see that the CNRs are the same when using VF on each observation angle. Those results are the same for TLS MP and TLS Cauchy. In the region behind the sphere ($\theta = 0^\circ$ to 60°), the last CNR has the highest error ($\approx 1.6\%$) as the scattered field is weak in this space. Those results confirm the theory that CNRs are independent of the direction of observation (i.e. we obtain the same CNRs from monostatic and bistatic response of an object).

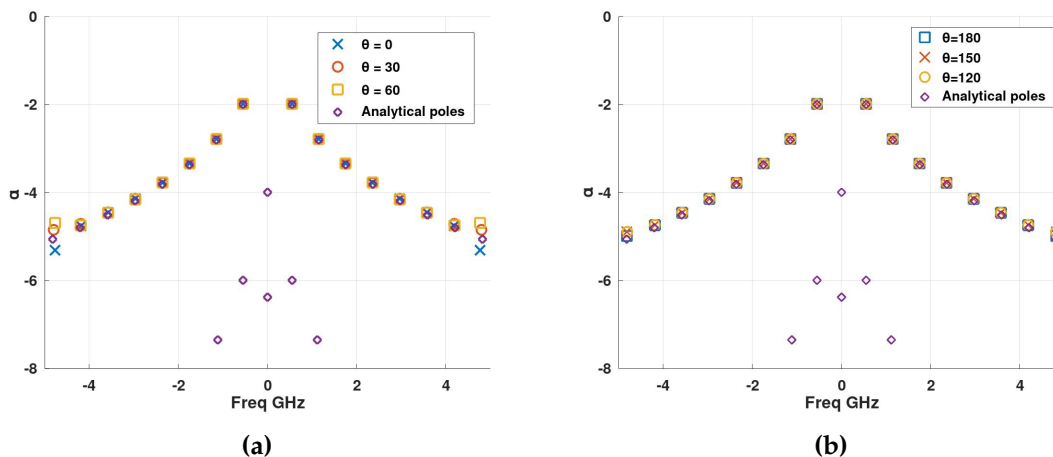


Figure 3.14 – CNRs extracted from a 15 cm diameter PEC sphere by using VF on different directions of observation.

3.3.3.4 Poles extraction results for different sphere sizes

In this part, we study the effect of varying the sphere's diameter on the CNRs values. We simulate 2 PEC spheres of 18 cm and 10 cm diameter respectively.

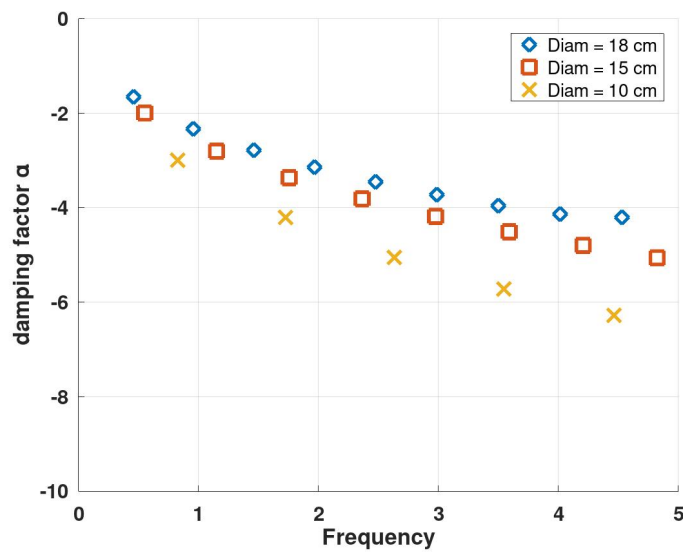
Fig. 3.15a shows the distribution of the complex CNRs for 3 PEC spheres with different diameters. Even though the CNRs are characteristic for each object, we can see that the CNRs distribution is a function of the size of the sphere. Taking the 15 cm diameter PEC sphere as a reference, a ratio between those sphere sizes ($\frac{l_{ref}}{l_{object}}$) and the CNRs ($\frac{f_{ref}}{f_{object}}$ and $\frac{\alpha_{ref}}{\alpha_{object}}$) can be computed. As expected, we find that the ratio between the sphere sizes is the same as the one between the CNRs for both the resonant frequencies and the damping factors. Meaning that there is a homothety between poles of objects having the same shape, but of different sizes.

The representation of poles using the Q-factor presented in chapter 2 allows a better description of the object as it is independent of its size. Fig 3.15b shows the Q-factor distribution as a function of resonant frequency for 3 PEC spheres of different diameter. We can see, that for resonances 1, 2 ..., n, the Q-factor is the same for any diameter of the sphere. Hence, the Q-factor can describe the resonant behaviour of the sphere while the resonant frequency allows to compute its diameter. Of course, these conclusions are always correct regardless of the form of the object.

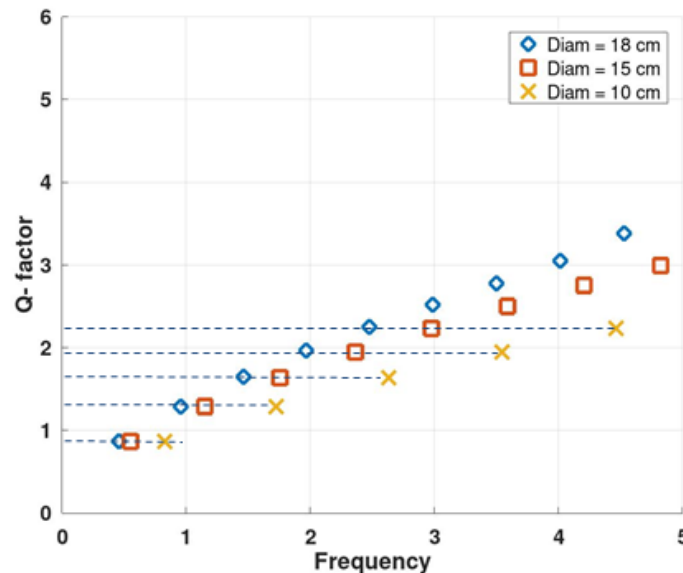
3.3.4 Study of the robustness to noise

Here, we compare the behaviour of VF, TLS Cauchy, and TLS MP in presence of noise. To do so, we start to numerically add an Additive White Gaussian Noise (AWGN) to the back-scattered signal. We choose different values of SNRs varying from 65 dB that corresponds to favorable measurements conditions, to 30 dB which conforms with less favorable conditions. This is done over 30 trials to get the mean error rate.

For a 65 dB SNR, TLS MP, and VF (3 iterations) have similar behaviours. The first three natural poles are accurately extracted, whilst TLS Cauchy has the highest error percentage. The results of each CNR estimation can be seen in fig. 3.16a and their relative error in fig. 3.16b. It should be noted that the three methods did not extract the eighth pair of complex poles and diverge from the theoretical poles in the same manner. If a simple comparison between the poles



(a) Damping Factor vs Resonant frequency



(b) Q- Factor vs Resonant frequency

Figure 3.15 – Poles distribution for EC spheres of different sizes.

obtained from these methods is done, one could think that they provide accurate results. However, thanks to the theoretical poles that are set as a reference, we are able to make an objective comparison about their accuracy.

With 30 dB SNR, the results indicate that TLS Cauchy still has the highest relative error, as seen in figure 3.16c and 3.16d. TLS MP and VF extract only the first pair of poles with a small error and present similar results. In this case, we apply between 12 and 15 iterations for VF where we get the minimum mean relative errors of the first 7 extracted CNRs as seen in fig. 3.17. Again, a mutual

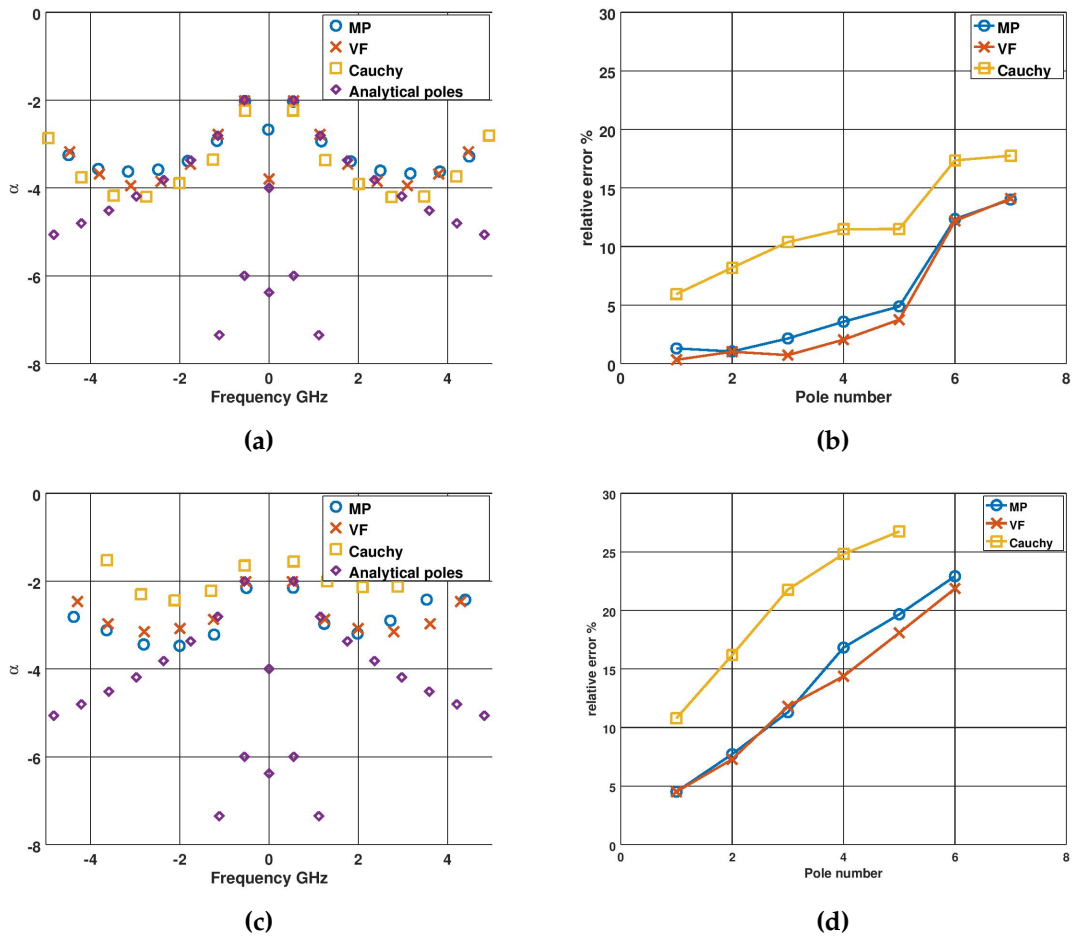


Figure 3.16 – (a) Poles estimated for a 65 dB SNR; (b) Relative error for 65 dB SNR; (c) Poles estimated for 30 dB SNR; (d) Relative error for 30 dB SNR.

validation or even the reconstruction of the scattered field, in time or frequency domain, would lead us to assume that the physical poles have been correctly extracted (Fig. 3.18). Nevertheless, from what we have seen till now, the higher order poles get affected by the noise levels and diverge from the theoretical ones, even though they can be used to properly reconstruct the scattered field. Indeed, for very noisy signals with SNR lower than 30 dB, the signal will not be reconstructed properly. This is due to the fact that only the first CNR can be accurately extracted at low SNRs, as will be seen in chapter 4, which is not sufficient for the accurate reconstruction of the scattered field.

Hence, we can conclude that it remains complicated to extract a significant part of the numerous natural poles from a noisy scattered field from a such challenging object as the sphere. Moreover, we note that MP and VF represent more promising results when exposed to noise than Cauchy. This test will also be

conducted later using the thin wire to compare the performance of the methods when applied on strong and weak resonating objects. For the remainder of this section, we have selected the use of VF in frequency domain as it is more robust than TLS Cauchy and the use of TLS MP in time domain.

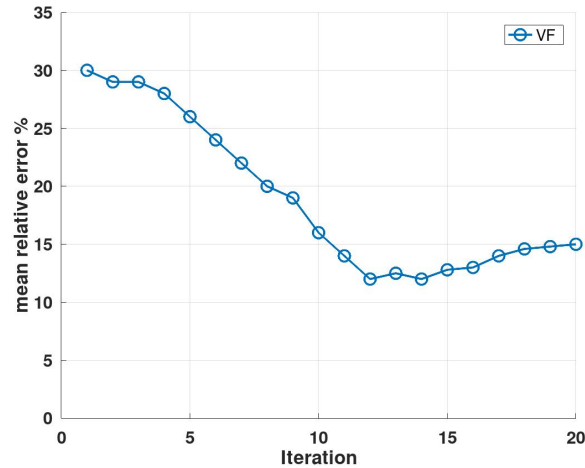


Figure 3.17 – Mean relative error of poles for different iterations using VF when applying 30 dB SNR.

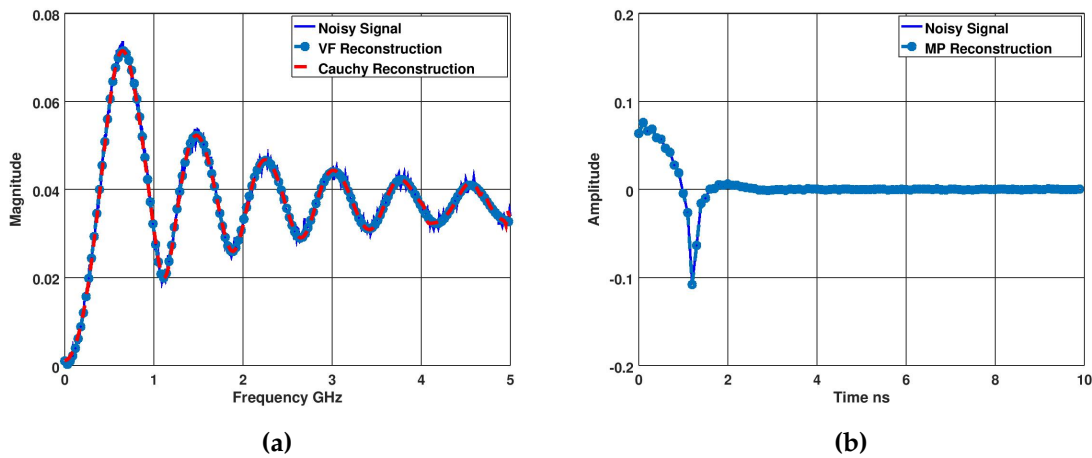


Figure 3.18 – (a) Frequency domain reconstruction using estimated poles from Cauchy and VF for 30 dB SNR; (b) Late Time response reconstruction using MP for 30 dB SNR.

VF with Multi Observation Angles

Theoretically, SEM poles extracted from the scattered field by an object are the same regardless of the direction as seen in 3.3.3.3. To take advantage of this fact and reduce the effects of noise on the accuracy of poles estimation, we use the functionality of VF that allows to estimate same poles from multiple transfer functions. VF is, hence, applied on an increasing number of scattered

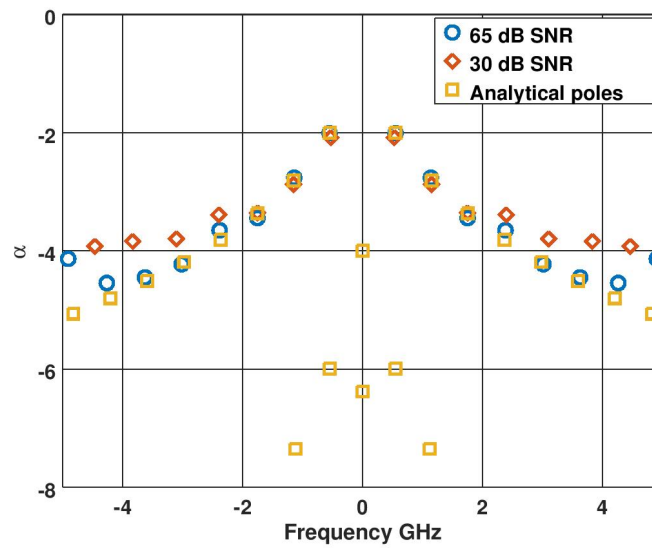


Figure 3.19 – Poles extracted using VF for 65 & 30 dB SNR when taking into account all observation angles of the scattered field.

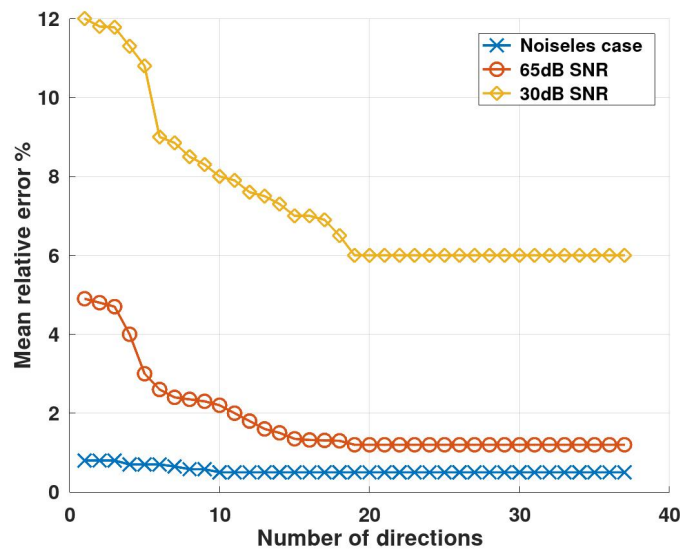


Figure 3.20 – Mean relative error versus the number of input data (observation angles) using VF.

field responses from one to 37 observation angles as we have 37 angles in θ direction as simulated in section 3.2. Fig. 3.19 illustrates the estimated poles extracted with VF when including the 37 observation angles at once with both values of SNRs. The average error in pole estimation was computed for the seven pair of natural poles of the first branch. This shows better convergence of poles compared to earlier when the extraction was done uniquely on the back-scattering direction. We can see in fig. 3.20 that the multi-input does not affect the accuracy of VF in the noiseless scenario. Nonetheless, the effect

of increasing the number of observation angles is evident with noisy signals, where VF estimates the SEM poles with a significantly higher precision once it works with more than 5 inputs.

3.3.5 Discussion and interpretation of the physical poles and their residues

3.3.5.1 Physical and mathematical poles

In paragraph 3.3.3, the model order M of TLS Cauchy and VF was fixed to 26. To validate this choice, we compute the error, using equation 2.52, between the back-scattered simulated field and the reconstructed one using equation 2.36 for M varying from 16 to 26. It should be noted that the scattered field reconstruction in frequency domain is done using the whole set of extracted poles and their associated residues, i.e. mathematical and physical poles.

Fig. 3.21 shows the mean relative error between the simulated and reconstructed scattered field for different values of M . This shows that by over-estimating the model order we get lower error levels but at the same time the error at $M=16$ is not high. Indeed, even with low values of M we can reconstruct the response because, for a given value of M , the methods estimate the pair of poles and residues which allow to reconstruct the scattered field the most accurate as possible. Hence, the evaluation of the reconstruction error cannot be an efficient criterion to evaluate the accuracy of the extracted CNRs.

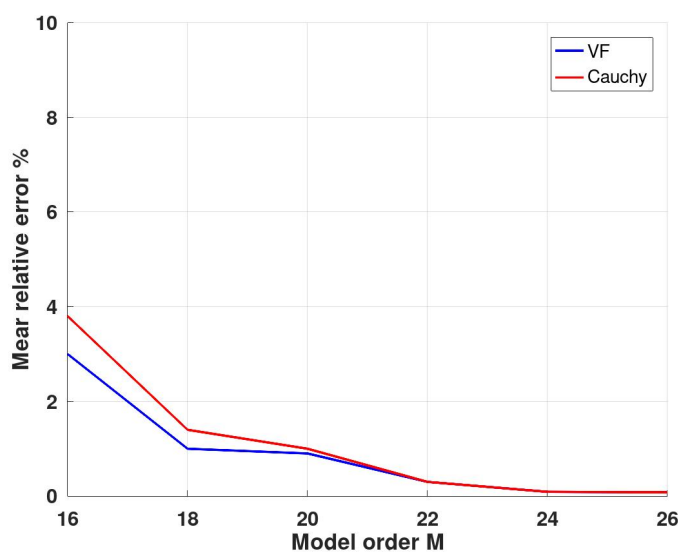


Figure 3.21 – Scattered field reconstruction error versus the model order values for VF and TLS Cauchy.

Indeed, the frequency response includes both early and late time responses, thus, if we reconstruct the scattered field using only physical poles that are related to the late time, we do not get the same response as we can see in fig 3.22. However, the IFFT of the reconstructed response from physical poles can be correlated with the late time response derived earlier. This can be considered as another way to validate the choice of the start of the late time response. We also used the eliminated mathematical poles in the reconstruction process, and we noticed that those poles can reconstruct the early time response. In fig. 3.23, we show the reconstructed early and late time responses. Thus, the mathematical poles can be considered related to the early time response. Those results confirm that the pole selection criteria proposed for SEM in frequency domain (section 2.5.3) are intrinsically linked to the temporal treatment of early time suppression. In addition, they have the advantage of being configurable and therefore automated in the context of an operational use.

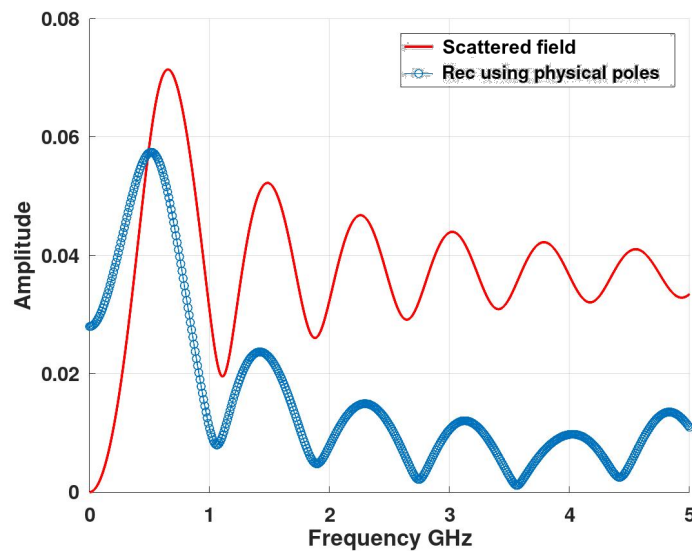


Figure 3.22 – Comparison between the amplitude of the back-scattered field response and the reconstruction using only physical poles.

3.3.5.2 Comparison between residues and scattered field

In Roussafi, 2016, it was shown that the residues can be correlated with the radiated field of an antenna at its resonant frequencies. As an antenna is a radiating element, the early time/ late time problem does not arise as the antenna does not need to be illuminated by an incident wave to radiate. Instead, we will try to pursue this analysis with objects illuminated by an incident plane wave. Hence, we study the distribution of residues associated to each CNR.

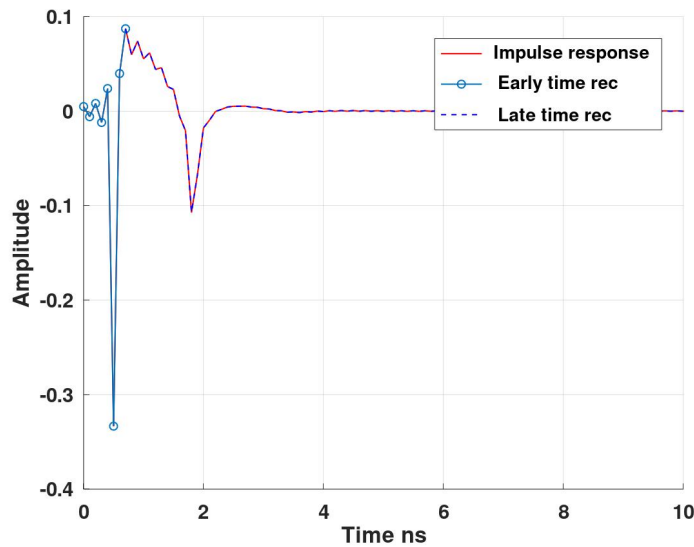
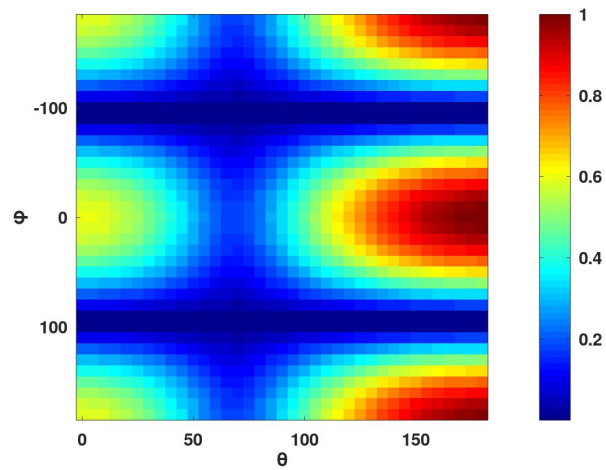


Figure 3.23 – Early and late time reconstruction (Rec) using mathematical and physical poles respectively.

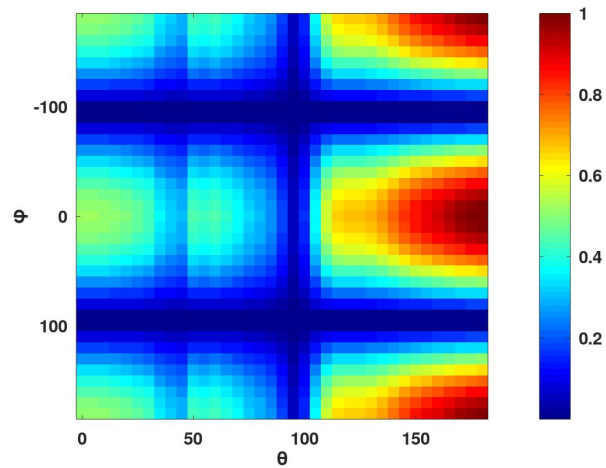
The comparison is done with the residues extracted using VF as they are the same as MP as shown in appendix B. The normalized amplitude of residues at the first three resonant frequencies and the scattered field are shown in fig. 3.24 to 3.26 for all observation angles. We also compare the residues with the late time response that is translated to the frequency domain using a FFT. We see that the residues and the scattered fields are not correlated at any resonant frequencies. In fact, those results are expected as the frequency response includes both early and late time responses and the residues are only related to the physical poles.

For this reason, we compare residues with the late time response and we observe a better correlation where their spatial distribution is similar. For the back-scattering direction ($\theta = 180^\circ$), we can see that the energy is mostly concentrated in this direction. This means that in the direction opposite to the incident wave (back-scattering) the amplitude of the late time is more important than the early time. However, in the other direction ($\theta = 0$), the late time energy is weak compared to the early time response.

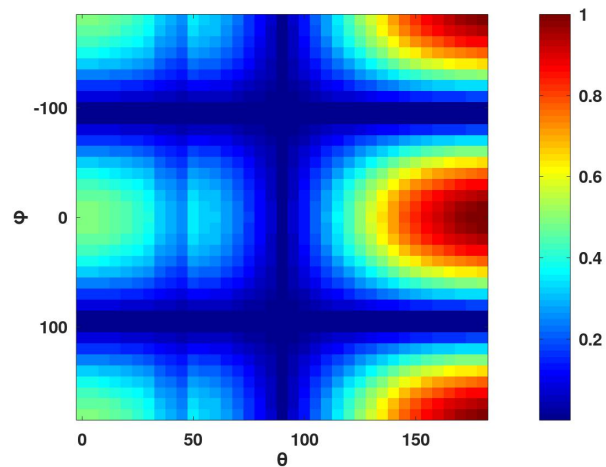
Indeed, the correlation between residues and the radiated field of the antenna in Roussafi, 2016 was possible as there is no phenomenon of late time/early time separation which does not apply here as we work with a scattered field and not a radiated one. That is why, the residues are compared with the late time response and it is seen that they both have almost the same spatial distribution.



(a) Scattered field response

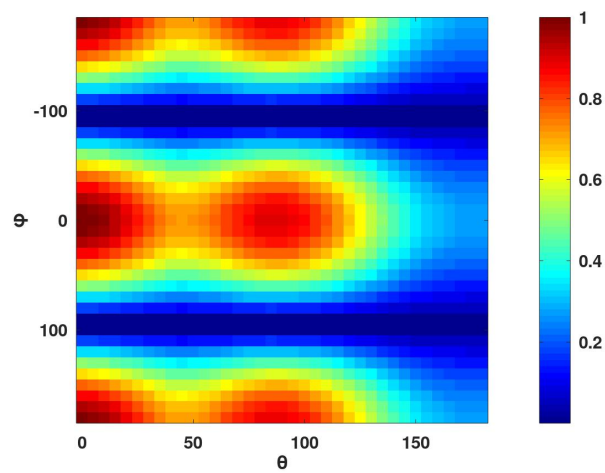


(b) Scattered field from Late Time response

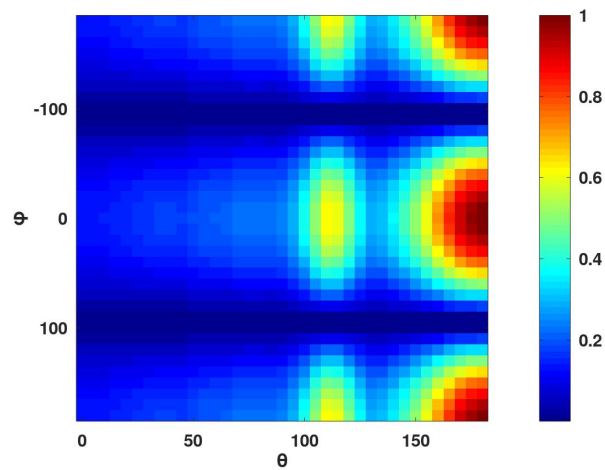


(c) Residues

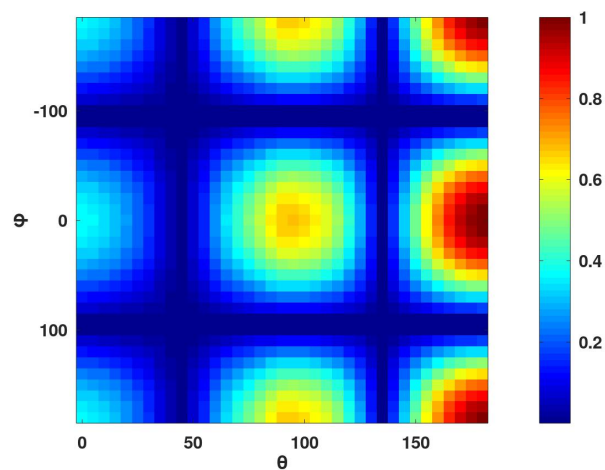
Figure 3.24 – Normalized amplitude of scattered field, scattered field from late time response only and residues related to the first resonant frequency ($f_1 = 0.55$ GHz).



(a) Scattered field response

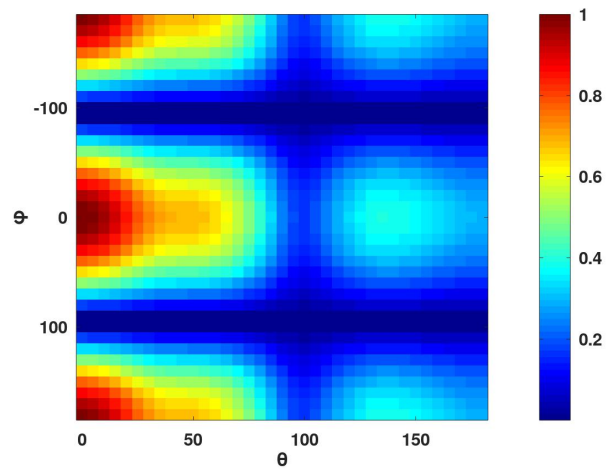


(b) Scattered field from Late Time response

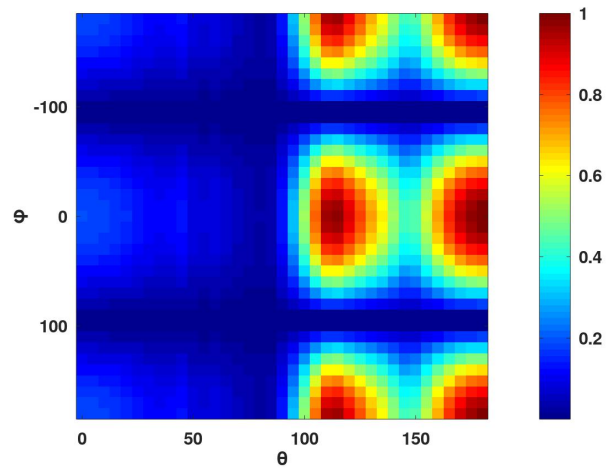


(c) Residues

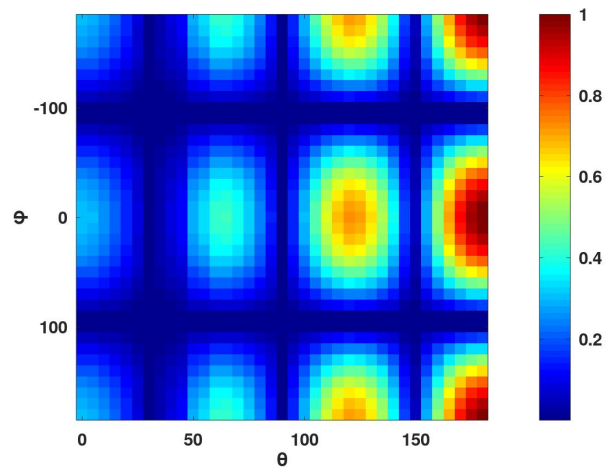
Figure 3.25 – Normalized amplitude of scattered field, scattered field from late time response only and residues related to the second resonant frequency ($f_2 = 1.15 \text{ GHz}$).



(a) Scattered field response



(b) Scattered field from Late Time response



(c) Residues

Figure 3.26 – Normalized amplitude of scattered field, scattered field from late time response only and residues related to the third resonant frequency ($f_3 = 1.75$ GHz).

3.4 SEM applied on the scattered field of a thin wire

In this section, the same processing and analysis conducted on the PEC sphere are being applied to a very different object, the thin wire, which resonates strongly. The analytical poles that are used as reference for the 15 cm length wire are obtained from (Tesche, 1973), and are presented on fig. 3.27. It can be seen that the CNRs are distributed over branches similarly to the PEC sphere. Indeed, the damping factors of the second branch are very low compared to the first one, so their extraction is expected to be difficult.

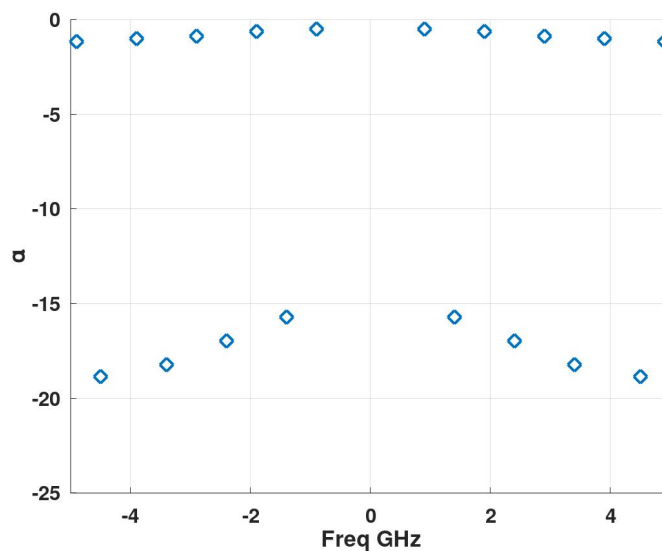
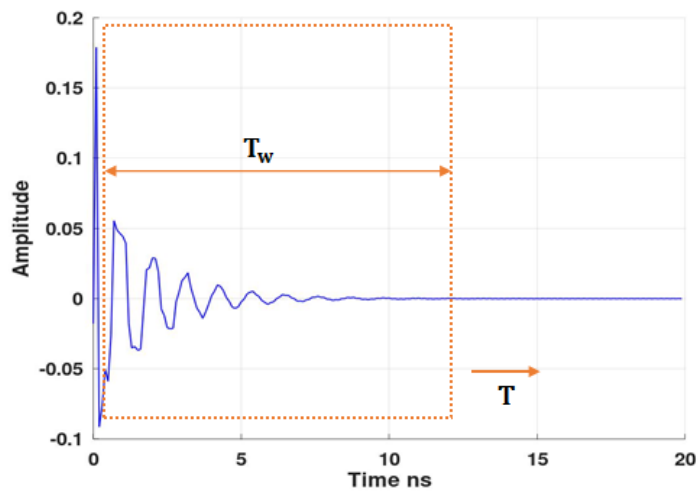


Figure 3.27 – Theoretical CNRs of a thin wire of 15 cm length.

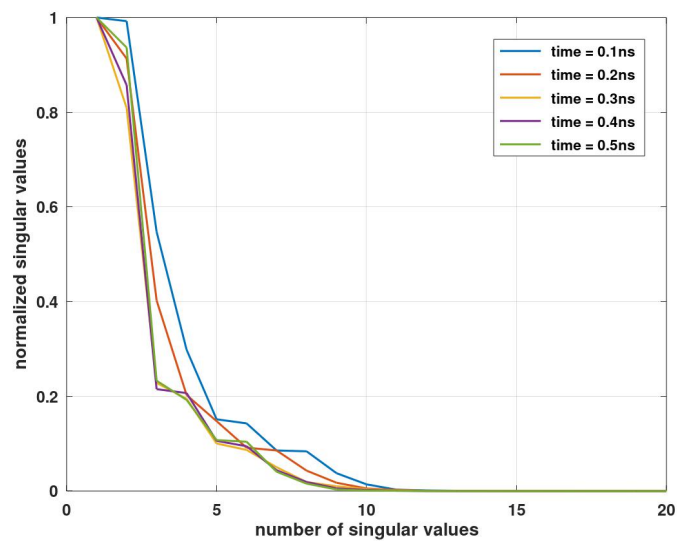
Before applying the SEM techniques in frequency domain, we need to compensate the phase as earlier. Thus, we apply equation 3.8 and 3.9 to compute the compensation distance r and then the phase is compensated.

Prior to the application of TLS MP, we need to separate the early and late time components. From equation 2.22, the start of late time is computed analytically from the knowledge of the size of the object. In case of normal incidence, the creeping waves circulate along the thin wire's length, hence, the late time should begin at: $L/2c = 0.25 ns$ after the early time. We validate this value by using the window moving technique to evaluate the stability of the singular values with the use of TLS MP on the impulse presented in fig 3.28a. T_w is chosen wide enough to include the entire impulse response. From the singular value analysis in fig. 3.28b, we observe that starting from $t = 0.3 ns$, they become more stable. This indicates the start of late time which removes the first peak presented in the impulse response. This value is in good concordance

with the analytic one as the thin wire is very resonating. This shows that the early time part is very short compared to the late time response. Thus, we can expect that, as the duration of the late time is important, we can afford to remove a bit beyond the early time without any consequence on the calculation of the physical poles.



(a)



(b)

Figure 3.28 – (a) Back-scattered impulse response at normal incidence and (b) singular values distribution extracted for windows at multiple time steps.

3.4.1 Comparison between VF, TLS Cauchy and TLS MP methods regarding poles extraction

The model order M of both VF and TLS Cauchy is overestimated to 16 as the thin wire presents less resonances than the PEC sphere. The additional CNRs are eliminated using criteria introduced in chapter 2 and we preserve only CNRs of the first branch. Moreover, for TLS Cauchy, the order p in equation 2.29 is fixed to 6 so we have a threshold of 10^{-6} to eliminate the singular values. This value is higher than the one set for the PEC sphere, which might be due to the strong resonating aspect of the thin wire which facilitates the extraction of CNRs.

As for TLS MP, to eliminate the weakest singular values, ϵ in equation 2.17 is fixed to 10^{-3} . The model order is fixed to 14. We proceed to the comparison of the extracted CNRs from VF, TLS Cauchy and TLS MP, with the analytical ones of fig. 3.27. Fig. 3.29 shows the extracted CNRs at both incident angles when the plane wave has: i) a normal incidence and ii) an incidence of 45° regarding the axis of the wire. As expected, it is impossible to extract CNRs from the second branch using the three techniques.

Indeed, the CNRs are characteristic for each object and independent of the incident angles. However, the wire is a particular object. If illuminated using a normal incidence, not all CNRs can be excited since the resonance phenomena of the wire are not significant when the incidence is normal. Fig. 3.30 shows the amplitude response of the back-scattered wave for both incident waves and we can see that at 45° additional peaks appear.

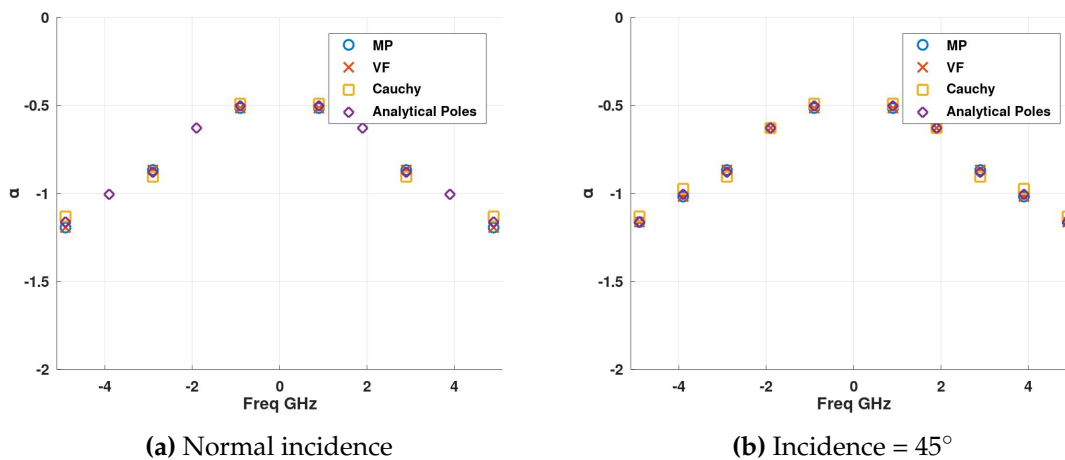


Figure 3.29 – CNRs extracted using VF, TLS Cauchy and TLS MP for two incident angles

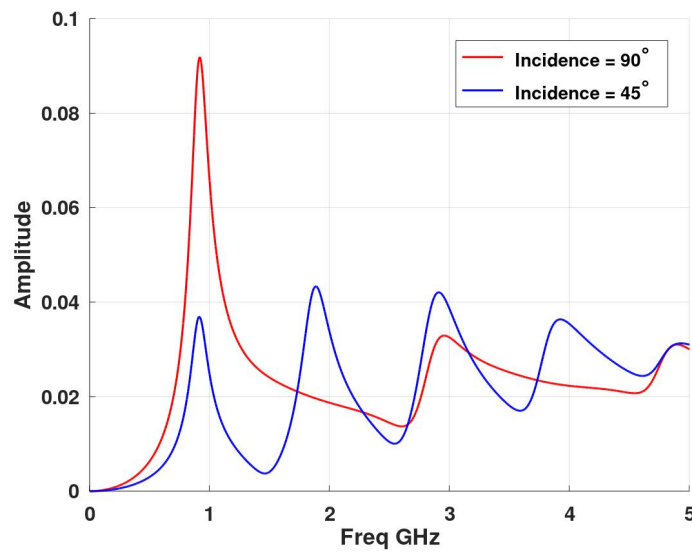


Figure 3.30 – Back-scattered field of a thin wire for both incident directions.

Sensitivity of VF and TLS Cauchy to phase variations

Now, we test the robustness of both VF and TLS Cauchy to phase compensation errors. Using equation 3.8, r is computed at $\lambda_{f_{max}}$ and ϕ_{max} . In this case, we get $r = 0.996$ m to which we introduce an error of $\pm 2\lambda_{f_{max}}$.

In fig. 3.31, we can see that Cauchy is still sensitive to phase variations whereas VF is barely affected. This confirms that, with two different objects, VF is more precise than Cauchy when phase errors occur.

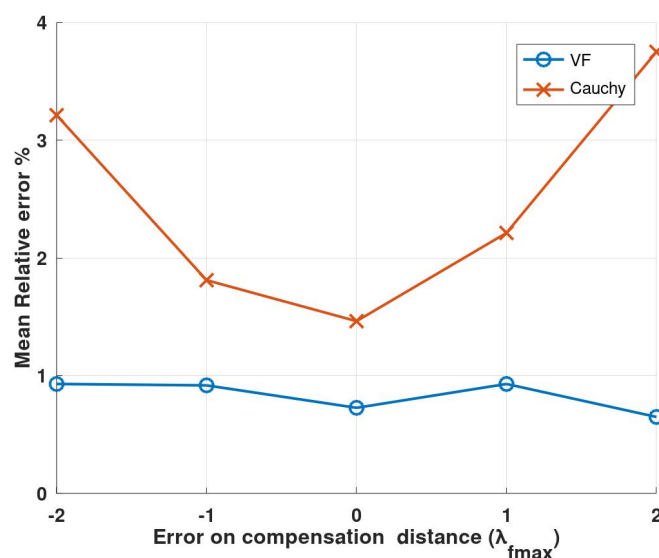


Figure 3.31 – Mean relative error for different phase errors of a thin wire.

3.4.2 Study of the robustness to noise

Now, we test the robustness of each method when applied on a noisy back-scattered field at 65 dB and 30 dB SNRs. We will show results for an incident wave impinging at 45° to excite the maximum number of CNRs within the frequency range. The mean error rate is obtained over 30 runs.

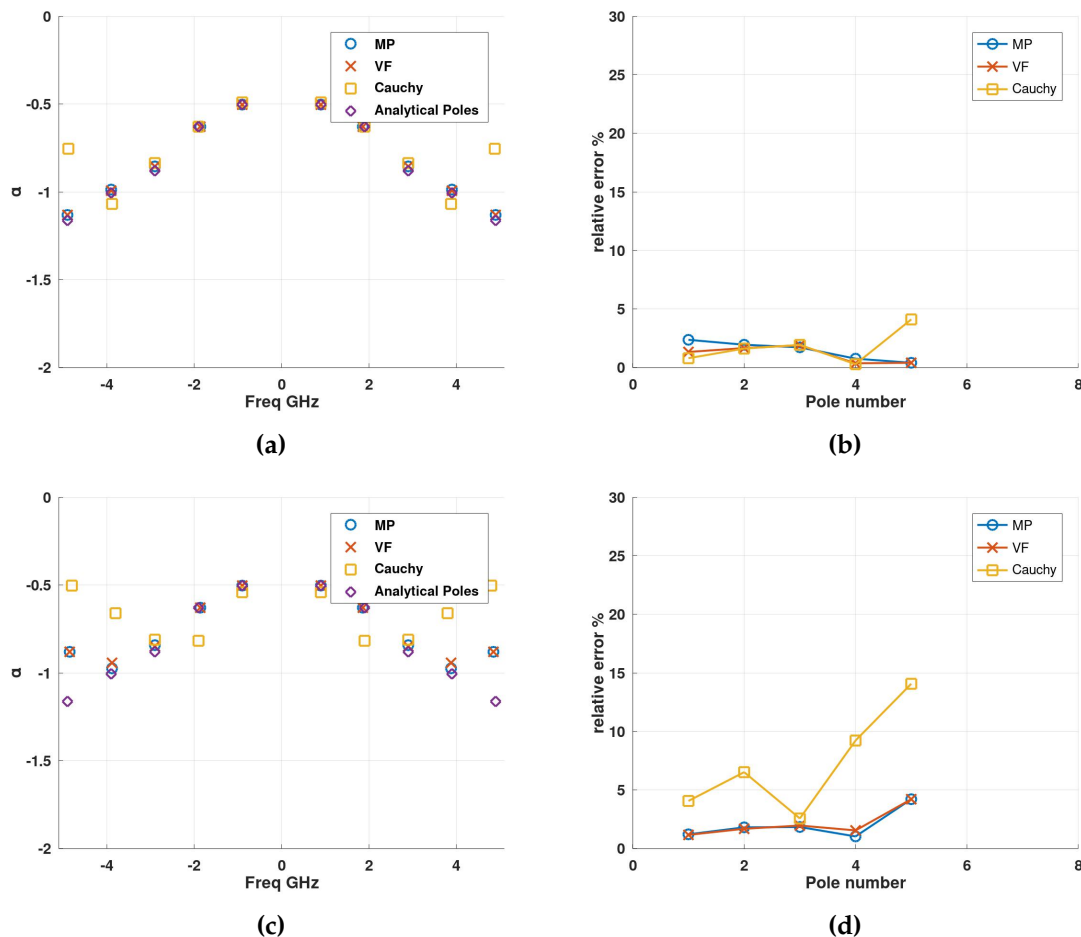


Figure 3.32 – Plan wave impinging at 45° on the thin wire: (a) Poles estimated for a 65 dB SNR; (b) Relative error for 65dB SNR; (c) Poles estimated for 30 dB SNR; (d) Relative error for 30dB SNR.

Fig. 3.32 shows results for CNRs estimation along with their respective relative error when compared to theoretical ones. With 65 dB SNR, TLS MP and VF have similar results with an estimated error less than 2% for all CNRs while with TLS Cauchy the last CNR diverge and has the highest error (4.8%).

When SNR starts to decrease, TLS Cauchy still exhibits the highest error for poles extraction where it can extract only the first CNR with small error. VF and TLS MP can extract the first four CNRs accurately while the last one diverges and has a relative error of almost 5%. It should be noted that Cauchy

can estimate the resonant frequencies with good accuracy but does not estimate well the damping factors in presence of noise which is why it has high relative error for poles estimation.

Similarly, as with the PEC sphere, we test the signal reconstruction in time and frequency domains. Fig. 3.33 depicts the reconstructed signals for a SNR of 30 dB which correlates with the scattered field. As the SNR is not too low, we are able to reconstruct the scattered field response even when some of the CNRs of higher order diverge. Moreover, we note that TLS MP and VF provide more promising results when exposed to noise than Cauchy.

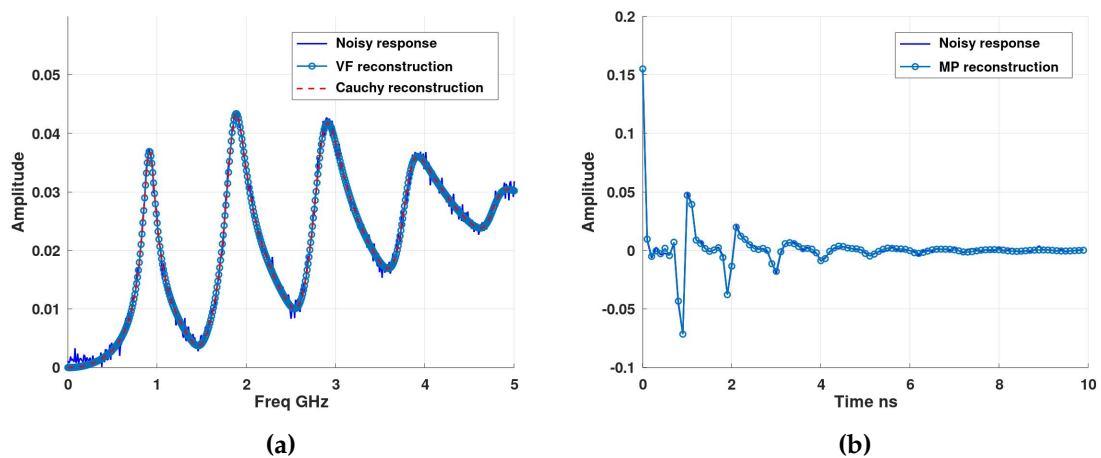


Figure 3.33 – Thin wire's (a) frequency domain reconstruction using estimated poles from Cauchy and VF at 30 dB SNR, and (b) late Time reconstruction using MP at 30 dB SNR.

VF with Multi Observation Angles

The same analysis of testing the extraction of poles on a vector containing several observation angles is done using the thin wire.

Fig. 3.34 shows that multi-input data has a minor effect on the accuracy of VF. In fact, VF is still relatively accurate when working with one observation angle (back-scattered direction) for the noisy signals. We can note that multi-observation improves the estimation error of CNRs starting from 3 input.

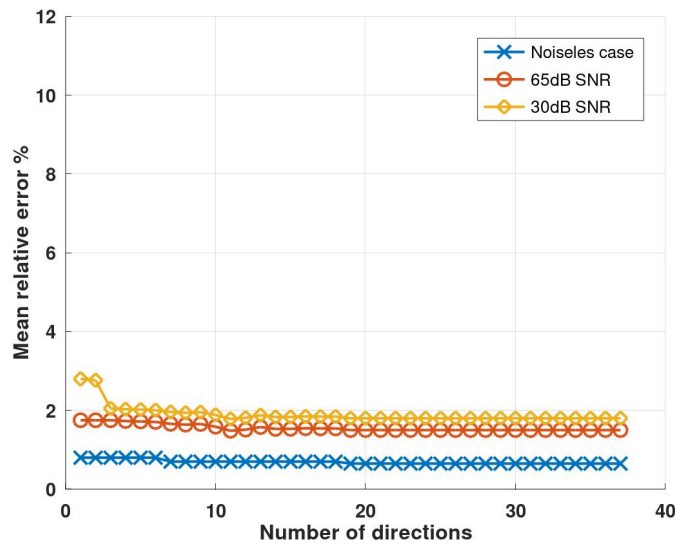


Figure 3.34 – Poles extracted for 65 & 30 dB SNR for all 37 directions of the thin wire.

3.4.3 Discussion and interpretation of the physical poles and their residues

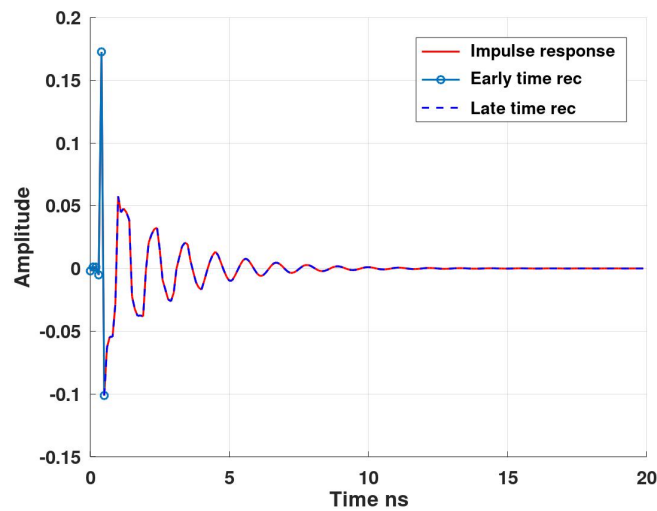
3.4.3.1 Physical and mathematical poles

In this section, we test the reconstruction of the scattered field using the extracted CNRs and their associated residues. Indeed, as the early time is integrated in the frequency response, we cannot reconstruct the field from only physical poles as seen with the PEC sphere.

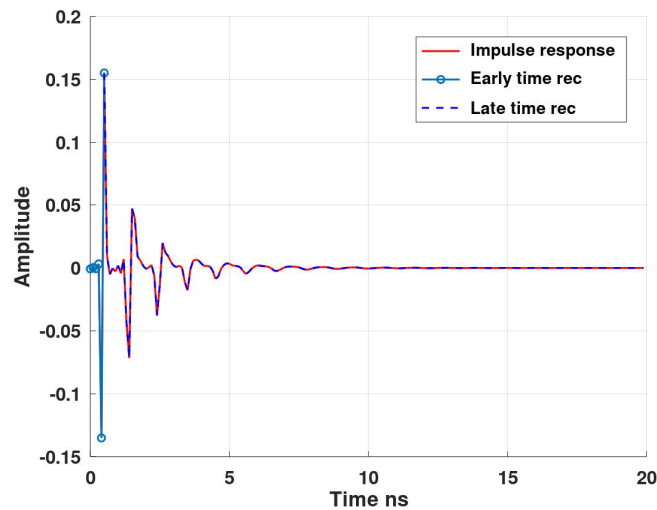
In fig. 3.35, we present the comparison between the back-scattered field, the reconstruction using physical poles and the reconstruction using mathematical poles for both incident waves. We can see that, as with the PEC sphere, the late time portion can be reconstructed accurately using the physical poles, whilst the early time is reconstructed using mathematical poles.

3.4.3.2 Comparison between residues and scattered field

In this section, a comparison is performed between the amplitude of the residues computed using VF, the scattered field and late time response that is translated into the frequency domain using FFT. The results are presented for the three odd resonant frequencies (f_1 , f_3 , f_5) and for both incident wave directions in fig 3.36 to 3.41.



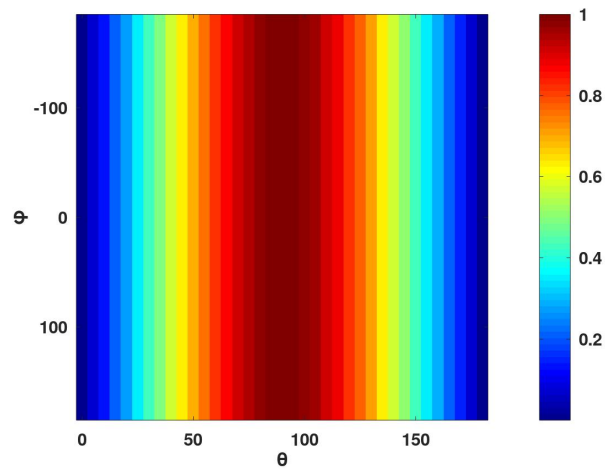
(a) Normal incidence



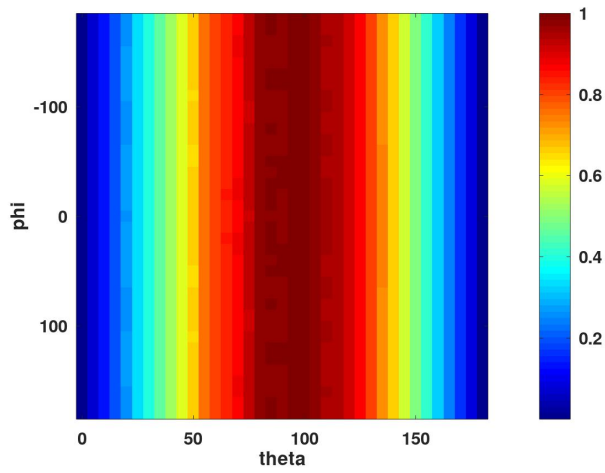
(b) Incidence=45°

Figure 3.35 – Early and late time reconstruction (Rec) using mathematical and physical poles respectively.

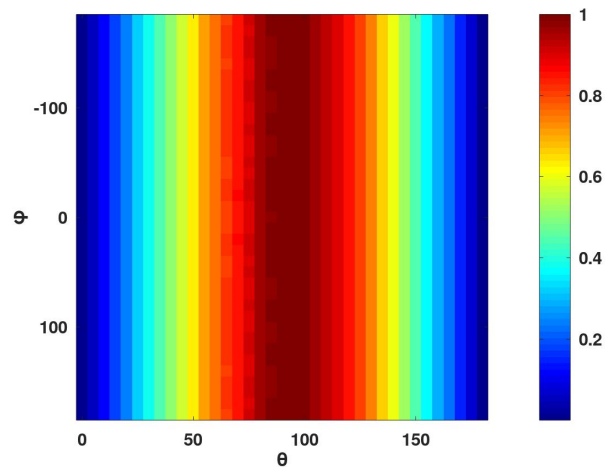
Again, the results show that the residues are correlated with the late time response at those resonant frequencies. We can also observe from the diagrams that the maxima and minima are almost located at the same places for the residues and late time response. Furthermore, the differences between the scattered field and the late time are relatively small, which can be explained by the fact that the specular reflection (early time) is not as important in backscattering for the thin wire as for the PEC sphere. As illustrated in fig. 3.35, since the thin wire is highly resonant, the energy contained in the oscillations specific to its geometry is greater than that contained in the early-time response.



(a) Scattered field

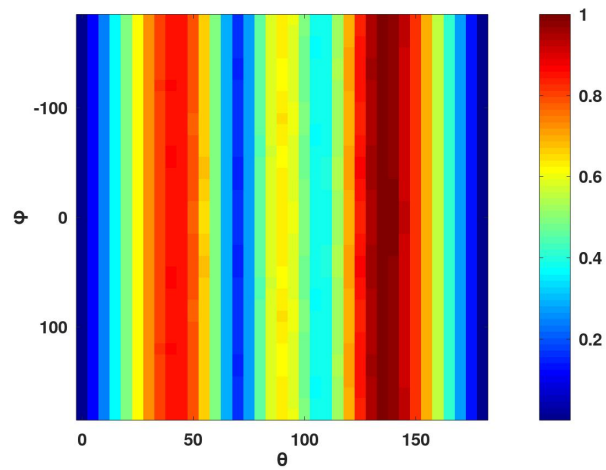


(b) Scattered field from Late Time response

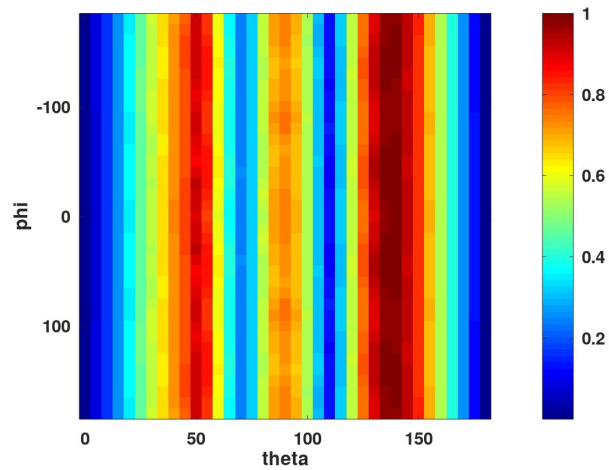


(c) Residues

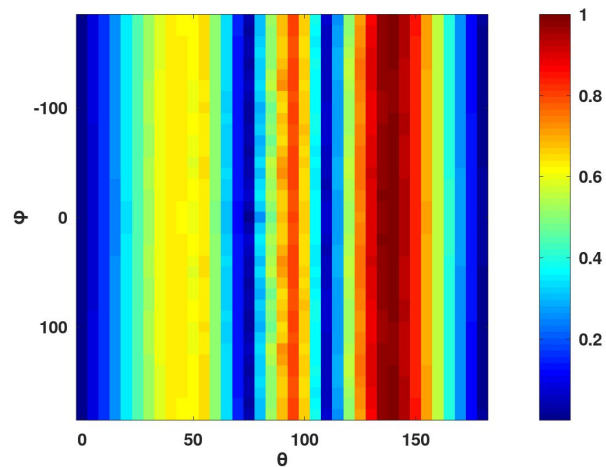
Figure 3.36 – Normalized amplitude of scattered field, late Time and residues related to the first resonant frequency ($f_1 = 0.9 \text{ GHz}$) of the thin wire for an incidence of 45° .



(a) Scattered field

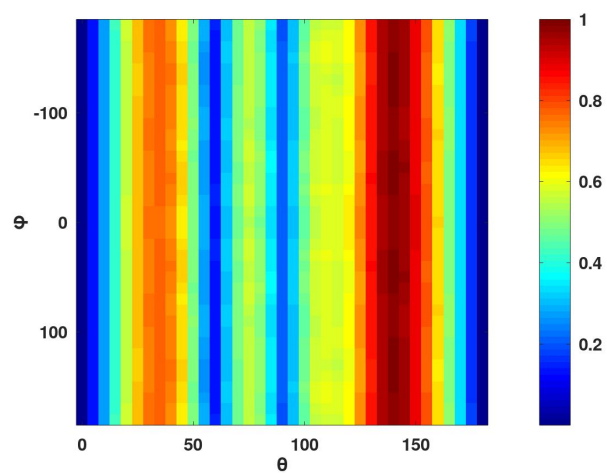


(b) Scattered field from Late Time response

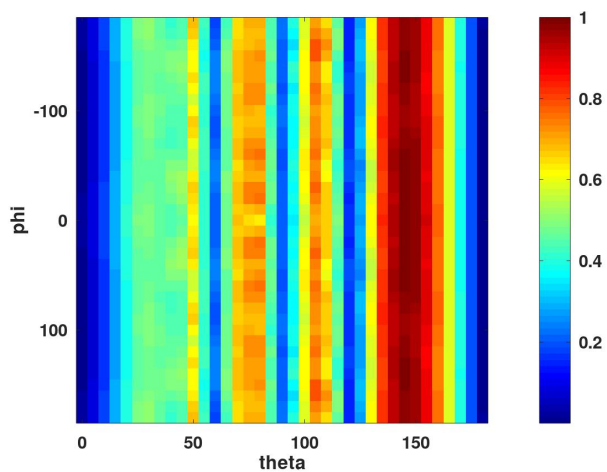


(c) Residues

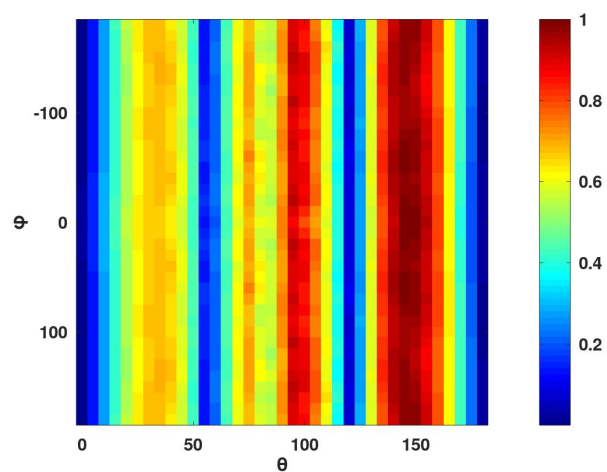
Figure 3.37 – Normalized amplitude of scattered field, late Time and residues related to the third resonant frequency ($f_3 = 2.9 \text{ GHz}$) of the thin wire for an incidence of 45° .



(a) Scattered field

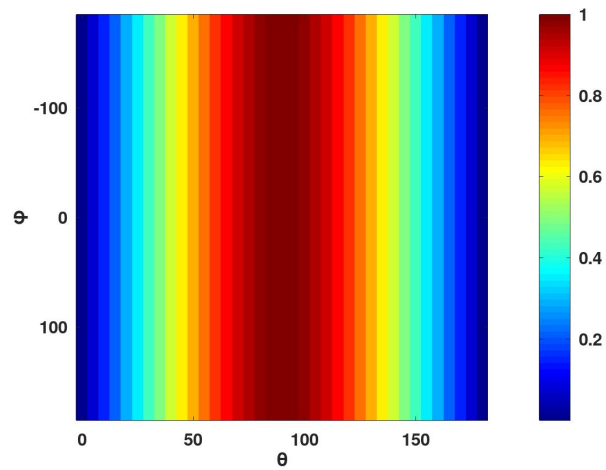


(b) Scattered field from Late Time response

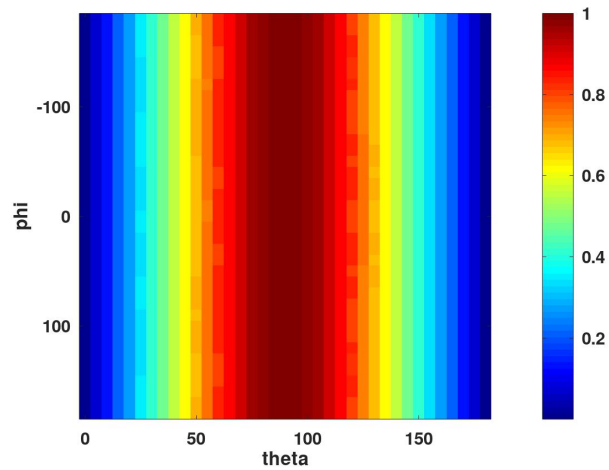


(c) Residues

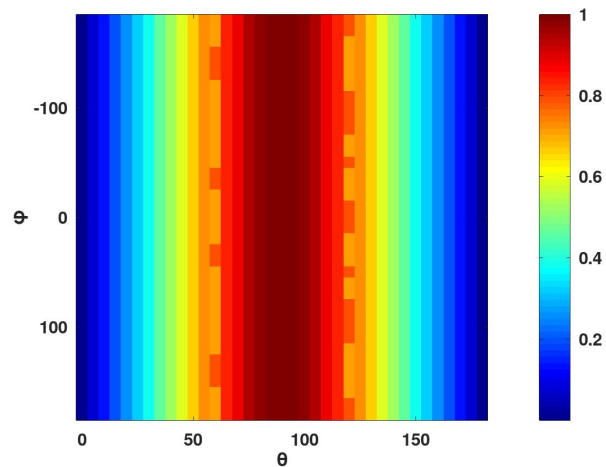
Figure 3.38 – Normalized amplitude of scattered field, late Time and residues related to the fifth resonant frequency ($f_5 = 4.9 \text{ GHz}$) of the thin wire for an incidence of 45° .



(a) Scattered field

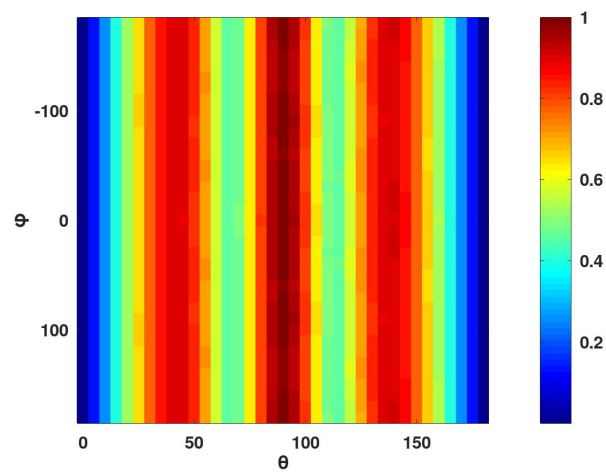


(b) Scattered field from Late Time response

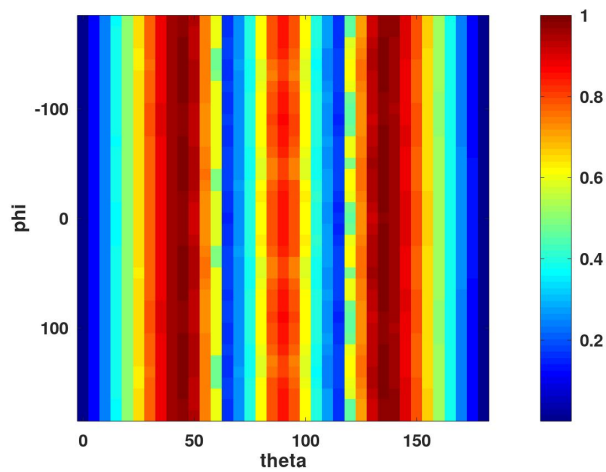


(c) Residues

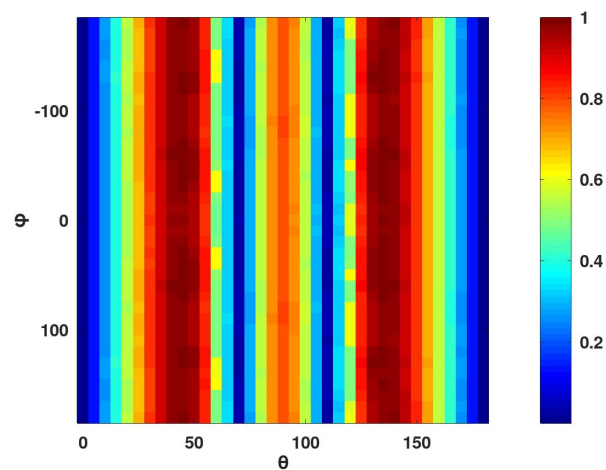
Figure 3.39 – Normalized amplitude of scattered field, late Time and residues related to the first resonant frequency ($f_1 = 0.9 \text{ GHz}$) of the thin wire for normal incidence.



(a) Scattered field

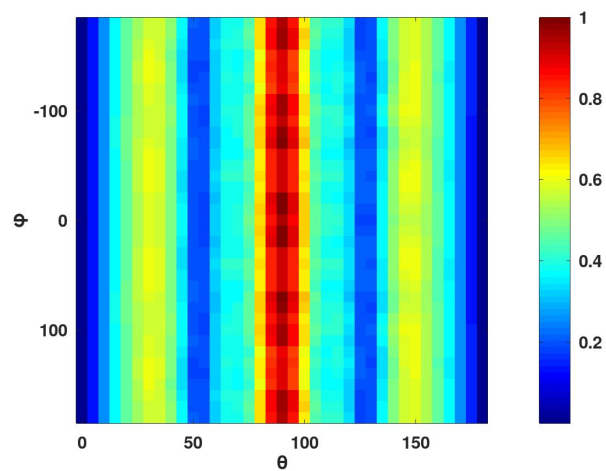


(b) Scattered field from Late Time response

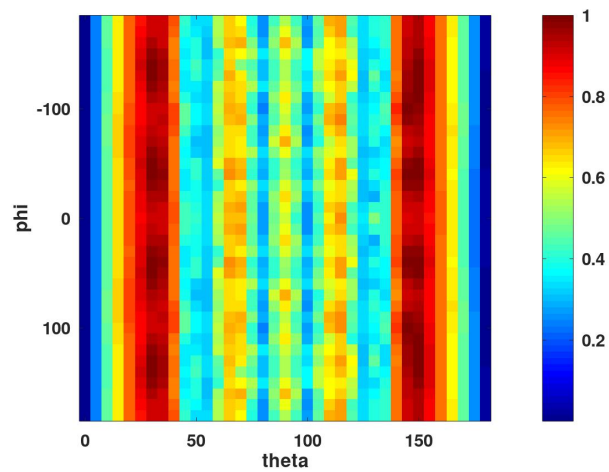


(c) Residues

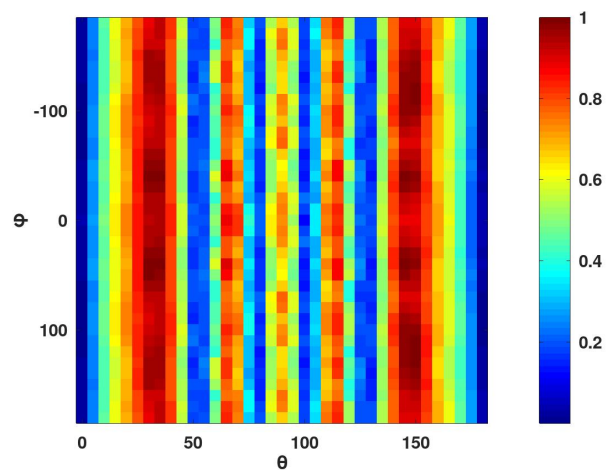
Figure 3.40 – Normalized amplitude of scattered field, late Time and residues related to the third resonant frequency ($f_3 = 2.9 \text{ GHz}$) of the thin wire for normal incidence.



(a) Scattered field



(b) Scattered field from Late Time response



(c) Residues

Figure 3.41 – Normalized amplitude of scattered field, late Time and residues related to the fifth resonant frequency ($f_5 = 4.9 \text{ GHz}$) of the thin wire for normal incidence.

3.5 Conclusion

In this chapter, we have used the SEM to represent the scattered field of an object accurately and compactly with just few parameters. Three extraction techniques of CNRs were compared: TLS MP in time domain, and VF and TLS Cauchy in frequency domain. They were applied on simulated scattered fields from two objects: a PEC sphere and a thin wire.

First, we have shown that in a noiseless case, all methods extract the CNRs with almost the same excellent precision. It has been shown that the SEM frequency techniques can be sensitive to poor compensation of the propagation channel. It was also demonstrated that in combination with the VF method, the CNRs of these objects could be calculated accurately when phase compensation errors exist. We have also confirmed that the criteria mentioned in chapter 2 allow to effectively eliminate the mathematical poles. As for TLS MP, the complexity lies in the separation between the late time and the early time, a method based on the stability of the singular values extracted using the TLS MP algorithm allowed a good estimation of the beginning of the late time.

Subsequently, we have performed a protocol to test the robustness to noise of these three methods by considering only the physical CNRs. It was shown that TLS MP and VF are more robust than TLS Cauchy when applied on the scattered field response from both objects. In case of a low resonating object such as the PEC sphere, the extraction of CNRs becomes difficult when noise levels are high with TLS Cauchy having the highest noise sensitivity. In addition, it remains complicated to extract a significant part of the numerous CNRs from a noisy scattered field from such a challenging object. However, in case of thin wire, VF and TLS MP can extract almost all CNRs with very low error, whilst Cauchy still had the highest errors. We also explored the functionality of VF allowing to compute the CNRs for multiple observation angles at once. It was shown that the multi-input data can indeed increase the accuracy of poles estimation from noisy signals, especially when dealing with low resonating objects like the PEC sphere.

Then, we evaluated the reconstruction of the scattered field using physical poles. Indeed, as the frequency response includes both early and late time components, it is not possible to reconstruct the frequency response through only the physical poles. However, this reconstruction can be correlated with the late time response as those physical poles are related to that part of the response of the object. The residues associated to each CNR were also compared with the

scattered field and the late time response. The correlation of residues with late time response was visible for both objects.

Although TLS MP and VF perform similarly in the presence of noise, in the remainder of this thesis we will use the VF method. This selection is driven by the fact that TLS MP necessitates the separation between late time and early time components which does not exist in frequency domain. Furthermore, that criteria for removing mathematical poles in frequency domain is efficient and easily automated.

Chapter 4

Classification of objects using their EM signatures

4.1 Introduction

Recognition and classification of targets is a challenging task in the radar signal processing area. In recent years, Artificial Intelligence (AI) has been largely explored for this purpose. Machine Learning (ML) and Deep Learning (DL) algorithms, two most commonly known AI families, have become increasingly popular where extensive studies have been conducted by researchers for classification purposes. Several algorithms are found in literature, that vary from simple models, like Support Vector Machines (SVMs), Decision Trees (DTs), K-Nearest Neighbour (KNN) or Naive bayes, to more complex models like Artificial Neural Networks (ANNs) (Narayanan et al., 2017).

Indeed, combining the SEM with a classification algorithm is an interesting research topic that has been seldom exploited and has not been applied to scattered fields emanating from all spatial directions. The work found in literature deals with simple classification cases: bi-class (Joon-Ho Lee, In-Sik Choi, and Hyo-Tae Kim, 2003) or multiclass (Garzon-Guerrero, Ruiz, and Carrion, 2013) but for the purpose of classifying four sizes of homothetic objects applied to limited directions of scattered fields. These studies have highlighted not only the evident qualities of the SEM (excellent classification from few data and no matter the aspect angle of the target) but also its limitations to noise that affect the higher order poles. They have therefore limited their approach to the first one or two complex poles to build the dataset. Moreover, they have trained their classifiers at different SNR levels or have applied Principal Component Analysis (PCA) before the extraction of resonances to reduce the effects of noise which is not very compatible with an operational context.

In this chapter, we aim to classify targets by using pre-processed data from the SEM technique presented in the previous chapters. To this end, supervised learning techniques have been explored for classification where each data is labelled. We chose to study the multi-class SVM, DT and ANNs classifiers as SVM and DT are two of the most basic and robust ML algorithms, while ANNs are more advanced and known for their reliability. To validate the interest of using SEM data, we compare classification performances when using raw data (frequency and time domain responses) and SEM data. First, we propose a fast and simple way to construct the dataset based on scattered field simulated using Mie series. Then, a novel solution is proposed to construct a dataset that is more robust and that is applicable to a wide variety of objects of a more complex shape.

4.2 Supervised Learning Techniques

In this section, we explain each of the classifiers used within this work. The SVM and DT algorithms are implemented with built-in functions in Python using scikit-learn library (Pedregosa et al., 2012). The ANNs are implemented using the Keras-Tensorflow (Chollet et al., 2015) library tool in Python.

4.2.1 Multi-class SVM

The SVM is originally a binary classifier introduced by Boser, Guyon, and Vapnik in 1992 (Boser, Guyon, and Vapnik, 1992). It consists in finding the optimal hyperplane to separate different data classes. By maximizing the margin, the SVM generates the largest separation distance possible between the separating hyperplane and the training examples on either side of it (fig. 4.1). We start by explaining the procedure of a Binary SVM.

Under the assumption that the data are linearly separable, the separating hyperplane is found by solving a decision function $F(\mathbf{x})$ for a feature vector \mathbf{x} of N dimension that belongs to either of two classes:

$$F(x_i) = w^T x_i + b \quad (4.1)$$

w is the weight vector that is normal to the hyperplane and b is a scalar bias. The distance between the defined hyperplane and the system's origin is given by $\frac{b}{\|w\|}$. In fact, the choice for this hyperplane is sensitive, thus, it is necessary

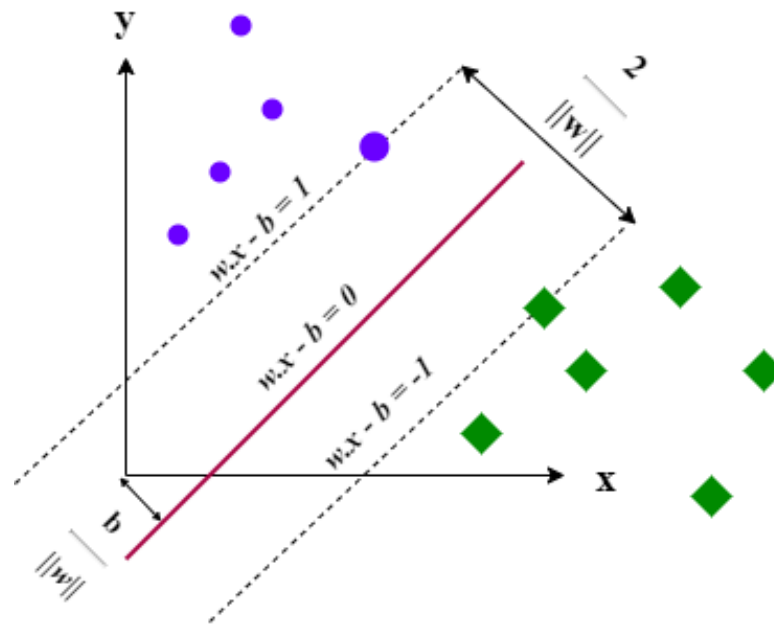


Figure 4.1 – Optimal hyperplane separation for a linearly separable bi-class classification

to maximize the "margin" between the two classes given by $\frac{2}{\|w\|}$ such that:

$$w^T x_i + b \geq 1, \quad \text{if } y_i = 1 \quad (4.2)$$

$$w^T x_i + b \leq -1, \quad \text{if } y_i = -1 \quad (4.3)$$

y_i is the class label $\in \{1, -1\}$. The optimal hyperplane is found by minimizing the following equation:

$$\frac{1}{2} \|w\|^2 + C \sum_{i=1}^N \xi_i \quad (4.4)$$

with constraints, if the data are non-linear, that are:

$$F(x_i) \geq 1 - \xi_i, \quad i = 1, \dots, N \quad (4.5)$$

where C is a regulation parameter, which adjusts the width of the margin to minimize the training error. ξ_i are non-negative slack variables.

If the data are not linearly separable, SVMs employ the kernel method to map the data onto a higher dimensional space where they become linearly separable by using the appropriate mapping $\phi : x \rightarrow \phi(x)$ (Schölkopf and Smola, [MIT press, 2001](#)). Hence, the scalar product of samples $\langle x_i, x_j \rangle$ becomes:

$$K(x, z) = \langle \phi(x_i), \phi(x_j) \rangle \quad (4.6)$$

where K is the kernel function. There are multiple types of K functions that exist:

— Polynomial kernels:

$$K(x, z) = (x_i^T x_j + 1)^q, \quad q > 0 \quad (4.7)$$

— Radial Basis Functions (RBF):

$$K(x, z) = e^{-\gamma \| \langle x_i, x_j \rangle \|} \quad (4.8)$$

— Hyperbolic Tangent:

$$K(x, z) = \tanh(\beta x_i^T x_j + \gamma) \quad (4.9)$$

γ is the data variance that depends on the number of variables. After choosing the appropriate kernel function, the hyperplane can be found by maximizing the following Lagrangian function:

$$\max_{\lambda} \left(\sum_{i=1}^N \lambda_i - \frac{1}{2} \sum_{i,j} \lambda_i \lambda_j y_i y_j K(x_i, x_j) \right) \quad (4.10)$$

constrained by

$$0 \leq \lambda_i \leq C, \quad \sum_{i=1}^N \lambda_i y_i = 0 \quad (4.11)$$

Once choosing the kernel function, the parameters C and γ must be carefully chosen. if C is too high, the margin that separates the classes decreases and the classification error on the training data also decreases. But this might increase the error on the test data. As a consequence, a low C value leads to a low miss-classification rate, whereas a higher C value raises the miss-classification rate and is more susceptible to over-fitting. Over-fitting is when the training model fits very well its training data that it cannot perform well against unseen data.

In order to apply the SVM in a multi-class configuration, different possibilities exist that are based on solving multiple binary SVM classifiers (Chih-Wei Hsu and Chih-Jen Lin, 2002). In this thesis, we use the one vs one (ovo) approach that is based on constructing $k(k - 1)/2$ classifiers (given k classes) and then treating the problem as a binary one. The idea is to map data points to high dimensional space to gain mutual linear separation between every two classes.

4.2.2 Decision Tree

DT methods build a decision model based on the actual values of attributes in the data. The dataset is recursively divided into smaller homogeneous subsets, resulting in a flowchart-like tree structure as seen in fig 4.2 (Safavian and Landgrebe, 1991). The DT is comprised of:

- Nodes: check the value of a certain parameter. A node that does not have a descendant of its own is called a leaf. Thus, a leaf contains the value of a class label. Any further nodes are called "internal nodes".
- Branch: correlates with the output of a test and connects to the next node or leaf.

They use various techniques to split the data like Gini index or entropy (Loh, 2011). The minimum amount of samples required to split a decision node is two. In this work, we use the Gini criterion to split the data in the nodes as it gives similar results while being less computationally intensive than entropy (Raileanu and Stoffel, 2004) .

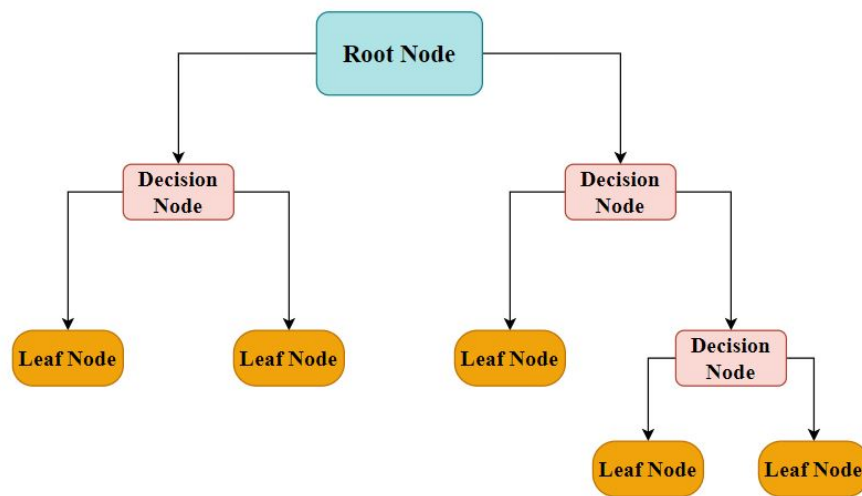


Figure 4.2 – Decision Tree classifier diagram

4.2.3 Artificial Neural Network

There are many types of neural network topology, the simplest being the feed-forward networks. They consist of neurons interconnected by synapses that are responsible for neuronal activities. From these neurons, networks can be established by organizing them into interconnected layers (Bebis and Georgiopoulos, 1994). An ANN consists of an input layer and an output layer and at least one hidden layer. The input layer is composed of input neurons that simply

transmit information to the remainder of the network. The output layer contains neurons representing the different classes of the data that the network is classifying (Sze et al., 2017). The hidden layers are connected to the input and output layers and can be of various types and sizes (number of neurons). In this work, we have considered the most used ANNs: Multi-Layer Perceptron (MLP) and Convolutional Neural Network (CNN).

Multi-Layer Perceptron

One of the well-known ANN models is the MLP. It comprises: an input layer with a number of neurons equals to the number of input data which simply pass information to the next layer; one or several hidden layers composed of various amount of neurons; and an output layer with a number of neurons equal to the number of classes. The neurons of the hidden layers and the output layer are called perceptrons. A perceptron is a neuron that is connected to the output of the previous layer and whose output is connected to the neurons of the next layer. It uses a non-linear activation function that is applied to a sum of products of the inputs related to their weights (Sze et al., 2017). The neuron j in layer m carries out the calculations indicated in equation 4.12.

$$y_j^m = f\left(\sum_{i=0}^{N_{m-1}-1} w_{ij} * y_i^{m-1}\right) \quad (4.12)$$

Where y_j^m is the output of the neuron j in the layer m , N_m is the number of neurons in the layer m , w_{ij} are the weights between the neurons of layer $m + 1$ and layer m , and $f(.)$ is the non-linear activation function. Various activation functions exist that can be used such as: Sigmoid (Narayan, 1997), hyperbolic tangent (Lecun et al., 1998a) and Rectified Linear Unit (ReLU) (Agarap, 2018). In this work, we use the ReLU function because of its computational efficiency, enabling the system to converge quickly and to prevent over-fitting.

Convolutional Neural Network

CNNs are composed of multiple layers of different types. Usually, the most common layers are convolution, pooling, and fully-connected layers. The Convolution layer is a filter layer, of specific length and width, that moves along the input data. It is composed of kernels or filters that are applied to extract specific features from the input vector (Sze et al., 2017).

The pooling layer is a sub-sampling layer used to reduce the size of the features computed using the convolution layer. They are, basically, composed of average or maximum pooling (*maxpool*) filters applied to incoming features through a sliding technique similar to the one used with Convolutional layers. Here, we use the *maxpool* layer that outputs the maximum input value.

Fully-connected (FC) layers are used to process the output features of the last convolution or pooling layer. They are composed of neurons connected to all previous layer's neurons.

4.3 Classification of the sphere's material

To validate and investigate the interests of using SEM data for classification, we opted to start by assessing this approach on spheres of different materials that vary from PEC spheres to dielectric ones. This is due to the fact that the UWB SF response of a sphere can be computed analytically using Mie series as seen in chapter 3. Thus, we do not need to use simulation software that take a considerable amount of time to compute the SF responses.

Therefore, we compute the UWB SF from 5 different classes of spheres that are: PEC sphere, sphere with a dielectric constant $\epsilon_r = 4$ and conductivity $\sigma = 0.5 \text{ S.m}^{-1}$, three lossless spheres with dielectric constant ϵ_r equal to 2, 4 and 9 respectively. They are enumerated from 0 to 4 respectively. The SF responses are recovered in the far-field region, in a bi-static configuration with a fixed emitter because varying the position of a mono-static Radar is of no interest for the sphere. The frequency band is fixed from 0.01 GHz to 5 GHz as in the previous chapter. All spheres are illuminated using an x -polarized incident plane wave propagating along z axis (as in fig 3.2). The SF is recovered for multiple observation angles where θ varies from 0° to 180° with 5° step and ϕ from -180° to 180° with 10° step. Fig. 4.3 shows the amplitude of the SF in the back-scattering direction ($\theta = 180^\circ$) for the 5 simulated spheres of 10 cm diameter.

In order to extract the SEM data, the pre-treatment shown in chapter 3 is applied on each simulated object. The SEM data are extracted by applying VF in frequency domain. Indeed, it was shown in chapter 3 that VF is more robust to noise and more accurate than TLS Cauchy. In addition, by working in frequency domain we avoid the necessity of having to determine the beginning of late time which is rather a hard task for dielectric objects.

We also compute the quality factor (Q-factor) of each pole, as in chapter 2, to replace the damping factor. This parameter is an important representation of the object as it is independent of its size which will help in generalizing the classification of spheres of different sizes. To confirm this hypothesis, we will compare the classification performances when using damping factors and Q-factors in the following sections. To validate the scattered field simulation and the CNRs values of the dielectric spheres, they were compared with those obtained using Mie series in (Mei et al., 2014).

From Fig. 4.4a and 4.4b we see that all classes of 10 cm diameter spheres exhibit 5 poles in the frequency range of interest. When the relative permittivity of the dielectric material increases, the sphere becomes a very strong resonating object, hence, it has a very low damping factor and a very high Q-factor. In Fig 4.4b, we do not show the rest of the Q-factors for both classes 3 and 4 for visibility as they are higher than 15.

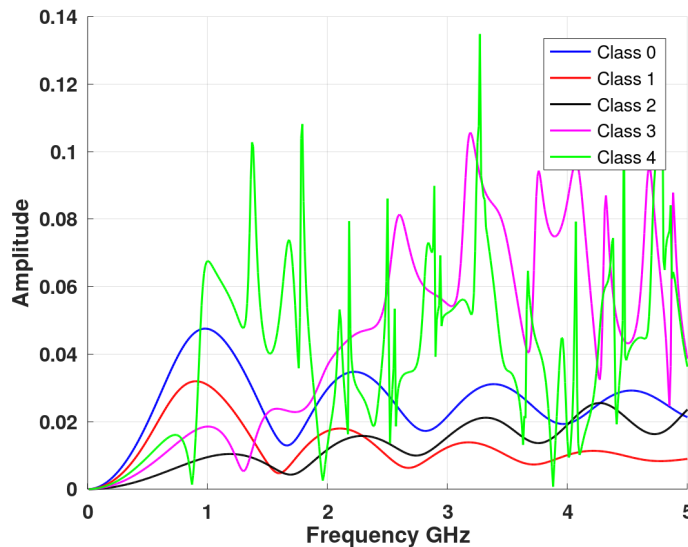
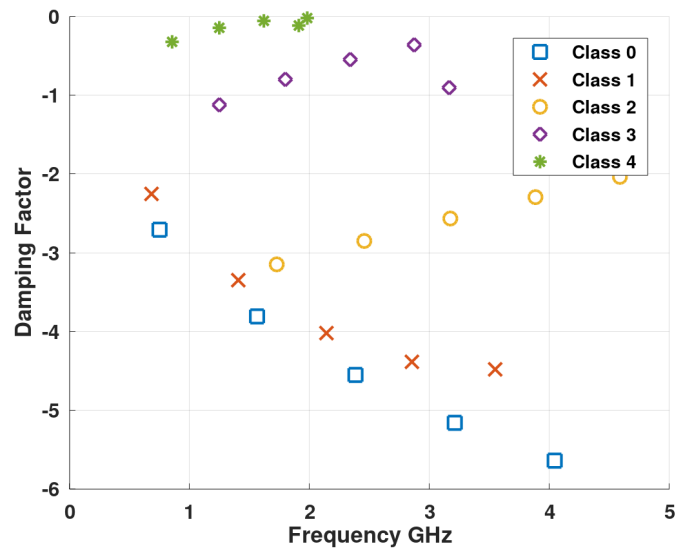


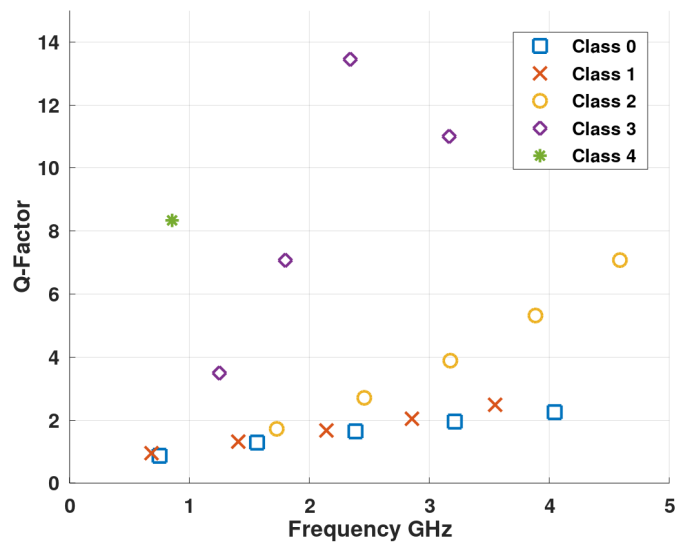
Figure 4.3 – Amplitude of the frequency response in the back-scattering direction for the 5 classes of spheres. The diameter of the spheres is 10 *cm*

4.3.1 Dataset construction

We start by creating datasets including the 5 sphere classes. In fact, having multiple sphere sizes represents an advantage for SF data as the object's response gets affected by a change in the size. For SEM data, the resonant frequencies and damping factor also change, however, by the use of Q-factor we expect



(a)



(b)

Figure 4.4 – (a) The first five natural poles and (b) Q-factors as a function of natural frequency of the 5 spheres of 10 cm diameter.

that this change will not present a problem. Hence, to have a balanced comparison between SEM and SF data, 13 sphere sizes are simulated for each of the 5 classes. Those dimensions are selected to ensure that each sphere exhibits at least one natural frequency within the frequency range ($[0.01 - 5]$ GHz).

Table 4.1 shows the diameters of the spheres where N represents the number of resonances in the frequency range. For spheres having $N \geq 5$ resonances in the frequency band, we chose the diameters varying from 10 cm to 18 cm with a 1 cm step, resulting in 9 objects for each class. For spheres having less

Table 4.1 – Diameters (cm) of spheres versus the number of resonances (N) for each sphere class

Class	N				
	1	2	3	4	$N \geq 5$
0) PEC	3	5	7	8.5	
1) $\epsilon_r=4, \sigma=0.5$	3	4.5	6	8	
2) $\epsilon_r=2$	4.5	6	8	9	[10:1:18]
3) $\epsilon_r=4$	3.5	5	6	7	
4) $\epsilon_r=9$	2.5	3.5	4.3	5	

than 5 resonances ($N < 5$ resonances), we chose diameters which provide N resonances, with N varying from 1 to 4.

To reduce the size of the datasets, we include data from the three following planes which are representative of the scattering properties of the sphere: $\phi = 0^\circ$ and θ varies (XoZ plane), $\phi = 90^\circ$ and θ varies (YoZ plane), $\theta = 90^\circ$ and ϕ varies (XoY plane). Thus, for each sphere size we have 111 observation angles (3 planes with 37 angles in θ or ϕ), making a total of 7215 samples for each of the three datasets as we have 13 spheres for each of the 5 classes.

4.3.1.1 Scattered Field dataset

The first dataset is constructed using the amplitude of the SF response in frequency domain. The classifiers employed do not support complex numbers, thus, we need to include only real numbers in the input vector. For that, to construct the most efficient dataset, we tested different possibilities based on the amplitude and phase of the SF responses as following:

- Amplitude and Phase responses
- Amplitude response only
- Phase response only

This preliminary study showed that using the phase alone had the same performances as using the amplitude, while adding the phase along with the amplitude was not relevant as it doubled the vector's size while maintaining the same performances. The results showing this comparison are presented in appendix D. The input vector is, hence, a 1-D signal of 500 frequency points and composed of 2 channels. The first channel represents the E_θ component and the second one is the E_ϕ component of the SF's amplitude.

The second dataset represents the SF in time domain. The transient impulse response is obtained by computing the IFFT of the complex SF response in frequency domain. Here, we include the first 10 ns of each signal, which constitutes 100 time points, as it starts to decay after (refer to fig. 4.5). The input vector is also a 1-D signal of 100 points and composed of 2 channels, one for each polarization.

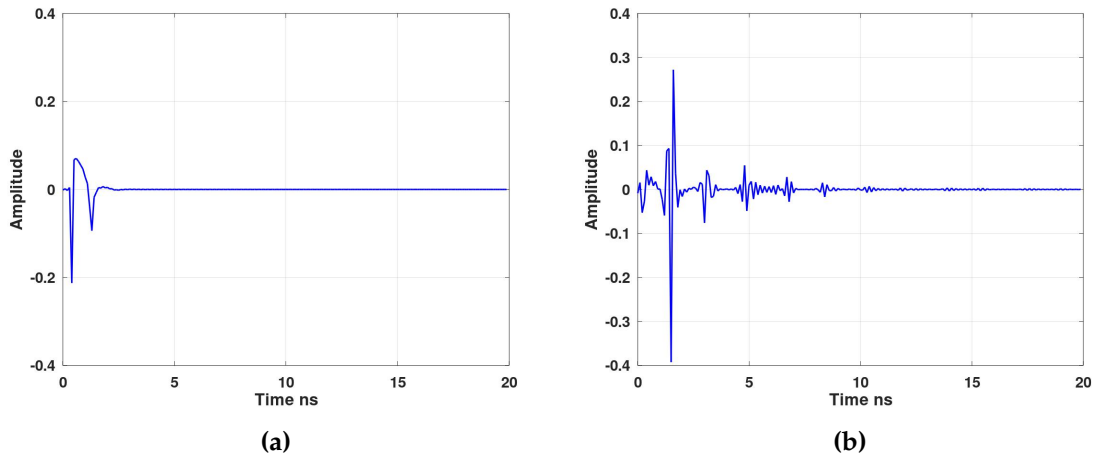


Figure 4.5 – Impulse response of 10 cm diameter sphere (a) PEC and (b) dielectric with permittivity 4

4.3.1.2 SEM dataset

For the third dataset that is based on SEM data, we use the pre-processed data from VF. Then, we have to pay attention to two factors: the number of the CNRs and the data to include in this dataset. Concerning the number of resonances, several points are considered:

- we saw in chapter 3 that, when SNR decreases, the higher order poles are the most affected,
- in addition, most objects have in average 5 to 6 poles in the frequency range $[0.1 - 5] \text{ GHz}$.

To this end, we chose to retain the first five natural frequencies of each object. In addition, for the smaller spheres having less than 5 resonances (see table 4.1), we will need to complement the missing data with some other value to preserve the same input vector's length that is 5. This ensures that information from other columns is not lost, and predictions can be made despite the missing values in the row. The most straight forward approach is to fill in the missing values with zero, hence, we will have sparse SEM data in this dataset. This original configuration is chosen to improve the generalization performance of

the classifiers when limiting factors (limited bandwidth, noise, etc.) impact the higher order poles. Indeed, it is not possible to extract more than one or two CNRs for very noisy signals, thus, this configuration allows to take this into account.

Regarding the second factor concerning what data to include in this dataset, we test several approaches to find the optimal dataset configuration. The first approach is based on adding the quality factor to be able to generalize to any object's size. The input vector is, thus, of length 5 and composed of 4 channels: natural frequencies, Q-factors and the residues amplitude of θ and ϕ components respectively. The residues are included because they contain additional information about the objects which can be significant when the natural frequencies and Q-factors are almost similar for some objects. We also test more conventional approaches by using the damping factor. Thus, we will have the following three cases:

- *case 1*: An original dataset as described above (four channels: natural frequencies, Q-factors and their respective residues);
- *case 2*: Q-factor is replaced by the damping factor (four channels: natural frequencies, damping factors, and their respective residues);
- *case 3*: we eliminate the residues from *case 1*, hence, the input vector has only the first two channels (natural frequencies and Q-factors).

In the rest of the thesis, we will use the following abbreviations to refer to the datasets: FD data, TD data and SEM data which are related to frequency domain, time domain and SEM data respectively. Note that case 1, 2 and 3 only refer to SEM data.

4.3.2 Training Phase

During this phase, the parameters of each classifier are tuned to achieve highest accuracy results for training data. Each dataset is split into 80% for the training and 20% for the testing. The 20% test samples are composed of random observation angles where each class has an equal number of samples. This is achieved over 10 trials to obtain the mean accuracy results of test data. Hence, the datasets are re-split to 80% and 20% and the algorithms are re-trained over every run.

4.3.2.1 Multi-class SVM

First, the SVM parameters are fixed according to the results using 'gridsearch' function. For that we defined, for each dataset, a matrix of C and γ values, the rbf kernel function and ran the 5-fold cross-validation. Results are given in fig. 4.6 for the 3 datasets when using rbf kernel function. We can see that the training parameters are much smaller for SEM data and offer a large choice of training parameters achieving 100% accuracy on the training data because they are easily separable compared to the other datasets based on raw data. The choice of optimum values, as given by the 'gridsearch' function, are reported in table 4.2. It is worth noting that for SEM data, if we choose another set of C and γ , we get same classification results.

Table 4.2 – Selected parameters of SVM classifier according with the datasets

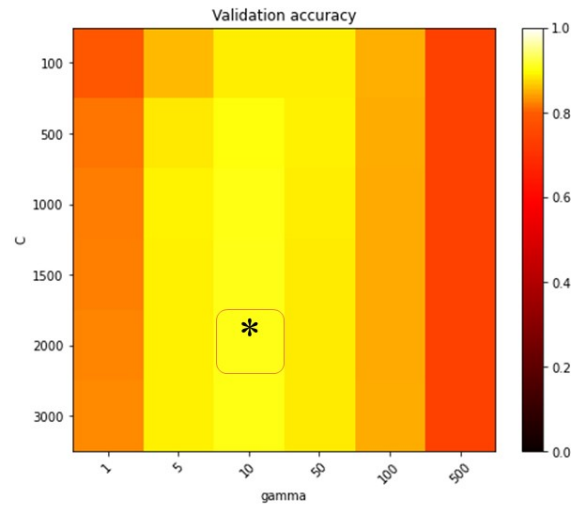
Data	Parameters		
	Function	C	γ
FD	rbf	2000	10
TD	rbf	1000	50
SEM	rbf	5	0.05

4.3.2.2 Decision Tree

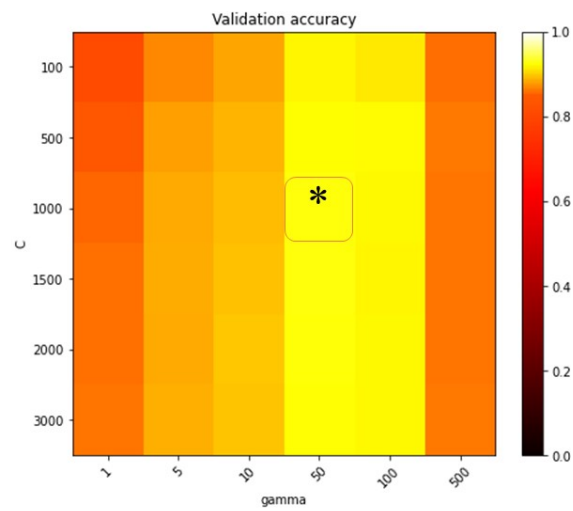
Second, for the DT algorithm, the Gini criterion is used to measure the quality of the split in the tree and decision nodes are randomly chosen to be further split. The trees produced from the learning phase using the 3 datasets are shown in fig. 4.7. We can see that the learning using SEM data produces the smallest tree (fastest learning) as the data are easily separable into 5 distinct classes. However, the DT algorithm produces a much larger tree after using FD and TD data in the learning process as the amount of data contained in the input vector is larger and more difficult to process than SEM data.

4.3.2.3 Artificial Neural Networks

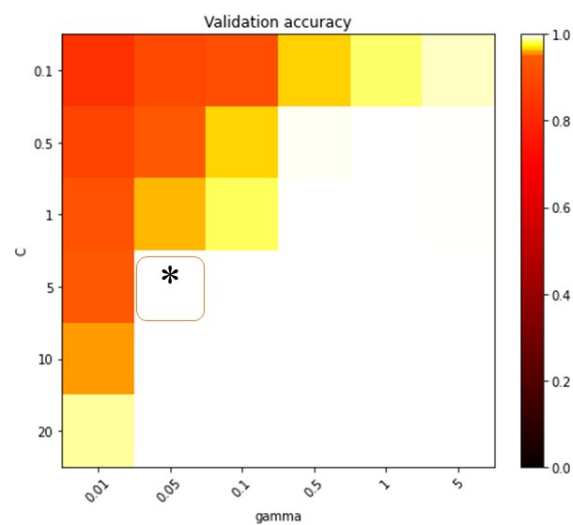
The optimal training parameters when using both NN classifiers are obtained through a series of trial and error. When using the MLP classifier, we apply one hidden layer while varying the number of neurons. Note that we have done tests with other topologies by increasing the number of hidden layers and have found that the performances are almost similar. We use the ReLU activation function with SEM data and SF data.



(a)



(b)

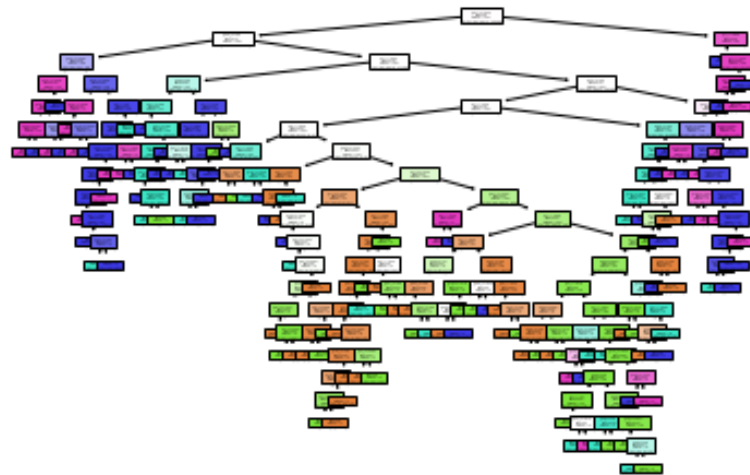


(c)

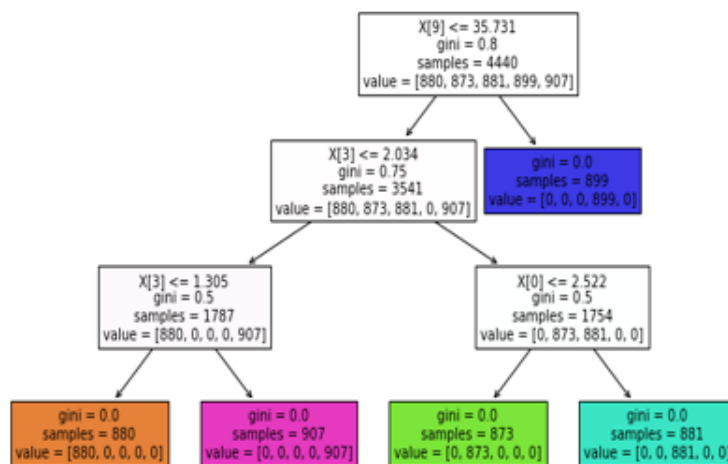
Figure 4.6 – SVM learning parameters when using rbf kernel function with: (a) FD data, (b) TD data and (c) SEM data. * indicates the optimum values chosen.



(a)

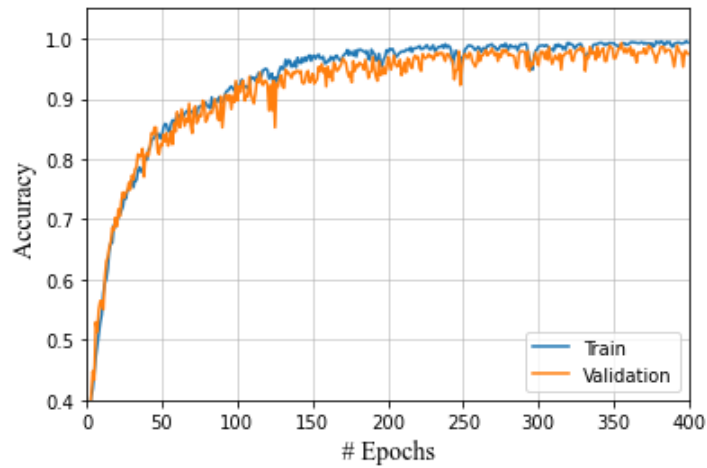


(b)

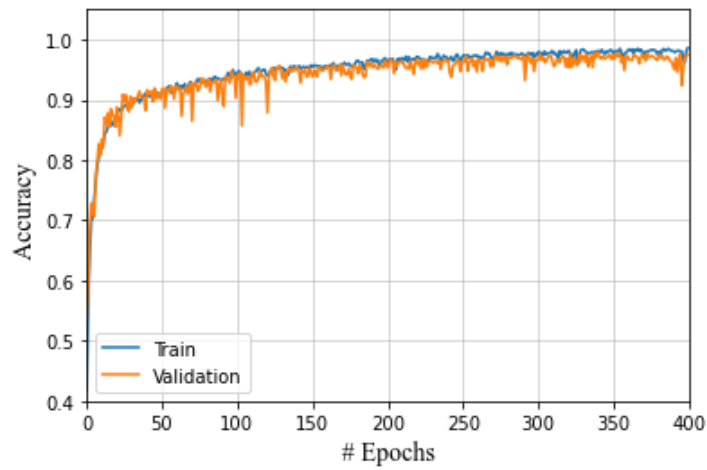


(c)

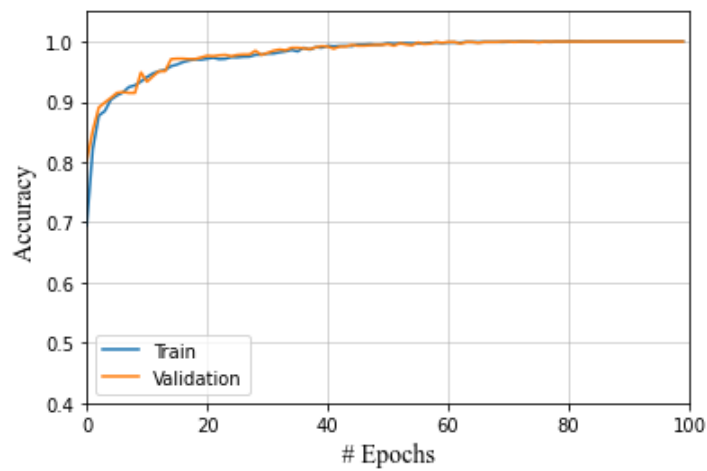
Figure 4.7 – Decision tree flowchart when DT algorithm is learning with: (a) FD data, (b) TD data and (c) SEM data



(a)



(b)



(c)

Figure 4.8 – Train and validation accuracy vs number of epochs when CNN classifier is learning with: (a) FD data, (b) TD data and (c) SEM data. 400 epochs are used with FD and TD data, while 100 epochs are used with SEM data.

For the CNN, we are adopting the LeNet-5 architecture to train with both SF data (Lecun et al., 1998b). The filter size is changed in order to be applied on 1-D input signals. For SEM data, we apply one convolutional (*conv*) layer with 6 filters, followed by one hidden layer with 32 neurons and ReLU function applied in all layers.

This is run over 100 epochs for SEM data and 400 epochs for SF data with a batch size of 100 for both MLP and CNN classifiers. The number of epochs is a hyperparameter describing the number of times that the algorithm will run through the entire training dataset while the batch size refers to the number of samples to process before updating a model. Both algorithms have an output layer composed of 5 neurons using the softmax activation function to compute the output probabilities. The learning rate is updated using the Adam optimizer (Kingma and Ba, 2014).

From fig. 4.8, we see the evolution of the accuracy curve with the number of epochs when using CNN with the different datasets. The validation curve represents the accuracy obtained on the validation set that is used to tune the hyper-parameters and to evaluate the model during the training process. We observe that the learning curve of SEM data is much smoother than those of SF data which present higher fluctuations. This shows that with few epochs (starting from 50) we get 100 % accuracy on the SEM training data. Conversely, both SF training data' accuracy do not exceed 98.5% at 400 epochs. This proves that SEM data are easier and faster to train than SF data.

Finally, table 4.3 shows the execution time values recorded during training phase of the 4 classifiers for each dataset. The values shown for SVM take into account only the training using the optimum parameters chosen earlier. The MLP and CNN classifiers consume much more time than SVM and DT as their calculations are more complex. In addition, the training runtime of classifiers using SEM data is much faster than those using raw data. The IFFT used to obtain time responses takes 0.05 sec when applied on a single observation angle. Additionally, the SEM pre-treatment using VF along with the phase compensation step shown in chapt. 3, accounts for 0.08 sec for a single observation angle.

4.3.3 Test Phase

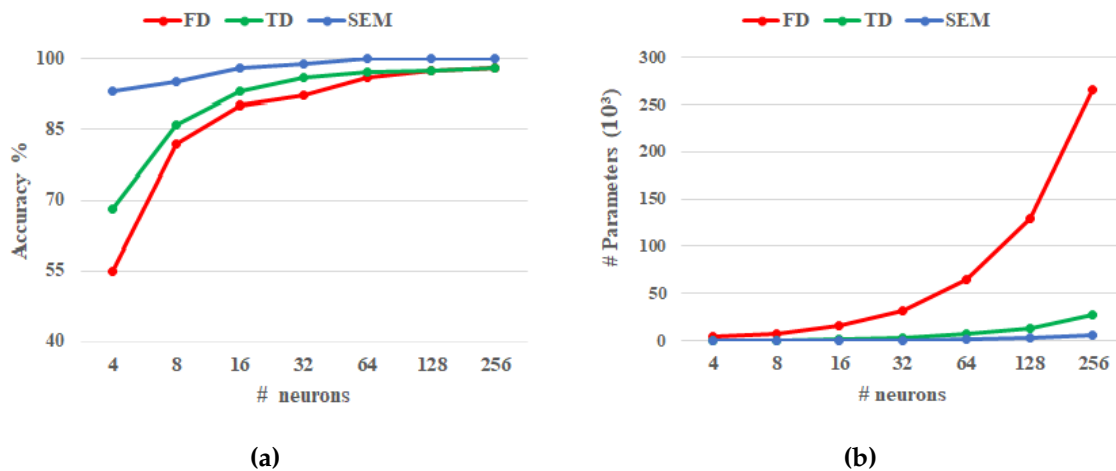
First, we present the mean accuracy results (% of data points classified correctly) when testing the 20% remaining samples of each dataset for various

Table 4.3 – Time consumption (sec.) of the four classifiers trained using the different datasets

Classifier	Time consumption (sec)		
	FD	TD	SEM
SVM	8.7	6.3	0.5
DT	5.3	4	0.2
MLP	180	150	12.3
CNN	352	212	17.6

amount of neurons using MLP classifier.

In fig. 4.9a, we can see that, for SEM data (*case 1*), starting from 32 neurons we obtain excellent accuracy (> 98%) while for SF datasets 256 neurons yields the highest accuracy of 97%. The number of parameters (weights) computed in the hidden layer increases with the number of neurons, as shown in fig. 4.9b where the FD data has the highest parameters as it has the longest input vector. Thus, we can see that the SEM dataset has both the highest accuracy and the lowest parameters computed using the MLP.

**Figure 4.9** – (a) Mean accuracy of the 5 spheres; (b) number of parameters vs. number of neurons in one hidden layer for the 3 datasets.

In addition, we test the 3 cases of SEM dataset construction. Fig. 4.10 shows that the MLP classifier trained using SEM data of both cases 1 and 2 has a higher accuracy (100%) for a number of neurons > 32 and is more stable (low variance) than the classifier trained without the residues. In fact, from fig. 4.4b, we see that some classes have very close natural frequencies and Q-factor, that is why, when trained with *case 3* without residues, it becomes more difficult

to separate those classes. This also shows that residues are indeed parameters that contain information about the object. The other classifiers, DT, SVM and CNN, have similar results but with a higher variance when trained without residues as seen in table 4.4. The standard deviation σ_d is 0 for *case 1* as the Q-factor is always constant which does not create any error with this test set. Thus, for the rest we will only work with SEM datasets of *cases 1* and 2 (i.e. with residues). Those results are interesting because the residues have never been used for identification or classification as they depend on the angle of observation. Therefore, this study shows that their variation with the frequency is also characteristic of the object since it improves the classification performance.

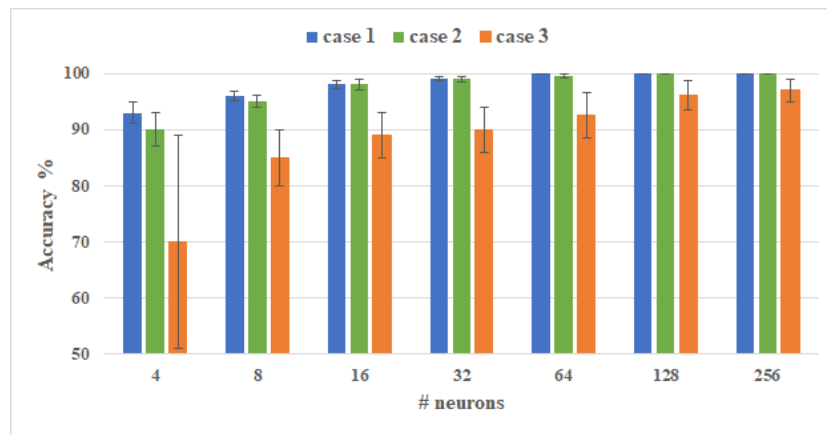


Figure 4.10 – Test results for the 3 cases of SEM datasets construction using MLP classifier while varying # neurons.

Table 4.4 – Accuracy (%) and standard deviation σ_d of each classifier when using the 3 cases of SEM data

Classifier	SEM data					
	case 1		case 2		case 3	
	Accuracy	σ_d	Accuracy	σ_d	Accuracy	σ_d
SVM	100	0	99.7	0.2	92	4.6
DT	100	0	99.7	0.2	91	5
MLP - 64 neurons	100	0	99.7	0.22	92	4
CNN	100	0	99.8	0.1	95	3

The performances of the classifiers are also evaluated with the following metrics: the Sensitivity (Sens) and the Specificity (Spec) of each class. Sens is the probability of classifying a sample as True Positive (TP) and Spec is the probability of classifying as True Negative (TN) and they vary from 0 to 1. They are computed as follows:

$$Sens = \frac{TP}{TP + FN}; \quad Spec = \frac{TN}{TN + FP} \quad (4.13)$$

FN is False Negative, and FP is False Positive.

Table 4.5 shows the accuracy performances of the classifiers when applied to the different test datasets. We can see that the SEM data (*case 1* or *2*) yields the highest recognition rate for all classifiers where the Sens and Spec are of 1. Additionally, the CNN model has better performances than SVM and DT when trained using FD or TD data. In this case, the Sens and Spec are higher than 0.97 for all classes. Thus, we see that the classifiers trained using SEM data holding the residues are more capable in distinguishing spheres having close characteristic poles and provide higher accuracy results while consuming much less computational cost than classifiers trained using raw data.

Table 4.5 – Accuracy (%) of the 20% test sets when using the four classifiers with the four datasets

Data	SVM	DT	MLP	CNN
FD	95	94.5	97	98.3
TD	97.5	96.5	97.5	98.5
SEM case 1	100	100	100	100
SEM case 2	99.7	99.7	99.7	99.8

4.3.4 Noisy test data

Now, we test the classifiers' ability to handle noisy data. Given that generating a dataset with different SNR levels is challenging and cannot be used to evaluate the noise sensitivity of the proposed method, we opted to assess the robustness of the classifiers to noise by evaluating them on noisy data that were not seen in the training phase. We chose the 15 cm diameter sphere as its noiseless response is already included in the training dataset. Several AWGN levels are added to the SF response of the 5 spheres of 15 cm diameter. This is applied to multiple observation angles included in the three main planes presented before. The SNR values are chosen such that 65 dB is one of the highest values that can be obtained, whilst 10 dB corresponds to an unfavorable condition.

As in the case without noise, VF is applied to extract the poles and residues from the noisy signals. In chapter 3, we showed that the noise highly affects the damping factor values more than the natural frequencies. Consequently, the Q-factor will also be affected by noise as it is computed using the damping factor. Note that when using VF with very noisy signals, a minimum of 10 iterations are needed for good convergence of poles and the model order M should be carefully selected where it should not be set too high to avoid numerous poles related to noise that affect the convergence of actual resonance poles.

Accuracy results of the classifiers are shown in fig. 4.11. For all SNR values, both ANN classifiers trained using SEM data (*case 1 or 2*) achieve high accuracy results that are better than SF data. For 10 dB SNR, results start to decrease but are still high and similar to those obtained in (Garzon-Guerrero, Ruiz, and Carrion, 2013) for the PEC sphere while, as opposed to our work, they trained their algorithms using noisy data with AWGN at various SNR levels. Indeed, we noticed from the flowchart of DT, that it is basing its decisions mainly on the Q-factor as it is constant for all sphere dimensions and in the presence of noise it is perturbed which in turn perturbs the classification. SVM is more like a black-box but its performances might be due to the same reasons as DT. However, ANNs are able to classify the noisy SEM data as they are capable of taking advantage of the extra information provided by the original structure of the SEM dataset proposed in this work (sparse data, Q-factor and residues) as they can identify the first resonant frequencies and their associated Q-factor and residues barely affected by noise. In addition, we can see in table 4.6 that the three dielectric spheres have the highest Sens values as they are strong resonating objects making the extraction of CNRs easier in presence of noise, confirming what we have seen before in chapter 3 with the thin wire.

For FD and TD data, the CNN classifier performs better than the other classifiers and has good performances for high SNR values. However, results start to degrade for SNRs lower than 20 dB as seen in fig. 4.11. From table 4.6, we see that for 10 dB SNR the Sens and Spec deteriorate for some classes. Hence, we can conclude that the proposed association of VF with an original input vector structure and ANN classifiers compensates for the noise sensitivity of SEM methods which then outperforms the results obtained using raw data, even at low SNR levels.

Table 4.6 – Sens and Spec (%) for SNR = 10 dB using CNN with the different datasets

Class	Sens			Spec		
	FD	TD	SEM	FD	TD	SEM
0	32	68	85	97	96	96
1	77	72	84	95	93	97
2	41	76	93	97	95	99
3	90	82	98	72	88	97
4	95	77	99	84	90	99

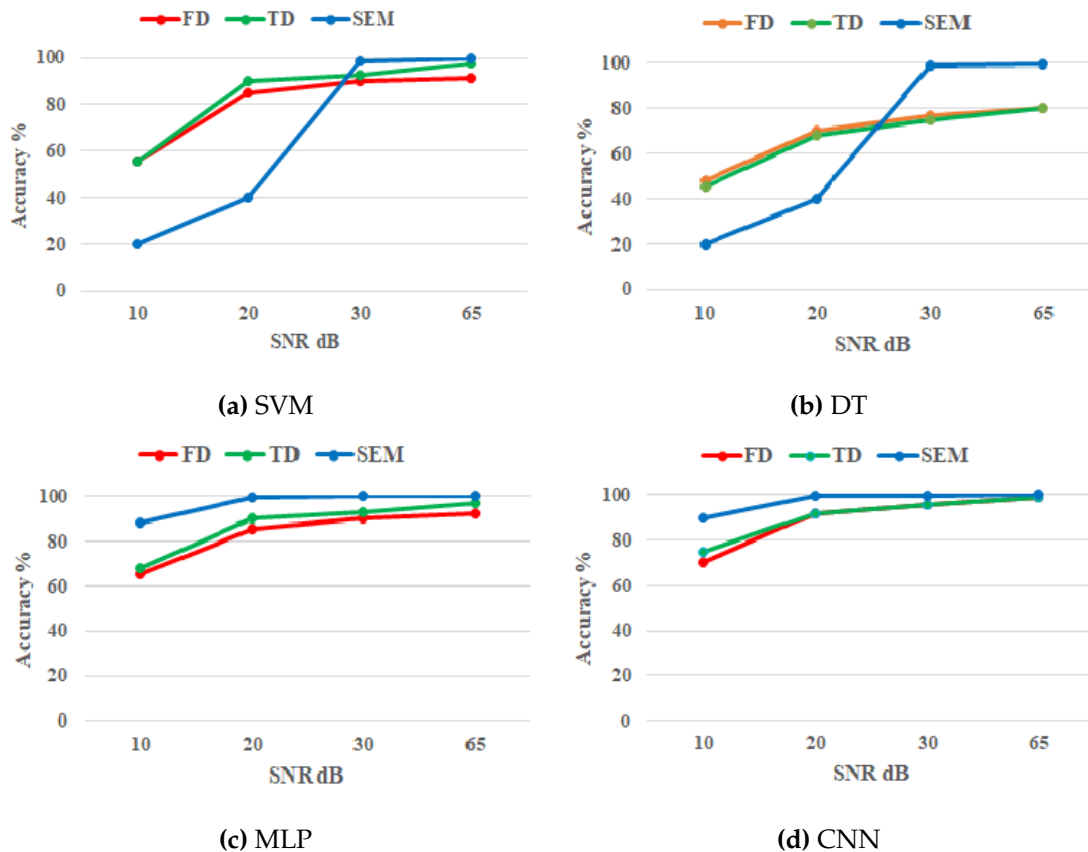


Figure 4.11 – Accuracy (%) of noisy data when testing several classifiers using the different datasets

4.3.5 Generalization using different sphere sizes

We test the generalization ability of all classifiers on larger and smaller spheres. First, we test this on noiseless SF responses and SEM data. The diameters are selected so that they are different than those included in the training sets where we have either the same number of resonances ($N=5$) or out of band CNRs. Increasing the object's diameter means, physically, that the first 5 natural frequencies are shifted down into the frequency band while decreasing it makes the first 5 natural frequencies shift upwards in the frequency band. Indeed, by increasing or decreasing the object's size, the SF response will be either dilated or compressed in the fixed frequency band of interest. Second, we test the generalization on noisy responses for the smaller and larger spheres.

4.3.5.1 Noiseless responses

For larger spheres, the accuracy results shown in fig. 4.12 indicate that all classifiers trained using SEM data of *case 1* perform an accuracy of 100% for all classes and for both 19 cm and 30 cm diameters. The Sens and Spec are of

1. These results are due to the Q-factor, associated to each natural frequency which is constant whatever the size of the sphere. On the contrary, the SEM data of *case 2* did not achieve accuracy results as high as *case 1* which shows that, as expected, replacing the damping factor by the Q-factor is important to be able to properly generalize the classification of sphere with sizes larger than those included in the training dataset.

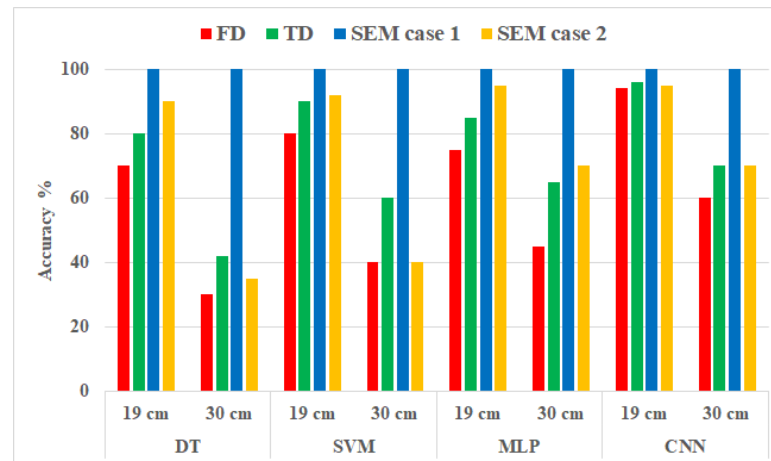


Figure 4.12 – Accuracy (%) of 19 and 30 cm diameter spheres using all classifiers with all datasets

Comparing SEM data (*case 1*) with TD and FD data, we find an overall gain of nearly 4% and 6% for SEM data respectively with CNN classifier when testing the 19 cm sphere diameter. Moreover, for larger spheres (30 cm diameter), results deteriorate for classifiers trained using raw data, as seen in table 4.7. This shows that classifiers trained using SEM data can be, efficiently, generalized to larger spheres having at least 5 resonances in the frequency range, whereas classifiers trained using SF datasets are progressively unable to classify larger spheres as their size becomes larger than those included in the training dataset.

Table 4.7 – Sens and Spec (%) of 30 cm diameter sphere using CNN with the different datasets

Class	Sens			Spec		
	FD	TD	SEM	FD	TD	SEM
0	38	60	100	88	87	100
1	32	67	100	77	85	100
2	46	35	100	58	55	100
3	43	72	100	58	62	100
4	80	79	100	75	78	100

Then, we test smaller sphere dimensions not included in the training dataset. Their sizes are listed in table 4.8. Table 4.9 shows the accuracy results, using

all classifiers, for data with only $N < 5$ resonances in the frequency range. The CNN classifier has the highest accuracies for FD and TD data while the other classifiers have almost 20% less accuracy for SF data. By using the sparse SEM data, we have 0% error except for $N=1$ where the algorithms miss-classify some samples from class 0 as seen in table 4.10.

However, for SF datasets, when the dimension decreases (i.e. smaller N), the accuracy decreases drastically where the Sens of some classes are lower than 0.5 for $N=1$. This shows that the pre-processing of the SF using the SEM method and the computation of the Q-factor to replace the damping factor, is an important step in a classification process in order to distinguish spheres that have different diameters than those included in the training dataset.

Table 4.8 – Smaller sphere diameters (cm) used for testing the generalization ability of the classifiers

Class	N			
	1	2	3	4
0) PEC	2.5	4	6	8
1) $\epsilon_r=4, \sigma=0.5$	2.5	4	5	7
2) $\epsilon_r=2$	4	5	7	8.5
3) $\epsilon_r=4$	3	4	5.5	6.5
4) $\epsilon_r=9$	2.2	3	3.8	4.5

Table 4.9 – Accuracy (%) for different number of resonances (N) using all classifiers with the different datasets

Data	N	Classifier			
		SVM	DT	MLP	CNN
FD	1	20	19	24	53
	2	30	30	32	56
	3	50	47	62	86
	4	70	65	73	92
TD	1	30	27	40	60
	2	48	42	50	78
	3	60	55	70	91
	4	76	70	83	95
SEM	1	98.5	98	98.5	98.5
	2	100	100	100	100
	3	100	100	100	100
	4	100	100	100	100

Table 4.10 – Sens and Spec (%) for N=1 resonance using CNN with noiseless responses

Class	Sens			Spec		
	FD	TD	SEM	FD	TD	SEM
0	42	48	93	90	95	100
1	68	77	100	77	90	98
2	59	68	100	78	84	100
3	44	90	100	82	74	100
4	51	32	100	90	95	100

4.3.5.2 Noisy responses

Following, we test the generalization to spheres of different dimension having noisy responses. This test is done using noisy data for the 30 cm diameter spheres and the smaller spheres having 1 resonance in the frequency band. We used the CNN classifier as it had the highest performances for SF data and same performances as MLP for SEM data in the noiseless case.

Fig. 4.13 and 4.14 show a decrease in the performances for all datasets when SNR level decreases. On one hand, the results obtained using noisy FD and TD data are as expected, since the classifier is already unable to accurately classify the spheres of 30 cm diameter from their noiseless responses. On the other hand, the loss in the performances when using SEM data can be explained by the fact that the Q-factors are affected by noise and that the natural frequencies of both sphere sizes are not included in the training dataset make it difficult to classify the spheres correctly. Additionally, when there is only one resonant frequency in the band, the low SNR might make this frequency similar to the one of another class creating the confusion and increasing that classification errors. Hence, the classifier detects less efficiently the spheres of smaller or larger diameters having very noisy responses. Nevertheless, the classification accuracy is still acceptable and far superior to the one obtained using raw data.

4.3.6 Discussion

Our approach in the previous section is intended to be global, with the objective of classifying the material of spherical objects of all sizes, and without a priori knowledge about the nature of the noise. In this context, the structure of the proposed SEM input vector satisfies this objective. First, including the Q-factors and the residues associated to each natural pole improves the robustness and allows the generalization to different object sizes. Second, the

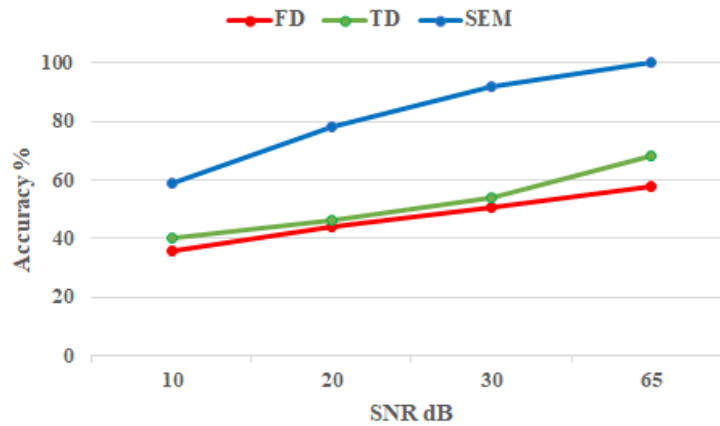


Figure 4.13 – Accuracy (%) for the 30 cm diameter spheres’ noisy responses at various SNRs when using CNN classifier with the different datasets

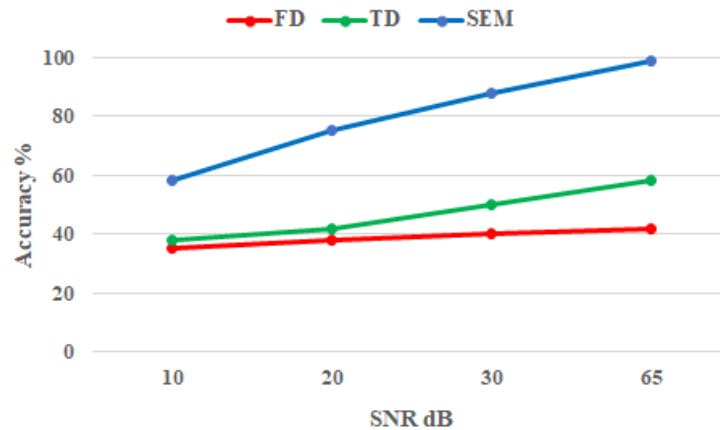


Figure 4.14 – Accuracy (%) of noisy responses for smaller spheres having 1 resonance in the frequency band at various SNRs when using CNN classifier with the different datasets

sparsity in the SEM dataset (replacing higher order poles with zeros) is beneficial to overcome the bandwidth limitations for small objects and to improve the robustness to noise by decreasing the weight of higher order poles during the classification process. These performances were also achieved with the use of more advanced classification algorithms. Indeed, our study has shown that at SNR levels ≤ 20 dB, the more basic algorithms (DT and SVM) do not take advantage of the additional information provided by the original format of the proposed SEM input vector. Conversely, ANNs are successful in taking advantage of the indirect but informative data (residues) and in handling sparse input data.

However, some limitations can be noted in this study: when testing noisy data

from a sphere size not included in the training set, the algorithms trained using SEM data did not achieve high accuracy results. Thus, to enhance the robustness of the classification, we propose to normalize the resonant frequencies which may improve the performances when classifying noisy responses of spheres of sizes outside the training set.

4.4 Normalization of the resonant frequencies

Indeed, results presented earlier have shown very promising performances when using SEM data in the training process. The Q-factor is very important to characterize the resonance behaviour of an object (a sphere of different composition in this section) while being independent of its size. However, the resonant frequencies vary with the object's size while respecting a certain homothety. To overcome the size dependency of the resonant frequencies, we normalize them with respect to the first resonant frequency, i.e. the fundamental frequency. Meaning that the initial value of the first channel of the input vector will always be 1. By normalizing, we will always have the same values for the first channel comprising the resonant frequencies no matter the size. This way the SEM dataset can be easily constructed from a single object size.

This approach is tested using a single dimension for the 5 classes of spheres. The dimension selected to be normalized is the 15 cm diameter for each sphere. In this case, we no longer include only the 3 main planes in the datasets as presented earlier, but we add data from all observation angles (37 angles in θ and ϕ). This is done to have enough data for the training process. Thus, in total we will have $37 \times 37 = 1369$ observation angles. We also take into account the sparsity of the SEM data, so we include normalized SEM data from smaller spheres. Thus, the dataset construction is done as in section 4.3.1 where the input vector includes: Normalized Resonant Frequencies (NRFs), Q-factor, residues amplitude for θ and ϕ polarizations.

The CNNs are deployed to classify using the normalized SEM dataset. The same topologies and parameters are used for the training of the CNN classifier. The datasets are also split into 80% for training and 20% for testing. Then, we test the same noisy data and the generalization using different sphere sizes. This is also done by normalizing the resonant frequencies of those data. The normalized confusion matrices showing the classification results using non normalized and normalized resonant frequencies in the SEM dataset are shown in fig. 4.15, 4.16 and 4.17. By comparing the confusion matrices, we see that it

is actually possible to classify the sphere's material using a single sphere size by normalizing the resonant frequencies. In addition, there is an increase of almost 20% for noisy data of unseen sphere dimensions when we normalize the resonant frequencies. This new SEM data structure is more robust as it allows to include only a single object's size in the dataset while producing the same classification results of noiseless data as the SEM dataset created using multiple sizes. In addition, the classification accuracy of noisy data from different sphere sizes are higher with this new dataset configuration.

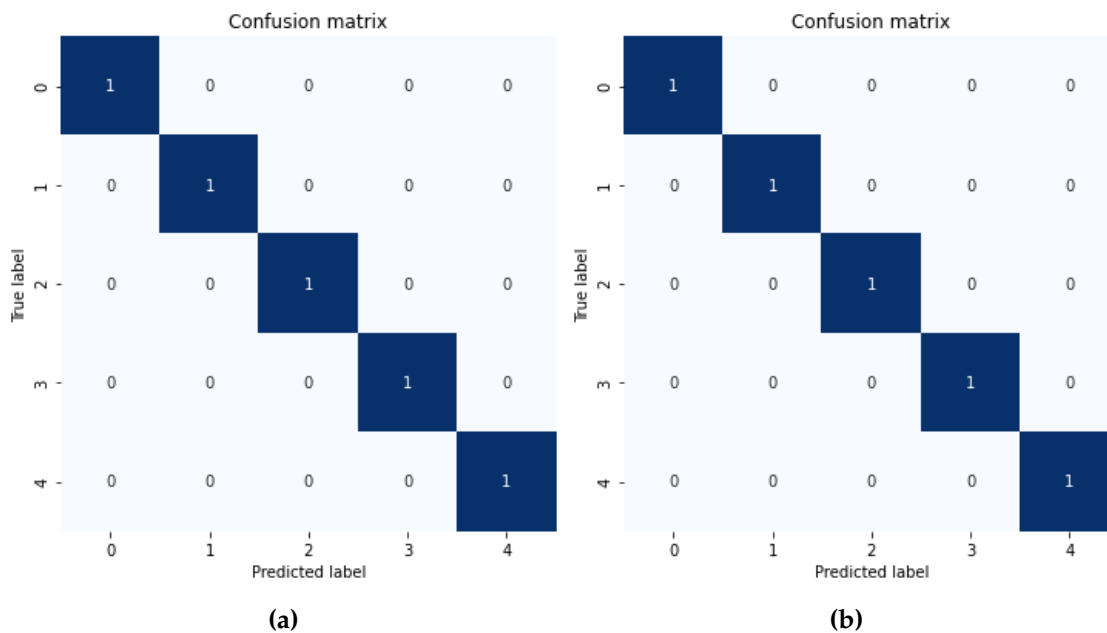


Figure 4.15 – Normalized confusion matrix using CNN classifier when testing 20% remaining samples of : (a) non normalized frequencies and (b) normalized frequencies

4.5 Classification of spherical and non-spherical objects

The study of SEM data for classification has been validated on spheres having different materials. In this section, we follow the same procedure not only for classifying the spheres but also to classify PEC objects of different shapes. This is done by expanding the original dataset containing the 5 classes of spheres with additional simulated objects. To avoid having to simulate several dimensions for each object, we fix their largest dimension to 15 cm. Then, the natural frequencies will be normalized as seen in the previous section. Table 4.11 shows the dimension of the simulated objects.

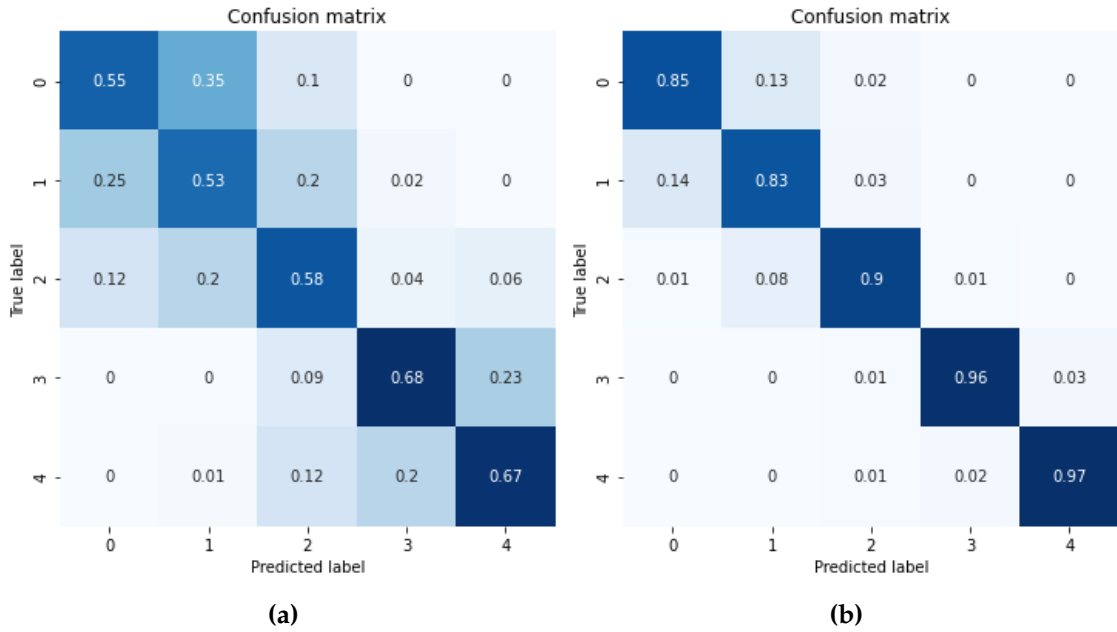


Figure 4.16 – Normalized confusion matrix using CNN classifier when testing generalization at 10 dB SNR for spheres of 30 cm diameter of : (a) non normalized frequencies and (b) normalized frequencies

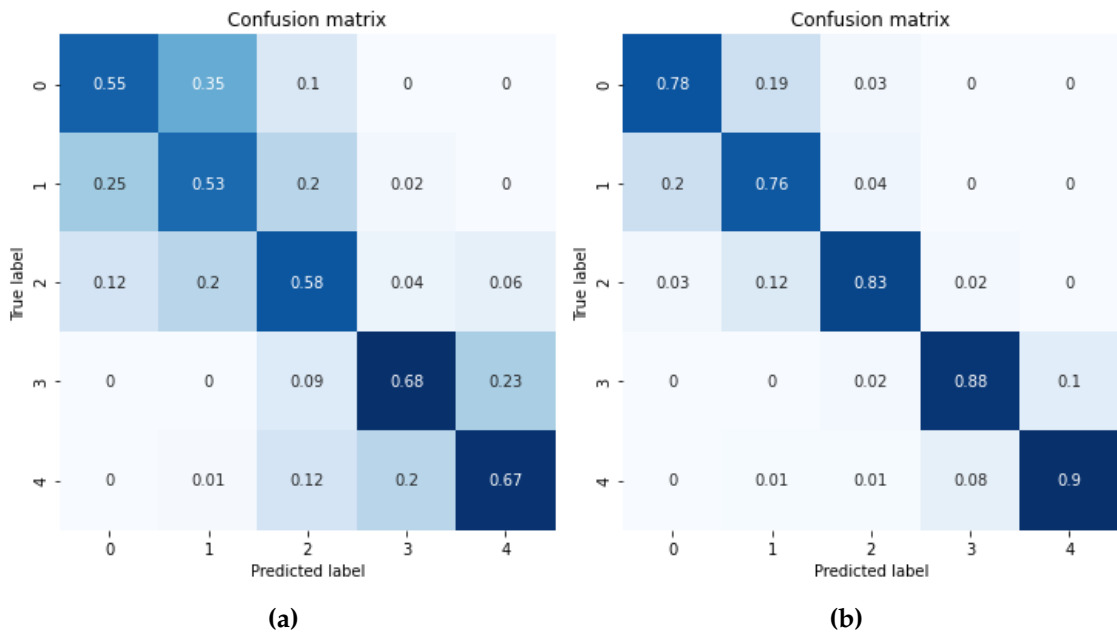


Figure 4.17 – Normalized confusion matrix using CNN classifier when testing generalization at 10 dB SNR for spheres having 1 resonance in frequency band of : (a) non normalized frequencies and (b) normalized frequencies

The classes are enumerated as follows:

- Class 5: Metal ring

Table 4.11 – Dimension properties and the propagating directions of the incident wave of each simulated object

Object	Dimension (m)	Incident angles
Metal ring	D = 0.15 Thickness = 0.001	$\theta=90^\circ$ $\phi = 0^\circ: 2^\circ: 90^\circ$
Thin wire	L/D = 100, L=0.15	$\theta = 0^\circ: 2^\circ: 90^\circ$ $\phi=0^\circ$
Thick cylinder	L/D = 1.5, L=0.15	$\theta = 0^\circ: 2^\circ: 90^\circ$ $\phi=0^\circ$
Ovoid	AR = 1.5, D=0.15	$\theta = 0^\circ: 2^\circ: 90^\circ$ $\phi=0^\circ$
Cube	width (w) = length (l) = height (h) = 0.15	$\theta = 0^\circ: 3^\circ: 45^\circ$ $\phi=0^\circ: 3^\circ: 45^\circ$
Rectangular solid	w= 0.15 l = h = w/2	$\theta = 0^\circ: 3^\circ: 90^\circ$ $\phi= 0^\circ: 3^\circ: 45^\circ$
Pyramid	square base = 0.15 h = 0.15 slope = 60°	$\theta = 0^\circ: 5^\circ: 180^\circ$ $\phi= 0^\circ: 3^\circ: 45^\circ$

- Class 6: Thin wire
- Class 7: Thick cylinder
- Class 8: Ovoid
- Class 9: Cube
- Class 10: Rectangular solid
- Class 11: Equilateral Pyramid

The simulations of those objects are carried out using CST's time solver. Unlike the sphere where the SF was recovered in a bi-static fashion where the emitter had a fixed position, here the SF is recovered in the back-scattering direction for both polarization states, θ and ϕ , where we work in a mono-static configuration. Indeed, we have adopted the monostatic setting, where the transmitter and receiver are collocated, since the selected objects are of complex shape as opposed to the sphere. Hence, the objects are illuminated using a plane EM wave with multiple incident directions chosen according to each object's symmetry planes as shown in table 4.11.

After that, VF is applied on the SF of each object to extract the CNRs (appendix C) and the residues. The datasets are constructed as before for the 3 data types. To form the sparse SEM data, instead of simulating smaller object sizes, we make use of the homothety of the poles and put artificial zeros in the dataset as we always have the same NRFs no matter the size.

As for SF responses from smaller object sizes, the response from the simulated object size is dilated in the frequency band and then the data are interpolated to have 500 frequency points. Fig. 4.18 shows that the interpolated amplitude response of a thin wire and a cube are in good agreement with the ones obtained using CST time solver.

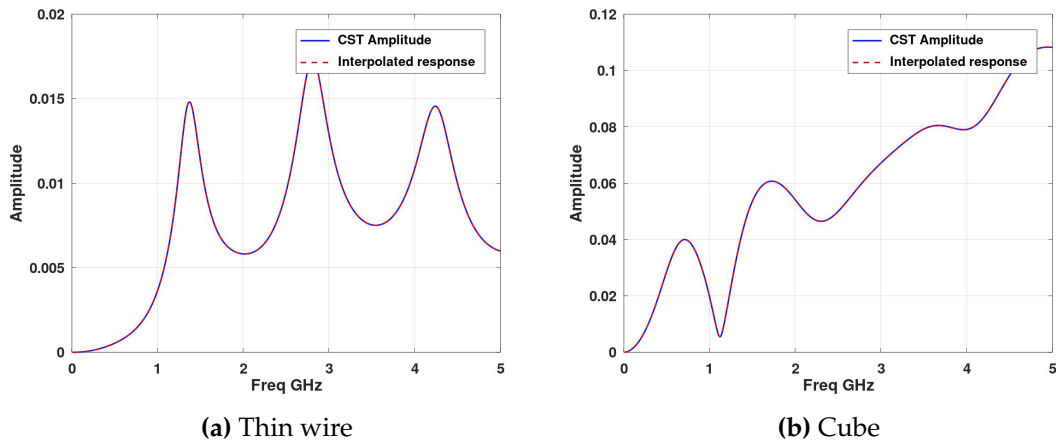


Figure 4.18 – Amplitude response of a thin wire and a cube of size = 10 cm when simulated using CST and interpolated

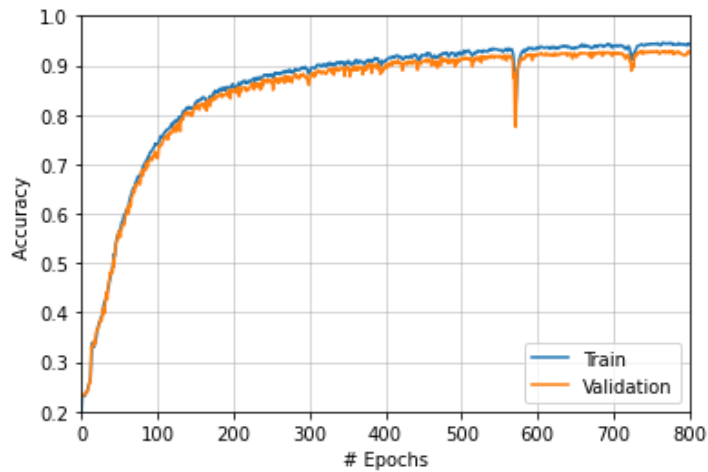
4.5.1 NN training results

The CNN is used as a classification algorithm as it achieved highest performances for SF and SEM data when dealing with the spheres. The topologies used are the same as in section 4.3.2.3. Only the number of epochs has been doubled because there is a greater amount of data as we have 12 classes instead of 5.

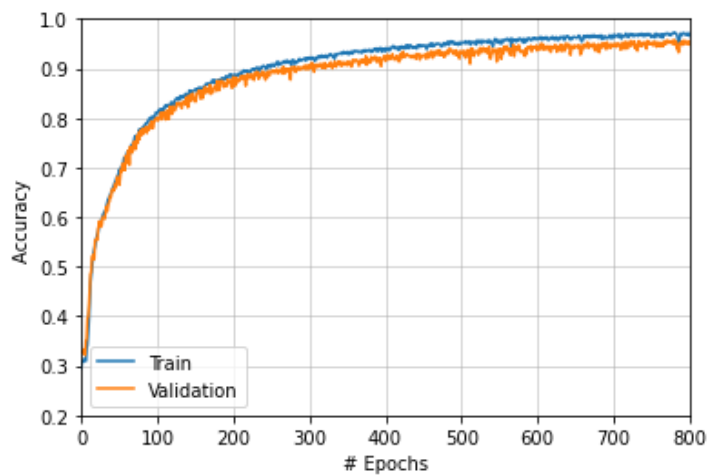
The datasets are divided into 80% for training and 20% for testing. Fig. 4.19 shows the training and validation accuracy as a function of the number of epochs for the 3 datasets. We can see that training curve converges quickly to 100% accuracy for SEM data at 125 epochs while presenting much less fluctuations than both SF data curves as the SEM data are easier to learn.

4.5.2 Classification results

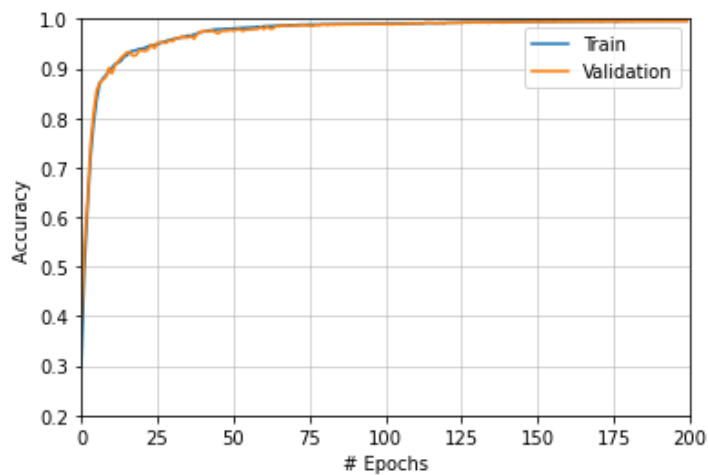
As before, accuracy results are averaged over 10 runs. Similarly to the material classification of the sphere, we start by testing the CNN with the 20% remaining samples. Fig. 4.20 shows the normalized confusion matrices for the 3 datasets. In this case, we note that CNN trained using FD and TD data do not classify all classes accurately where the mean accuracy does not exceed 94%. On the



(a)



(b)



(c)

Figure 4.19 – Train and validation’s accuracy for CNN classifiers vs number of epochs when learning with: (a) FD data, (b) TD data and (c) SEM data. 800 epochs are used with FD and TD data, while 200 epochs are used with SEM data

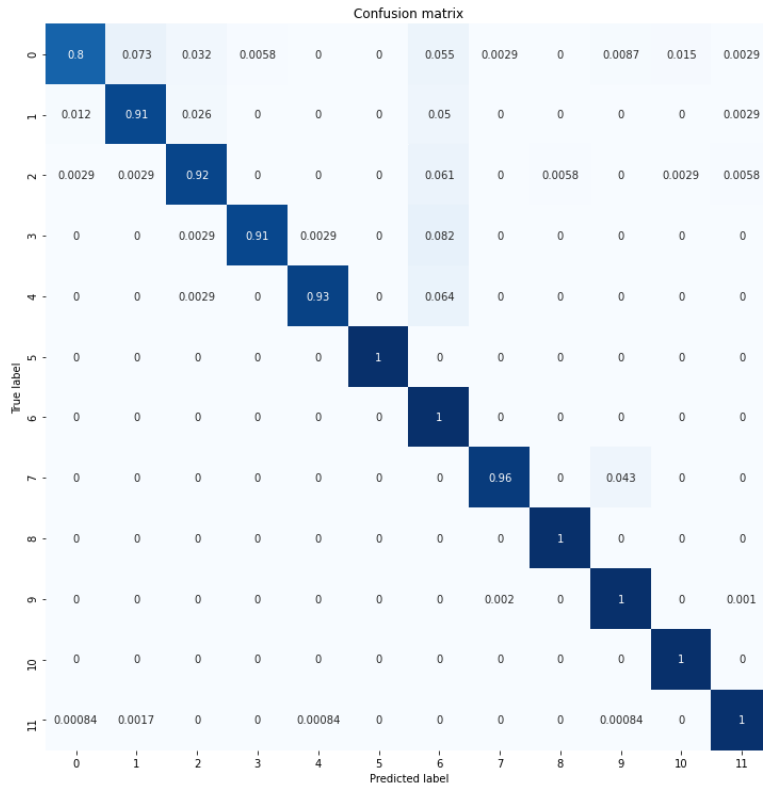
contrary, when trained with SEM data, the accuracy reaches 99.8% where it miss-classifies only some samples from class 1 (mixed sphere) with class 11 (pyramid).

Then, we test the generalization of the CNN on different object sizes and noisy data not included in the training set. First, we test noisy data from a size that has already been seen during training (15 cm) where the 5 first resonant frequencies are present. Results in fig. 4.21 indicate that the performances of CNN trained using normalized SEM data are better than that of SF data, with a gain of almost 20% for SEM at high noise levels (10 dB SNR).

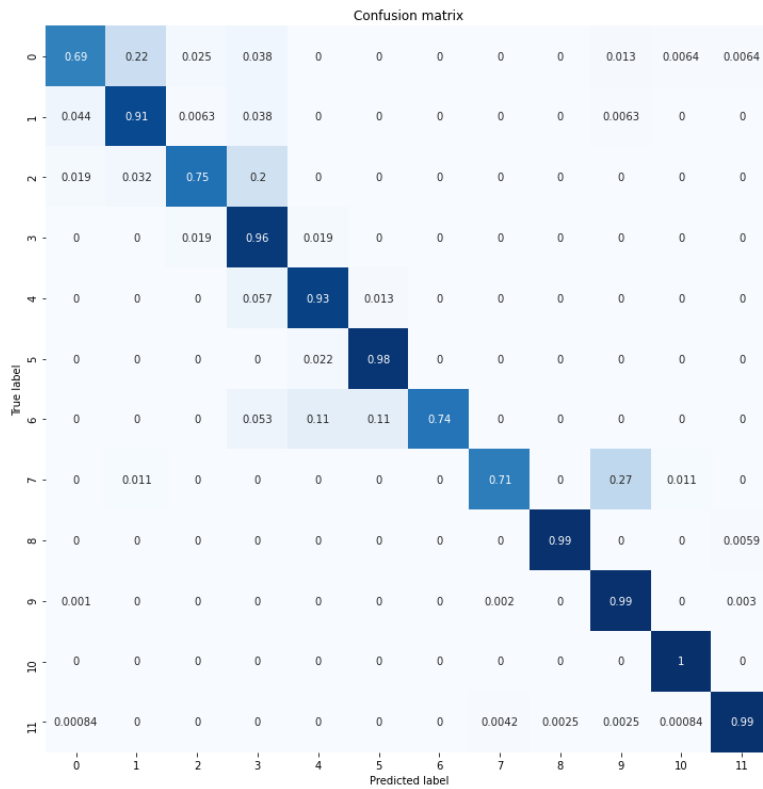
Following, we show the results of noiseless and noisy responses from objects of larger and smaller dimension. The larger dimension is chosen to be 30 cm while the smaller one is chosen where there is only one CNR in the frequency band for each object. Table 4.12 shows those accuracy results, and they confirm that the SEM data can distinguish the object classes correctly no matter the size from their noisy and noiseless responses as opposed to SF data. These results are very interesting, especially when there is only a single noisy natural frequency, in the sense that, this frequency does not provide information ($f_0 = 1$) and the classification is therefore done on the first Q-factor and residues. All those results prove that a NN classifier trained using SEM data can efficiently distinguish the classes of different objects at low SNR levels and for any observation angle.

Table 4.12 – Accuracy results of the generalization of noiseless and noisy responses from larger object sizes (30 cm) and smaller objects having 1 resonance in the frequency band

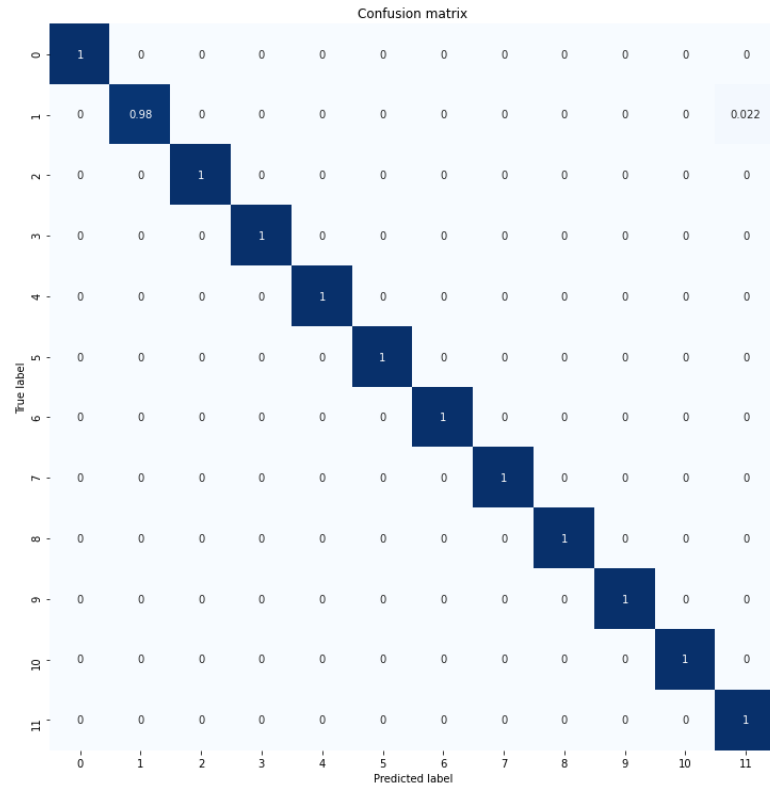
Test generalization	Data		
	FD	TD	SEM
Noiseless larger objects	54	62	99.8
Noisy larger objects	51	56	88
Noiseless smaller objects	52	55	99.7
Noisy smaller objects	49	53	80



(a)



(b)



(c)

Figure 4.20 – Normalized confusion matrix using CNN classifier when testing 20% remaining samples of: (a) FD data, (b) TD data and (c) SEM data.

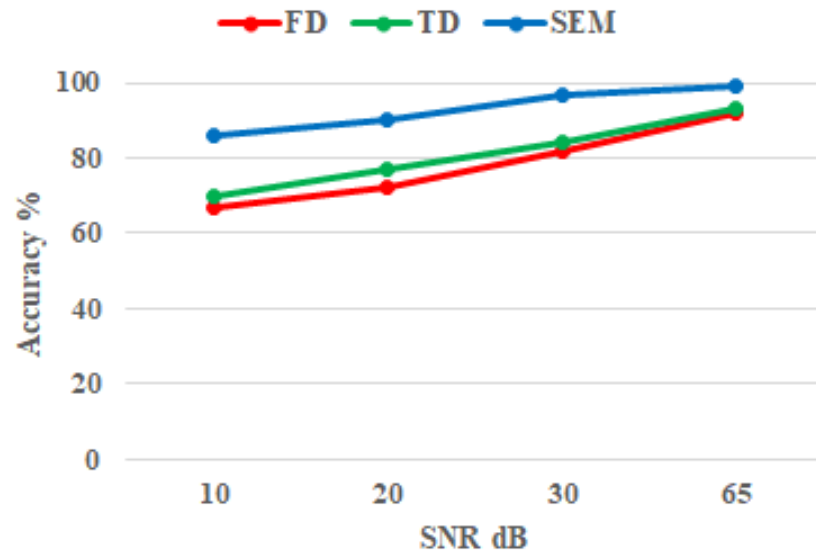


Figure 4.21 – Accuracy (%) of noisy responses of objects' dimension included in the training phase at various SNRs when using CNN classifier with the different datasets

4.6 Calculation of object dimensions

In chapter 3, we have seen that from the homothety we can deduce the CNR of an object of any size. Indeed, we need to fix a reference frequency (f_0 in GHz), which will be the fundamental resonant frequency of each object, and then from the knowledge of the object's reference size (l_{ref}) we can determine a coefficient k that will serve in computing the size of an unknown object as follows:

$$k = \frac{l_{object}}{\lambda_0} = \frac{l_{ref}}{\lambda_{0ref}} \quad (4.14)$$

$$l_{object} = k \times \lambda_0 = k \times \frac{c}{f_{0object}} \quad (4.15)$$

f_{object} and l_{object} are the first natural frequency and dimension of the object under test respectively. This step is done after the classification of objects.

To verify this, we simulate a PEC cube of an unknown size. Indeed, this approach can be applied to all objects, but we will verify it through this example. First, the SF response is recovered in the back-scattering direction for both field components when the cube is illuminated using a EM plane wave polarized along z axis and propagates in the x axis, as in fig. 4.22. Then, we apply VF to extract the resonances from the noiseless response, shown in fig. 4.23, with a model order that is fixed to 26 (chapt. 3).

The input vector is constructed as before, by taking: the first 5 natural frequencies and normalizing them, their respective Q-factors and residues. We use the previously trained CNN to identify the object. Among the 12 classes, this test predicts that this data belongs to class 9 which is the PEC cube.

The second step will be to determine its size. We fixed as reference the first natural frequency of the 15 cm cube length which is equal to 0.4GHz. From equation 4.14, we get $k = 0.15 \times \frac{0.4}{c} = 0.2$. By replacing k in equation 4.15, we obtain $l_{object} = 0.2 \times c / 0.245 = 24.49$ cm. Indeed, the cube simulated has a size of 25 cm. This error of 0.5 cm is due to the extraction of poles using VF where the model order should be refined.

4.7 Conclusion

In this chapter, four supervised learning techniques are studied, two of which are machine learning algorithms: SVM and DT and the other two are of deep

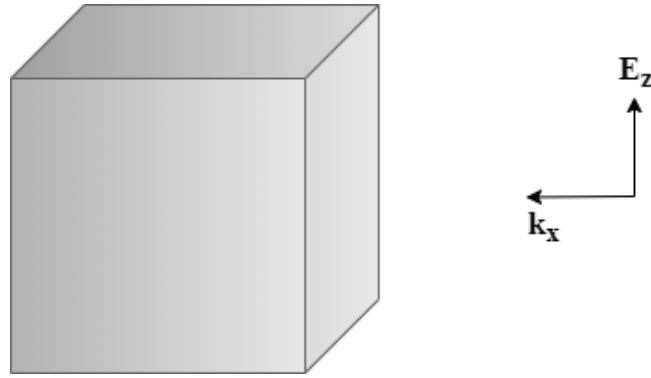


Figure 4.22 – Simulation of a PEC cube of unknown size

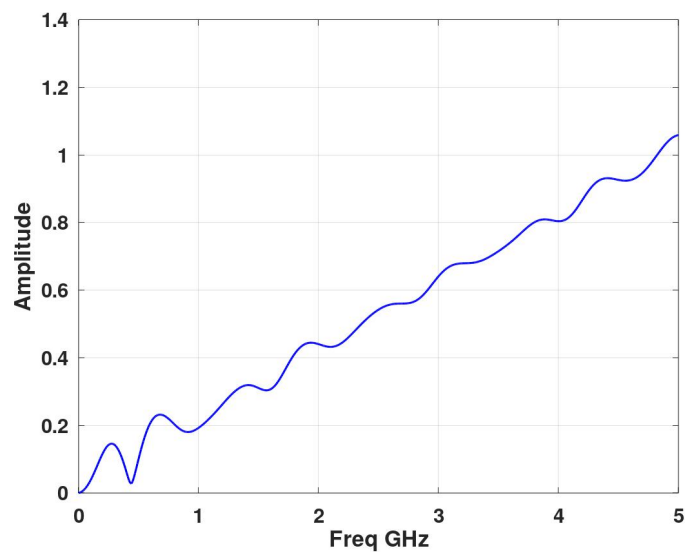


Figure 4.23 – Amplitude response of the PEC cube

learning: MLP and CNN. The classification of objects is first validated using spheres of different materials, then it is applied to the classification of multiple objects of complex shape. Three datasets are constructed based on the raw scattered field, in time and frequency domains, and the proposed pre-processed SEM data. They are constructed from multiple noiseless responses where the SEM data has a specific sparse input vector including the natural frequencies and their associated Q-factors and residues.

The comparison between classification based on SEM and raw datasets confirms that the proposed method allows to classify from a single observation angle while being efficient, aspect independent, and with low computational cost. We have shown the interest in exploiting the residues, which are usually excluded because they depend on the observation angle, but their frequency

dependence is useful for the classification. Moreover, the use of Q-factor instead of damping factor allows to accurately distinguish objects of different sizes not included in the training dataset. Additionally, the sparsity of the SEM input vector associated with ANN classifiers allows to maintain high classification rates even at low SNRs without including noisy data in the training phase.

However, the validation with the spheres showed some difficulty in the classification of noisy data from spheres of unseen sizes. Hence, by normalizing the natural frequencies in the SEM input vector, the classification of noisy data of objects of any size became more accurate compared to raw data as the normalized frequencies remain the same for an object regardless of its size. This also makes the construction of a dataset easier and faster as we no longer have to include multiple sizes of an object. Thus, we can note that combining ANN algorithms with VF can compensate for the noise sensitivity of SEM methods by surpassing the results obtained from FD or TD data even at low SNRs and without prior training with noisy data. In addition, the reduced SEM input vector size enables rapid convergence of the neural networks.

In addition, classification results using SF data could have been enhanced by applying deeper neural network topologies. However, this would have increased considerably the amount of time necessary to train the network which is already much higher than the one used for training with SEM data.

Finally, we have seen that, after the classification process, we can determine the size of the object under test from the knowledge of its first non-normalized resonant frequency. This study shows that there is no need to create a classifier to determine the size of each object as this can be done mathematically by fixing a reference.

Following the classification of objects, we will proceed to the classification of the orientation of those objects by the use of residues in the next chapter.

Chapter 5

Identification of the object's orientation

5.1 Introduction

After classifying the objects in chapter 4 by the use of SEM data, the second stage is to determine the orientation of each object according to the antennas system. The geometry of the problem defined for this objective will be explained in the following section. Indeed, as seen in chapter 3, the residues are related to the scattered field response and vary with the observation and incident directions, hence, they can be considered to detect the location of the observer and the orientation of the object.

We start to validate this approach using the spheres simulated in chapter 4. A comparison of the classification efficiency using residues and raw data is carried out using the four classification algorithms defined earlier: SVM, DT, MLP and CNN, in order to determine the most robust classifier for this application. For this purpose, the space surrounding the sphere is split into multiple angular sectors to locate the receiving antenna. Then, we test the robustness to noise and the generalization ability to unseen data of each classifier, all while comparing performances when using raw data and residues.

Following, we proceed to the partitioning of the rest of the objects into angular sectors and test the robustness when using the three datasets (FD, TD and residues) of the selected most robust classifier. Once the receiving antenna has been localized (i.e. the angular sector is identified), the next piece of information sought is the polarization of the incident wave, which will indicate the rotation of the antenna with respect to the object (this is equivalent to determining the object orientation relatively to the antenna's coordinate system). Finally, the same procedure will be applied on a more complex object.

5.2 Geometrical definition of the problem

We make use of the coordinate system defined in Balanis, 2005 (fig.5.1) to represent the scattered field of an object. Thus, the spatial variation of the scattered field is along the azimuth (ϕ) and elevation (θ) planes with respect to the direction of the incident plane wave.

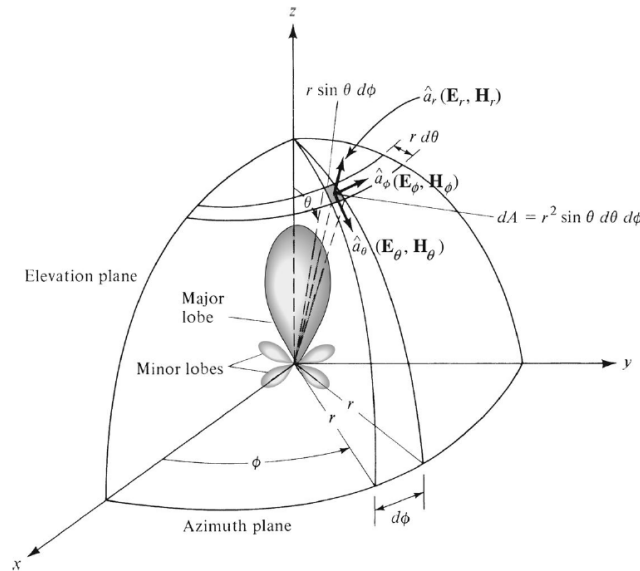


Figure 5.1 – Coordinate system for an antenna radiation pattern (Balanis, 2005).

In this work, determining the direction and orientation of the antenna in the object's coordinate system consists of identifying, first, the angular sector containing the direction of the wave vector of the scattered field, and second, the rotation of the antenna around the scattered wave direction.

5.2.1 Detection of the angular sector

As explained below, the space surrounding each object will be split into multiple angular sectors in the azimuth and elevation planes. The objective will be to determine the angular sector containing the scattered wave vector (which is equivalent to determining the direction of the receiving antenna) using the classification algorithms. Two categories of objects are distinguished:

- **Spherical objects:** Due to the shape of the sphere, determining its orientation makes no sense. However, we can determine the position of the receiving antenna in a bi-static configuration because a mono-static one will always provide the same scattered field regarding the position of the antenna.

- **Non-spherical objects:** In case of a non spherical object, measurements are performed in a mono-static scenario where the scattered field varies with the incidence direction of the illuminating wave (i.e. position of the Rx/Tx antenna). As seen above, each object is split into angular sectors according to the symmetries of its geometry. For example, a thin wire oriented along z axis has a symmetry plane in the azimuth plane, so we deal with only the upper half. Additionally, it has a rotational symmetry along z axis, so the mono-static scattered field does not vary in the azimuth plane.

5.2.2 Rotation of the antenna around the scattered wave direction

Once the angular sector is identified, we define a plane perpendicular to the incident wave vector to represent the rotation of the polarization of the incident field in this plane. This is the same as having the rotation of the object with respect to the direction of the incident wave. Having a rotated incident wave or a rotated object means that the scattered wave will be expanded in both θ and ϕ field components.

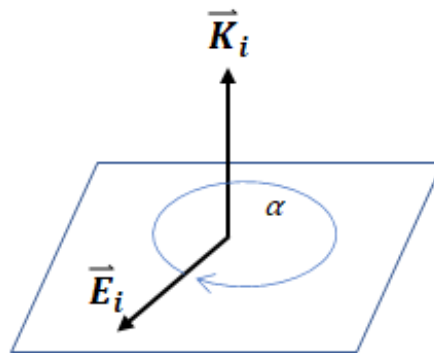


Figure 5.2 – Rotation of the incident field by an angle α around the travelling direction of the wave.

The angle α will be used to define the orientation of the linear polarization of the incident wave. This is represented in fig. 5.2 for an incident plane wave travelling with an incident wave vector \vec{K}_i . Retrieving α is the same as retrieving the rotation of the object around the incidence direction.

Therefore, by identifying the angular sector and the α angle, we will be able to determine the unique orientation of the antenna in the coordinate system of the object.

5.3 Identification of angular sector for spherical objects

First, we validate this approach with the sphere as it is a simple object with an analytical solution representing its scattered field response. We have seen in chapter 3 that the radiation pattern of the scattered field by the sphere has two symmetry planes, thus, we only work with one quarter of the sphere.

For this purpose, we split the sphere into 8 angular sectors, where each sector contains various observation angles in θ and ϕ planes as seen in fig. 5.3. This number of sectors was chosen to limit the number of classes used to validate this approach. Those sectors will serve as our 8 classes that we aim to classify to determine the position of the antenna in one of those sectors.

Each angular sector includes the following observation angles according to fig. 5.1:

- sector 0: $0 \leq \phi \leq 90 ; 0 \leq \theta \leq 30$;
- sector 1: $0 \leq \phi \leq 40 ; 35 \leq \theta \leq 65$;
- sector 2: $0 \leq \phi \leq 40 ; 70 \leq \theta \leq 110$;
- sector 3: $0 \leq \phi \leq 40 ; 115 \leq \theta \leq 150$;
- sector 4: $50 \leq \phi \leq 90 ; 35 \leq \theta \leq 65$;
- sector 5: $50 \leq \phi \leq 90 ; 70 \leq \theta \leq 110$;
- sector 6: $50 \leq \phi \leq 90 ; 115 \leq \theta \leq 150$;
- sector 7: $0 \leq \phi \leq 90 ; 155 \leq \theta \leq 180$.

5.3.1 Dataset Construction

For each of the 5 spheres of different materials simulated in chapter 4, we create datasets that contain 8 classes corresponding to the angular sectors of each sphere created above. In every dataset we include the 13 sphere sizes simulated earlier. It can be noted that the multiple dimensions are mostly beneficial to the raw data since, as we will see later, the residuals are independent of the object size. Thus, each dataset holds 4810 samples ($37 (\theta) \times 10 (\phi) \times 13$ sizes of spheres as seen in chapter 4).

5.3.1.1 Scattered Field dataset

For the FD and TD datasets, they are constructed as in chapter 4 with the same input vector's length. Thus, for frequency responses, we include the amplitude

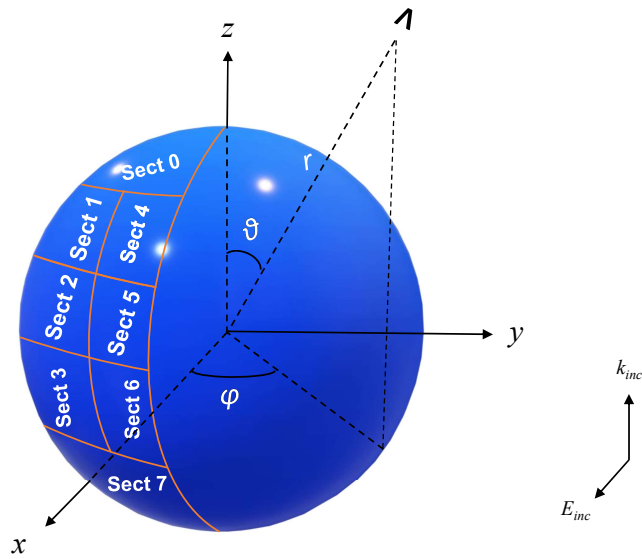


Figure 5.3 – Sphere’s angular sectors.

of both E_θ and E_ϕ field components, while for time response, we include the first 10 ns of the signal for both field components.

5.3.1.2 Residues dataset

For the residue’s dataset, the input vector is also of length 5 and comprised of 2 channels representing the amplitude of residues related to both field components E_θ and E_ϕ respectively. The natural frequencies and the Q-factor are eliminated as they do not vary with the observation and incident angles. Additionally, the dataset contains sparse data due to the reasons mentioned in chapter 4.

In fact, using residues over raw SF data will present some merits which are:

- first, we have much less data in the input vector. The residues dataset is 100 times and 20 times smaller than the SF datasets in frequency and time domains respectively.
- second, the amplitude of the residues is independent of the object’s size.

Indeed, the natural frequencies at which the residues are derived are inversely proportional to the size of the object, i.e. for each object, the residues are independent of its size since they are computed at the same electrical length. Fig. 5.4 shows the amplitude diagram of residues associated to the first resonant frequency of a PEC sphere of 15, 10 and 5 cm diameters. Consequently, they

are unique to each object but informative about the orientation of that object. Thus, we can expect that determining the position of the receiving antenna using the residues will be faster than raw data, and suitable for generalization however, as there is less data, the residues might be more sensitive to noise. In addition, we will later investigate the performances when the dataset containing residues is constructed using a single sphere size instead of 13.

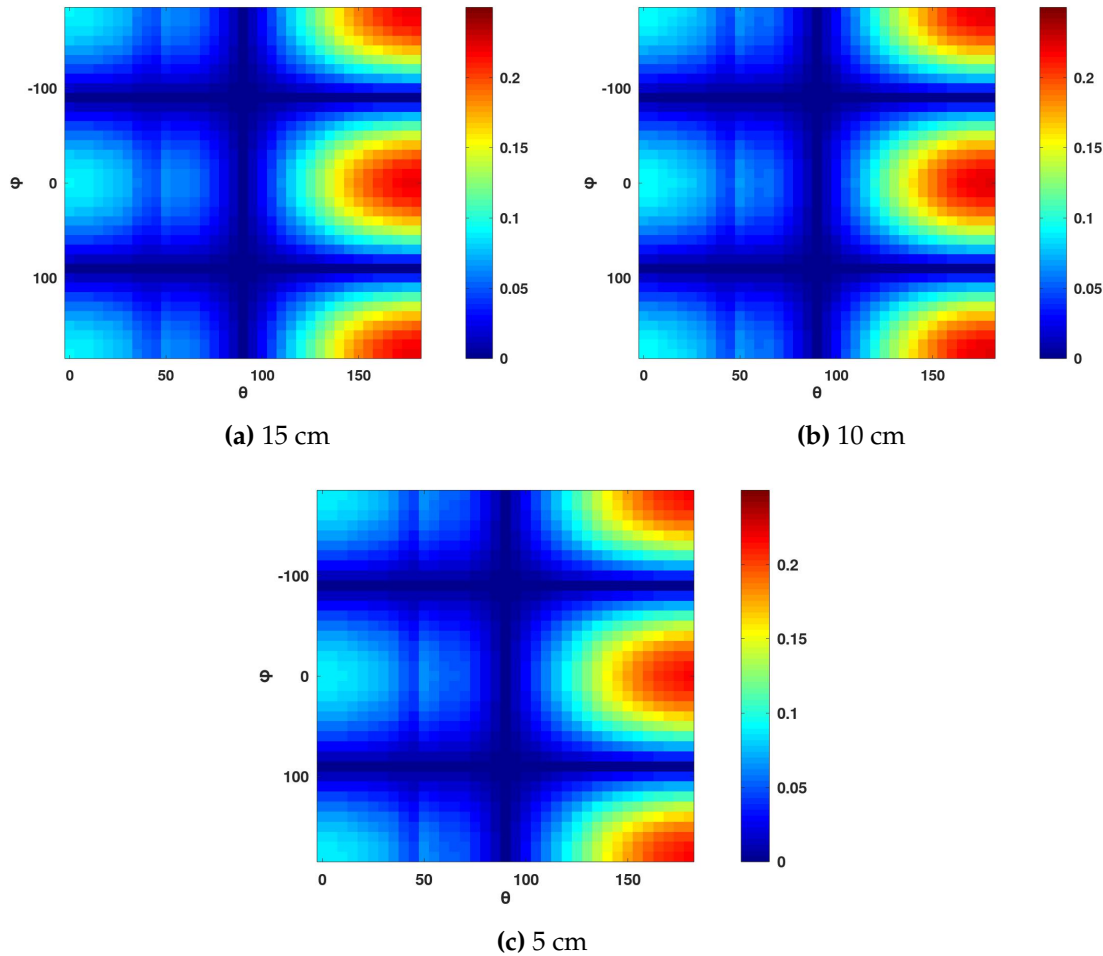


Figure 5.4 – Residues amplitude associated to the first resonant frequency for PEC spheres of 3 different diameters.

5.3.2 Training Phase

During this phase, the parameters of each classifier are tuned to achieve highest accuracy results for training data. Each dataset is split into 80% for the training and 20% for the testing. The remaining 20% are composed of various observation angles that are not present in the training set where each class has an equal number of samples. The mean accuracy results of test data are averaged over 10 runs as in chapter 4.

5.3.2.1 Multi-class SVM

Similarly to what was done in chapter 4, the SVM parameters are found by using 'gridsearch' function. The training results are given in fig. 5.5 when using rbf kernel function for the three datasets. We can see that, inversely to the classification of objects, the accuracy does not reach 100% for residues data and the values that achieve highest accuracy for training are limited. Additionally, we can observe that the training with raw data requires a fine tuning of C and γ as a slight change in those values impacts the training performances.

Table 5.1 shows the optimum training parameters. Due to the complexity of the problem, the training parameters are higher than those used for SEM data in chapter 4 because the separation between classes is more difficult.

Table 5.1 – Parameters of SVM classifier for angular sector classification

Data	Parameters		
	Function	C	γ
FD	rbf	2500	5
TD	rbf	2500	50
Residues	rbf	50	50

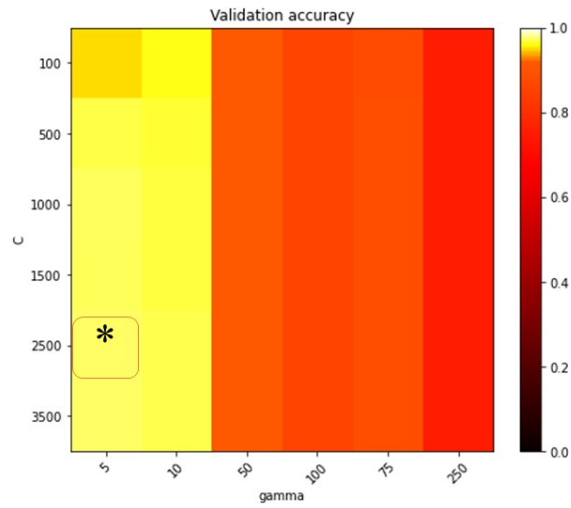
5.3.2.2 Decision Tree

The DT classifier's parameters are also left random where the Gini criterion is used to split the data in the decision nodes. Fig. 5.6 shows the trees produced during the learning phase using the different datasets. The trees are larger than those in chapter 4, but the one using residues is still smaller than the other two. Indeed, the problem at hand, to separate the data into 8 distinct classes, is more difficult than the previous classification problem. Thus, we expect that the DT classifier will have the most difficulty in classifying the test data.

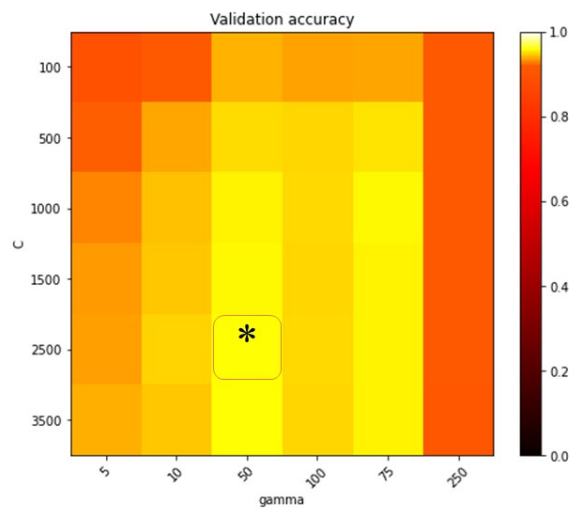
5.3.2.3 Artificial Neural Networks

As earlier, we try to find the optimal training parameters through trial and error. For the MLP classifier, we apply three hidden layers each with 64 and 256 neurons for residues and both SF data respectively. We apply the ReLU activation function in both layers and for all datasets (SF and residues).

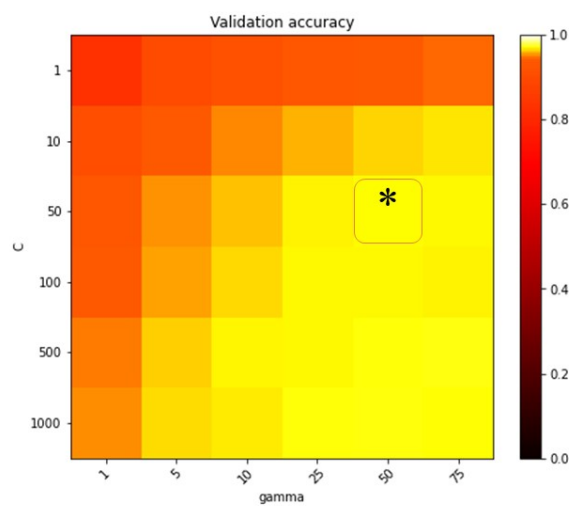
For the CNN classifier, the LeNet-5 architecture is also adopted for SF datasets, while for residues dataset we use one convolutional layer with 12 filters followed by two hidden layers with 32 neurons each. The number of epochs is



(a)

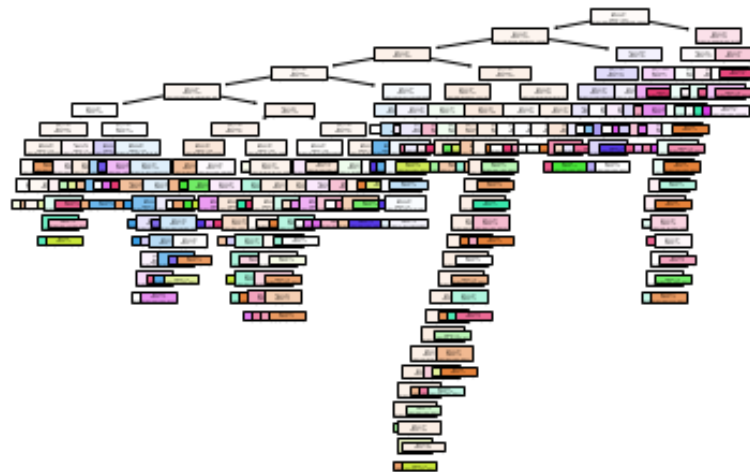


(b)

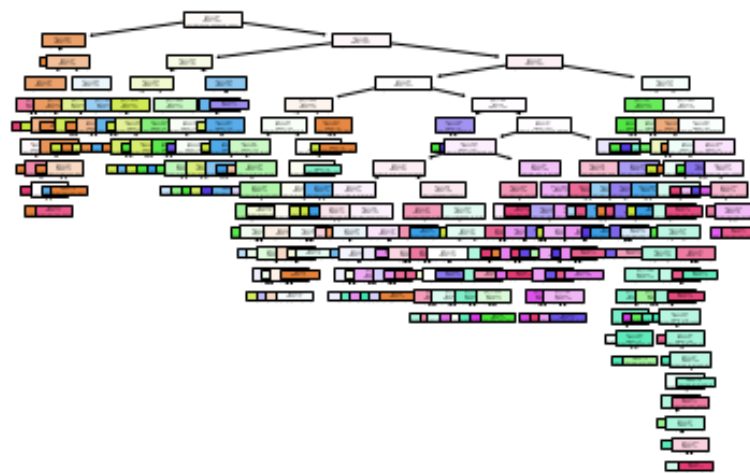


(c)

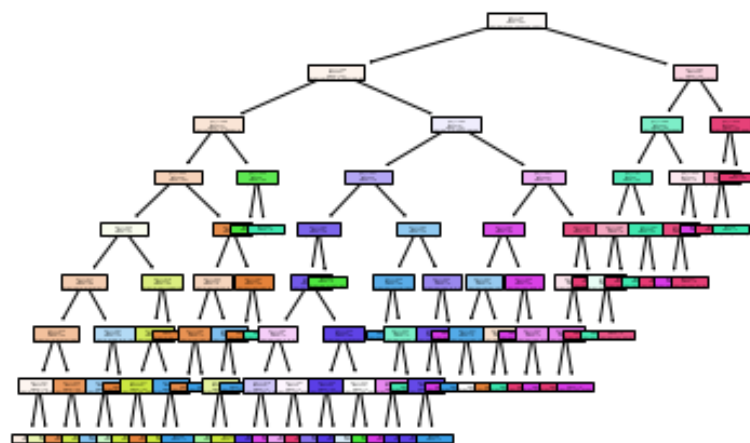
Figure 5.5 – SVM learning parameters when using rbf kernel function with: (a) FD data, (b) TD data and (c) residues data. * illustrates the selected optimum values.



(a) FD data

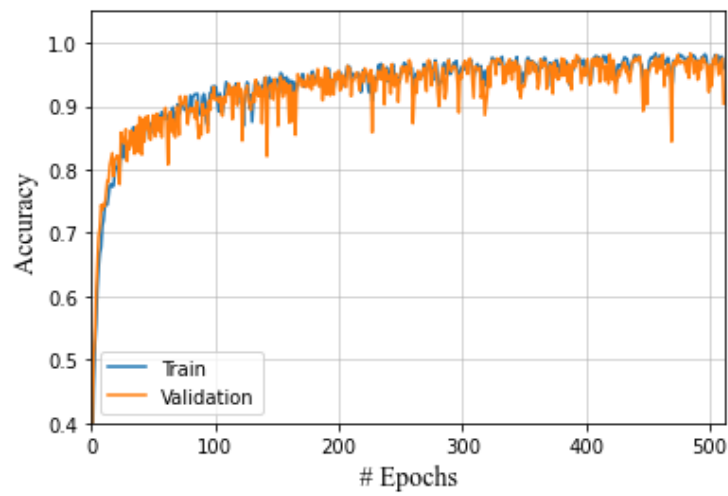


(b) TD data

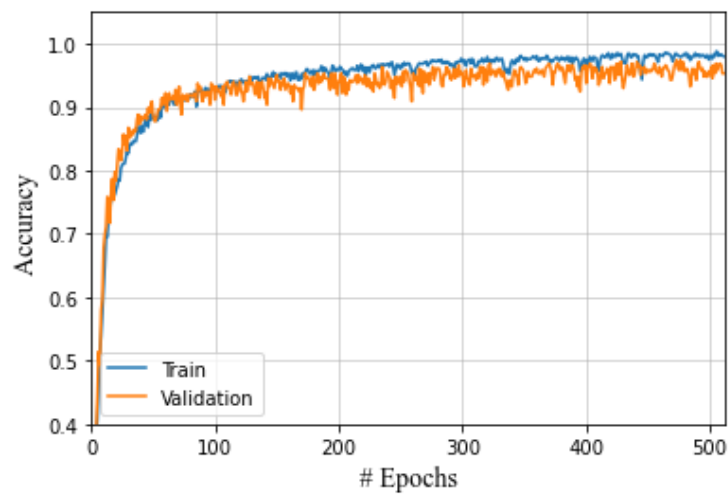


(c) Residues

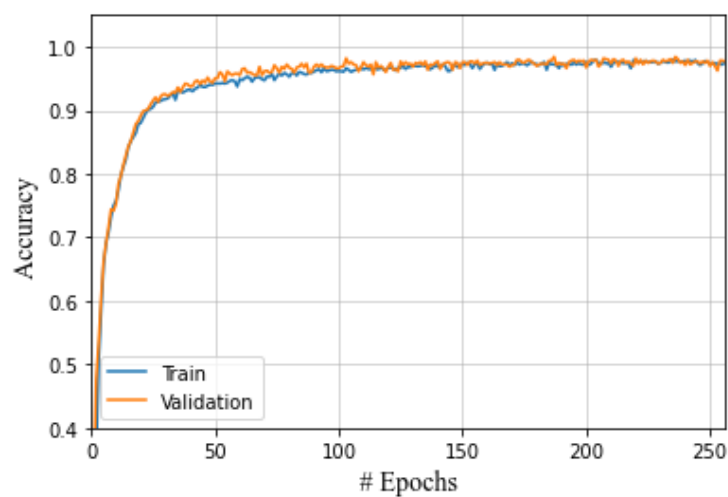
Figure 5.6 – Decision tree flowchart-like tree structure when learning with the three datasets.



(a) FD data



(b) TD data



(c) Residues

Figure 5.7 – Train and validation accuracy for CNN classifiers when learning with the three datasets.

256 for residues and 512 for SF data with a batch size of 100 for both MLP and CNN. The output layer is composed of 8 neurons representing the number of sectors and using the softmax activation function.

Fig. 5.7 shows the evolution of the accuracy curve as a function of the number of epochs when using CNN with the 3 datasets. We can observe the fluctuations that exist in the three curves due to the complexity of the problem making the convergence harder than the earlier classification task. However, we can notice that training with residues makes the convergence faster, starting from 150 epochs approximately, as opposed to SF data that starts to converge at 300 epochs with much more fluctuations in the training curves.

5.3.3 Test Phase

We start by testing the 20% remaining samples for the 5 spheres. In fact, the performances are almost similar for all spheres, hence, we present the results of the PEC sphere and compare the results of the residues, FD and TD datasets. The results of the four other spheres can be found in appendix E.

Table 5.2 shows that residues data has highest performances using ANN classifiers (MLP & CNN) with 1% error rate. For SF data, DT has the lowest performances where Sens and Spec values do not exceed 70% for all classes. Hence, DT is not a classifier that is suited for this problem as it is prone to over-fitting. This first test shows that, in a noiseless case, identifying the angular sector containing the direction of the observer is possible when using the residues associated to each pole and gives improved results compared to raw data and at a lower computational cost during training.

Table 5.2 – Accuracy (%) of angular sectors classification for the 20% test sets

Data	SVM	DT	MLP	CNN
FD	96	52	96	97
TD	96	78	96	97
Residues	98	94	99	99

5.3.4 Noisy data

The next step is to test the same noisy data simulated in chapter 4 for a sphere of 15 cm diameter. It is observed that, as earlier, the CNN classifier has the highest performances for SF data, while for residues data the CNN and MLP classifiers

have similar performances. Indeed, DT still does not perform well when testing with noisy data which shows that it is very sensitive to data variation.

Under high SNR values, SVM, MLP and CNN trained using the residues have almost the same levels of accuracy as classifiers trained using both TD and FD data. Nevertheless, when SNR decreases, as expected, there is a loss of almost 12% for residues compared to SF data (refer to fig. 5.8) as there are only 5 data points for residues while for FD data there are 500 frequency points. In fact, as the SNR starts to decrease, the residues become highly perturbed since they are computed through the resonance poles which are also affected by noise. Only the residues associated to the first pole have the less distortions but as we will see in the following section, having one residue is not enough to determine the angular sector accurately for a sphere. Furthermore, it is observed that most of the miss-classified samples actually exist at the border of the sectors, for example, the border region between sector 1 and 4 (fig. 5.3), thus, it remains acceptable. For the rest of the section, we will no longer use DT as it has the lowest performances for the three datasets.

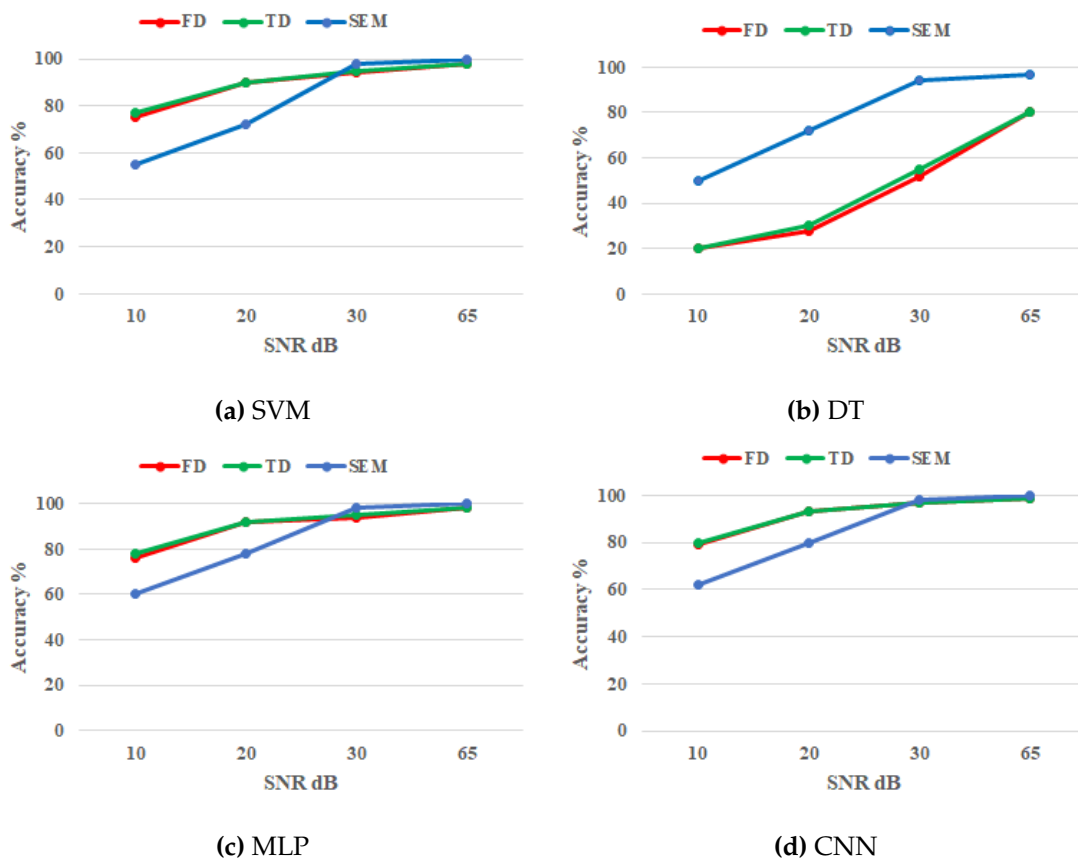


Figure 5.8 – Accuracy (%) of noisy data when identifying the angular sectors of a PEC sphere.

5.3.5 Generalization using different sphere sizes

Finally, we test the noiseless and noisy responses from larger and smaller sphere sizes simulated in chapter 4.

5.3.5.1 Noiseless responses

As seen earlier, the residues' amplitude remains constant for different sizes as they are computed for the natural frequency of the SF response. On the other hand, the FD and TD responses depend upon the object's size.

Fig. 5.9 shows that classifiers trained using both raw SF data are unable to determine the angular sectors of all larger PEC sphere sizes where the accuracy does not exceed 30% for the 30 cm diameter sphere. In addition, the Sens and Spec values of most classes do not exceed 40%. On the contrary, classifiers trained using residues achieve high performances where the ANN classifiers have 0.9% and 3% error for 19 and 30 cm diameters respectively. This confirms the benefit of using residues to generalize the classification of the observation angle for larger spheres.

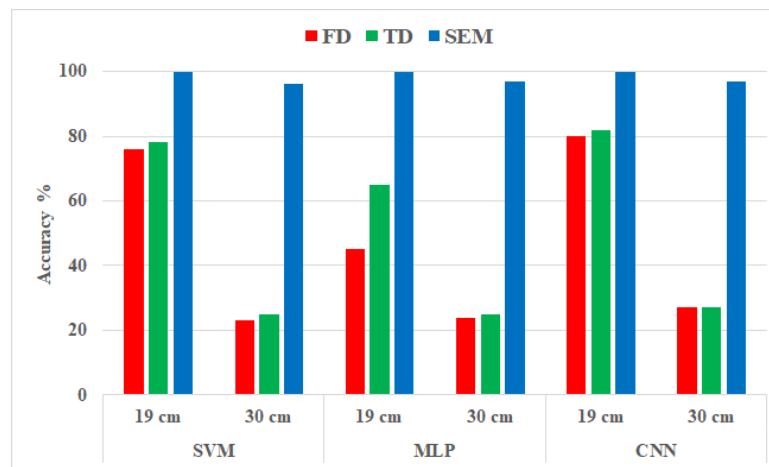


Figure 5.9 – Accuracy (%) of angular sectors classification of larger PEC spheres.

For smaller spheres, we test the classification capability on different sizes where the residues test sets include $N < 5$ natural frequencies (and thus, less than 5 associated residues). The accuracy results are listed in table 5.3. When the sphere's size decreases, classifiers trained using raw SF data become unable to detect the observation angle where for the smallest spheres it is impossible to classify some classes. We can note that the CNN classifier performs better than the rest, but it still has low accuracy when the sphere's size is different than those included in the training set. For classifiers trained using residues, MLP

and CNN classifiers perform best where it is observed that spheres with more than 1 resonance in the frequency band are easily classified with only 6% error for $N=2$ with both MLP and CNN. However, when there is one resonance it is more difficult to determine accurately some of the sphere's sectors through the residues associated to the first pole. This is because the amplitude value of residues associated to the first CNR are almost similar for some sectors. Nevertheless, the accuracy obtained using residues is 57% higher than those obtained with SF data which presents very promising results.

Table 5.3 – Accuracy (%) of angular sectors classification for different number of resonances N of the PEC sphere

Classifier	N	Data		
		FD	TD	SEM
SVM	4	93.5	94	96
	3	79	80	94
	2	29.5	45	92
	1	17.8	18	72
MLP	4	94	94	99.4
	3	79	80	99.5
	2	30	40	94
	1	18	18	75
CNN	4	95	95	99.5
	3	80	82	99.5
	2	33	48	94
	1	20	20	77

5.3.5.2 Noisy responses

Afterwards, we test the generalization to noisy responses issued from spheres of larger or smaller sizes. Similarly to what was conducted in chapter 4, this test is done using noisy data from the 30 cm diameter PEC sphere and the smaller one having 1 resonance in the frequency band. Moreover, we use the CNN to classify the sectors as it had the highest performances.

Fig. 5.10 and 5.11 show the results when testing both spheres and with the three datasets. As expected, CNN trained using FD or TD data has very low accuracy for all SNR values as it was already unable to classify the sectors from the noiseless responses of small and large spheres. We also notice that the performances when using residues for classification of the 30 cm diameter sphere's sectors is similar to the one seen in section 5.3.4. Indeed, as the residues remain roughly constant when the object's size is changed, it is normal to get the same

results as before. However, the sectors of the smaller sphere having one resonance are difficult to classify accurately at different SNRs as the classification from its noiseless response was a rather difficult task.

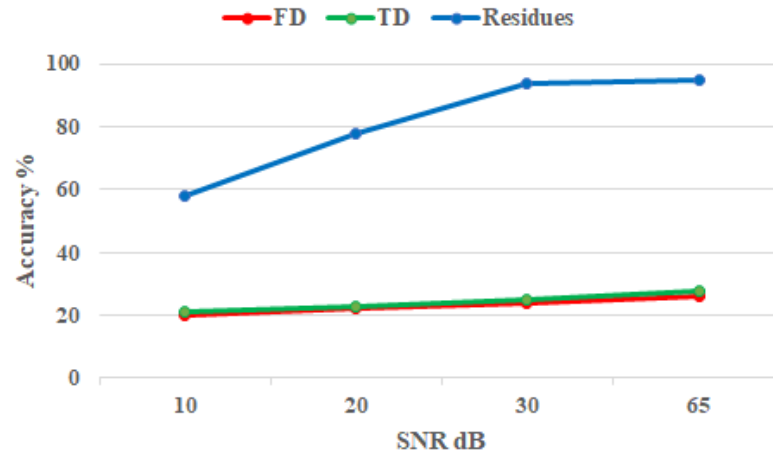


Figure 5.10 – Angular classification accuracy (%) of a 30 cm diameter PEC spheres at various SNRs when using CNN classifier with the three datasets

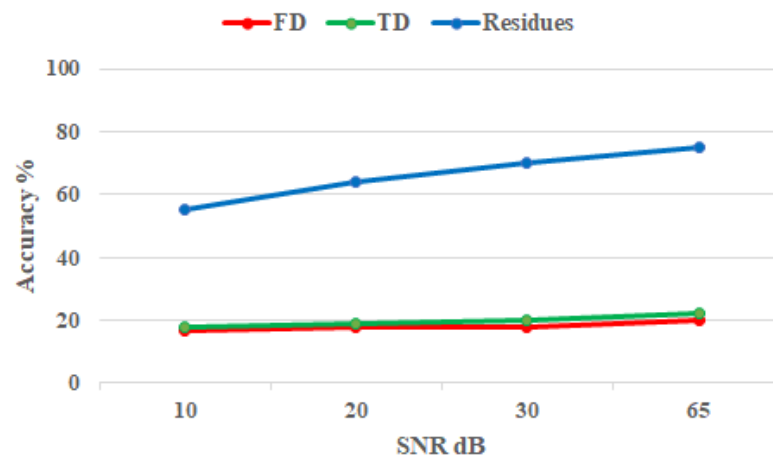


Figure 5.11 – Angular classification accuracy (%) of noisy responses of a smaller PEC sphere having 1 resonance at various SNRs when using CNN classifier with the three datasets

5.3.6 Optimization of dataset construction

From what we have seen so far, using the residues to determine the position of the receiving antenna is possible even when there is much less information concerning the frequency spectrum compared to raw data. The results are very promising as the classifiers trained using residues can generalize to any sphere

size. Furthermore, we have 100 times and 20 times fewer inputs in the residues dataset than in the FD and TD datasets respectively. However, the dataset was constructed using multiple sphere sizes whose responses contain 5 natural resonances in the frequency band. This constitutes a computational time that is high especially when simulating other objects using simulation software. Thus, as what was done in chapter 4, we will optimize the dataset construction by including a single sphere size. This will be achieved by taking the sphere of 15 cm diameter and extending the dataset with sparse data representing the smaller spheres having less than 5 resonances.

The CNNs are deployed to classify using this optimized SEM dataset. The same topologies and parameters are used for the training of the CNN. The dataset is split into 80% for training and 20% for testing. Then, we test the same noisy data and the generalization using different sphere sizes. Table 5.4 shows the accuracy of test data and generalization when training CNN using the new optimized dataset that included a single sphere size and the old one having 13 sphere sizes. This comparison shows that it is possible to classify the sphere's sectors accurately when the dataset includes a single dimension with only 3% loss in the accuracy results compared to the old dataset. This new structure for the dataset allows to include only a single object's size in the dataset while producing classification results, of noiseless and noisy data, comparable to the residues dataset created with multiple sphere sizes.

Table 5.4 – Comparison of the accuracy obtained using residues from the old dataset having 13 sphere sizes and the new dataset with only one sphere size

	Accuracy %	
	Old dataset	Optimized dataset
Test phase	99	96.3
Noisy data at 10dB SNR	63	62
Generalization to large sphere	97	94.2
Generalization to small sphere	77	75

5.4 Identification of angular sectors for non spherical objects

The study of SEM data for identification of the antenna position, through the use of ML and DL algorithms, has been validated on spheres having different materials. In this section, we apply the same concept to determine the position of the angular sector of PEC objects (metal ring, thin wire, thick cylinder, ovoid, cube, rectangular solid and pyramid), having a size of 15 cm and illuminated in a mono-static mode. Every object is divided into angular sectors depending on the symmetry of its geometry.

The CNN will be used as a classification algorithm because it achieved highest performances for SF and residues data. The topologies and learning parameters used are the same as in section 5.3.2.3. We will present the results obtained using the thin wire which is a very resonating smooth object and the rectangular solid that is a sharp object with edges more difficult to treat. The results for the rest of the objects can be seen in appendix E. The datasets are also created as in section 5.3.1. For the smaller objects having less than 5 resonances in frequency band, we use the interpolated SF responses as presented in chapter 4 to complete the datasets.

To increase the amount of data in each sector and to take into account the rotational angle α of the incident wave (refer to section 5.2.2), we include data derived from various rotational angles where α varies from 0° to 90° with a 10° step. This will allow to diversify the polarization of the incident wave and consequently the scattered field. Thus, we will be able to detect the angular sector for various rotation of the object or the incident wave.

In fact, the amplitude response is a function of α , as in fig. 5.12 where we present the simulated amplitude response of the scattered field by the thin wire with various rotations of the incident wave using CST time solver. Consequently, the residues amplitude is also a function of α . Mathematically, this amplitude can be calculated by multiplying the amplitude of E_θ or E_ϕ (when the incident wave is normal to the object) by the cosine or sine of α respectively. Thus, we follow this strategy to increase the quantity of data without simulating all the possibilities of incident wave or object rotations. We have taken into account all the rotation possibilities of the object by considering both field components θ and ϕ , and by illuminating the objects at multiple directions.

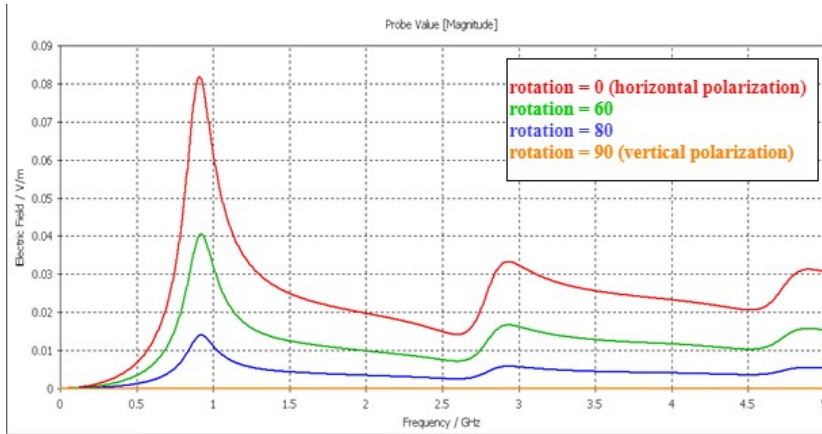


Figure 5.12 – E_θ Amplitude response of a thin wire orientated along z axis, when illuminated with a normal incident wave having different polarizations.

5.4.1 Thin wire

The thin wire is illuminated with various incident angles where θ varies from 0° to 90° . As explained in section 5.2.2, we only deal with the upper half of the thin wire as it is symmetrical along the azimuth plane. In addition, the SF response is the same whatever the angle ϕ when thin wire is orientated along z axis, thus, ϕ is chosen constant and equal to 0° . At $\theta = 0^\circ$ the scattered field is non-existent when the thin wire is orientated along z axis, as it is very thin.

We chose to divide it into 9 sectors, distributed as follows:

- sector 0: $2 \leq \theta \leq 10$;
- sector 1: $12 \leq \theta \leq 20$;
- sector 2: $22 \leq \theta \leq 30$;
- sector 3: $32 \leq \theta \leq 40$;
- sector 4: $42 \leq \theta \leq 50$;
- sector 5: $52 \leq \theta \leq 60$;
- sector 6: $62 \leq \theta \leq 70$;
- sector 7: $72 \leq \theta \leq 80$;
- sector 8: $82 \leq \theta \leq 90$;

Thus, we have 9 classes representing the 9 sectors. After creating the 3 datasets based on SF data and residues, we split the data into 80% for training and 20% for testing. Then, we will test the generalization ability of CNN to noisy and noiseless data of thin wire sizes unseen during training.

Test phase

The first test on the 20% remaining samples is carried. The accuracy obtained using residues as input data is of 97.8% while for both SF data we get 96%. Fig 5.13 shows those accuracy results along with the standard deviation obtained

over 10 runs. Those first results show that, as with the sphere, it is possible to detect the illuminated angular sector in one of the 9 sectors of the thin wire either with residues or raw data.

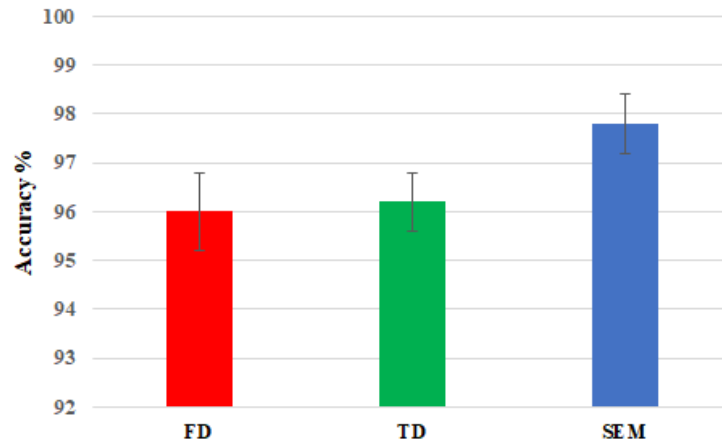


Figure 5.13 – Accuracy (%) on the 20% remaining samples of thin wire when using CNN.

Noisy data

After the test phase, we proceed to the test of noisy data of 15 cm wire length for which the noiseless response is already included in the training datasets. This is tested at multiple SNRs as before.

Fig. 5.14 shows the accuracy results when using the three datasets. We see that the accuracy when using residues or raw data are almost similar with only 2% difference at 10 dB SNR. This is due to the fact that the thin wire is a strong resonating object, so the extraction of CNRs in a noisy environment is not very hard and, thereby, the calculation of residues is quite precise even at low SNRs.

Generalization ability

The generalization is then tested using a thin wire of size 30 cm that has more than 5 resonances in the frequency band and a small one of size 5 cm having a single resonance. First when classifying using their noiseless responses, results using residues are more promising than when using TD or FD data as seen in fig. 5.15. As expected, it is impossible to classify the sectors of both sizes accurately using SF data. However, when using residues, we can classify the 30 cm length wire with only 5% error. As what was seen with the sphere, it is, indeed, more difficult to classify the sectors of the 5 cm length wire due to the presence of only one resonance where the accuracy is of 72%.

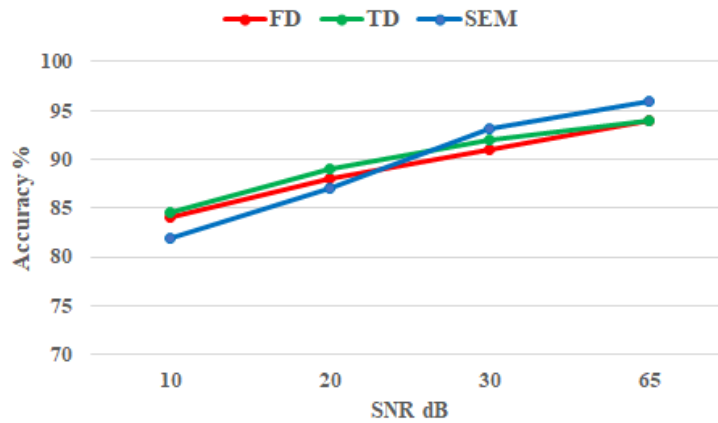


Figure 5.14 – Accuracy (%) of noisy data of the thin wire at different SNRs when using CNN.

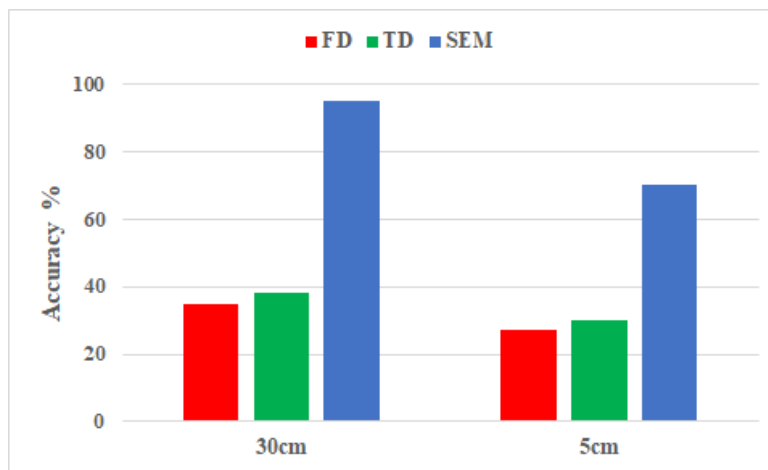


Figure 5.15 – Accuracy (%) of generalization to noiseless data of larger and smaller thin wires when using CNN.

Following, we test the noisy responses of both object sizes. Fig. 5.16 show the results of larger and smaller thin wires respectively at 10 dB SNR when using residues. The classification accuracy is high for the large object where it reaches 80% at 10 dB SNR. For the small thin wire, the accuracy is low (62%) which is normal as there is only a single CNR in the frequency band. The results when using raw data are low and do not exceed 30%.

5.4.2 Rectangular solid

This object is illuminated with various incident angles as was shown in table 4.11 in chapter 4. Unlike the previous objects, the rectangular solid (along with the cube and pyramid) is a polyhedron shape with edges. We initially divide the object into 8 sectors as follows:

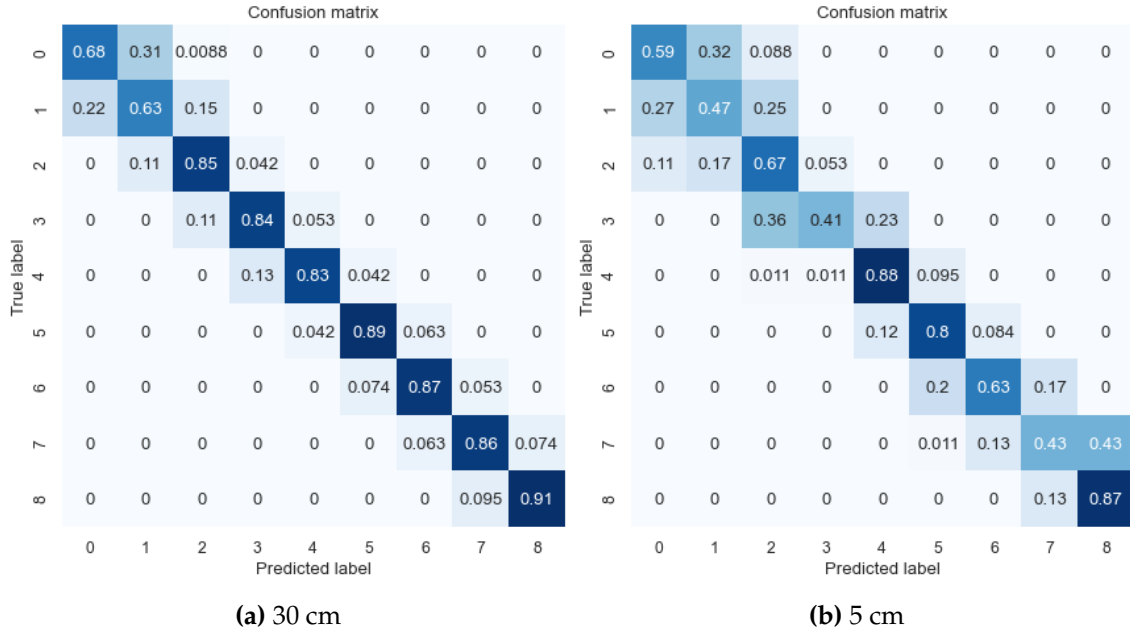


Figure 5.16 – Normalized confusion matrices of noisy data when identifying the angular sectors of the thin wire using residues for two different sizes.

- sector 0: $0 \leq \phi \leq 21$; $0 \leq \theta \leq 21$;
- sector 1: $24 \leq \phi \leq 45$; $0 \leq \theta \leq 21$;
- sector 2: $0 \leq \phi \leq 21$; $24 \leq \theta \leq 45$;
- sector 3: $24 \leq \phi \leq 45$; $24 \leq \theta \leq 45$;
- sector 4: $0 \leq \phi \leq 21$; $47 \leq \theta \leq 69$;
- sector 5: $24 \leq \phi \leq 45$; $47 \leq \theta \leq 69$;
- sector 6: $0 \leq \phi \leq 21$; $72 \leq \theta \leq 90$;
- sector 7: $24 \leq \phi \leq 45$; $72 \leq \theta \leq 90$.

Thus, we have 8 classes representing the 8 sectors. After creating the 3 datasets based on SF data and residues, we split the data into 80% for training and 20% for testing.

Test phase

The first test on the 20% remaining samples is carried. The accuracy obtained using residues as input data is of 82% while for both SF data we get 90%. We noticed that part of the miss-classified samples belong to data related to the edges of this object (sector 2 to 5) where we have $\theta = 45^\circ$ as seen in fig. 5.17a.

One solution proposed to tackle this issue is to re-create the sectors differently by having a sector that includes the edge corner area. This way, the classification error within this area might decrease. For this, we will now have 10 sectors where sectors 4 and 5 cover the edge area (fig. 5.17b):

- sector 0: $0 \leq \phi \leq 21$; $0 \leq \theta \leq 21$;
- sector 1: $24 \leq \phi \leq 45$; $0 \leq \theta \leq 21$;
- sector 2: $0 \leq \phi \leq 21$; $24 \leq \theta \leq 33$;
- sector 3: $24 \leq \phi \leq 45$; $24 \leq \theta \leq 33$;
- sector 4: $0 \leq \phi \leq 21$; $36 \leq \theta \leq 51$;
- sector 5: $24 \leq \phi \leq 45$; $36 \leq \theta \leq 51$;
- sector 6: $0 \leq \phi \leq 21$; $54 \leq \theta \leq 69$;
- sector 7: $24 \leq \phi \leq 45$; $54 \leq \theta \leq 69$;
- sector 8: $0 \leq \phi \leq 21$; $72 \leq \theta \leq 90$;
- sector 9: $24 \leq \phi \leq 45$; $72 \leq \theta \leq 90$.

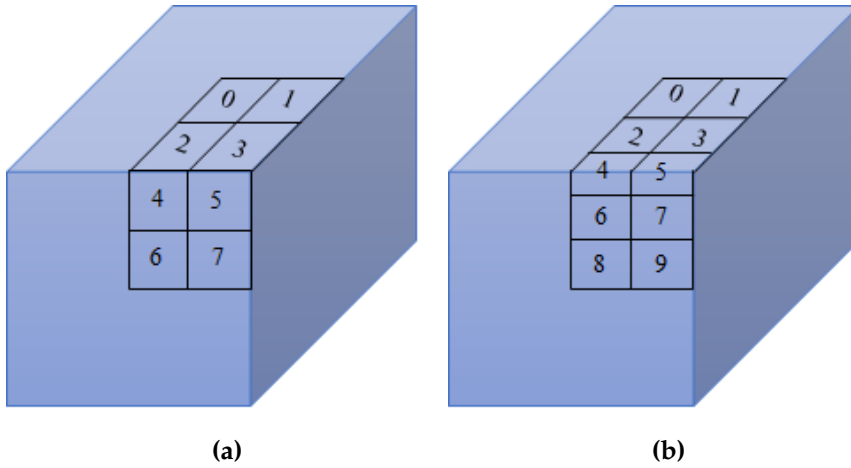


Figure 5.17 – Rectangular solid when partitioned into (a) 8 sectors and then (b) 10 sectors.

With this new dataset we redo the train and test phases. The test results using residues increases by 8% while for SF data it increases by 5% as seen in fig. 5.18. That is why, we will use this new dataset to evaluate the robustness to noise and the generalization to different data in the following sections.

In this test phase, the results of the residues accuracy are lower than those of raw data, which might be due to the discontinuities in the shape of this object, making the residues computation more difficult than for the smooth objects. Additionally, it was noticed that another important part of the miss-classified samples belongs to data having two or one resonances in the frequency band. This is also the case for the cube and the pyramid.

Noisy data

As before, we test the CNN robustness to noise at different SNRs. Fig. 5.19 shows the accuracy results when using the 3 datasets and we see that residues still show higher sensitivity to noise than raw data. Most of the miss-classified samples, when using residues, belong to data having a single or two resonances in the frequency band and to data that exist in the borders of each sector.

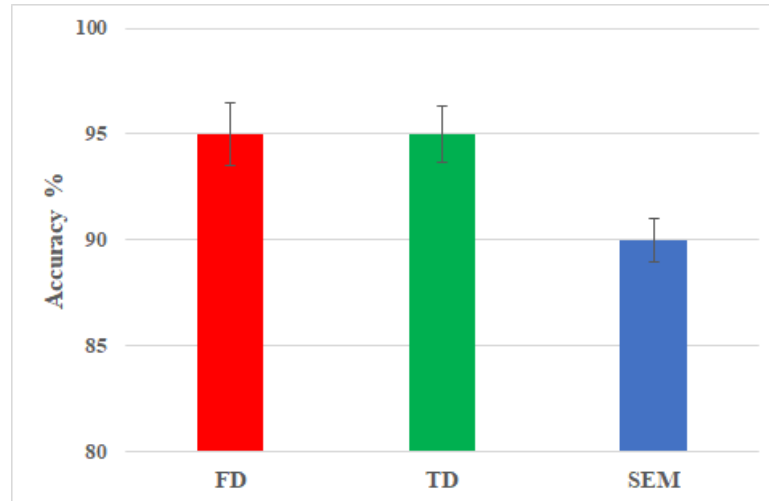


Figure 5.18 – Accuracy (%) on the 20% remaining samples of rectangular solid when using CNN.

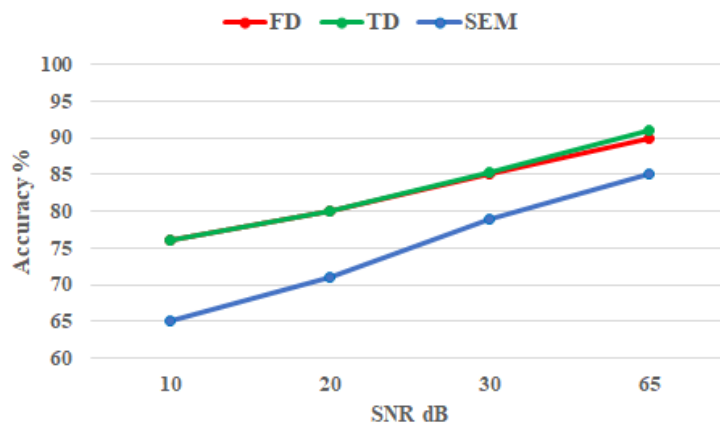


Figure 5.19 – Accuracy (%) of noisy data of the rectangular solid at different SNRs when using CNN.

Generalization ability

The large dimension chosen is 30 cm and the small dimension, where there is only a single resonance, is of 3 cm. In case of noiseless responses, the behaviour using raw data is still the same as that of the thin wire and the sphere where we cannot classify the sectors for both sizes. Conversely, by using the residues the accuracy is higher where it can reach 90% for the 30 cm length object and 65% for the small one as seen in fig.5.20.

Regarding performances in the presence of noise when using residues, the accuracy obtained at 10 dB SNR for the 30 cm length object is similar to the one obtained with the sphere as the 5 resonances are present in the frequency band where we get 62% accuracy. However, for the 3 cm length object, the accuracy

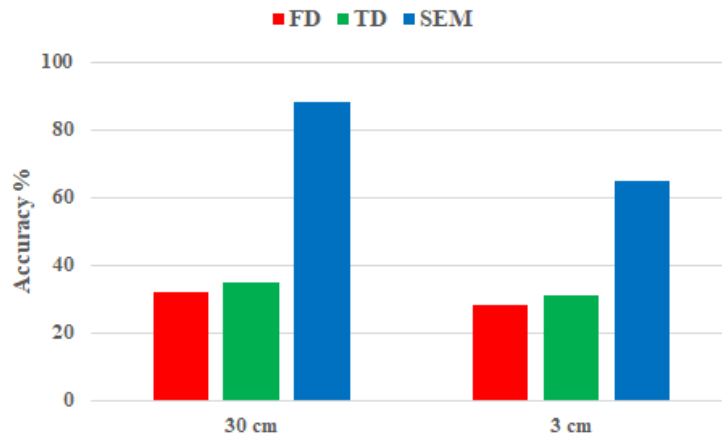


Figure 5.20 – Accuracy (%) of generalization to noiseless data of larger and smaller rectangular solids when using CNN.

decreases to 52% as it is more difficult to classify from only residues associated to the first resonances. In addition, with raw data (FD or TD data) we get very low performances that do not exceed 30%. The normalized confusion matrices showing classification of each class using residues at 10 dB SNR are present in fig. 5.21. It can be noticed that the confusion mostly arises in the sectors that are adjacent to each other.

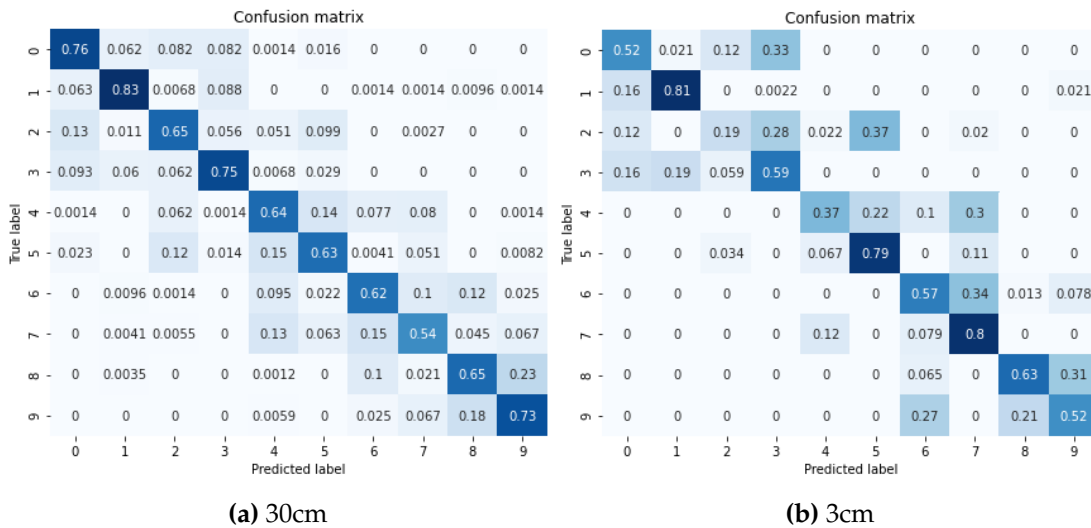


Figure 5.21 – Normalized confusion matrices of noisy data when identifying the angular sectors of the rectangular solid using residues for two different sizes not included in the datasets.

5.4.3 Discussion

The two objects evaluated in this section were chosen since they are representative of all the other simulated objects, which can be divided into two categories:

objects that do not present sharp edges (thick cylinder, ovoid, etc.) that have similar performances as the thin wire, and the remaining objects that perform more like the rectangular solid. Therefore, we can try to draw an analysis that is sufficiently representative of their behaviour. First of all, the proposed solution has significant advantages. One is the compactness of the dataset, which makes it easier to train the algorithms. Moreover, the construction of this dataset is fast since the residues are independent of the object size, thus, its construction can be made from the scattered field from a single object size. Lastly, the performance obtained in terms of generalization to other object sizes is excellent and largely surpasses the one obtained from the scattered field, even when training with many object sizes. Indeed, it can be observed that once an object size is not included in the training set, the performance of algorithms trained using raw data drops.

However, there are some weaknesses in the proposed method. One of the intrinsic weaknesses of using compressed data, especially residues, is their sensitivity to noise. Besides the estimation quality of the residues with noise sensitive SEM method, the classification algorithms are basing their decisions on only tens of parameters in the best case (5 resonances of the object), or two in the worst case (one resonance of the object). This is to be compared with the 500 frequency points of the scattered field and it explains the low accuracy of classification of small objects, especially when those objects have edges that strongly scatter the field, which is detrimental in a monostatic configuration. Nevertheless, it is worth noting that the performance remains acceptable, and that in all cases, the capacity for generalization of the proposed method has overcompensated the noise sensitivity of the residues.

5.5 Calculation of object orientation

In this section, we try to estimate the orientation of the object under test. So far, we have seen that we can detect the angular sector using the residues, by splitting the scattered field of each simulated object into multiple angular sectors. Indeed, determining the sector of the object gives an approximate estimation of the position of the receiving antenna along the azimuth and elevation planes as defined in section 5.2. Additionally, we have increased the data volume by incorporating residues amplitude of different polarizations of the incident wave. This way, we anticipate being able to determine the sector and the orientation of the object from the knowledge of both θ and ϕ field components.

In fact, finding the rotational angle α of the incident wave with respect to the object (shown in section 5.2.2) is equivalent to finding the α angle of the object with respect to the incident wave, as in fig. 5.22. α can be determined as follows:

$$\tan(\alpha) = \frac{|Res_{\theta_{meas}}|}{|Res_{\phi_{meas}}|} \quad (5.1)$$

$$\alpha = \tan^{-1}\left(\frac{|Res_{\theta_{meas}}|}{|Res_{\phi_{meas}}|}\right) \quad (5.2)$$

where $Res_{\theta_{meas}}$ and $Res_{\phi_{meas}}$ are the measured residues of both field components.

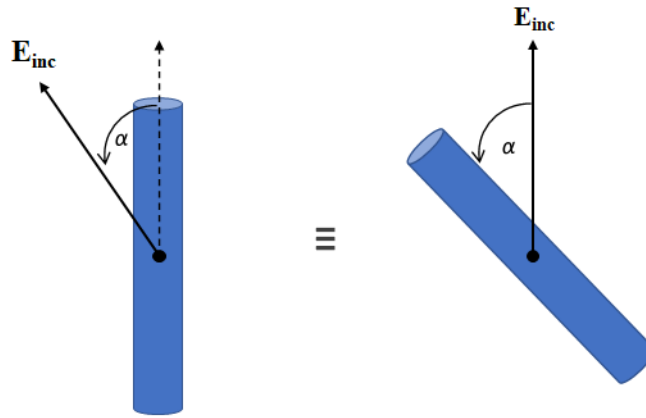


Figure 5.22 – Rotation of the incident wave (left) and the object (right) by an angle α with respect to the object and the antenna axis respectively.

To validate this assumption, we will test it using both of the previously presented objects: thin wire and rectangular solid. We simulate both objects in a mono-static configuration where the incident wave has multiple directions and is rotated by an angle varying from 5° to 85° with 20° step about y axis. Those rotations are not included in the training set. The size of both objects is fixed such that their scattered field response encompasses five resonances.

The residues are extracted for various observation angles of the scattered field of both objects. First, we need to determine the angular sector containing the receiving antenna. With the use of the pre-trained CNN, we are able to classify each sample accurately where the accuracy is 100% for all sectors of both objects. This way, we have a first idea about the location of the receiving antenna about elevation or azimuth planes.

Then, we will estimate the α angle using equation 5.2. This is due to the fact that, in case of noisy signals, those residues are the least affected by noise, unlike residues related to poles of higher order. From both field components, we compute accurately the rotation angles for both objects with 0% error. Thus, we can note that we can easily determine the incident wave orientation with respect to the object or inversely. Hence, we have developed a simple and complete scheme allowing to determine the object's orientation.

In the following section, we will apply this procedure to determine the orientation of a more complex shaped object where we will also study the effect of noise when applying equation 5.2.

5.6 Case study: cylinder with one hemispherical end

In this section, we study a more complex object formed by the merge of two PEC objects: a thick cylinder and a hemisphere. The cylinder has a length of 15 cm and the hemispherical has a radius of 7.5 cm (fig. 5.23). The object is simulated using CST time solver and it is illuminated using a EM plane wave with dual polarizations. When the rotational axis of the object is along z axis, the incident angle of the plane wave varies along the elevation plane (θ angle) from 0° to 180° with 3° step while ϕ is constant and fixed to 0° . VF is then applied on the recovered scattered fields in the back-scattering direction to compute the CNRs and their associated residues. Fig 5.24 shows the amplitude response in three different directions and their first five CNRs. Once those data are well extracted, we proceed to the construction of the dataset using the residues to determine the orientation of this object.

We divide this new object into 9 sectors as follows:

- sector 0: $0 \leq \theta \leq 18$;
- sector 1: $21 \leq \theta \leq 39$;
- sector 2: $42 \leq \theta \leq 60$;
- sector 3: $63 \leq \theta \leq 81$;
- sector 4: $84 \leq \theta \leq 102$;
- sector 5: $105 \leq \theta \leq 123$;
- sector 6: $126 \leq \theta \leq 144$;
- sector 7: $147 \leq \theta \leq 165$;
- sector 8: $168 \leq \theta \leq 180$;

As previous, the input vector is comprised of two channels representing the residues computed from E_θ and E_ϕ components of the scattered field. We increase the amount of data samples by adding multiple data from the rotation of the incident wave. This way, we will be able to determine the orientation of

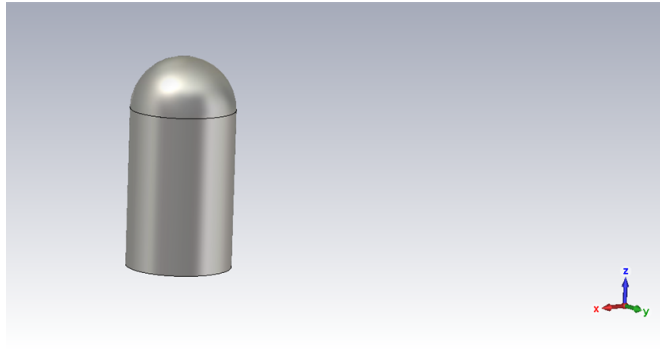


Figure 5.23 – The simulated PEC cylinder with a hemispherical end oriented along z axis

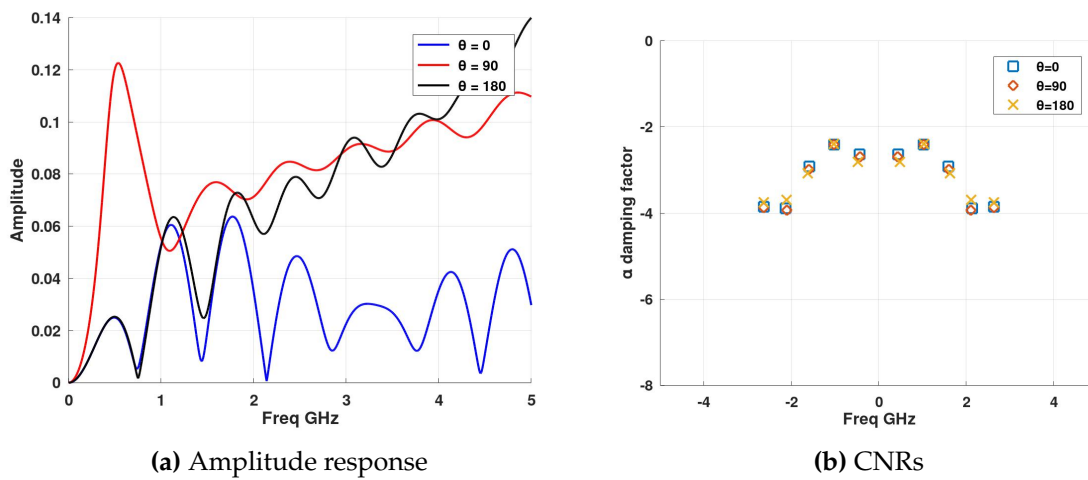


Figure 5.24 – (a) Amplitude response of E_θ in the back-scattering direction and (b) the first 5 CNRs of the cylinder with a hemispherical end

the object along elevation and azimuth planes whatever the rotation of the object or the incident wave. Additionally, sparse data are added to the dataset to take into account noisy data and when there is less than 5 resonances in the frequency band. This is done by replacing residues related to higher order poles by artificial zeros.

We use the CNN topology defined in section 5.3.2.3 and the training is done on 80% of the dataset. From fig. 5.25, we notice that the accuracy of training data does not exceed 90%. We also obtain the same level of accuracy with the test set (20% remaining samples). It is observed that an important part of the miss-classified samples belong to data having a single residue in this frequency range. The normalized confusion matrix of the test results is shown in fig. 5.26. It can be seen that the confusion mostly exists between sectors that are symmetrical to the horizontal plane. This can be due to the fact that this object is

nearly symmetrical despite its rounded end. So the amplitude of the scattered field is similar at low frequencies for supplementary observation angles and consequently, so does the residues related to the first order pole. This can be observed in fig. 5.27 for two supplementary observation angles. For these reasons, the residues associated with the first resonant frequency are somewhat alike for supplementary angles, leading to a slight confusion between two sectors associated to those angles.

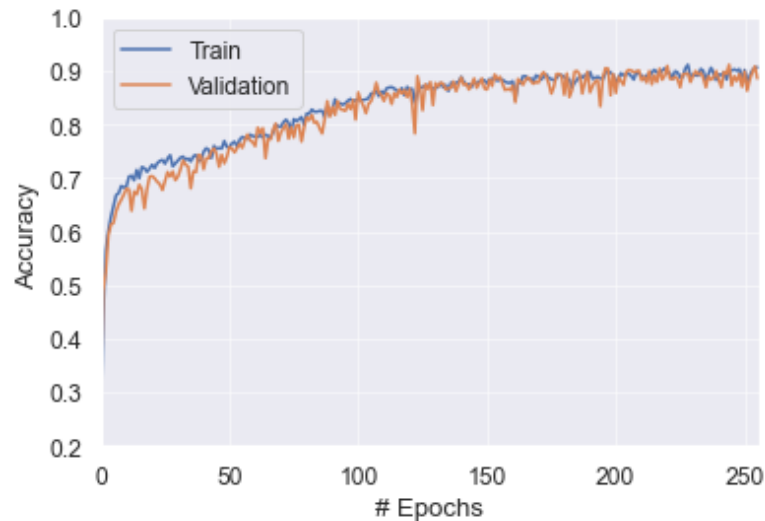


Figure 5.25 – Train and validation accuracy for CNN classifier when trained using residues of the new object

To verify if we can detect the sector accurately and determine the orientation of this object, we rotate it by 45° around y axis and illuminate it using a EM incident plane wave at multiple incident angles where θ varies from 0° to 180° with 5° step. Additionally, we test this approach with noiseless and noisy data at 30 dB and 10 dB SNR. VF is then applied on those raw data to extract the residues and then, the input vector is constructed using residues computed from E_θ and E_ϕ field components.

Using the previously trained CNN, we introduce those new data for classification. Indeed, we are able to determine the sector where each data belong to for noiseless data with 96% accuracy. When SNR = 30 dB we get 90% accuracy as their responses contain 5 residues for each field component. For 10 dB SNR, the accuracy decreases and is equal to 52% as the noise highly affects the residues related to poles of higher order. Thus, only residues associated to the fundamental pole remain almost unaffected by noise but as we have seen earlier, those residues are almost similar for sectors containing supplementary angles.

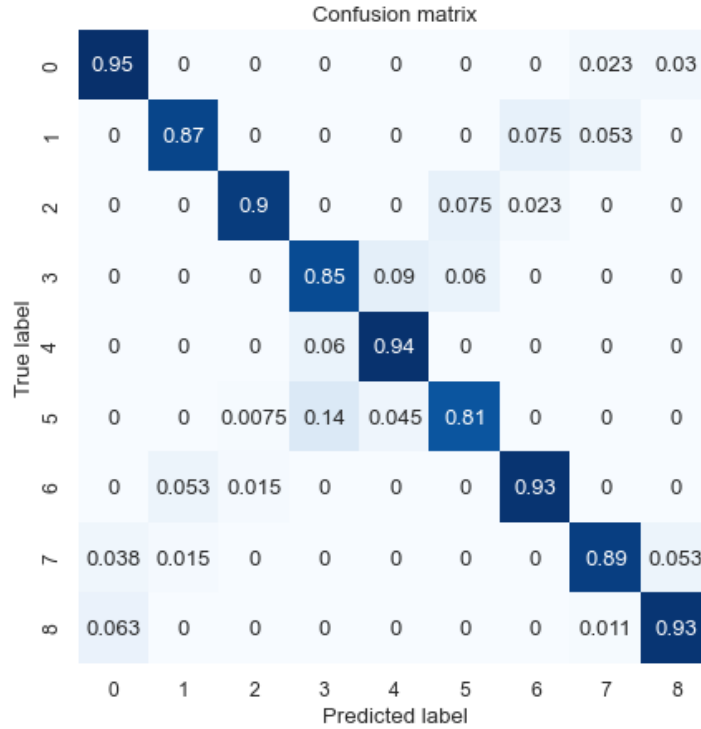


Figure 5.26 – Normalized confusion matrix of the 20% remaining samples used during the test phase

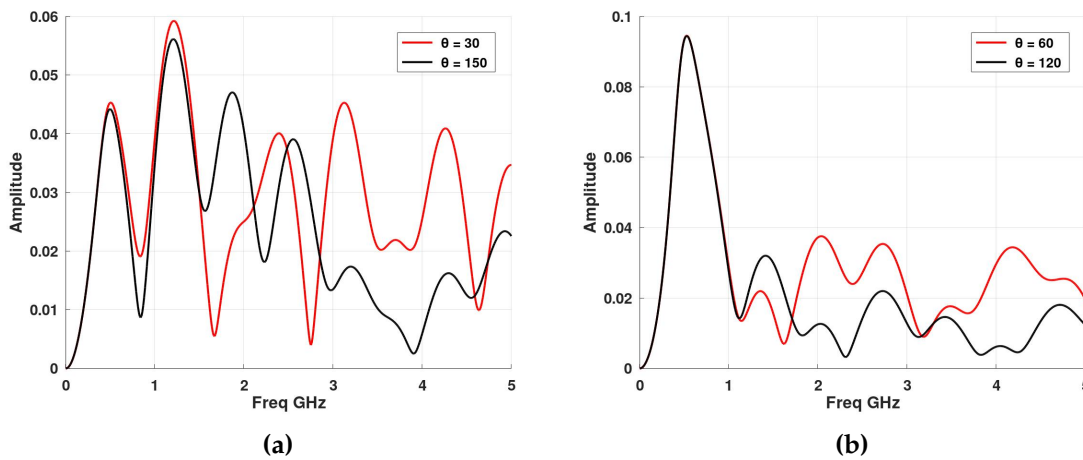


Figure 5.27 – Amplitude response at different supplementary observation angles of the cylinder with a hemispherical end

Now, we apply equation 5.2 to compute the orientation angle of this object. We test this approach with the noiseless and noisy signals at 10 and 30 dB SNRs. For the noiseless case, we get the exact value with $\alpha = 45^\circ$ for all observation angles. When testing with noisy signals, we noticed that the noise affects both field polarizations and there exists an error in the computation of α that increases when SNR value is low. Fig.5.28 shows the estimated angle α for various observation angles and at both noise levels.

Thus, we can see that with a more complex object, it is possible to estimate its orientation from the knowledge of its residues with high accuracy. However, the accurate identification of the angular sector and the orientation is more complicated when there are two resonances or less in the frequency band (i.e. for small objects) and when the data are very noisy.

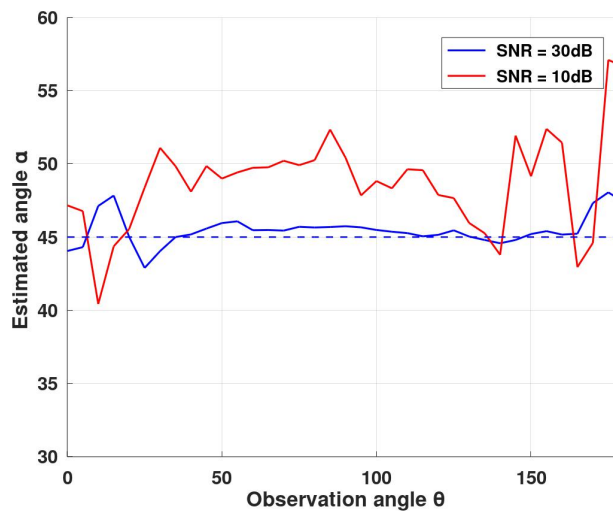


Figure 5.28 – Estimated angle α computed for each observation angle and at two SNR values.

5.7 Conclusion

The residues are parameters associated to each CNR and are dependent upon observation angle and polarization of the incident wave. Based on these two facts and after the classification of objects carried in the previous chapter, we aim at identifying the position of the angular sector and the orientation of each object using the residues in this chapter.

Firstly, this is achieved by dividing each object into multiple angular sectors where each sector contains various observation angles. Thus, we can determine the angular sector containing the incident vector of the plane wave. Indeed, this allows to get an approximate position of the receiving antenna along azimuth (ϕ variation) and/ or elevations (θ variation) planes. Datasets were created for each object separately, since each object has its own geometric symmetries. The comparative classification results indicate that, even though the residues are affected by noise and are more sensitive than raw data, the proposed approach

offers excellent classification rates whatever the size of the object. This generalization capability to different object sizes when using residues, facilitates the dataset constitution and offers interesting perspectives in radar applications.

Secondly, in order to determine the orientation of each object with respect to the antenna system (α angle), we make use of residues related to both field components to compute α . We also simulated a more complex object formed from the merge of two PEC objects to apply this approach. The results using residues proved that, using this procedure enable the accurate estimation of the orientation of an object. However, the computation of α is affected by noise and the error increases when SNR decreases. The limitation of this solution, allowing to determine the object orientation, is that it requires that the antenna system to be equipped with dual polarized transmission and reception.

Chapter 6

General Conclusion

6.1 Thesis objectives review

In this thesis, we have studied the SEM technique to achieve our objective of identification and classification of objects from their UWB response using ML and DL. This was done by compressing the UWB scattered field data to be able to classify objects from few parameters independently from the location of the observer and the illuminator. Extraction of the resonant poles is, however, very sensitive to noise and the first objective of this thesis was to study several SEM extraction methods and to determine which is the most robust to noise. The second objective was to apply the SEM formalism to classify several objects of different forms and materials using ML and DL algorithms. In this context, not only the CNRs are studied but also the residues that depend upon observation angle, and hence, they can be used to determine the orientation of each object with respect to the antenna system.

6.2 Thesis contributions summary

In chapter 2, we have reviewed the techniques used to characterize the UWB scattered far field response of objects. We found that different models exist allowing to describe the response of an object, either from their resonances or scattering centers. The scattering centers and alternative techniques presented require a spatial diversity and depend upon incident and observation angles. This is why we chose to study the resonances of an object which are independent of these aspect angles. In this context, we studied the resonances of an object that can be modeled using the SEM technique. Several algorithms used within this work were presented, which are: TLS MP in time domain, TLS Cauchy and VF in frequency domain. Lastly, we presented the quality factor

computation which can be used to characterize the resonance behaviour of an object independently of its size. Using a synthetic signal, it was seen that the number of CNRs calculated needs to be overestimated, thus, criteria allowing to filter the CNRs according to their contribution were proposed in order to keep only the physical dominant CNRs.

In chapter 3, we applied the SEM techniques, presented previously, to study the resonances of two objects: a PEC sphere which resonates weakly and a thin wire which resonates strongly. Selecting these simple and well-studied objects enabled us to use their theoretical CNRs to validate the SEM methods. In this research, the simulated targets have been treated in a free-space environment using several simulation software. In time domain, we proposed to evaluate the singular values distribution which allowed to accurately separate the late time response from the early time. Then, in frequency domain, before applying TLS Cauchy or VF, we have studied the impact of channel mis-estimation on phase compensation. We shown that VF is the most robust method to this problem. Criteria mentioned in chapter 2 to eliminate CNRs related to early time part and noise have also been validated. The performances of these three methods were compared in the presence of noise where it was shown that TLS Cauchy is the least robust whereas both VF and TLS MP have similar results and are more robust. We also studied the residues associated to the CNR of each object. We have shown that residues amplitude is correlated with the late time response of the scattered field at each natural resonant frequency.

Then, in chapter 4, we have used the CNRs for the classification of several objects with both ML and DL algorithms. We chose to apply VF method to avoid the late time/ early time separation and apply automatic poles selection as described in chapter 2. Three datasets were constructed using noiseless responses that are based on: raw data in TD and FD, and SEM data. An original SEM dataset including sparse data has been proposed and validated. This format improves the classification of small objects (i.e. having few resonances in the frequency band) and decreases the effect of noise on high order CNRs. Several classifiers were tested, and it was found that a NN classifier paired with SEM data achieves better results when testing noisy data not seen during training phase. We also confirmed that integrating the Q-factors in the input vector along with the resonant frequencies allows to distinguish objects of any size, and that incorporating the residues allows to separate objects having very similar resonant frequencies and/or Q-factors. Additionally, we verified that the datasets using SEM data can be constructed using a single object size

while maintaining same performances as the one constructed using multiple sizes, and we have shown that normalizing the resonant frequencies gives better results when dealing with noisy responses from unseen object sizes. Finally, we have seen that, after the classification process, we can determine not only the shape but also the size of the object under test from the knowledge of its first non normalized resonant frequency. All these contributions allowed us to propose an object classification method that is more robust to noise, with an excellent capacity for generalization, while considerably simplifying the constitution of the dataset.

Finally, in chapter 5, we used the residues to identify the position of the receiving antenna and its orientation in relation to the object. This was achieved by dividing each object into multiple angular sectors where each sector contains various observation angles corresponding to the locations of the receiving antenna. The classification step revealed that using residues with an NN classifier is more prone to noise compared to raw data (almost 10% less accuracy) but, on the other hand, it allowed better generalization to unseen object sizes. Then, we showed that by using dual polarization we can compute analytically the orientation of the receiving antenna related to the object or reciprocally. Thus, we presented a procedure allowing to, efficiently, describe the object orientation in free space from few parameters and regardless of their sizes. Hence, this study brought very promising results for future object classification with UWB radar signal while using simpler but reliable and faster techniques than those using raw data.

6.3 Thesis limitations and perspectives

Object recognition and classification rely on accurate extraction of the target's CNRs. Regarding the extraction of natural resonances, we have established a procedure for using the SEM methods in an optimal way. Extracting the resonances from frequency domain responses presents an advantage by removing the late time identification step. However, in case of very low SNRs, the extraction procedure becomes perturbed with noise. Thus, an additional *Newton* step can be incorporated in the VF algorithm, as shown in Lefteriu et al., 2013, ensuring better convergence of CNRs with noisy signals.

One of the principal limitations in the classification stage is the necessity to include the fundamental frequency in the input vector which implies a very low minimum frequency to illuminate the target (depending on its size) which is

not always possible. Indeed, we assume that the bandwidth of the incident pulse is wide enough such that it covers the first few dominant resonant frequencies of the object. Thus, the classification of objects will not work properly without the fundamental frequency. Furthermore, the time required to compute the poles and residues by the VF algorithm may vary, mainly in low SNRs, requiring more iterations and finer tuning of the initial parameters for a good convergence, which is to be integrated into the total computation time.

The scope of this thesis was confined to PEC and dielectric objects in free space. In this context, it can be applied mainly to the classification of flying objects (drones, airplanes, etc) because the coupling with another object or a support has not been considered in this thesis, even if promising studies on the subject have been conducted (Baum, 1993; Lee et al., 2013). Thus, this work can be extended to buried objects, as in (Baum, 1993), where Baum described a procedure allowing to extract resonances of an object buried in a lossy media. Other research activities have also addressed the detection of subsurface objects where they are situated under an interface at a particular depth (Vitebskiy and Carin, 1995; Geng, Jackson, and Carin, 1999; Wang et al., 2001). In that case, the scattered field is not solely dependent on the object alone as interactions between the object and the interface arise. The previously mentioned studies have shown that these interactions depend upon the dielectric contrast, the depth and orientation of the object.

Currently, UWB radar target recognition and classification still have some challenges. One difficulty is that when extracting the scattered wave from the object, a lot of electromagnetic and noise interference and complex background clutter are present. Further developments of target recognition schemes that use the resonance feature sets are believed to be of great potential benefit to the radar community. Therefore, it will be of interest to validate our approach (the use of resonances for object classification and for orientation detection) using real measurements. In this context, the analysis and deconvolution of the antenna response should be considered. Consequently, by embedding the extraction of these features into the radar target recognition process, the procedure for target identification and classification will become more reliable and intelligent.

Bibliography

- Adve, R. and T. Sarkar (1994). "The effect of noise in the data on the Cauchy method". In: *Microwave and Optical Technology Letters* 7, pp. 242–247.
- Agarap, Abien Fred (2018). "Deep Learning using Rectified Linear Units (ReLU)". In: *ArXiv* abs/1803.08375.
- Balanis, Constantine A (2005). *Antenna theory: analysis and design*. Wiley-Interscience.
- Baum, C. (Jan. 1976). "The singularity expansion method". In: *Transient Electromagnetic Fields* 10. DOI: [10.1007/3540075534_8](https://doi.org/10.1007/3540075534_8).
- Baum, C. E. et al. (1991). "The singularity expansion method and its application to target identification". In: *Proceedings of the IEEE* 79.10, pp. 1481–1492. ISSN: 1558-2256.
- Baum, Carl (Apr. 1993). "The Sem Representation of Scattering from Perfectly Conducting Targets in Simple Lossy Media". In: *Philips Lab., Kirtland Air Force Base, Tech.* ISBN: 9781315141084. DOI: [10.1201/9781315141084-3](https://doi.org/10.1201/9781315141084-3).
- Bebis, G. and M. Georgiopoulos (1994). "Feed-forward neural networks". In: *IEEE Potentials* 13.4, pp. 27–31. ISSN: 0278-6648. DOI: [10.1109/45.329294](https://doi.org/10.1109/45.329294). (Visited on 07/23/2018).
- Bennett, C.L. and G.F. Ross (1978). "Time-domain electromagnetics and its applications". In: *Proceedings of the IEEE* 66.3, pp. 299–318. DOI: [10.1109/PROC.1978.10902](https://doi.org/10.1109/PROC.1978.10902).
- Bhattacharyya, Nandan, Jawad Y. Siddiqui, and Y.M.M. Antar (2019). "Study On The Physical Aspect Of Singularity Expansion Method". In: *2019 URSI Asia-Pacific Radio Science Conference (AP-RASC)*, pp. 1–3. DOI: [10.23919/URSIAP-RASC.2019.8738352](https://doi.org/10.23919/URSIAP-RASC.2019.8738352).
- Bohren, C.F. and D.R. Huffman (1983). "Absorption and Scattering of Light by Small Particles". In: John Wiley.
- Boonpoonga, Akkarat et al. (May 2017). "Simple Estimation of Late-Time Response for Radar Target Identification: Late-time Estimation for Identification". In: *Radio Science* 52. DOI: [10.1002/2016RS006237](https://doi.org/10.1002/2016RS006237).
- Boser, Bernhard, Isabelle Guyon, and Vladimir Vapnik (Aug. 1992). "A Training Algorithm for Optimal Margin Classifier". In: *Proceedings of the Fifth Annual*

- ACM Workshop on Computational Learning Theory* 5. DOI: [10.1145/130385.130401](https://doi.org/10.1145/130385.130401).
- Bufler, Travis D., Ram M. Narayanan, and Traian Dogaru (2015). "SVM based target classification using RCS feature vectors". In: vol. 9461. *SPIE Proceedings*, pp. 123–132.
- Burrows, M.L. (2004). "Two-dimensional ESPRIT with tracking for radar imaging and feature extraction". In: *IEEE Transactions on Antennas and Propagation* 52.2, pp. 524–532. DOI: [10.1109/TAP.2003.822411](https://doi.org/10.1109/TAP.2003.822411).
- Carriere and Moses (1991). "High-resolution parametric modeling of canonical radar scatterers with application to radar target identification". In: *IEEE 1991 International Conference on Systems Engineering*, pp. 13–16. DOI: [10.1109/ICSYSE.1991.161070](https://doi.org/10.1109/ICSYSE.1991.161070).
- Chantasan, Nattawat, Akkarat Boonpoonga, and Santana Burintramart (2014). "Radar target identification using Cauchy method". In: *2014 International Electrical Engineering Congress (iEECON)*, pp. 1–4. DOI: [10.1109/iEECON.2014.6925932](https://doi.org/10.1109/iEECON.2014.6925932).
- Chapelle, O., P. Haffner, and V. N. Vapnik (1999). "Support vector machines for histogram-based image classification". In: *IEEE Transactions on Neural Networks* 10.5, pp. 1055–1064. DOI: [10.1109/72.788646](https://doi.org/10.1109/72.788646).
- Chaudhuri, S. (1980). "A time domain synthesis of electromagnetic backscattering by conducting ellipsoids". In: *IEEE Transactions on Antennas and Propagation* 28.4, pp. 523–530. DOI: [10.1109/TAP.1980.1142373](https://doi.org/10.1109/TAP.1980.1142373).
- Chauveau, J., N. de Beaucoudrey, and J. Saillard (2006). "Study of resonances of scattering objects: comparison with resonant circuits and characterization using Q-factor". In: *IEEE AP-S International Symposium*, pp. 3271–3274. DOI: [10.1109/APS.2006.1711310](https://doi.org/10.1109/APS.2006.1711310).
- (2007a). "Modification of resonance poles of a conducting target by a dielectric coating". In: *2007 European Radar Conference*, pp. 440–443. DOI: [10.1109/EURAD.2007.4405032](https://doi.org/10.1109/EURAD.2007.4405032).
- (2007b). "Selection of Contributing Natural Poles for the Characterization of Perfectly Conducting Targets in Resonance Region". In: *IEEE Transactions on Antennas and Propagation* 55.9, pp. 2610–2617. DOI: [10.1109/TAP.2007.904081](https://doi.org/10.1109/TAP.2007.904081).
- Chauveau, Janic, Nicole Beaucoudrey, and J. Saillard (Jan. 2007). "Characterization of perfectly conducting targets in resonance domain with their quality of resonance". In: *Progress in Electromagnetics Research-pier - PROG ELECTROMAGN RES* 74, pp. 69–84. DOI: [10.2528/PIER07041602](https://doi.org/10.2528/PIER07041602).

- Chen, Kun-Mu and D. Westmoreland (1981). "Impulse response of a conducting sphere based on singularity expansion method". In: *Proceedings of the IEEE* 69.6, pp. 747–750. DOI: [10.1109/PROC.1981.12053](https://doi.org/10.1109/PROC.1981.12053).
- Chi-Chih Chen (1998). "Electromagnetic resonances of immersed dielectric spheres". In: *IEEE Transactions on Antennas and Propagation* 46.7, pp. 1074–1083. DOI: [10.1109/8.704811](https://doi.org/10.1109/8.704811).
- Chih-Wei Hsu and Chih-Jen Lin (2002). "A comparison of methods for multi-class support vector machines". In: *IEEE Transactions on Neural Networks* 13.2, pp. 415–425. DOI: [10.1109/72.991427](https://doi.org/10.1109/72.991427).
- Chollet, François et al. (2015). *Keras: The Python Deep Learning library*. <https://keras.io>.
- Chuang, C. w. and D. L. Moffatt (1976). "Natural Resonances of Radar Targets Via Prony's Method and Target Discrimination". In: *IEEE Trans. Aerosp. Electron. Syst.* AES-12.5, pp. 583–589. ISSN: 2371-9877. DOI: [10.1109/TAES.1976.308260](https://doi.org/10.1109/TAES.1976.308260).
- Copeland, J. R. (1960). "Radar Target Classification by Polarization Properties". In: *Proceedings of the IRE* 48.7, pp. 1290–1296. DOI: [10.1109/JRPROC.1960.287653](https://doi.org/10.1109/JRPROC.1960.287653).
- Du, Lan et al. (2006). "A two-distribution compounded statistical model for Radar HRRP target recognition". In: *IEEE Transactions on Signal Processing* 54.6, pp. 2226–2238. DOI: [10.1109/TSP.2006.873534](https://doi.org/10.1109/TSP.2006.873534).
- Garzon-Guerrero, J. A., D. P. Ruiz, and M. C. Carrion (2013). "Classification of Geometrical Targets Using Natural Resonances and Principal Components Analysis". In: *IEEE Transactions on Antennas and Propagation* 61.9, pp. 4881–4884. DOI: [10.1109/TAP.2013.2266091](https://doi.org/10.1109/TAP.2013.2266091).
- Geng, N., D.R. Jackson, and L. Carin (1999). "On the resonances of a dielectric BOR buried in a dispersive layered medium". In: *IEEE Transactions on Antennas and Propagation* 47.8, pp. 1305–1313. DOI: [10.1109/8.791948](https://doi.org/10.1109/8.791948).
- Grant, L. L. and M. L. Crow (2011). "Comparison of Matrix Pencil and Prony methods for power system modal analysis of noisy signals". In: *2011 North American Power Symposium*, pp. 1–7. DOI: [10.1109/NAPS.2011.6024892](https://doi.org/10.1109/NAPS.2011.6024892).
- Gustavsen, B. (2006). "Improving the pole relocating properties of vector fitting". In: *IEEE Trans. Power Del.* 21.3, pp. 1587–1592. ISSN: 1937-4208. DOI: [10.1109/TPWRD.2005.860281](https://doi.org/10.1109/TPWRD.2005.860281).
- Gustavsen, B. and A. Semlyen (1999). "Rational approximation of frequency domain responses by vector fitting". In: *IEEE Trans. Power Del.* 14.3, pp. 1052–1061. ISSN: 1937-4208. DOI: [10.1109/61.772353](https://doi.org/10.1109/61.772353).

- Hadhrami, E. A. et al. (2018). "Classification of ground moving radar targets using convolutional neural network". In: *2018 22nd International Microwave and Radar Conference (MIKON)*, pp. 127–130. DOI: [10.23919/MIKON.2018.8405154](https://doi.org/10.23919/MIKON.2018.8405154).
- Harrington, R.F. (2001). *Time-Harmonic Electromagnetic Fields*. IEEE Press Series on Electromagnetic Wave Theory. Wiley. ISBN: 9780471208068.
- Heyman, E. and L. Felsen (1983). "Creeping waves and resonances in transient scattering by smooth convex objects". In: *IEEE Transactions on Antennas and Propagation* 31.3, pp. 426–437. DOI: [10.1109/TAP.1983.1143087](https://doi.org/10.1109/TAP.1983.1143087).
- Hua, Y. and T. K. Sarkar (1991). "On SVD for estimating generalized eigenvalues of singular matrix pencil in noise". In: *IEEE Trans. Signal Process.* 39.4, pp. 892–900. ISSN: 1941-0476. DOI: [10.1109/78.80911](https://doi.org/10.1109/78.80911).
- Hua, Y. and T.K. Sarkar (1989). "Generalized pencil-of-function method for extracting poles of an EM system from its transient response". In: *IEEE Transactions on Antennas and Propagation* 37.2, pp. 229–234. DOI: [10.1109/8.18710](https://doi.org/10.1109/8.18710).
- Hua, Y. and T.K Sarkar (1990). "Matrix pencil method for estimating parameters of exponentially damped/undamped sinusoids in noise". In: *IEEE Trans. Acous. Speech Signal Process.* 38.5, pp. 814–824. ISSN: 0096-3518. DOI: [10.1109/29.56027](https://doi.org/10.1109/29.56027).
- Jang, S. et al. (2005). "Quantitative comparison between Matrix Pencil method and state-space-based methods for radar object identification". In: *URSI Radio Science Bulletin* 2005.313, pp. 27–38. DOI: [10.23919/URSIRSB.2005.7909523](https://doi.org/10.23919/URSIRSB.2005.7909523).
- Joon-Ho Lee, In-Sik Choi, and Hyo-Tae Kim (2003). "Natural frequency-based neural network approach to radar target recognition". In: *IEEE Transactions on Signal Processing* 51.12, pp. 3191–3197. DOI: [10.1109/TSP.2003.818908](https://doi.org/10.1109/TSP.2003.818908).
- Jouny, I., F.D. Garber, and S.C. Ahalt (1993). "Classification of radar targets using synthetic neural networks". In: *IEEE Transactions on Aerospace and Electronic Systems* 29.2, pp. 336–344. DOI: [10.1109/7.210072](https://doi.org/10.1109/7.210072).
- Kennaugh, Edward Morton (1952). "Polarization properties of radar reflections". In.
- Kennaugh, E.M. and D.L. Moffatt (1965). "Transient and impulse response approximations". In: *Proceedings of the IEEE* 53.8, pp. 893–901. DOI: [10.1109/PROC.1965.4068](https://doi.org/10.1109/PROC.1965.4068).
- Khodjet-Kesba, Mahmoud (Nov. 2014). "Automatic target classification based on radar backscattered ultra wide band signals". Theses. Université Blaise Pascal - Clermont-Ferrand II. URL: <https://tel.archives-ouvertes.fr/tel-01312183>.

- Kim, K.-T and H.-T Kim (July 1999). "One-dimensional scattering centre extraction for efficient radar target classification". In: *Radar, Sonar and Navigation, IEE Proceedings - 146*, pp. 147–158. DOI: [10.1049/ip-rsn:19990321](https://doi.org/10.1049/ip-rsn:19990321).
- Kingma, Diederik and Jimmy Ba (Dec. 2014). "Adam: A Method for Stochastic Optimization". In: *International Conference on Learning Representations*.
- Kottapalli, K. et al. (1991). "Accurate computation of wide-band response of electromagnetic systems utilizing narrow-band information". In: *IEEE Transactions on Microwave Theory and Techniques* 39.4, pp. 682–687. DOI: [10.1109/22.76432](https://doi.org/10.1109/22.76432).
- Kristensson, G. (1984). "Natural frequencies of circular disks". In: *IEEE Transactions on Antennas and Propagation* 32.5, pp. 442–448. DOI: [10.1109/TAP.1984.1143356](https://doi.org/10.1109/TAP.1984.1143356).
- Kumaresan, R. (1990). "Identification of rational transfer function from frequency response sample". In: *IEEE Trans. Aerosp. Electron. Syst.* 26.6, pp. 925–934. ISSN: 2371-9877. DOI: [10.1109/7.62245](https://doi.org/10.1109/7.62245).
- Lecun, Y. et al. (1998a). "Gradient-based learning applied to document recognition". In: *Proceedings of the IEEE* 86.11, pp. 2278–2324.
- (1998b). "Gradient-based learning applied to document recognition". In: *Proceedings of the IEEE* 86.11, pp. 2278–2324. DOI: [10.1109/5.726791](https://doi.org/10.1109/5.726791).
- LeCun, Yann, Y. Bengio, and Geoffrey Hinton (May 2015). "Deep Learning". In: *Nature* 521, pp. 436–44. DOI: [10.1038/nature14539](https://doi.org/10.1038/nature14539).
- Lee, W. et al. (2012). "Computation of the Natural Poles of an Object in the Frequency Domain Using the Cauchy Method". In: *IEEE Antennas and Wireless Propagation Letters* 11, pp. 1137–1140. ISSN: 1536-1225. DOI: [10.1109/LAWP.2012.2219846](https://doi.org/10.1109/LAWP.2012.2219846).
- Lee, Woojin et al. (2013). "Identification of an object located on the ground using its natural poles using both FD and TD data". In: *2013 IEEE Antennas and Propagation Society International Symposium (APSURSI)*, pp. 23–24. DOI: [10.1109/APS.2013.6710672](https://doi.org/10.1109/APS.2013.6710672).
- Leekul, P. and M. Krairiksh (2018). "Measured natural frequencies of mangosteens". In: *2018 IEEE Asia-Pacific Conference on Antennas and Propagation (APCAP)*, pp. 334–335. DOI: [10.1109/APCAP.2018.8538096](https://doi.org/10.1109/APCAP.2018.8538096).
- Leekul, P., M. Krairiksh, and T. K. Sarkar (July 2014). "Application of the natural frequency estimation technique for mangosteen classification". In: *Asia-Pacific Conference on Antennas and Propagation*, pp. 928–930. DOI: [10.1109/APCAP.2014.6992653](https://doi.org/10.1109/APCAP.2014.6992653).

- Lefteriu, S. et al. (2013). "On the Convergence of the Vector-Fitting Algorithm". In: *IEEE Trans. Microw. Theory Techn* 61.4, pp. 1435–1443. ISSN: 1557-9670. DOI: [10.1109/TMTT.2013.2246526](https://doi.org/10.1109/TMTT.2013.2246526).
- Li, L. and C. Liang (2004). "Analysis of resonance and quality factor of antenna and scattering systems using complex frequency method combined with model-based parameter estimation". In: *Progress in Electromagnetics Research-pier* 46, pp. 165–188.
- Liu, Hongwei et al. (Mar. 2012). "Robust radar automatic target recognition algorithm based on HRRP signature". In: *Frontiers of Electrical and Electronic Engineering* 7. DOI: [10.1007/s11460-012-0191-1](https://doi.org/10.1007/s11460-012-0191-1).
- Loh, Wei-Yin (Jan. 2011). "Classification and Regression Trees". In: *Wiley Interdisciplinary Reviews: Data Mining and Knowledge Discovery* 1, pp. 14–23. DOI: [10.1002/widm.8](https://doi.org/10.1002/widm.8).
- Long, Yunliang (1994). "Determination of the natural frequencies for conducting rectangular boxes". In: *IEEE Transactions on Antennas and Propagation* 42.7, pp. 1016–1021. DOI: [10.1109/8.299607](https://doi.org/10.1109/8.299607).
- Mautz, J. and R. Harrington (1978). "Reviews and abstracts - Electromagnetic scattering from a homogeneous body of revolution". In: *IEEE Antennas and Propagation Society Newsletter* 20.2, pp. 4–4. DOI: [10.1109/MAP.1978.27344](https://doi.org/10.1109/MAP.1978.27344).
- Mei, Zicong et al. (Mar. 2014). "The natural resonant singularity expansion method (SEM) poles for a dielectric sphere in various environments". In: *Microwave and Optical Technology Letters* 56. DOI: [10.1002/mop.28169](https://doi.org/10.1002/mop.28169).
- Mie, G. (1908). "Beiträge zur Optik trüber Medien, speziell kolloidaler Metallösungen". In: *Annalen der Physik* 330, pp. 377–445.
- Moffatt, D. and R. Mains (1975). "Detection and discrimination of radar targets". In: *IEEE Transactions on Antennas and Propagation* 23.3, pp. 358–367. DOI: [10.1109/TAP.1975.1141078](https://doi.org/10.1109/TAP.1975.1141078).
- Narayan, Sridhar (1997). "The generalized sigmoid activation function: Competitive supervised learning". In: *Information Sciences* 99.1, pp. 69–82. ISSN: 0020-0255. DOI: [https://doi.org/10.1016/S0020-0255\(96\)00200-9](https://doi.org/10.1016/S0020-0255(96)00200-9). URL: <http://www.sciencedirect.com/science/article/pii/S0020025596002009>.
- Narayanan, Uma et al. (2017). "A survey on various supervised classification algorithms". In: *2017 International Conference on Energy, Communication, Data Analytics and Soft Computing (ICECDS)*, pp. 2118–2124. DOI: [10.1109/ICECDS.2017.8389824](https://doi.org/10.1109/ICECDS.2017.8389824).

- Ning, Wu, Wugun Chen, and Xinggan Zhang (2003). "Automatic target recognition of ISAR object images based on neural network". In: *International Conference on Neural Networks and Signal Processing, 2003. Proceedings of the 2003*. Vol. 1, 373–376 Vol.1. DOI: [10.1109/ICNNSP.2003.1279287](https://doi.org/10.1109/ICNNSP.2003.1279287).
- Pedregosa, Fabian et al. (Jan. 2012). "Scikit-learn: Machine Learning in Python". In: *Journal of Machine Learning Research* 12.
- Penghui WANG Lei SHI, Lan DU Hongwei LIU Lei XU Zheng BAO (2011). "Radar HRRP statistical recognition with temporal factor analysis by automatic Bayesian Ying-Yang harmony learning". In: *Frontiers of Electrical and Electronic Engineering* 6.
- Raileanu, Laura and Kilian Stoffel (May 2004). "Theoretical Comparison between the Gini Index and Information Gain Criteria". In: *Annals of Mathematics and Artificial Intelligence* 41, pp. 77–93. DOI: [10.1023/B:AMAI.0000018580.96245.c6](https://doi.org/10.1023/B:AMAI.0000018580.96245.c6).
- Rao, B.D. (1990). "Relationship between matrix pencil and state space based harmonic retrieval methods". In: *IEEE Transactions on Acoustics, Speech, and Signal Processing* 38.1, pp. 177–179. DOI: [10.1109/29.45568](https://doi.org/10.1109/29.45568).
- Rezaiesarlak, R. and M. Manteghi (May 2013). "Short-Time Matrix Pencil Method for Chipless RFID Detection Applications". In: *IEEE Trans. Antennas Propag* 61.5, pp. 2801–2806. ISSN: 1558-2221. DOI: [10.1109/TAP.2013.2238497](https://doi.org/10.1109/TAP.2013.2238497).
- Rioul, O. and M. Vetterli (1991). "Wavelets and signal processing". In: *IEEE Signal Processing Magazine* 8.4, pp. 14–38. DOI: [10.1109/79.91217](https://doi.org/10.1109/79.91217).
- Rothwell, E.J. et al. (1994). "A radar target discrimination scheme using the discrete wavelet transform for reduced data storage". In: *IEEE Transactions on Antennas and Propagation* 42.7, pp. 1033–1037. DOI: [10.1109/8.299610](https://doi.org/10.1109/8.299610).
- Roussafi, Abdellah (2016). "Modélisation compacte du rayonnement d'antennes ULB en champ proche/champ lointain : mise en application en présence d'interface". Thèse de doctorat dirigée par Dauvignac, Jean-Yves et Fortino, Nicolas. PhD thesis. URL: <http://www.theses.fr/2016AZUR4137>.
- Roy, R. and T. Kailath (1989). "ESPRIT-estimation of signal parameters via rotational invariance techniques". In: *IEEE Transactions on Acoustics, Speech, and Signal Processing* 37.7, pp. 984–995. DOI: [10.1109/29.32276](https://doi.org/10.1109/29.32276).
- Safavian, S. and D. Landgrebe (1991). "A survey of decision tree classifier methodology". In: *IEEE Trans. Syst. Man Cybern.* 21, pp. 660–674.
- Sarrazin, François et al. (2011). "Comparison between Matrix Pencil and Prony methods applied on noisy antenna responses". In: *2011 Loughborough Antennas Propagation Conference*, pp. 1–4. DOI: [10.1109/LAPC.2011.6113978](https://doi.org/10.1109/LAPC.2011.6113978).

- Sarrazin, François et al. (2014). "Accuracy of Singularity Expansion Method in Time and Frequency Domains to Characterize Antennas in Presence of Noise". In: *IEEE Trans. Antennas Propag* 62, pp. 1261–1269. ISSN: 1558-2221. DOI: [10.1109/TAP.2013.2294216](https://doi.org/10.1109/TAP.2013.2294216).
- Sathyamurthy, Anuradha, G. Varalakshmi, and Jyothi Balakrishnan (2019). "Discrimination of Complex Radar Targets Using the Dominant Poles Determined in the Time and Frequency Domains". In: *IETE Journal of Research*.
- Schwegmann, C. P. et al. (2017). "Subsidence feature discrimination using deep convolutional neural networks in synthetic aperture radar imagery". In: *2017 IEEE IGARSS*, pp. 4626–4629. DOI: [10.1109/IGARSS.2017.8128031](https://doi.org/10.1109/IGARSS.2017.8128031).
- Schölkopf, Bernhard and Alexander Smola (MIT press, 2001). *Learning with Kernels: Support Vector Machines, Regularization, Optimization, and Beyond*. ISBN: 9780262256933. DOI: [10.7551/mitpress/4175.001.0001](https://doi.org/10.7551/mitpress/4175.001.0001).
- Stahl, Herbert (1998). "Spurious poles in Padé approximation". In: *Journal of Computational and Applied Mathematics* 99.1. Proceeding of the VIIIth Symposium on Orthogonal Polynomials and Their Application, pp. 511–527. DOI: [https://doi.org/10.1016/S0377-0427\(98\)00180-0](https://doi.org/10.1016/S0377-0427(98)00180-0).
- Sze, V. et al. (2017). "Efficient Processing of Deep Neural Networks: A Tutorial and Survey". In: *Proceedings of the IEEE* 105.12, pp. 2295–2329. DOI: [10.1109/JPROC.2017.2761740](https://doi.org/10.1109/JPROC.2017.2761740).
- Tantisoparak, T. et al. (2016). "Nondestructive Determination of the Maturity of the Durian Fruit in the Frequency Domain Using the Change in the Natural Frequency". In: *IEEE Transactions on Antennas and Propagation* 64.5, pp. 1779–1787. DOI: [10.1109/TAP.2016.2533660](https://doi.org/10.1109/TAP.2016.2533660).
- Taylor, J.D. (1995). *Introduction to Ultra-Wideband Radar Systems*. CRC Press. ISBN: 9781003068112.
- Tesche, F. (1973). "On the analysis of scattering and antenna problems using the singularity expansion technique". In: *IEEE Trans. Antennas Propag* 21.1, pp. 53–62.
- Vitebskiy, S. and L. Carin (1995). "Moment-method modeling of short-pulse scattering from and the resonances of a wire buried inside a lossy, dispersive half-space". In: *IEEE Transactions on Antennas and Propagation* 43.11, pp. 1303–1312. DOI: [10.1109/8.475103](https://doi.org/10.1109/8.475103).
- Wang, Yong et al. (2001). "Complex natural resonances of conducting planar objects buried in a dielectric half-space". In: *IEEE Transactions on Geoscience and Remote Sensing* 39.6, pp. 1183–1189. DOI: [10.1109/36.927439](https://doi.org/10.1109/36.927439).

- Wanielik, G. (1995). "Signatures and signal processing for narrow- and broad-band polarimetric radars". In: *Journal of Electromagnetic Waves and Applications* 9.3, pp. 291–308. DOI: [10.1163/156939395X00497](https://doi.org/10.1163/156939395X00497). eprint: <https://www.tandfonline.com/doi/pdf/10.1163/156939395X00497>. URL: <https://www.tandfonline.com/doi/abs/10.1163/156939395X00497>.
- Yang, J. and T. K. Sarkar (2016). "Accurate Interpolation of Amplitude-Only Frequency Domain Response Based on an Adaptive Cauchy Method". In: *IEEE Trans. Antennas Propag* 64.3, pp. 1005–1013. ISSN: 0018-926X. DOI: [10.1109/TAP.2016.2518651](https://doi.org/10.1109/TAP.2016.2518651).
- Yinan Yang et al. (2006). "Target Classification and Pattern Recognition Using Micro-Doppler Radar Signatures". In: *Seventh ACIS International Conference on Software Engineering, Artificial Intelligence, Networking, and Parallel/Distributed Computing (SNPD'06)*, pp. 213–217. DOI: [10.1109/SNPD-SAWN.2006.68](https://doi.org/10.1109/SNPD-SAWN.2006.68).
- Zaky, Y., N. Fortino, and J-Y. Dauvignac (2021). "Classification by Deep Learning and SEM". In: *Webinaire Groupement De Recherche (GDR) Ondes*.
- Zaky, Y. Y. et al. (2020). "Comparison of SEM methods for poles estimation from scattered field by canonical objects". In: *IEEE Radar Conference (RadarConf20)*, pp. 1–6. DOI: [10.1109/RadarConf2043947.2020.9266410](https://doi.org/10.1109/RadarConf2043947.2020.9266410).
- Zaky, Yasmina (2020). In: *Ma thèse en 180 secondes*. URL: <https://youtu.be/N6Wy7rNYIzs>.
- Zaky, Yasmina et al. (2021a). *Classification d'objets à partir de leurs résonances en utilisant les réseaux neuronaux*. Neuvième Conférence Plénière du GDR ONDES. Poster. URL: <https://hal.archives-ouvertes.fr/hal-03485167>.
- Zaky, Yasmina et al. (2021b). "Objects classification based on UWB scattered field and SEM data using machine learning algorithms". In: *2021 18th European Radar Conference (EuRAD)*.
- Zaky, Yasmina et al. (June 2021c). *Submitted: Generalization Ability of Deep Learning Algorithms Trained using SEM Data for Objects Classification*. URL: https://www.techrxiv.org/articles/preprint/Generalization_Ability_of_Deep_Learning_Algorithms_Trained_using_SEM_Data_for_Objects_Classification/14706390/1.
- Zaky, Yasmina et al. (2022). "Classification d'objets à partir de leurs signatures électromagnétiques en utilisant les réseaux neuronaux convolutifs". In: *Journées Nationales Microondes (JNM2022)*.

Appendix A

Extraction of poles from the E_ϕ component

In this section, we show that the extraction of poles can be done using the E_ϕ component of the scattered field for the PEC sphere. Similar to the treatments realized on the E_θ component, we need to compensate the phase and identify the beginning of late time before applying the SEM techniques. In fig. [A.1](#) we can see that the impulse and frequency responses, in the back-scattering direction ($\phi = 90^\circ$ plane), are the same as the ones seen for E_θ component in chapter [3](#). Thus, the same late time value is applied to eliminate the early time and the phase is compensated exactly as before.

From those responses we extract the resonances that are the same as the analytic CNRs as in fig. [A.2](#). Thus, we can see that the CNRs can be estimated accurately by applying the SEM techniques on both the E_θ and E_ϕ components, and we can conclude that the CNRs are, indeed, independent from the polarization of the wave. Following, we compare the residues associated to each CNR (extracted using VF) with the scattered field and late time responses. From fig. [A.3](#) to [A.5](#), we see that the residues' amplitude are almost correlated with the late time response. As expected, no correlation exists with the scattered field response as it contains both early and late time responses.

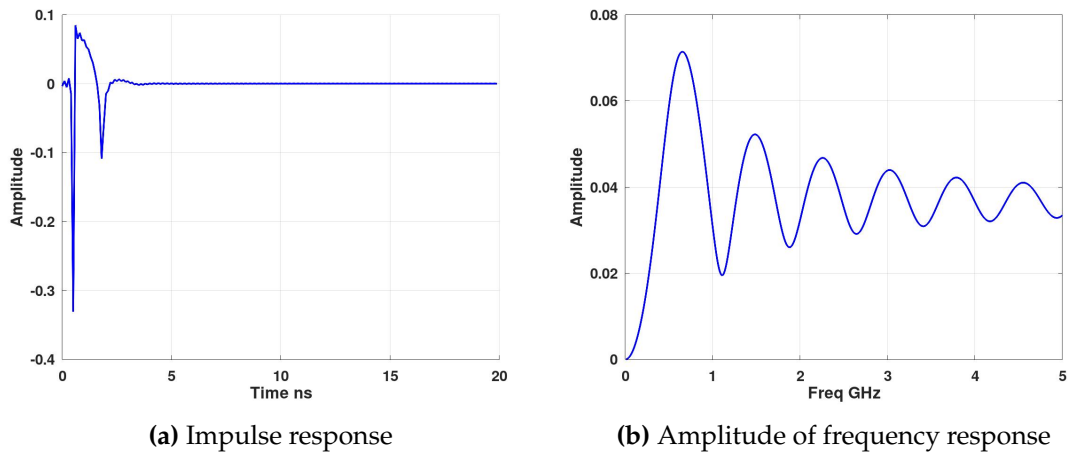


Figure A.1 – Impulse response and amplitude response of E_ϕ of the PEC sphere in the back-scattering direction

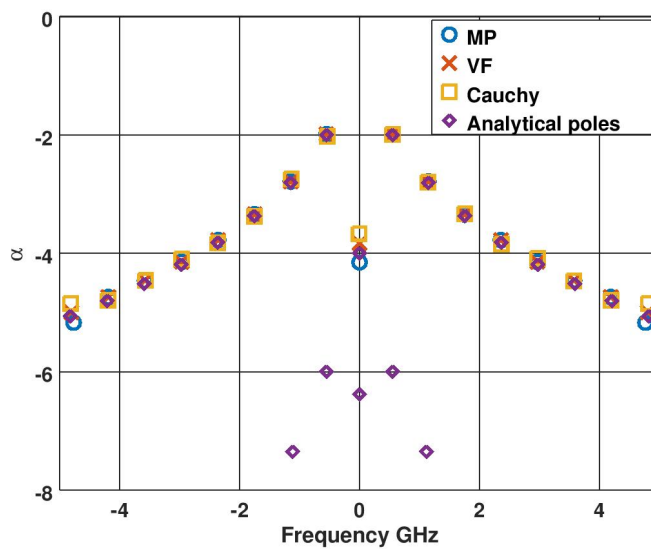
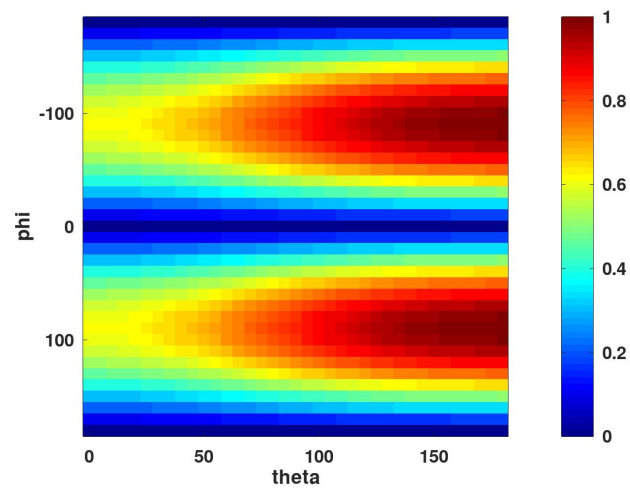
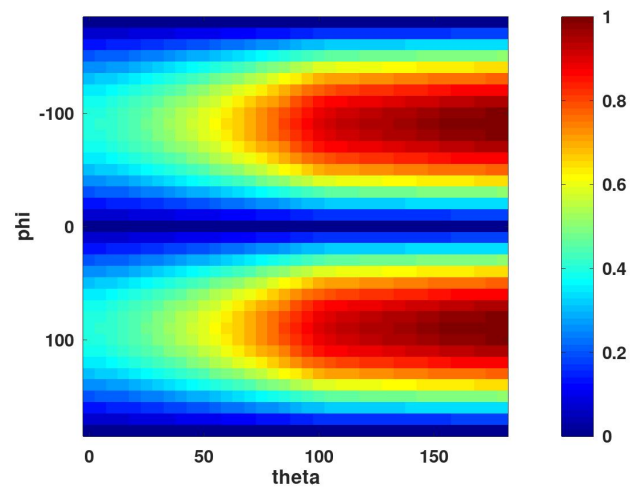


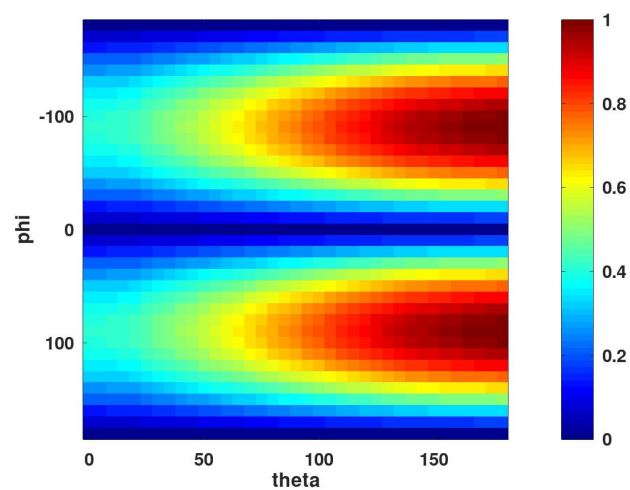
Figure A.2 – Estimated Physical poles of 0.15 m diameter sphere compared with the theoretical ones



(a) Scattered field

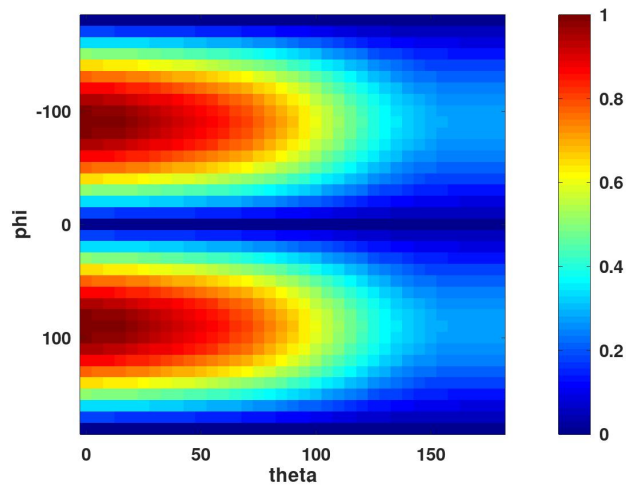


(b) Late Time

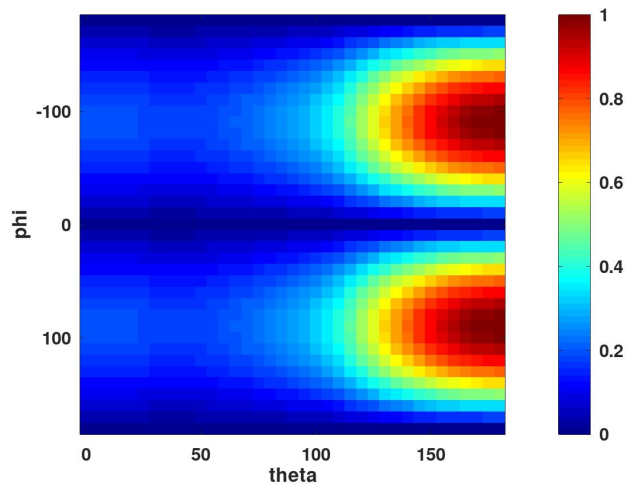


(c) Residues

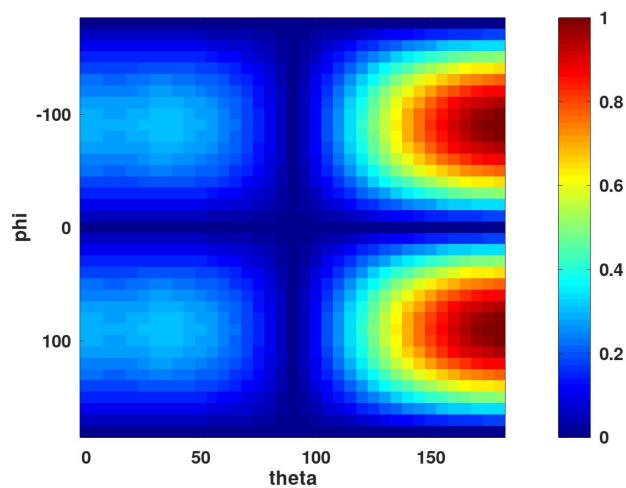
Figure A.3 – Normalized amplitude of scattered field, scattered field from late time response only and residues related to the first resonant frequency ($f_1 = 0.55 \text{ GHz}$)



(a) Scattered field

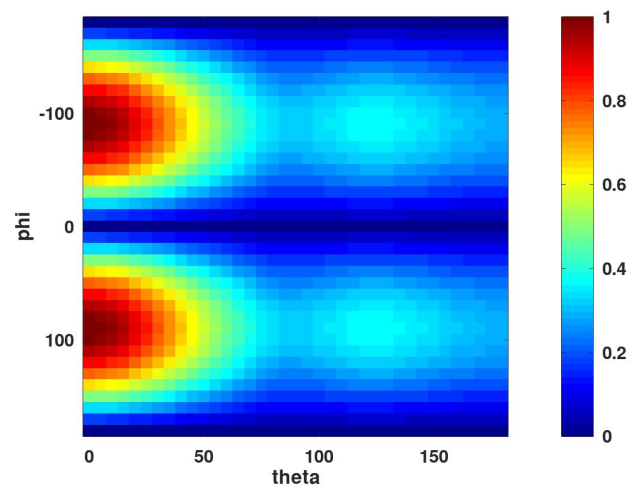


(b) Late Time

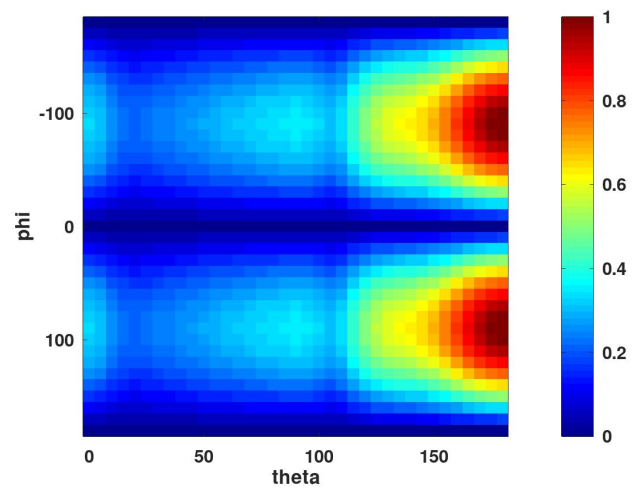


(c) Residues

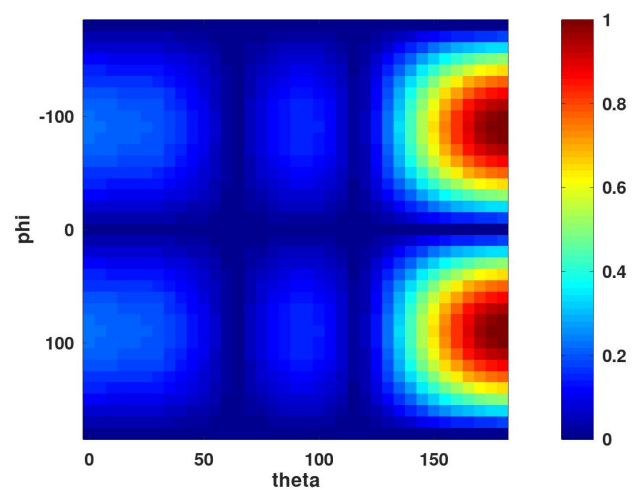
Figure A.4 – Normalized amplitude of scattered field, scattered field from late time response only and residues related to the second resonant frequency ($f_2 = 1.15 \text{ GHz}$).



(a) Scattered field



(b) Late Time



(c) Residues

Figure A.5 – Normalized amplitude of scattered field, scattered field from late time response only and residues related to the third resonant frequency ($f_3 = 1.75$ GHz).

Appendix B

Comparisons between residues extracted by TLS MP and VF

We compare the normalized amplitude of the residues extracted using VF and MP on the E_θ component of the scattered field from a 15 cm diameter PEC sphere. Indeed, the residues are associated to the physical poles characterizing the late time response, hence they are expected to be the same when extracted either in time domain or in frequency domain. In fig. B.1 to B.4, we show the normalized residues of the PEC sphere for the first 4 resonant frequencies. From this, we see that using both techniques leads to the same residues. We also compute the mean relative error between both residues and find that it is less than 0.1% for all directions and for all resonant frequencies.

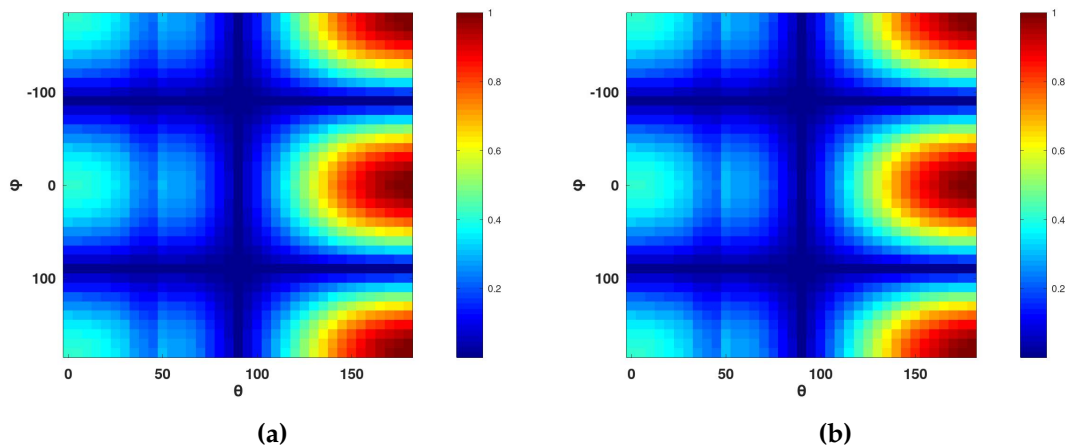


Figure B.1 – Residues' amplitude related to the first resonant frequency ($f_1 = 0.55$ GHz) extracted using (a) MP and (b) VF

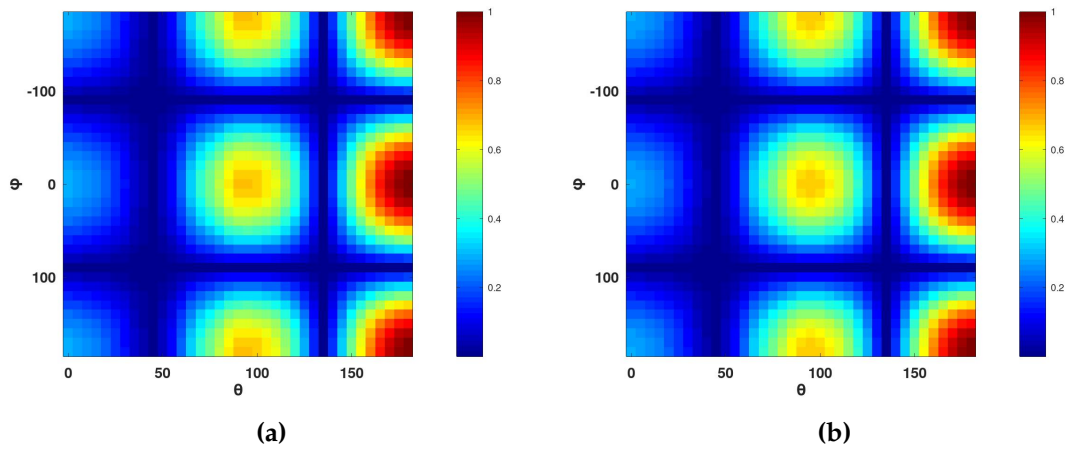


Figure B.2 – Residues' amplitude related to the second resonant frequency ($f_2 = 1.15 \text{ GHz}$) extracted using (a) MP and (b) VF

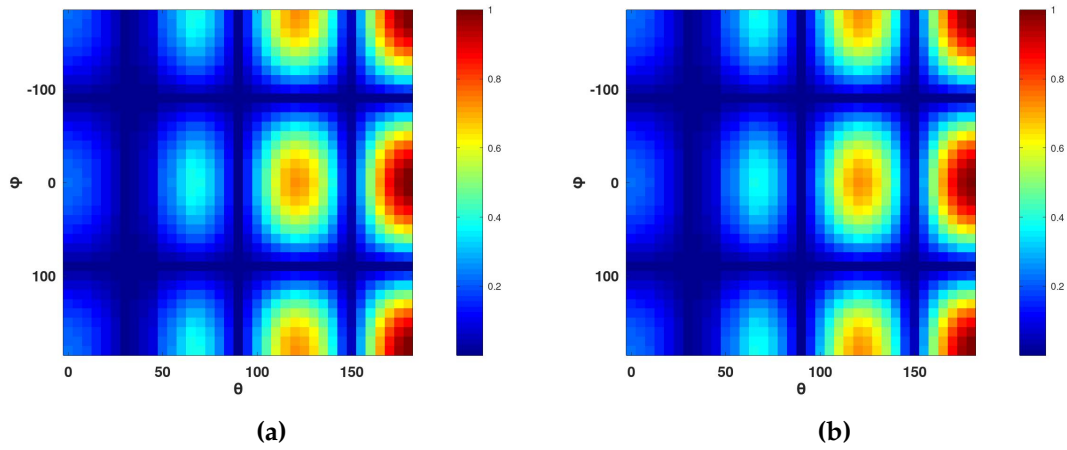


Figure B.3 – Residues' amplitude related to the third resonant frequency ($f_3 = 1.75 \text{ GHz}$) extracted using (a) MP and (b) VF

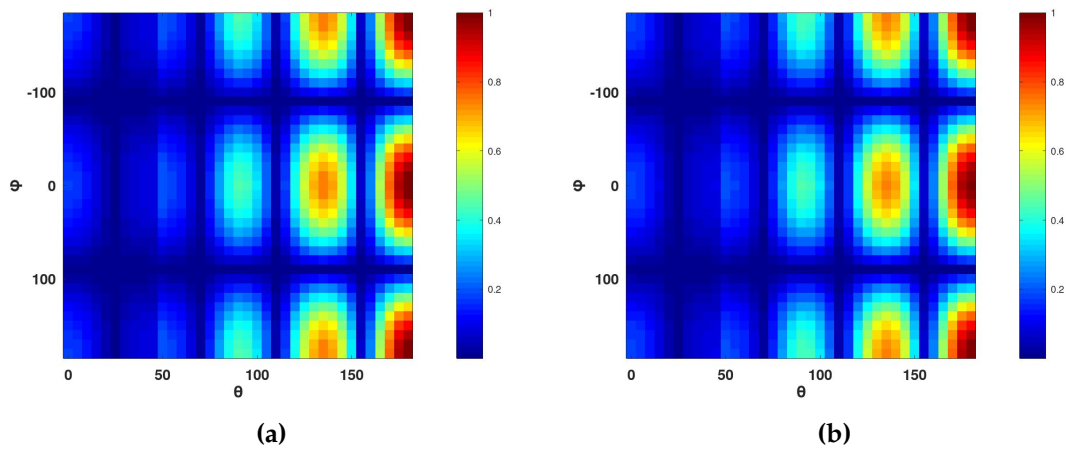


Figure B.4 – Residues' amplitude related to the fourth resonant frequency ($f_4 = 2.35 \text{ GHz}$) extracted using (a) MP and (b) VF

Appendix C

Resonances of non spherical PEC objects

The PEC objects are simulated using CST time solver. A probe is placed at 1 m from each object to recover the back-scattered response for multiple incident angles (table 4.11). The objects are shown in fig. C.1.

The singularities are extracted using VF algorithm with a model order fixed at 26. The following results are presented for one of the two field components.

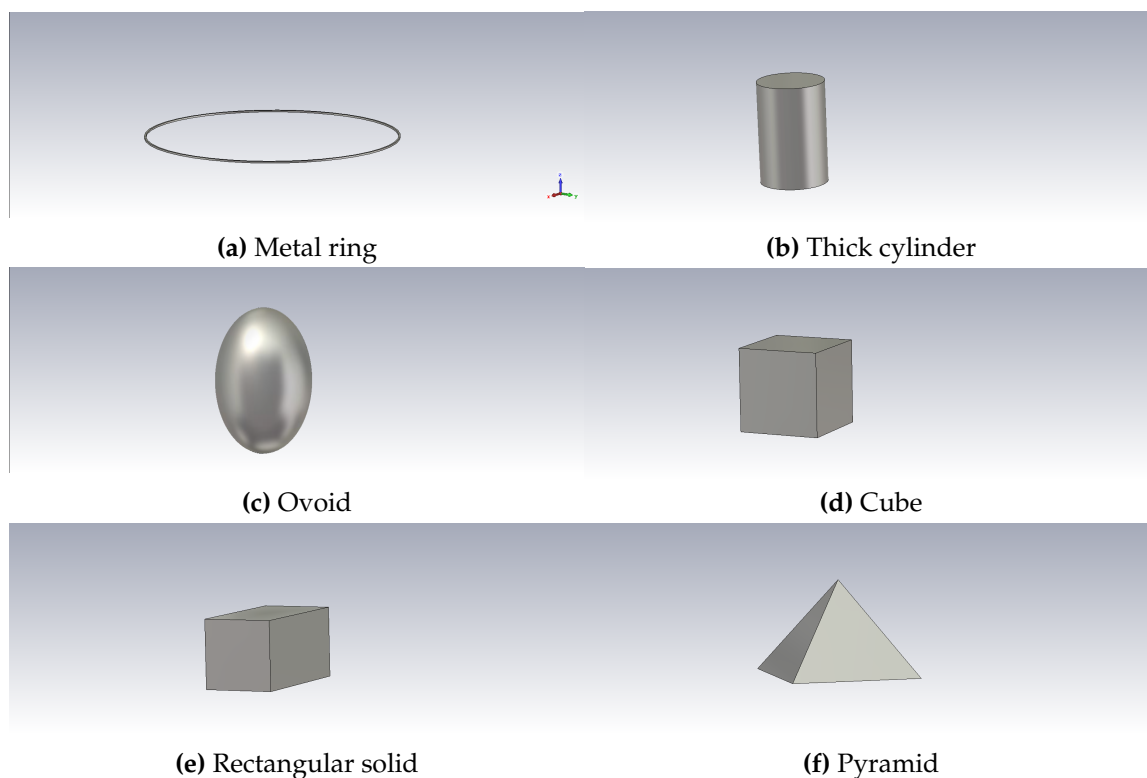


Figure C.1 – Non spherical PEC objects.

- **Metal ring:** The amplitude response and the CNRs extracted at different incident angles are shown in fig. C.2, for the E_ϕ component. We can notice

that resonance peaks appear clearly in the amplitude response, meaning that the metal ring is a strong resonating object like the thin wire. This is observed with the CNRs were the damping factors are low.

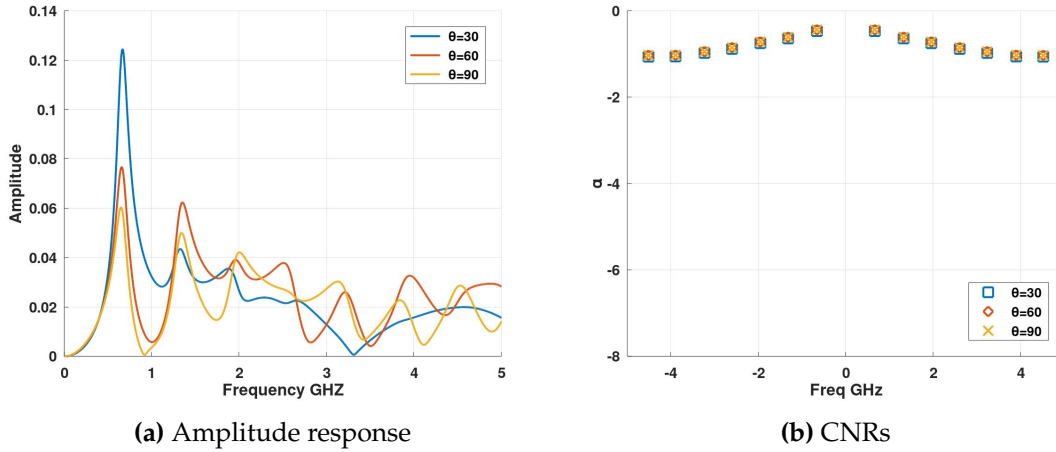


Figure C.2 – Amplitude response and CNRs of E_ϕ of the metal ring in the back-scattering direction

- **Thick cylinder:** The thick cylinder, with a ratio of $L/D = 1.5$, is a weak resonating object as seen from its amplitude response and CNRs distribution in fig. C.3, for the E_θ component.

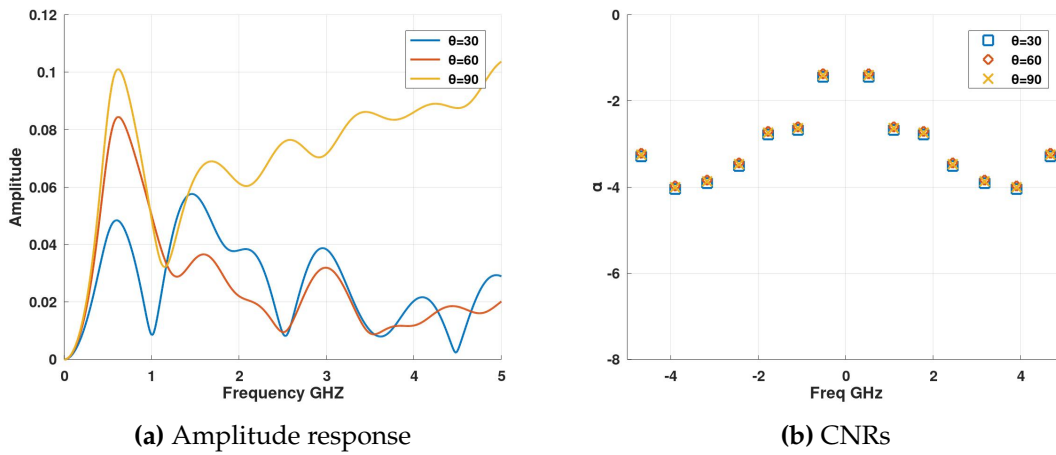


Figure C.3 – Amplitude response and CNRs of the thick cylinder in the back-scattering direction

- **Ovoid:** Fig. C.4 shows the amplitude response and CNRs at different incidence angles, for the E_θ component, when the incident wave is polarized vertically. The PEC ovoid (axial ratio = 1.5) behaves like a PEC sphere where there is multiple resonances in this frequency band.

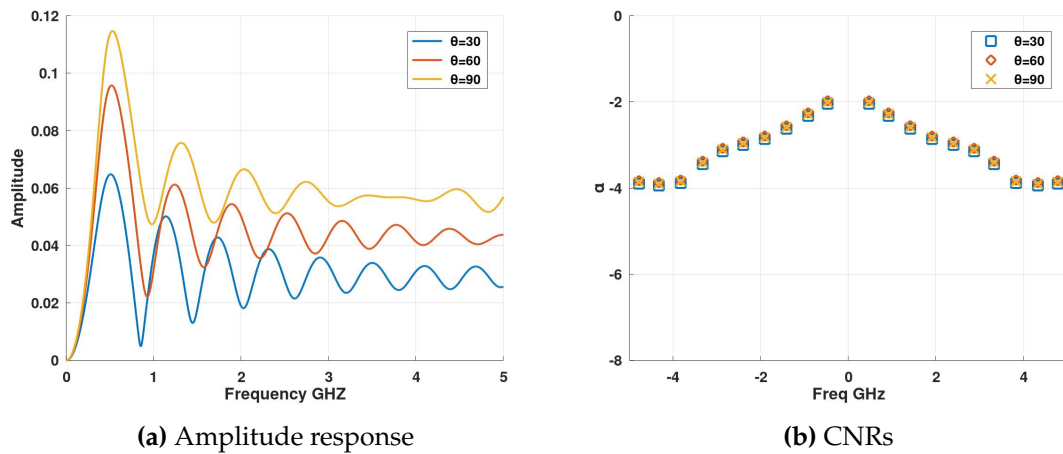


Figure C.4 – Amplitude response and CNRs of an ovoid in the back-scattering direction

- **Cube:** The amplitude response and the CNRs of the rectangular solid are shown in fig.C.7 for multiple incident angles and for E_θ component.

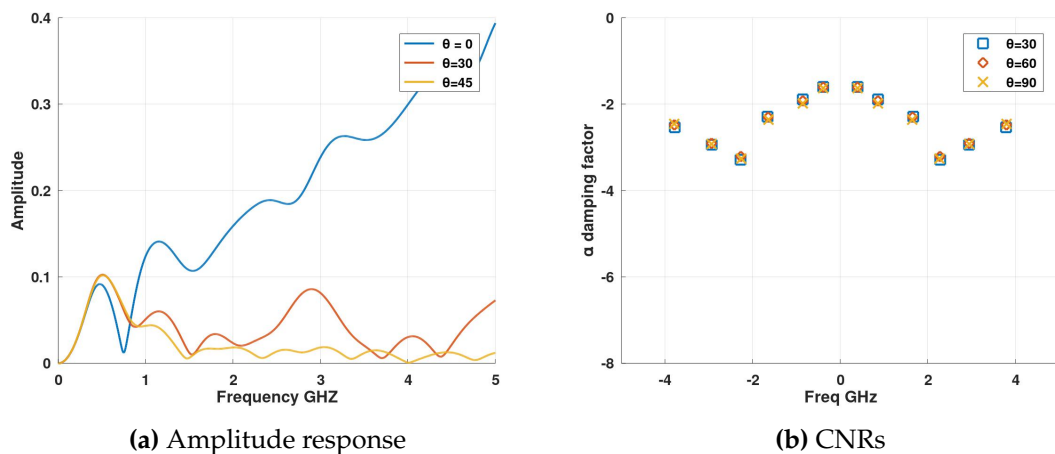


Figure C.5 – Amplitude response and CNRs of a cube in the back-scattering direction

- **Rectangular solid:** The amplitude response and the CNRs of the rectangular solid, having a square face, are shown in fig.C.7 for multiple incident angles and for E_θ component.

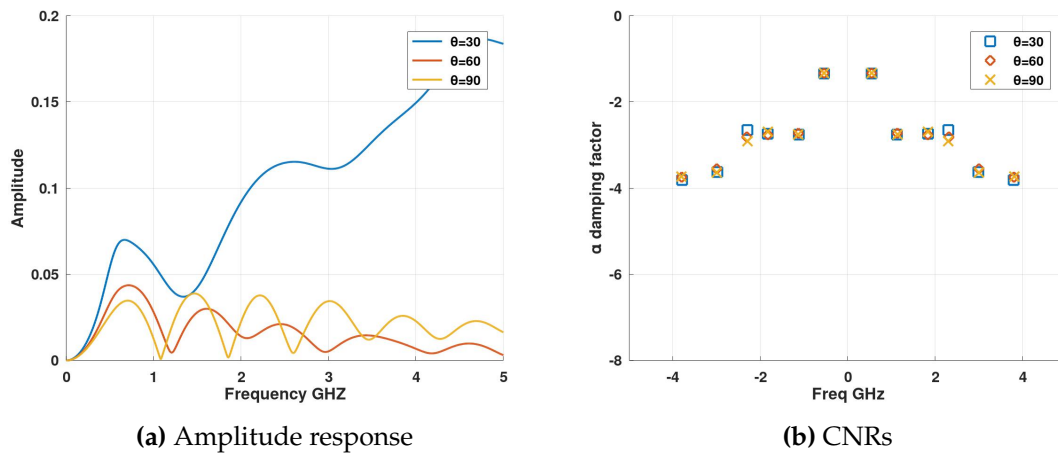


Figure C.6 – Amplitude response and CNRs of a rectangular solid in the back-scattering direction

- **Pyramid:** The amplitude response and the CNRs of the PEC pyramid are shown in fig.C.7 for multiple incident angles and for E_θ component.

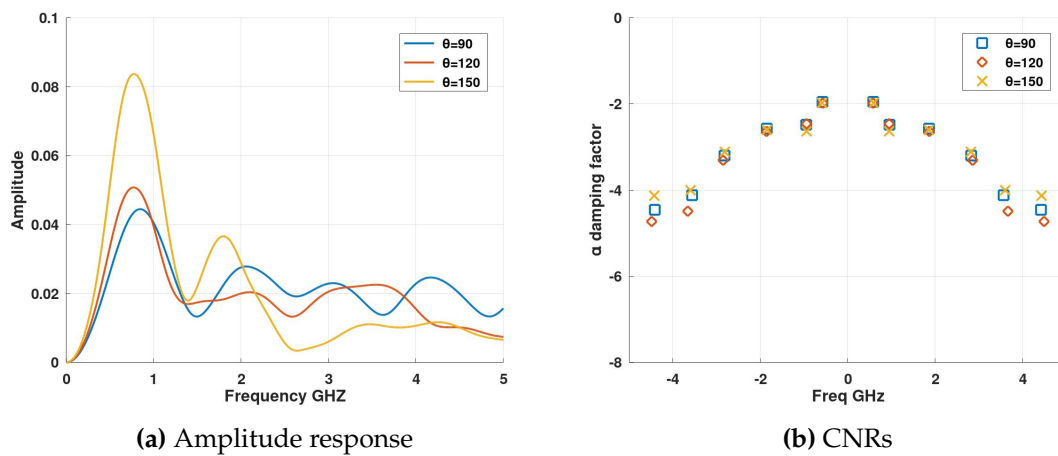


Figure C.7 – Amplitude response and CNRs of a pyramid in the back-scattering direction

Appendix D

Scattered field dataset construction

In order to find the optimal structure of the dataset using FD responses, we assessed three different forms based on the amplitude and phase of the SF responses of the 5 spheres. Indeed, we can not use the complex frequency response directly as the classifiers only support real numbers. The 3 datasets used for evaluation are constructed from the following data:

- Amplitude + Phase responses
- Amplitude response
- Phase response

Table D.1 – Accuracy (%) and σ_d of CNN trained using each dataset of FD data

Datasets	FD data					
	Amplitude + Phase		Amplitude		Phase	
	Accuracy	σ_d	Accuracy	σ_d	Accuracy	σ_d
20% test data	97	2.3	98.3	1	98.2	0.9
Noisy data 10dB	65	4	68	3	67.5	2.6
Sphere diameter = 30cm	45.2	5.5	60	4.5	43.4	5.3
Smaller sphere = 1 resonance	55	6.2	53	4.8	52	4

Those 3 structures are evaluated using CNN with same training parameters presented in 4.3.2. Table D.1 shows accuracy results and standard deviation σ_d for multiple datasets when using CNN with the 3 cases of FD data. The results show that all three dataset structures have similar performances and that by using the amplitude response we get slightly better results when testing with larger spheres. This decrease in the accuracy when using amplitude and phase

can be due to either of two reasons: first, the CNN topology might have needed some modifications in the training parameters as the data are larger for this dataset or, second, as the phase alone has less accuracy than the amplitude, so, the combination of both might be decreasing the accuracy. Hence, we choose to construct the FD dataset using solely the amplitude response.

Appendix E

Angular sector classification

Spherical objects

Table E.1 summarizes the results obtained when classifying angular sectors of the 5 sphere types with CNN classifier trained using noiseless SEM data. The classification results using CNN are presented as it was shown that it has the best performances over the other classifiers.

Those results are presented for the following test data: larger sphere size of 30 cm diameter ($\varnothing = 30$ cm), smaller spheres having less than 5 resonances in the frequency band (4 to 1 resonances in the frequency band). Finally, the noisy data of 10 dB SNR of 15cm diameter sphere is presented. We notice that the accuracy of noisy data of both dielectric spheres are the highest as they are very resonating so the CNR extraction is easier at low SNR making the residues computation quite accurate.

Table E.1 – Accuracy (%) of angular sectors classification of different test data for the 5 spheres using CNN classifier trained using SEM data

Test data	Spheres				
	PEC	$\epsilon_r=4, \sigma=0.5$	$\epsilon_r=2$	$\epsilon_r=4$	$\epsilon_r=9$
$\varnothing = 30$ cm	97	96	99	98	98
4 resonances	99.7	99.5	99.2	98	98
3 resonances	99.5	98.5	99.5	96	96
2 resonances	94	90.8	90	90	90
1 resonance	77	72	75	70	70
10 dB SNR	62	57	58	72	74

Non spherical PEC objects

For the other objects, the results are summarized in table E.2. The metal ring, the ovoid and the thick cylinder are cut into 10 sectors in the same manner as the thin wire shown in section 5.4.1 in chapter 5. The cube and the pyramid are cut into 6 and 8 sectors respectively. Both of those objects have the least performances like the rectangular solid seen in chapter 5. This confirms that objects with sharp edges are harder to treat.

Table E.2 – Accuracy (%) of angular sectors classification of different test data for the non spherical PEC objects using CNN classifier trained with SEM data

Test data	PEC objects				
	Ring	Thick cylinder	Ovoid	Cube	Pyramid
20% remaining samples	98	96	96	85	83
Noiseless larger objects	95	94	94	90	88
Noisy larger object 10dB SNR	79	72	75	64	60
Noiseless smaller objects	76	72	75	64	60
Noisy smaller object 10dB SNR	65	60	60	56	52